The dynamics and characterization of self-assembly in biopolymers and biosystems

Fernando Rafael Jativa Guzman
ORCID Identifier: 0000-0001-5679-3968

Submitted in total fulfilment of the requirements of the degree of Doctor of Philosophy

May 2021

DEPARTMENT OF BIOMEDICAL ENGINEERING

THE UNIVERSITY OF MELBOURNE

Abstract

Biological self-assembly is the foundation of the strength and elasticity which characterizes nature-derived biomaterials, including the cell's architecture. Thus, an in-depth understanding of the mechanics behind this process can open the doors to various biomedical applications. For this purpose, this research employed novel experimental and characterization techniques to study self-assembly in biopolymers and biosystems. Initially, a droplet dissolution technique in liquid crystalline stages was used to analyze the process of self-assembly in two important biopolymers, silk and cellulose. Here, we report an effective and simple approach based on droplet dissolution in a liquid binary phase for the formation of silk fibroin transparent spheres as well as cellulose microbeads, both of which can span several hundred micrometers in diameter. The microstructure of the spheres formed at different ethanol concentrations was characterized by electron microscopy. High concentrations of ethanol caused droplets to be encased in a thin shell which collapses once it is taken out of the liquid phase. Generally, low ethanol concentrations produce transparent silk spheres and solid cellulose microbeads. This work on biopolymers demonstrates that controlled droplet dissolution self-assembling may be explored as a novel and effective way to tailor the microstructures of nature-derived biomaterials. The spheres generated in this manner have several different characteristics which can have multiple potential uses, such as templates for scaffolds, microcarriers, as well as photonics and nano-technological applications.

The second part of this thesis investigated self-assembling in biosystems. Cell aggregates are an important tool in studying tissue remodelling, extracellular matrix formation, cell-cell interaction, and last but not the least, tissue-like biomechanical properties. A medium-throughput method was designed to characterize the mechanical properties of mesenchymal cell aggregates. This study was the first to present a precise and fast method to determine the Young's modulus of mesenchymal cell aggregates, utilizing a step-by step aspiration technique.

We were also able to recreate conditions that very closely resemble the *in vivo* environment, where the cells were found to be stretched, and the spheroids are soft and elastic

Finally, potential applications of the self-assembled cell aggregates were explored in lung disease study and drug screening, specifically for Idiopathic Pulmonary Fibrosis (IPF). We demonstrated that the cell aggregates from IPF patients show an increase in stiffness, therefore mechanical testing of spheroids is an effective technique to study this disease. It was also found that a novel compound, PF670462, modulates the effect of TGF- β and inhibits the fibrotic response of IPF cell aggregates. That is, this drug softens IPF spheroids and downregulates fibrogenic gene expression, therefore providing basis for the potential use of PF670462 in IPF treatment.

Declaration

I, Fernando Jativa, declare that:

1. i. this thesis comprises only my original work, except where indicated in the Preface;

2. ii. due acknowledgement has been made in the text to all other material used;

3. iii. the length of this thesis is fewer than the maximum word limit in length, exclusive of tables, bibliographies, and appendices.

Signed:

_____

Preface

All research work and thesis preparation were carried out under the supervision of Prof. Peter Lee, Prof. Alastair Stewart, and Prof. Xuehua Zhang, with helpful discussions, advice and editorial feedback also provided by Ms. Trudi Harris, MSN Shenna Langenbach, Dr. Asres Berhan, Dr. Bryan Gao, Dr. Bernd Wicklein, MSc Gabriela Cabezas and Dr. Hannah Alcantara. Significant experimental contributions have been provided by other laboratories. Dr. Salajkova prepared the initial CNC solution which I used for the cellulose study. Dr. Bernd Wicklein and Dr. Christina Schütz performed Polarized Optical Microscopy (POM) in the shrinking droplet, using a polarized microscopy cell designed by Dr. Michael Agthe (schematics included); provided additional SEM images and the final version of the schematic of cellulose assembling. Finally, Mr. Yanqi Wu helped in the development of the image analysis software for aspiration. Chapter 10 includes a detailed account of thesis contributions for each chapter.

This research was funded in part by the Australian Research Council (ARC) through ARC Linkage Grant (LP160100635), and was additionally supported by the Ecuadorian Government through their Excellence Scholarship program.

Third-party copyright material was used for all figures in Chapter 2 – Literature Review. Permissions were obtained in all cases to use this material in the open access version of the thesis.

Communications

Peer-reviewed publications:

1) Berhan A, Harris T, Jaffar J, **Jativa F**, Langenbach S, Lönnstedt I, Alhamdoosh M, Ng M, Lee P, Westall, G, Wilson N, Wilson M, Stewart A.G. (2020) Cellular microenvironment stiffness regulates eicosanoid production and signaling pathways. *Am J Respir Cell Mol Biol.* (2020) doi: 10.1165/rcmb.2020-0227OC

2) **Jativa F**, Berhan A, Harris T, Wu Y, Xumei G, Jaffar J, Westall G, Lee P, Stewart A.G. Modeling the mechanical properties of human lung mesenchymal cell aggregates. In Progress

3) Keenan CR, Langenbach SY, **Jativa F**, Harris T, Li M, Chen Q, Xia Y, Gao B, Schuliga MJ, Jaffar J, Prodanovic D, Tu Y, Berhan A, Lee PVS, Westall GP and Stewart AG (2018) Casein Kinase 1δ/ε Inhibitor, PF670462 Attenuates the Fibrogenic Effects of Transforming Growth Factor-β in Pulmonary Fibrosis. *Front Pharmacol*. 9:738. doi: 10.3389/fphar.2018.00738

4) **Jativa F**, Zhang X. Transparent Silk Fibroin Microspheres from Controlled Droplet Dissolution in a Binary Solution. *Langmuir*. 2017;33(31):7780-7787. doi:10.1021/acs.langmuir.7b01579

5) Lu Z, Rezk A, **Jativa F**, Yeo L, Zhang X. Dissolution dynamics of a suspension droplet in a binary solution for controlled nanoparticle assembly. Nanoscale. 2017;9(36):13441-13448. doi:10.1039/c7nr02704d

6) **Jativa F**, Schütz C, Bergström L, Zhang X, Wicklein B. (2015) Confined self-assembly of cellulose nanocrystals in a shrinking droplet. *Soft Matter*. (2015) ;11(26):5374-5380. doi:10.1039/c5sm00886g

Conference presentations and abstracts:

1) Lab-on-a-Chip and Microfluidics World Congress, San Diego, USA 2018

   Oral Presentation

   Jativa F, Berhan A, Harris T, Lee P, Jaffar J, Westall G, Stewart AG (2018) Multi-dimensional Anti-Fibrotic Drug Screening Approaches in Human Lung Fibroblast Spheroids

2) American Thoracic Society Conference, San Diego, USA 2017

   Accepted abstract

   Berhan A, Harris T, Langenbach S, Schuliga M, **Jativa F**, Lee P, Jaffar J, Westall G, Stewart AG (2018) Softening Cellular Microenvironments Augments Glucocorticoid Actions

3) Australia's Medtech Conference & International Conference on Mechanics in Medicine and Biology, Melbourne 2017

   Oral Presentation

   Jativa F, Berhan A, Harris T, Lee P, Jaffar J, Westall G, Stewart AG (2017) Biomechanics and Funcitonality of Human Lung Multi-Cell Aggregates and 3D Mesenchymal Spheroids

4) American Thoracic Society Conference, in San Diego 2016

   Poster Presentation

   Jativa F, Schuliga M, Wang Z, Harris T, Jaffar J, Westall, G, Lee P, Stewart AG (2016) Increased Stiffness and Changes in TGFbeta-Induced Gene Expression in Lung Fibroblast Spheroids from IPF Fibroblasts

5) Organ on a Chip World Congress, Boston, USA 2016
   Oral Presentation
   Jativa F, Wang Z, Harris T, Lee P, Jaffar J, Westall G, Stewart AG (2016)
   Increased stiffness of lung fibroblast cell aggregates in idiopathic pulmonary fibrosis

6) International Workshop on Cell and Tissue Mechanobiology, Beijing, China 2016
   Oral Presentation
   Increased stiffness of lung fibroblast cell aggregates in idiopathic pulmonary fibrosis

7) American Thoracic Society Conference, San Diego, USA 2015
   Accepted abstract
   Stewart AG, Harris T, Wong A, **Jativa F**, Chen, W, Lee P, (2015)
   Airway smooth muscle spheroids: stiffness and glucocorticoid responsiveness

Other collaborations during candidature:

8) Alcantara, H.J.P., **Jativa, F**., Doronila, A.I. et al. Localization of mercury and gold in cassava (Manihot esculenta Crantz). Environ Sci Pollut Res 27, 18498–18509 (2020). https://doi.org/10.1007/s11356-020-08285-3

Acknowledgments

This work would not have been completed without the people I will mention below—colleagues, friends, and family who have very willingly shared their knowledge and experience with me during the course of this research work. Firstly, I am immensely grateful to my supervisors, Prof. Peter Lee and Prof. Alastair Stewart, who have mentored me throughout this journey. Their wisdom and constant guidance helped me shape not only my research questions, but also my critical thinking, laboratory skills, and multidisciplinary knowledge in Bioengineering and Pharmacology. Their constructive criticisms and advice encouraged me to keep pushing the boundaries not only of my work, but also of myself.

I would also like to thank my first supervisor Prof. Xuehua Zhang, who supported my PhD application and acceptance into the program. I truly appreciate her guidance at the beginning of the project, and even after her departure to a new institution, continued to share her insights and guidance selflessly. It was really challenging to change supervisors and project direction, but I always felt supported in this process. Without her intellectual creativity, the initial impetus that led to this study would have remained unexplored. Her support was essential for me to publish and complete the first part of this thesis.

I am in great debt to the Ecuadorian government who was instrumental in the achievement of this research by awarding me an Ecuadorian Excellence Scholarship which allowed me to pursue my PhD at the University of Melbourne; the School of Engineering and the Department of Pharmacology and Therapeutics, without which this multidisciplinary study wouldn't have been possible; the Biological Optical Microscopy Platform (BOMP) which provided technical assistance for sample and imaging processing; and Newman College, which provided not only a residential scholarship, but also a supporting and diverse community which became my new home.

I also have immense gratitude to the following people who have either collaborated and/or helped me in the different parts of this research: Dr. Bernd Wicklein, Dr. Christina Schütz, Dr. Lennart Bergström, Dr. Ziyang Lu, Dr. Leslie Yeo, Dr. Chenglong Xu, Dr. Simon Crawford, Dr. Allison Van De Meene, Dr. Paul McMillan, Dr. Ellie Cho, Ms. Laura Leone, Dr. Zhexing Wang, Dr. Gao Xumei, Dr. Jade Jaffar, Dr. Glen Westall, Dr. Michael Schuliga, Dr. Narelle tunstall, Dr. Tatiana Kameneva, Prof. Spas Kolev, Dr. Augustine Doronila, and Dr. Hannah Alcantara.

To the incredibly kind and supportive members of the Stewart Lab across the years, Meina Lee, Yanqi Wu, Qianyu Chen, Mehdi Zia, Nithya Fernandopulle, Tina Cheng, Maria Bellesis, Kexin Shi, Danica Radojicic, I want to extend my appreciation for all your help. My special thanks go to Ms. Trudi Harris and Ms. Shenna Langenbach for the training, technical and personal guidance. To Asres Berham, who is not only a great researcher and colleague, but a good friend who have inspired me with his kindness and admirable work ethics.

A big thank you to my bestfriend Martin Reinoso, who unhesitatingly supported my idea to apply for the scholarship and study in Australia. Two decades of friendship and his willingness and readiness to help me in many different ways has never faltered. In the last 7 years here in Australia, he was a family who always encouraged me to not give up and stay strong in the PhD journey.

To my parents Fernando and Nancy, and my siblings Andres and Caro, who supported my dream and encouraged me to start this journey, and across the years and distance have always been there for me. I miss you especially now, and I hope we can meet altogether soon.

Above all, I want to thank my loving wife Hannah Alcantara, who I met at the beginning of this journey and supported me relentlessly despite many setbacks and challenges. It was not easy in many points, but your company and love made it all worth it.

This thesis is for you Hannah, and Raphaela, our daughter.

Table of contents

List of Tables

List of Figures

Ethics Statements

All experiments using cells from animal or human origin were conducted in accordance with the Australian Code of Practice for the Care and Use of Animals for Scientific Purposes, and the National Statement on Ethical Conduct in Human Research.

Chapter 1: Thesis Introduction

1.1 Foreword

The concept of self-assembly has been accepted as a foundation in pattern formation and formation of complex structures. Nearly all nature-derived biomaterials' composition and the resulting functionalities depend on self-assembly. This ubiquitous process refers to the organization of molecules into well-ordered and defined entities and is the basis of the strength and plasticity that can be seen in biopolymers and biosystems, constituting in this way a foundation for a plethora of applications, including but not limited to the fields of photonics, nano-technologies, and biomedicine. In addition, the understanding of how some nature-derived biomaterials self-assemble spontaneously can lead to novel synthetic biomaterials which has significant applications in the biomedical industry.

A range of nature-derived biomaterials exhibit self-assembly. The following thesis studies the dynamics and characteristics of self-assembling in selected biopolymers and biosystems, specifically: silk, cellulose, and mesenchymal cells. The characterization of the structural properties of self-assembling biomaterials is an important step in defining its functionalities and applications. One of their most important property is the fact that their bioactive components can be potentially situated in target locations within their internal arrangement. The study of the aggregates formed from mesenchymal cells helped us understand the complex associations within the spheroid and from there formulate some hypotheses relating to whole tissues and organs. The application of mesenchymal cell aggregates in disease characterization and drug screening was thereby explored as a result.

1.2 Research Aims

The overall goal of this thesis is to improve the current understanding of biological self-assembling through the development of novel experimental methods and characterization techniques. The biopolymers silk and cellulose were selected due to their natural abundance and unique physical properties. This dissertation also explored self-assembling of a biosystem consisting of mesenchymal cells, chosen due to their multipotency and important implications in biomedicine. The results of this research will enhance our understanding of the self-assembly process in biomolecules and biosystems, which can lead to significant implications in bio-nanotechnogy and biomedicine.

The specific aims of this thesis are:

Aim 1. To evaluate the self-assembling process of silk and cellulose biopolymers by droplet diffusion in liquid crystalline phases, and to characterize the resulting structures.

Aim 2. To evaluate the self-assembling process of a biosystem of mesenchymal cells and to design a mechanical testing methodology for the characterization of the cell aggregates obtained.

Aim 3. To explore the potential applications of cell aggregates as a tool for disease modelling and drug discovery.

1.3 Contributions of the Thesis

The main contributions of this thesis are as follows:

1.3.1 The Formation of Transparent Silk Fibroin Microspheres

Silk is a natural polymer that has a wide range of applications. To generate silk spheres, a sessile microdrop from a silk fibroin liquid solution was submerged in a surrounding phase of ethanol in toluene at low concentrations. The droplet goes through two phases. Initially we observed volume growth due to the intake of organic solvents from the surrounding phase. The second phase consist in the self-assembling of silk during the droplet dissolution process. The

study shows this is an effective method way to assemble silk spheres with switchable transparency. Additionally, the silk internal and surface structure is characterized, and co-related to the dissolution rate. The resulting transparent spheres could be utilized as an optical element in bioelectronics or microcarriers. The details of this study are presented in Chapter 4.

1.3.2 The Formation of Cellulose Microbeads

For this study, polarized light microscopy was used to observe the self-assembling of cellulose nanocrystals (CNC) in a shrinking droplet. By controlling the droplet dissolution rate, it is possible to follow the spatial evolution and coalescence of birefringent spheroids, and effectively control the morphology of the resulting microbeads. The nematic microstructure is revealed through electron microscopy, and it appears to be independent of the dissolution rate due the formation of tactoids in the early stages of the dissolution process. Our findings, presented in Chapter 5**,** provide detailed information about the structural self-assembling of aqueous crystalline CNC and offer exact nanostructures that could be useful in photonic and nanotechnological applications.

1.3.3 The Development of a Methodology to Study the Mechanical Properties of Cell Aggregates

Cell aggregates are important tool to study tissue remodelling, extracellular matrix formation, cell-cell interaction and tissue-like biomechanical properties. More recently, there have been an increased interest in the development of methods to characterize the mechanical properties of these spheroids. And although several studies effectively characterize ‘viscous′ liquid-like cell aggregates, the mechanical properties of ‘elastic’ solid-like spheroids still require further study.

In Chapter 6 we proposed a medium-throughput model to determine the mechanical properties and the characterization of mesenchymal 3D spheroids. This is the first work that present a precise technique to establish the Young’s modulus of elastic cell aggregates using

step-by-step aspiration. We show that mesenchymal cells form spheroids of regular spherical formation with a smooth and elastic exterior.

1.3.4 The Application of 3D Spheroids in the Study of Idiopathic Pulmonary Fibrosis

In Chapter 7 we explored the preliminary applications of mechanical testing in the study of biosystems. Samples from healthy donors and patients with Idiopathic Pulmonary Fibrosis (IPF) were compared and studied. Furthermore, the self-assembling of cells into spheroids demonstrated that mechanical testing is an effective tool to characterize samples from patients with the disease. Also, the self-assembling of cell into spheroids showed that fibroblast spheroids imitate some of the important properties of fibroblasts in IPF lungs including high collagen production, increased levels of active transforming growth factor beta (TGF-β), and increased stiffness. Lastly, self-assembled spheroids may depict a new assays system for pre-clinical drug evaluation, and warrant further research.

1.4 Thesis Outline

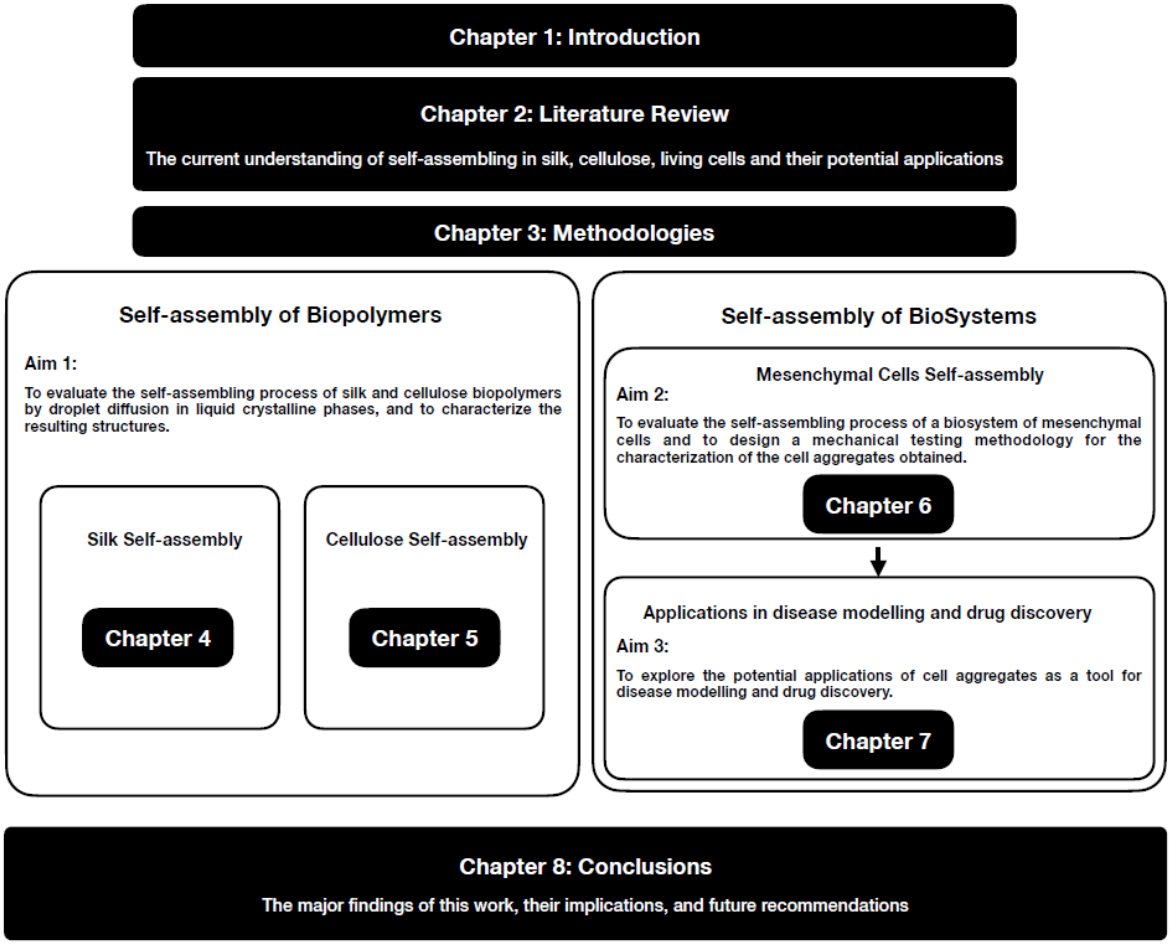

Figure 1.1. Thesis Outline

Chapter 2 starts by reviewing the current understanding of the dynamics of self-assembling and the differences between equilibrium and non-equilibrium systems. The self-assembling dynamics are contrasted between particles, molecules and living organisms, and their respective assembled structures are discussed briefly. As a basis for the subsequent chapters, biopolymers self-assembly is explored in detail, with special emphasis in cellulose and silk; as well as biological systems self-assembling with a focus in the application for cell aggregates. The materials and methodologies employed in all the experiments pertaining to the different experiments are detailed in Chapter 3.

Chapter 4 and 5 address **Aim 1** of the thesis, which is to evaluate the self-assembling process of biopolymers by droplet diffusion in liquid crystalline phases. The methodology,

results and discussion are described in these chapters. Silk and cellulose shrinkage rates are determined by contact angle measurements and image analysis. In Chapter 4, regulated droplet dissolution was examined as a new and efficient way to tailor transparent silk fibroin microspheres. In Chapter 5, polarized light microscopy of cellulose self-assembly showed tactoid formation into birefringent spheroids, while electron microscopy disclosed the nematic microstructure of the assembled cellulose.

Chapter 6 and 7 describe the self-assembling of biosystems and its applications. Chapter 6 addresses **Aim 2,** which is to evaluate the self-assembling process of a biosystem of mesenchymal cells. The details of the methodology for cell spheroid characterization are described in this chapter. The experimental study was achieved through mechanical testing of a spheroid through micro-pipette aspiration. Chapter 7 addresses **Aim 3** by evaluating the applications of cell aggregates in the study of lung diseases and drug discovery.

Finally, Chapter 8 summarizes all finding of the thesis, conclusions and possible advancements of the current work

Chapter 2: Literature Review

2.1 Self-assembly

2.1.1 Introduction to Self-assembly

To better understand self-assembly, it is necessary first to introduce hierarchies and hierarchical structures. From a conceptual point of view, hierarchies are a way to logically order systems that are not continuous but made of different parts Each of these hierarchies has unique characteristics and belong to a specific scale. (Salthe, 2012).

There are two know logical forms of hierarchy: compositional and subsumption. The compositional hierarchy is a reductionist theory, which assumes that we can derive critical knowledge by subdividing a system. In contrast, subsumptive hierarchy does not focus only on the system itself but assumes that critical information is found in other prior systems, such as ancestry (Salthe, 2012).

The present thesis focuses on compositional hierarchy theory and how can it be applied to understand the role of atoms, molecules, and nanoclusters in modelling complex systems. Compositional hierarchy, also known as "scale hierarchy", allow us to outline defined structures at a given scale and thus expand our understanding of a material or biological process.

A typical example of scale hierarchy are materials with more than one structure at different scales (Lakes, 1993). As Lakes (1993) states: “the hierarchical order of a structure or a material may be defined as the number (n) of levels of scale with recognized structure” (p. 511). Hierarchical structures can be found in nature but also in manufactured materials. If it is man-made, the structural hierarchy may be tailored for specific applications. At its basis, hierarchical structures also can be the footing to synthesize unique formations with advantageous characteristics (Lakes, 1993).

The hierarchical structure can determine the physical, chemical and mechanical properties of a material. Therefore, extensive research is needed to understand materials’

hierarchical structure, assembly process, and novel hierarchical assemblies (A. Wang, Huang, & Yan, 2014). It is here that self-assembly plays a key role, as it reveals how several of these complex hierarchical structures are formed and can be used in turn to create assemblies with advanced properties.

There are various approaches that have tried to define what self-assembly (SA) is, as it is not a standardized subject. Self-assembly it is found in nature and in applied science. However, although many fields have found uses for SA, the term has been overused for things that may not fit in the criteria. One of the concepts that is used to define self-assembly states that "Self-assembly is the autonomous organization of components into patterns or structures without human interaction" (George M. Whitesides & Grzybowski, 2002, p. 2418). These components form complex, stable and larger structures through forces of attraction and repulsion, and it is important to notice there is no external work to help. Another definition with more limitation says that SA is "the spontaneous formation of organized structures from many discrete components that interact with one another directly and/or indirectly, through their environment" (Grzybowski, Wilmer, Kim, Browne, & Bishop, 2009, p. 1112). By using the word "discrete", this definition omits pattern formation where the geometry of single particles is not relevant for the assembling process (Grzybowski et al., 2009). Other definitions include the way SA occurs "spontaneously" to form ordered aggregates (G. M. Whitesides & Boncheva, 2002). There are some rules that have been proposed to help identify SA, including that the final product must be reversible; the components should move respect to each other; and that it usually demands to take place in fluid phases or at an interface to permit the movement of the elements (Philp & Stoddart, 1996; George M. Whitesides & Grzybowski, 2002). Furthermore, SA requires that the elements are in equilibrium while between aggregated and non-aggregated phases, or that they regulate their place when in an aggregate, respecting to the other's position (George M. Whitesides & Grzybowski, 2002).

Moreover, hierarchical self-assemblies consist of ordered levels that primarily turns elementary molecular units into organized secondary constructions using noncovalent interactions; these work as the building blocks that can structure more intricate formations in further levels (Datta, Saha, & Stang, 2018). The changing nature of the many levels allows for more structural and functional prospects (A. Wang et al., 2014).

Molecular SA is what is behind the building of nanostructures, thus it should prove to be useful in different ways. It could certainly be the most labour-saving, cost-effective technique to build the nanoscale structures of the future (Comrie, 2011; Patch & Smalley, 2003). Molecular SA gives us a prototype for the relation that exists between the practical appearance and the conformational change of molecules, thus helping us understand proteins and other biomolecules (Okabayashi, Ishida, & O'Connor, 2003). This system is made up of molecules or segments that interconnect. They can be similar or different, and the interaction carries them to an ordered state. Moreover, the molecular structure dictates the formation of the assembly. It is also found everywhere in materials science, biology and chemistry. The interactions are mostly weak and noncovalent (G. M. Whitesides & Boncheva, 2002).

A very common example of self-assembly is DNA (Pinheiro, Han, Shih, & Yan, 2011). It is not the only one, however, other examples include proteins (Dill & MacCallum, 2012), opals (S.-H. Kim, Lee, Yang, & Yi, 2011; Vogel, Retsch, Fustin, Del Campo, & Jonas, 2015), lipid vesicles (I. A. Chen & Walde, 2010), colloids (D. Evans & Wennerström, 1999), among others. Also, organized fluids like micelles and microemulsions, and supramolecular assemblies (Mackay, 2003). As mentioned before, proteins have been researched. Polypeptides, in this regard, are inexpensive, and have a straightforward formation in water. This results in making it perfect to study for better understanding (Boden, 2003). Surfactants, like soap or detergent, have also been investigated since they form a wide range of structures. They have the benefits of being able to compartmentalize and encapsulate material for drug delivery (John,

McPherson, & Bose, 2003). SA also provides a feasible way to build three dimensional microstructures (G. M. Whitesides & Boncheva, 2002).

There is a distinction in SA that authors make among equilibrium self-assembly (ESA) or static self-assembly and dynamic self-assembly (DySA) (Grzybowski et al., 2009). This is done by taking the thermodynamic result of the aggregates. As its name suggests, ESA refers to structures that reach a global or local equilibrium and there is no dissipation of energy. While the formation is occurring, it might need energy, but after it is done, it becomes stable (George M. Whitesides & Grzybowski, 2002). To further understand this, "At thermodynamic equilibrium, SA evolves the system's components intro a structure that corresponds to the minimum of an appropriate thermodynamic potential" (Grzybowski et al., 2009, p. 1112). These systems also have the benefit that they form crystals and can self-heal if hurt (G. M. Whitesides & Boncheva, 2002). In this type of assembly one can find organic crystals (Desiraju, 1995; Moulton & Zaworotko, 2001), inorganic crystals (Aizenberg, Muller, Grazul, & Hamann, 2003; Blake et al., 1999), supramolecular structures (Holliday & Mirkin, 2001; Lehn, 1988; Philp & Stoddart, 1996) and others.

In DySA, on the other hand, the interactions that cause the formation of structures happen if there is dissipation of energy (Grzybowski et al., 2009; George M. Whitesides & Grzybowski, 2002). DySA systems work when there is low entropy and can arrange themselves into complex structures, and by the dissipation of energy, they increase their entropy (Grzybowski et al., 2009). For DySA to happen, externally delivered energy must adjusts at the minimum one kind of interaction. But the forces in play should not all repulse or attract, they should fight one another (Grzybowski et al., 2009). One complex example of this is biological cells self-assembly (Grzybowski et al., 2009).

2.1.2 Characterizing the Self-assembling Process

There are different methods available to characterize the self-assembly process. One of the most effective methods to investigate changes during the self-assembling process is dynamic light scattering (DSL), also known as photon correlation spectroscopy. DSL scatters light from small-scale particles, which can be used to measure the Brownian motion of the macromolecules in the solution and determine the particle size. (Benkirane, Meignen, Boyer, & Verine, 1989; Stetefeld, McKenna, & Patel, 2016).

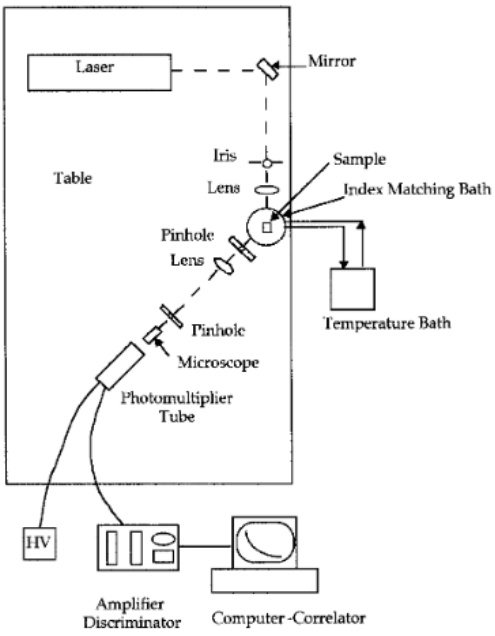

As shown in Figure 2.1, a laser sends a beam to a sample, and the light is scattered at a given angle. This output signal gets digitized through a photon counting system, and the resulting "scattering intensity" measurement is sent to an autocorrelator which calculates the particle size (Pecora, 2000).

Figure 2.1. Diagram of a Photo Correlation Spectroscopy. Reproduced with permission.[1]

Examples of DSL applications for the study of self-assembly includes hybrid hydrogel system (Kopecek, 2009; J. Yang, Wu, Konak, & Kopecek, 2008), amelogenins proteins (Moradian-Oldak, Leung, & Fincham, 1998), copolymers (Stepanek et al., 2010), peptides (R. Zhang, Yang, Chu, Hartley, & Kopecek, 2015), and magnetic nanoparticles (Lim, Yeap, Che, & Low, 2013).

[1] Reprinted by permission from [Springer Nature]: [Springer Nature [Journal of Nanoparticle Research] [Dynamic Light Scattering Measurement of Nanometer Particles in Liquids, R. Pecora, 2000]

Surface sensitive synchrotron X-ray techniques as X-ray reflectivity (XRR) and small-angle X-ray scattering (SAXS) can also be used to study the self-assembling process and resulting biomaterials (Ochbaum & Bitton, 2018). XRR is used in thin surfaces to determine surface roughness, thin-film thickness and density (DLS, 2021). SAXS is used for nanomaterials in liquid or powder form, and grazing incidence small-angle X-ray scattering (GISAXS) is a complementary technique used in surfaces containing nanoparticles, pores and other non homogeneities (Panalytical, 2021).

X-ray methods have been used to characterize the self-assembly process of nanofibers (Pizzey et al., 2008), peptides (Ochbaum & Bitton, 2018), nanorods (Pietra et al., 2012), nanocrystals (Pietra et al., 2012), magnetic nanospheres (Josten et al., 2017), silica films (Dourdain et al., 2011) and other biological and inorganic materials (Brezesinski et al., 2006; Lee, Lee, Kim, & Park, 2004; Paik, Ko, Gordon, Doan-Nguyen, & Murray, 2011; Raghuwanshi, Ochmann, Hoell, Polzer, & Rademann, 2014; Tronin, Lvov, & Nicolini, 1994; H. Zhang, Nayak, Wang, Mallapragada, & Vaknin, 2017)

Another method used to observe the self-assembly process is interferometric scattering microscopy (iSCAT). This technique has a high resolution for particles up to 5 nm, thus allowing the study of nano-objects as proteins, viruses and DNA (Ortega-Arroyo & Kukura, 2012; Taylor & Sandoghdar, 2019). An exciting example of the use of iSCAT in self-assembly is presented by Garmann et al. (2018) to measure the kinetics of MS2 bacteriophage capsids around MS2 RNA. The authors measured the diameter of an assembling capsid using standard light dispersion, with temporal resolutions of up to 1 ms. However, to obtain data temporal data with durations of up to 600 s, they balanced the microscope to a mechanical control drift. This way, they measured changes in the magnitude of a single capsid through time scales stretching over six orders of magnitude. The dynamics of self-assembly by iSCAT have also

been explored in the formation of micellar or vesicular aggregates (Lebedeva, Palmieri, Kukura, & Fletcher, 2020)

Finally, a technique that will later be presented in the dissertation is polarized optical light microscopy (PLM). This technique is of particular interest in self-assembly as the polarized light allows to observe tiny crystals and obtain crystallographic data (Carlton, 2011). As molecules self-assemble in a liquid solution, crystal domains appear, which can be observed with PLM. As there is a wide range of literature exploring the formation of nano-crystals and PLM, in section 2.2.3 we will discuss crystals, tactoids formation, nematic domains and PLM.

2.1.3 Applications of Self-assembly

Self-assembly could have various uses and has already found some, from understanding how life works, to the bodies of nanostructures. It is one answer to building aggregates with elements that go between the sizes from nanometers to micrometers. This makes the study important to the manufacturing of nanotechnology (G. M. Whitesides & Boncheva, 2002; George M. Whitesides & Grzybowski, 2002). One specific example comes from Alien Technologies, that has built radio-frequency identification with shape recognition and fluid transport (Grzybowski et al., 2009; Yeh & Smith, 1994). Nowadays, nanocrystal self-assembly through different processes is allowing new expansion in mechanical, optical and electronic applications (Boles, Engel, & Talapin, 2016). Things that have been developed using nanomaterials include aggregates in inorganic chemistry and low energy cluster beams (Mileni, 2003).

One of the fields that would be the most benefited by SA is the biomedical. A way to treat cancer could be to use a nano-carrier system for local delivery of the anti-cancer drug (Engström et al., 2020). Furthermore, self-assembled RNAi structures can be controlled to build nanoparticles for nanomedicine (Jang & Ahn, 2017). Production of pharmaceutical

compounds can also be improved by controlling the self-assembly of colloidal structures by changing their surface potentials (Zupkauskas, 2019).

A technique called crystallization-driven-self-assembly has also proven to be useful in distinct aspects, such as emulsion stabilizer (Inam et al., 2018), semiconducting materials (Choi, Yang, & Choi, 2018), light harvesting and optoelectronic materials (X. H. Jin et al., 2018; Qian et al., 2014). Also, SA can help in the recognition and decontamination of chemical and biological vehicles (Mackay, 2003).

2.2 Cellulose

2.2.1 Introduction

In a year, approximately 10^{11} tons of cellulose are produced. This makes cellulose the most abundant organic material on Earth. However, this material also degrades, which makes it the most renewable as well (Perez & Samain, 2010). Cellulose was discovered and defined by Anselme Payen in 1838. He found it as remains after treating the plant tissue with acid and ammonia (R. M. Brown & Saxena, 2007). The word in itself, “cellulose”, talks about the sugar in cells (Perez & Samain, 2010).

The main sources where this material derives from are the tissues of plants like trees, cereal straw, cotton, flax and other similar ones. As a matter of fact, it is the main structural element of the cell-wall in the majority of plants. Nevertheless, it has also been found in prokaryotic and eukaryotic organisms, fungi, algae and others. Finally, it can also come from animals, like the membrane of the tunicates (for more examples, see *Figure 2.2*) (Perez & Samain, 2010).

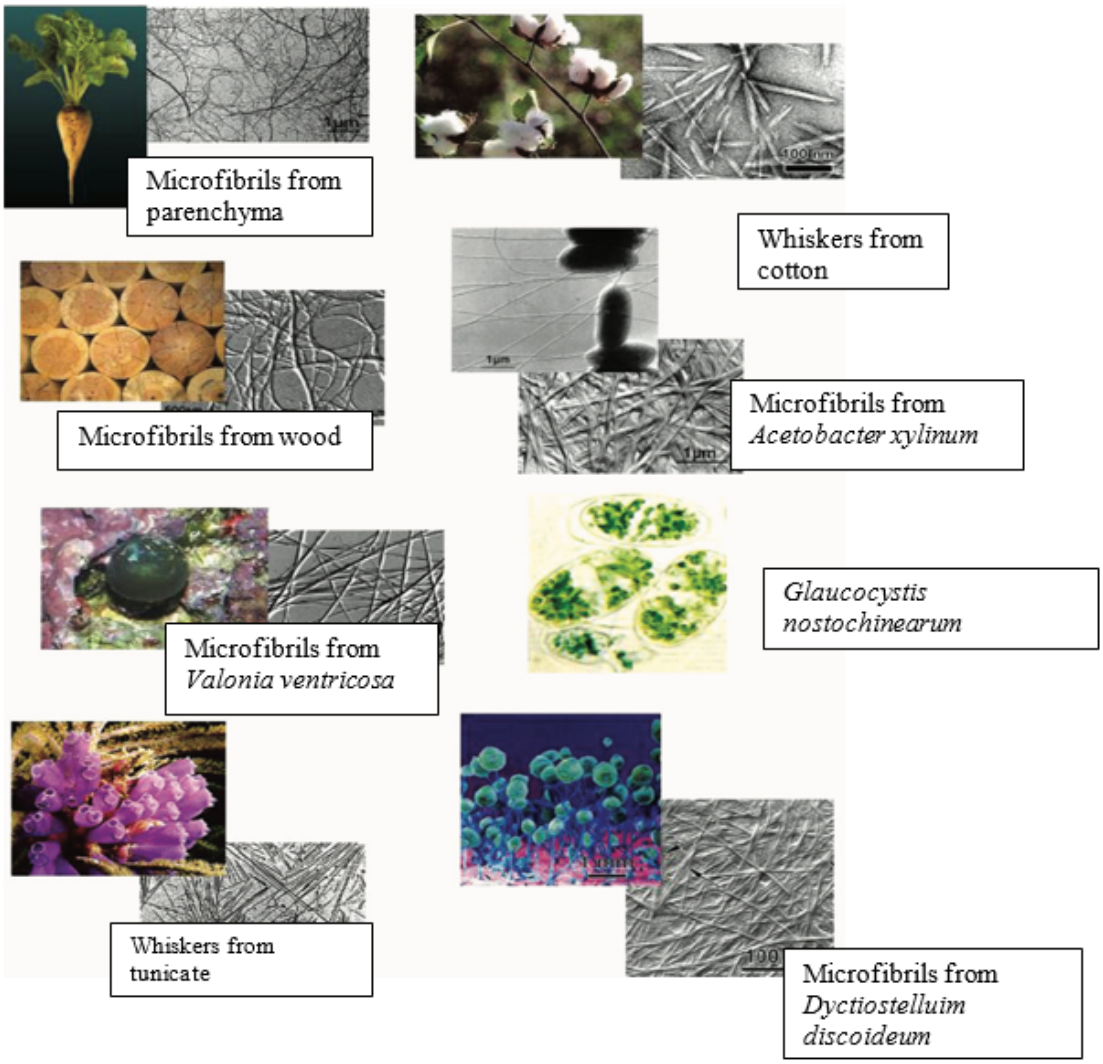

Figure 2.2. Examples of cellulose in nature. Reproduced with permission.[2]

Furthermore, cellulose and its by-products have been used throughout history in industrial endeavours. It comes from the basis of building wooden ships, and its complementary materials, like rope (Perez & Samain, 2010). And it continues now with paper, cellulose acetate, etc. For example, cellophane is made from the cellulose of trees, cotton and others. Furthermore, ethyl cellulose has pharmaceutical applications, it can be used for nail coating, food packaging, vitamin coating, and others (McKeen, 2013). It has also been an important part of the textile industry (Eichhorn, Hearle, Jaffe, & Kikutani, 2009).

[2] Reprinted from Advances in Carbohydrate Chemistry and Biochemistry, Vol 64, Perez & Samain. Structure and Engineering of Celluloses, Pages 25-116., Copyright 2010 with permission from Elsevier.

As it was mentioned before, cellulose is a renewable source and this characteristic makes it part of research for a myriad of more sustainable products. One example is biofuels, which could end up being more sustainable than petroleum. This second-generation biofuels could come from non-food biomass, like straw, wastes and feedstocks. Canada invested USD 500 M to research biodiesel and ethanol from cellulose. This is still in development, as it still has limitations before becoming commercial (Sims, Mabee, Saddler, & Taylor, 2010). Another sustainable research is that of the biogenic nanomaterials extracted from cellulose, which are later used to fabricate multifunctional materials as they have unique properties, they are not bad for the environment, and there can be energy efficient ways to produce them (Wicklein & Salazar-Alvarez, 2013).

Moreover, the nanofiber biopolymers can also be used to coat surfaces, thus changing the properties of each. These nanofibers exhibit high surface density and this allows control over the affinity of the adsorbing elements. One of the applications of nanofibrillated cellulose is a biocompatible and non-deteriorating support for enzymes. Or, with electron transport, through a mix of freeze-drying or compression, it was possible to devise a flexible magnetic aerogel (Wicklein & Salazar-Alvarez, 2013).

Other research has focused on forming new structures with the mechanical structures of cellulose. For this reason, several models have emerged, like nanofibrillated cellulose resistant to compression, or nanofibrillated cellulose based-aerogels (Silva, Habibi, Colodette, Elder, & Lucia, 2012).

2.2.2 Structure

Cellulose is comprised of β-1, 4-linked glucan chains; these chains may be organized in distinct forms to make various types of cellulose (*Figure 2.3*). Normally, "cellulose is produced in a hierarchical manner with the glucan chains associating with each other to form crystalline and noncrystalline regions that are assembled into higher-order structures such as

the microfibril" (R. M. Brown & Saxena, 2007, p. xiii). Diverse crystalline structures of cellulose might be detected in the same microfibril, and this is according to how the glucan chains are combined. Also, in its habitat, cellulose is accessed in the form cellulose I crystalline, where the glucan chains are ordered side-by-side to one another. In varying amounts that came from various sources, two structures of the natural crystalline polymer, cellulose Iα and Iβ have been found. Not only those, but other crystalline and noncrystalline structures have been detected; in addition, some of these are able to be transformed from one shape to another with chemical of physical processes (R. M. Brown & Saxena, 2007).

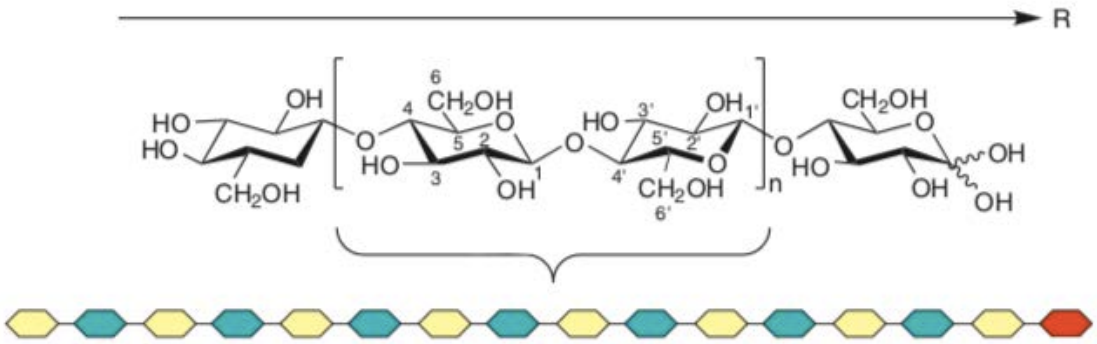

Figure 2.3. Molecular representation of the chain structure of cellulose; n indicates the number of repeating disaccharide units in a given cellulose chain. The reducing end of the chain is indicated. Reproduced with permission. [3]

2.2.3 Microfibrillated Cellulose

Destructuring natural fibres can be done by withdrawing the cellulose microfibril's sub elements (Dufresne, 2017). To produce this microfibrillated cellulose to obtain nano-scale elements, an intense mechanical treatment is needed. It depends on the raw material, nevertheless, to apply the chemical treatments before or after the mechanical fibrillation (Siró & Plackett, 2010). The resulting material is microfibrillated cellulose and it comprises nanosized cellulose fibrils that have a high aspect ratio (Dufresne, 2017). The cellulose nanocomposites that are obtained are basically two-phase materials, where "one of the phases

[3] Reprinted from Advances in Carbohydrate Chemistry and Biochemistry, Vol 64, Perez & Samain. Structure and Engineering of Celluloses, Pages 25-116., Copyright 2010 with permission from Elsevier.

has at least one dimension in the nanometer range (1-100nm)" (Siró & Plackett, 2010, p. 471). These elements have benefits if compared to conventional composites, as they possess better mechanical, thermal and barrier characteristics, besides more transparency, recyclability, and they are lighter (Oksman, Mathew, Bondeson, & Kvien, 2006). Cellulose that has been chemically modified has been probed to improve filler dispersion of hydrophobic polymers (Siró & Plackett, 2010).

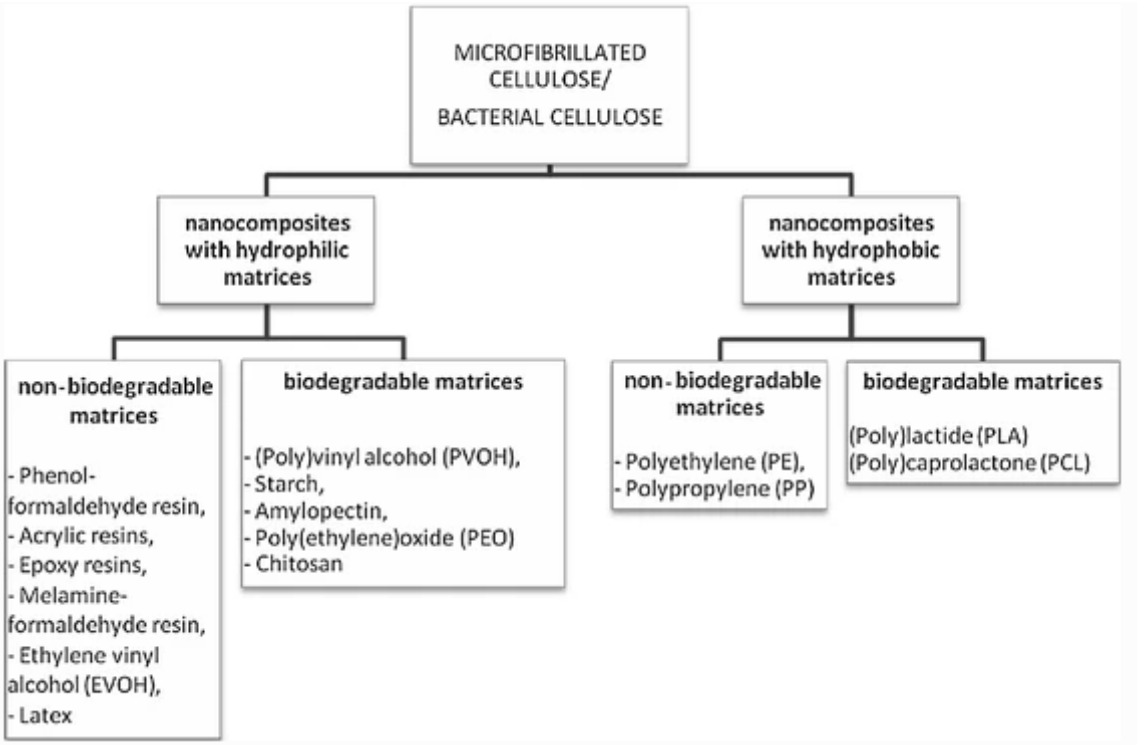

Figure 2.4. Classification of nanocomposites based on nanocellulosic materials (e.g. microfibrillated cellulose, bacterial cellulose) reported in the literature. Reproduced with permission.[4]

An example of this can be microfibrils from sugar beet that were processed to filaments with acid hydrolysis. With the formation of cellulose nanofibrils there was higher tensile modulus and tensile strength (Siró & Plackett, 2010). Battista & Smith (2002) were the first to show that cellulose nanocrystals can be obtained by sonication after acid hydrolysis of cellulose.

[4] Reprinted by permission from Springer Nature Customer Service Centre GmbH: [Springer Nature] [Cellulose] (Microfibrillated cellulose and new nanocomposite materials: a review, Siró & Plackett), [COPYRIGHT] (2010)

Furthermore, they showed it was possible to form gels and liquid crystalline phases by varying the concentration and suspension media. This discovery led to several industrial applications as absorbents, pellets, structural materials and gels and creams (Battista & Smith, 2002).

At present, we have a more comprehensive understanding of the crystallization processes and the different states found in the transition from liquid to solid states, known as mesophases. Of particular interest to this dissertation is the state of matter known as liquid crystals (LCs), characterized by having the properties of a liquid (i.e. flow) and the specific orientation of solid crystals. LCs transition from an isotropic state in which molecules are randomly organized to a nematic phase in which molecules have a parallel orientation (Tuinier, 2016).

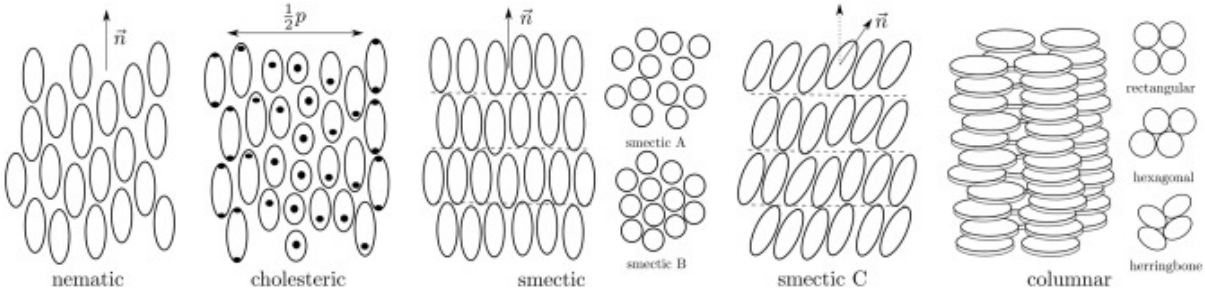

Figure 2.5. Molecular arrangements in liquid crystalline mesophases. In a nematic mesophase, molecular orientations are correlated, while molecular positions are not. The average orientation is termed a director, n. In a cholesteric mesophase the average molecular orientation twists through the medium with a certain periodicity, while positions of molecules are not correlated. In a smectic A mesophase molecules lie in planes. Molecular axes are perpendicular to these planes but otherwise are not ordered within the planes. Smectic B has a hexagonal packing of molecules in the planes, while in smectic C the director is tilted in the planes. Columnar mesophases are often formed by disc-shaped molecules. The most common arrangements of columns in two-dimensional lattices are hexagonal, rectangular, and herringbone. In the herringbone mesophase molecules are tilted with respect to the columnar axis. Reproduced with permission.[5]

[5] Reprinted Under a Creative Commons license, (2018), Journal of Molecular Liquids. Introduction to liquid crystals, Andrienko, Denis. This is an open access article distributed under the terms of the Creative Commons CC-BY license, which permits unrestricted use, distribution, and reproduction in any medium, provided the original work is properly cited.

As shown in *Figure 2.5*, LCs can be classified in nematics, cholesterics, smectics, and columnar mesophases (Andrienko, 2018). The nematic phase is the best known of all the phases (Carlescu, 2020). It also has the most basic formation, it is fluid, and it is the least organized of the phases (Bruce, Deschenaux, Donnio, & Guillon, 2007). Here, long molecules will start to organize in subdomains with a specific direction. This direction changes across the solution and has the name of the director. The ideal equilibrium configuration of the director is rarely seen when optically inspected, however with polarized microscopy we can observe the nematic changes and crystal formation, which tend to follow the direction of the director (Andrienko, 2018).

It is important to mention that the transition from isotropic to nematic mesophase starts with the nucleation of LCs microdroplets also known as tactoids. For tactoids to form, there has to be an attractive force to collect mesogens in a microdroplet and a repulsive force that will order the mesogens in liquid crystalline orientation. When the conditions of the isotropic dispersion reach a critical point (changes in temperature, concentration, etc.), very small anisotropic microdroplets will start to appear. These microdroplets, also known as tactoids, can be easily observed by polarized optical microscopy (POM) because the orientation leads to birefringence (P. X. Wang & MacLachlan, 2018). (P. X. Wang & MacLachlan, 2018).

When in the anisotropic phase, small tactoids appear. Shearing disrupts the liquid crystal texture. Moreover, the sheared suspension exposes interference colors at the time they are seen between crossed polars. The tactoids can form in a period of minutes or hours. These tactoids are ellipsoidal ordered regions, and they increase with time. Furthermore, these tactoids are seen as uniformly birefringent. After some more time, the tactoids repose and come together generating patterns that have fingerprint-like strokes, as seen in *Figure 2.6*. Thus, chiral nematic films that display these characteristics can be prepared (J. F. Revol, Bradford, Giasson, Marchessault, & Gray, 1992).

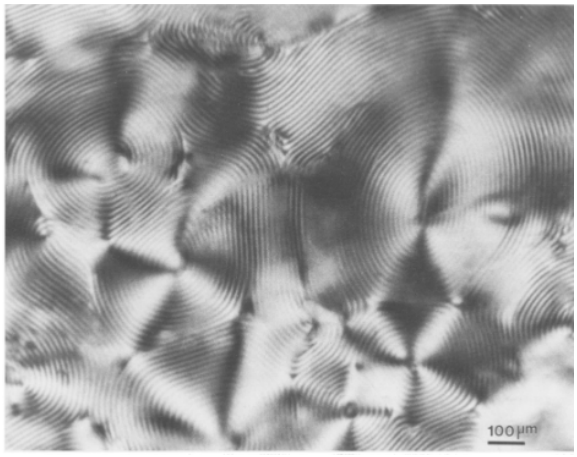

Figure 2.6. Optical micrograph (crossed polars) of the anisotropic phase formed from an aqueous suspension of cellulose crystallites (3 ± 0.1% by weight) 1 day after sonication or shearing. Birefringent multidomains are dearly seen with superimposed extinction contours (fingerprint-like). The periodic lines, characteristic of the cholesteric texture, have a spacing of ~ 15 pm, corresponding to half the cholesteric pitch. The cellulose concentration in this phase is 3 ± 0.1% by weight, indicating that the difference in concentrations between the two phases should be small. Reproduced with permission.[6]

From what is seen in *Figure 2.6*, the molecular axes and rods are aligned; this corroborates the nematic position of the crystallites. Additionally, the nematic regions could be the core of the tactoids (J. F. Revol et al., 1992).

The colloidal suspensions have a stability that exists as there is an interplay within the electric double layers. A peculiarity of the suspensions is the chiral nematic order, although is not obvious how it gets there. After the water evaporates from the suspensions, the phase makes a tight film that holds the chiral nematic organization (J. F. Revol et al., 1992)

2.2.3.1 Grinding

One of the processes to obtain fibres is done by the friction of grinding discs. For this a pair of nonporous ceramic grinding discs that have a malleable clearance between them are utilized. At the same time the upper disk is static, the lower disk rotates at a high speed. Raw material is put into a hopper, and centrifugal force scatters it into the clearance. Here, the material is ground. While this happens, the cellulose slurry passes between the stones and cellulose fibres are obtained (Dufresne, 2017). This type of fibrillation has various advantages, as it can microfibrillate a hefty amount of materials. The result can also include long fibre without the need for a pretreatment. Also, it has no clogging tendency (Nair, Zhu, Deng, &

[6] Reprinted from International Journal of Biological Macromolecules, Vol 14, Issue 3, R J. F. Revol, H. Bradford, J.Giasson, R. H. Marchessault, D. G. Gray, Helicoidal self-ordering of cellulose microfibrils in aqueous suspension, Pages No. 170-172, Copyright (1992), with permission from Elsevier.

Ragauskas, 2014). The grinding treatment has to be repeated several times to get uniform nano fibrils. There is a large energy consumption in this mechanism. As the duration of the fibrillation of the cellulose increases, important enhancements in the mechanical properties ensue including tensile strength and strain. The nano fibrils have better sheet density and tensile properties (Nair et al., 2014).

2.2.3.2 High Pressure Homogenization (HPH)

HPH is an effective technology for the cellulose nanofibers. The procedure includes attacking fluid stream facing itself in a reaction chamber (Saelee, Yingkamhaeng, Nimchua, & Sukyai, 2016). In the development of it, the pulp fibres encounter high shear, cavitation, high pressure and turbulence, since there is a fast change in pressure at the moment the fibres go through the homogenization chamber. Furthermore, all of these experiences have broken down amorphous regions, diminished the extent of the cellulose fibres, generated absolute disruption of cells, and finally delivered the cellulose nanofibers (M. Li, Wang, Li, Cheng, & Adhikari, 2014).

2.2.3.3 High-intensity Ultrasonication

For high-intensity ultrasonicaiton, the fibres are usually cleaned with distilled water and then put into a distilled water bath (H.-P. Zhao, Feng, & Gao, 2007). The ultrasound energy will be conveyed to the cellulose chains throughout cavitation. In this process, there is the forming, expanding and collapsing of cavities in water. The energy given by cavitation is of 10–100 kJ/mol. This way, the micron-sized cellulose will eventually disintegrate into nanofibers (*Figure 2.7*). The product will be aggregated nanofibers that have an ample dispersion in width (W. Chen et al., 2011).

This process has a very vigorous oscillating power, and the cellulose fibres get isolated from others like it because of the movement of hydrodynamic forces that the ultrasound constructs (Q. Cheng, Wang, & Rials, 2009). When the ultrasonication is over, the sample

cools down at room temperature and nanofibers can be collected. The defibrillation is rapid when working with cellulose fibres (Dufresne, 2017).

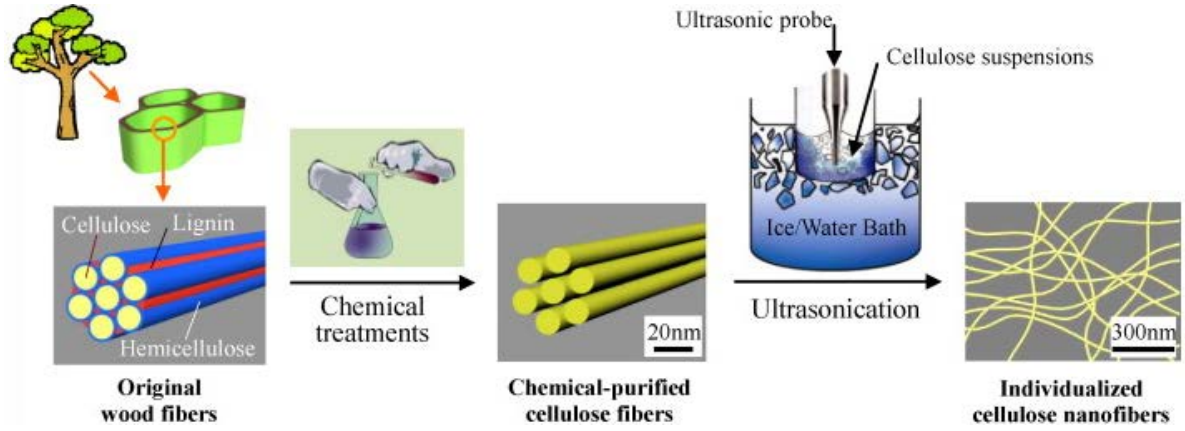

Figure 2.7. Procedure for individualizing cellulose nanofibers. Reproduced with permission.[7]

2.2.3.4 Ball Milling

This mechanism induces heavy cyclic deformation in fibres. A ball mill comprises "a hollow cylindrical shell rotating about its axis, which is usually horizontal" (Dufresne, 2017, p. 59). It contains some balls of materials like stainless steel, or rubber, and they perform like grinding media. The diminishing of size occurs by impact, when the balls fall from almost the top of the shell. The size of the ball is what should be attentively chosen instead of powders. It is this together with milling time that end up being the main criterion for the fibre morphology (Dufresne, 2017). From this, in a 2 h ball milling process, Dufrese (2017) obtained homogeneous microfibrillated cellulose 8-100 nm.

Amongst other methods for obtaining microfibrillated cellulose, are fibre fibrillation, purification of cellulose, cryocrushing, aqueous counter collision, twin-screw extrusion, electrospinning (Dufresne, 2017).

[7] Reprinted from Carbohydrate Polymers, Vol 83/Issue 4, Wenshuai Chen, Haipeng Yu, Yixing Liu, Peng Chen, Mingxin Zhang, Individualization of cellulose nanofibers from wood using high intensity ultrasonication combined with chemical pretreatments, Pages No. 1804-1811, Copyright (2011), with permission from Elsevier.

2.2.4 Cellulose Nanocrystals

Not only is there microfibrillated cellulose, but also cellulose nanocrystals, which are nanocomposites that also have the benefits of cellulose, as they are renewable, sustainable and are copious in nature. Moreover, they present low cost, light weight, unique morphology and nanoscale dimension (Lahiji, Reifenberger, Raman, Rudie, & Moon, 2008). They are, as well, the main constitutive polymeric pattern of cellulose based fibres (Y. Habibi, Lucia, & Rojas, 2010).

Cellulose nanocrystals were observed when it was discovered that degraded cellulose fibres, which were boiled in acidic solution, came to a maximum after some time. With transmission electron microscopy, pictures of dried suspensions unveiled the existence of aggregates of needle like elements. Later it was known that they presented the same crystalline form of the model original fibres (Y. Habibi et al., 2010; Thakur & Thakur, 2015).

2.2.4.1 Acid Hydrolysis

The most common process to prepare them, relies on acid hydrolysis to dissolve amorphous chains in the cellulose fibres and thus have crystal domains. This method has been explored widely (Kontturi & Vuorinen, 2008; Marchessault, Morehead, & Walter, 1959; O'Connor & Hruska, 2005). The result comprises an element of cellulose microfibrils (Dufresne, 2017), like a similar crystallinity. What the acid hydrolysis does is coax a rapid diminishing in the degree of polymerization (Thakur & Thakur, 2015). Then, it decreases unhurriedly when in lengthened hydrolysis times. After this mechanism, homogenous crystallites are produced. Nowadays, it is common to use strong acid hydrolysis to produce cellulose nanocrystals, where there are strictly controlled conditions for the time, temperature and agitation. Other things taken into consideration are the essence of the acid and the ratio between the acid and the fibres. The resulting suspension is thinned with water and then it

receives consecutive centrifugation. Finally, dialysis against distilled water is used to discard free acid molecules (Y. Habibi et al., 2010; Pandey, Reddy, Mohanty, & Misra, 2014).

As to the structure, the width spans a few nanometers, however the length covers a larger scope that goes from tens of nanometers to considerable micrometers. The length varies depending on the diminishing degree of polymerization of the material being used. The cross section's morphology of the cellulose nanocrystals rests on the material of the cellulose fibres. For example, the cross section found in the nanocrystals of *Valonia Ventricosa* was approximately square, while the cross section from the tunicate was rectangular. Distinct features are also seen in the axis of the nanocrystals. If they are from bacterial cellulose, they will have ribbon-like forms (Y. Habibi et al., 2010; J. F. Revol, 1982).

Although acid hydrolysis is the most common technique for the extraction of nanocrystals in cellulose, there are other mechanisms to do this.

2.2.4.2 Enzymatic Hydrolysis Treatment

This treatment is known to be more specific than acid hydrolysis, and it also has the convenience that is less corrosive (Henriksson, Henriksson, Berglund, & Lindström, 2007). Besides, it also has the upper hand in that it causes less material loss when comparing with other processes (Dufresne, 2017).

One example that has been studied has been with *Trichoderma reesei*. There are three processes that occur when cellulase enzymes operate *in vitro* with insoluble cellulosic substrates (Behera & Varma, 2019). First, there are chemical and physical transformations in lingering solid-phase cellulose. Second, initial hydrolysis helps the delivery of soluble intermediates that are in the external part of it. Finally, secondary hydrolysis involves the

"hydrolysis of soluble intermediates to lower molecular weight intermediates, and ultimately to glucose" (Y. H. Zhang & Lynd, 2004, p. 808). This can be seen in *Figure 2.8.*

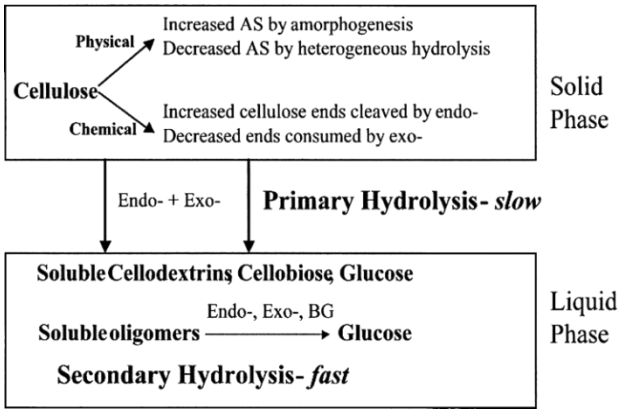

Figure 2.8. Mechanical hypothesis of enzymatic hydrolysis for cellulose by *T. reesei* cellulase. Reproduced with permission.[8]

Moreover, microwave assisted enzymatic hydrolysis has been used to produce nanocrystals from recycled pulp. To separate each crystallite, ultrasonication was used. The nanoparticles were rod-like, and their lengths and widths were between 100 nm and 1.8 µm, and 30 and 80 nm (Dufresne, 2013, 2017).

2.2.4.3 Tempo Oxidation

What this process does is "selectively oxidize C6 primary hydroxyl groups to carboxyl groups" (Dufresne, 2017, p. 137). The reaction happens on the exterior of the cellulose fibres, but also in the amorphous areas. When the carboxyl composition is raised, cellulose starts to scatter in aqueous solution. However, the crystalline domains persist unscathed and can be liberated (Dufresne, 2013, 2017).

Tahiri and Vignon (2000) reported that native cellulose samples present in the I-form of cellulose are difficult to oxidise. They also found no residual C6-signal, so primary alcohol products were fully oxidized. This technique has been explored by others (da Silva Perez, Montanari, & Vignon, 2003; Youssef Habibi, Chanzy, & Vignon, 2006; Z.-Y. Qin, Tong, Chin, & Zhou, 2011).

[8] Copyright (2004) Wiley. Used with permission from Yi Zheng Percival Zhang, Lee R. Lynd, Toward an aggregated understanding of enzymatic hydrolysis of cellulose: Noncomplexed cellulase systems, Biotechnology and Bioengineering, John Wiley and Sons. Copyright © 1999-2020 John Wiley & Sons, Inc. All rights reserved.

2.2.4.4 Ionic Liquid

Ionic liquids are liquids comprised of ions that are fluid at or below 100 °C. They have unique physiochemical characteristics, like wide liquid extent, low vapor stress, high thermal balance, amongst others (H. Wang, Gurau, & Rogers, 2012). In one example, for this process, cellulose nanocrystals were prepared by administering the microcrystalline cellulose with 1-butyl-3-methylimidazolium hydrogen sulfate ionic liquid. Then, [BMIM]HSO4 was added to the microcrystalline cellulose for 1 h. All of this was done at distinct temperatures ranging between the 70 and 90°C. The resulting suspension needed to be purified with sonication and centrifugation. The ionic liquid reacts similarly to acids in acid hydrolysis. The ionic liquid is not depleted and can be regenerated. The result was needle-like nanocrystals that have a length and width of 50-300 nm and 14-22 nm (Dufresne, 2017). Others have used different ionic liquids for cellulose (Dadi, Varanasi, & Schall, 2006; Swatloski, Spear, Holbrey, & Rogers, 2002).

Other treatments to obtain nanocrystals are ammonium persulfate oxidation, periodate oxidation, ultrasonication- assisted $FeCl_3$-catalyzed hydrolysis, subcritical water, liquefaction and acidic deep eutectic solvents (Dufresne, 2017).

2.2.5 Self-assembly of cellulose nanocrystals

As previously described, when we obtain CNC by TEMPO-mediate oxidation, there is a change in the charge in the surface of cellulose molecular groups that allow them to be dispersed in the solution. However, if we remove these charges, or we either dry the fibrils, the cellulose crystals will re-assemble in a new structure.

This final structure of the cellulose assembly will depend on the method we used to precipitate the CNC. A simple method to achieve this is by removing the water phase either by diffusion or evaporation. Due to cellulose's longitudinal structure, the assembly follows similar patterns as those observed in rod-like particles, DNA fragments, and other polysaccharides

(Folda, Hoffmann, Chanzy, & Smith, 1988; Livolant & Leforestier, 1996; J. F. Revol & Marchessault, 1993). The self-assembly of CNC starts by forming tactoids, which are liquid crystals (LCs) as defined previously. Tactoids generate birefringent patterns that have a chiral-nematic ordering and can be preserved after the sample is completely dry. Furthermore, the resulting assemblies can be engineered to achieve exceptional mechanical properties, including compression resistance, tensile strength and toughness (Laaksonen et al., 2011)

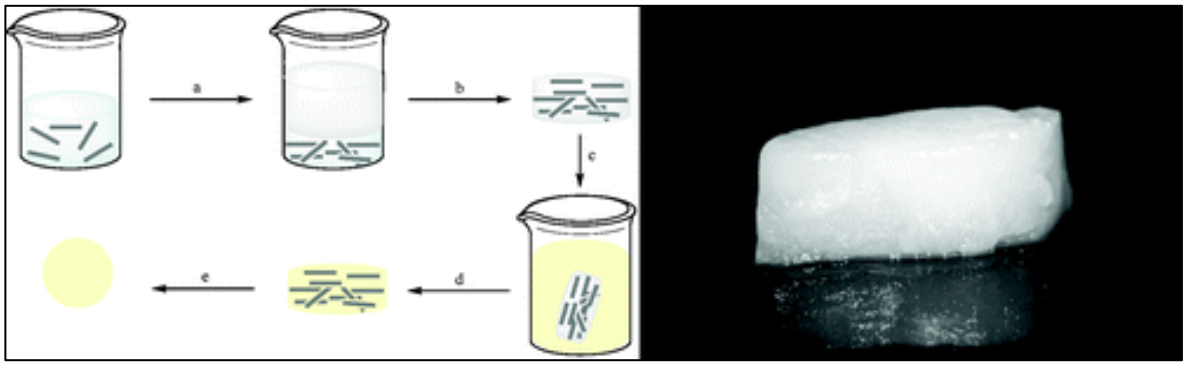

Figure 2.9. Dispersed CN composites schematic (left) Schematic representation of the template approach to obtain well-dispersed polymer/CN composites: (a) a nonsolvent is added to a dispersion of CNs in the absence of any polymer, (b) solvent exchange promotes the self-assembly of a gel of CNs, (c) the gelled CNs scaffold is interpenetrated with a polymer by immersion in a polymer solution, before the nanocomposite is (d) dried and (e) compacted. (right) The obtained gel after completing step b above. Reproduced with permission.[9]

Therefore, there are numerous reported applications for materials obtained by CNC self-assembling (Y. Habibi et al., 2010). For example, we have coatings for decorative or security purposes (J. F.; Revol, Godbout, & Gray, 1995), three-dimensional soft gels (Capadona et al., 2009), nanocomposites (Capadona et al., 2009; S. Qin et al., 2020), functional papers (Hanamura, Sawada, & Serizawa, 2021), green materials (Hata & Serizawa, 2021), flexible electronic devices (Pang et al., 2020), sensors (D. Zhang et al., 2022) , multifunctional films (Lagerwall et al., 2014), and others.

[9] Reprinted with permission from Chem. Rev. 2010, 110, 6, 3479–3500 Publication Date:March 4, 2010 https://doi.org/10.1021/cr900339w. Copyright 2021 American Chemical Society; and,
Reprinted with permission from Biomacromolecules 2009, 10, 4, 712–716 Publication Date:March 3, 2009 https://doi.org/10.1021/bm801090. Copyright 2021 American Chemical Society.

It is of particular relevance to the present thesis the work by Uetani et al. (2013), in which cellulose self-assembling was achieved by droplet evaporation. As shown in Figure 2.9, as the water evaporates, nematic mesophases appear inside the droplet. These domains aggregate the rod-like CNC into rings, which are stable even after the sample has completely dried. This experimental designed inspired the method presented in later chapters, in which we use a droplet inside a liquid to control the cellulose self-assembly.

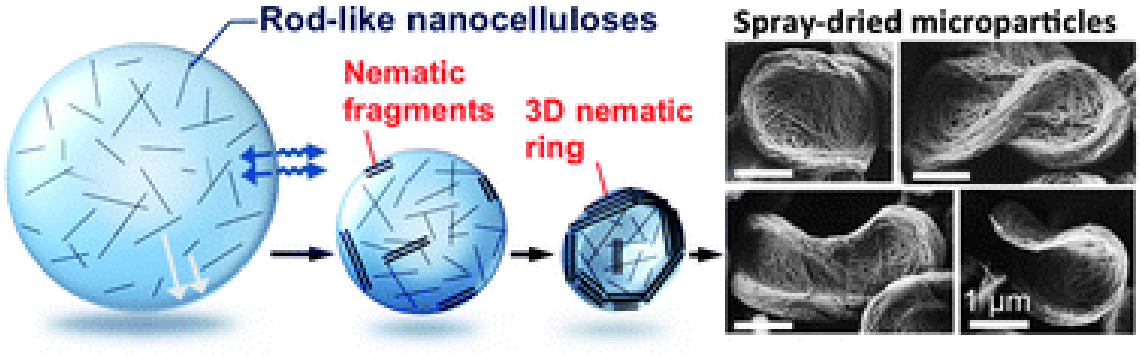

Figure 2.10. Cellulose self-assembly by evaporation (left) Schematic illustration of the evaporation-induced self-assembly (EISA). (right) Nematic rings obtained after the sample has dried. Reproduced with permission[10].

2.3 Silk

2.3.1 Introduction

Silk is one of the most interesting materials that has come from nature, and in a range of sizes. Nothing else in nature is as tough or as strong. It has fascinated scientists from different fields while they have tried to make us of its properties. From history, silk has been an important material, and this follows into our society. The *Bombyx mori* (silkworm) is a larva that eats a mulberry leaf that has been at the center of a profitable textile business (*Figure 2.11*) (Koh et al., 2015; Tansil et al., 2011; Vollrath, Porter, & Holland, 2013).

[10] Reprinted with permission licence 1134301-1.(2021) Royal Society of Chemistry.

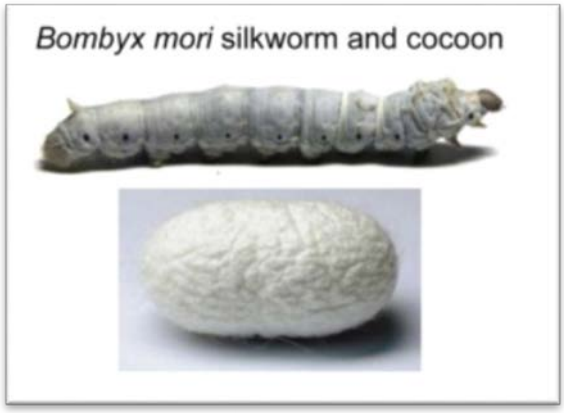

Figure 2.11. Photos of silkworm larva and cocoon of *Bombyx mori*. Reproduced with permission.[11]

The production of silk applies to different arthropods to mites, centipedes, insects and crustaceans. However, the silk that is produced the most is that from the silkworm previously mentioned. It is a domesticated *B. mori* moth that does not live in the wild anymore. These moths were tamed in China (Pereira, Silva, & de Zea Bermudez, 2015)

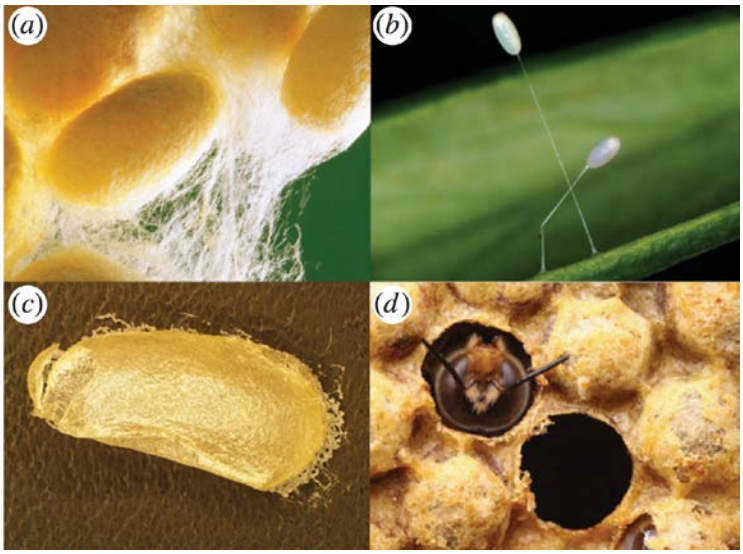

Figure 2.12. Canonical and non-canonical silks. (a) Silkworm (*B. mori*) cocoon fibres, a canonical silk. (b – d) Non-canonical silks produced by other insect species. (b) Lacewing (*M. signata*) egg-stalk silk(c) Sawfly (*Nematus oligospilus*) cocoon silk. (d) Honeybee (*Apis mellifera*) silk and wax on cell caps of a hive. Reproduced with permission.[12]

The silkworm *Bombyx mori* cocoons produce fibres that are utilized in different contexts, for example in clothes or for medical sutures (C. P. Brown, Whaite, MacLeod, Macdonald, & Rosei, 2014). The applications of this silk are also considered a multifaceted technological source for products

[11] Reprinted from Biomaterials, Vol 32, Issue 36, Natalia C. Tansil,Yang Li,Leng Duei Koh,Teng Choon Peng,Khin Yin Win,Xiang Yang Liu,Ming-Yong Han, The use of molecular fluorescent markers to monitor absorption and distribution of xenobiotics in a silkworm model, Pages No. 84, Copyright (2011), with permission from Elsevier.

[12] Reprinted from Proceedings B, Vol 282/Issue 1809, Andrew A. Walker, Chris Holland, Tara D. Sutherland, More than one way to spin a chrystallite: multiple trajectories through liquid crystallinity to solid silk, Pages No. 1-9, Copyright (2015), with permission from The Royal Society.

that will probably sell in the future transforming different fields, like biomedicine and optics (Pereira et al., 2015) . In *Figure 2.13* we can observe the process to purify silk into a fibroin solution. Sericin is removed by degumming with lithium bromide and dialysing with water or polyethylene glycol (Rockwood et al., 2011). Silk fibroin can be then used for multiple applications as sponges, hydrogels, films, microparticles and others.

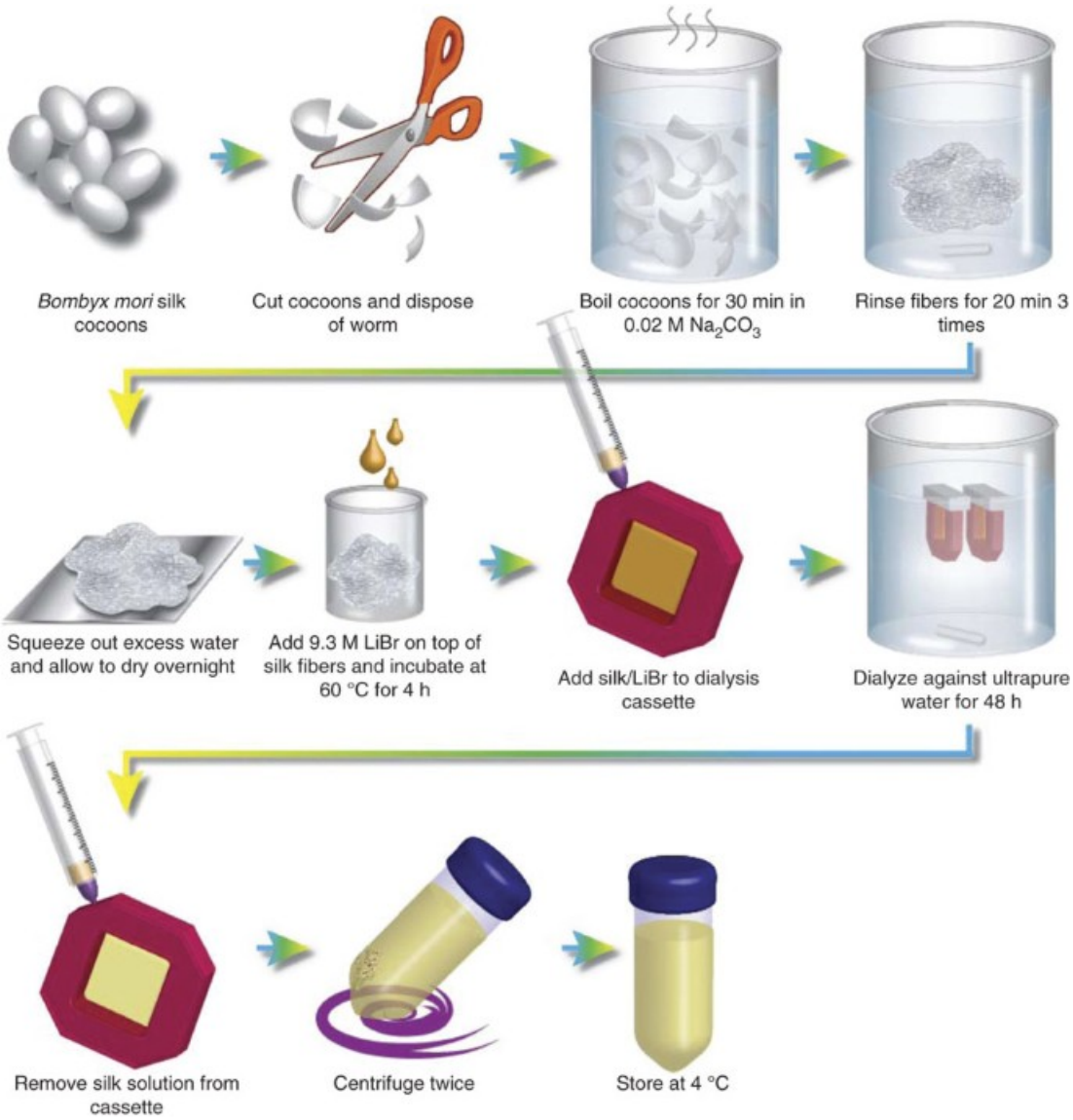

Figure 2.13. Regenerated fibroin solution from cocoons. Reproduced with permission.[13]

[13] Reprinted by permission from Springer Nature, [Springer Nature] [Nature] [(Materials fabrication from Bombyx mori silk fibroin, Danielle N Rockwood, Rucsanda C Preda, Tuna Yücel, Xiaoqin Wang, Michael L Lovett & David L Kaplan)], [Copyright 2011]

In nature, it has been proposed that self-assemble of silk consists of these steps: a silk fibroin suspension structures in the gland ahead of spinning. This hydrogel consists of silk chains in silk I formation; this is thought to be needed in the in-between for the prealignment of silk fibroin molecules. After spinning, the metastable silk I formation changes into a balanced silk II formation (Q. Lu et al., 2012).

2.3.2 Silk Architecture

Silks have proteins as the structural component; these proteins are spun, or turned, from a gel-like feedstock, or dope, to become solid. This is done by being extracted from the silk gland to the outside by pultrusion (Vollrath et al., 2013; Walker, Holland, & Sutherland, 2015).

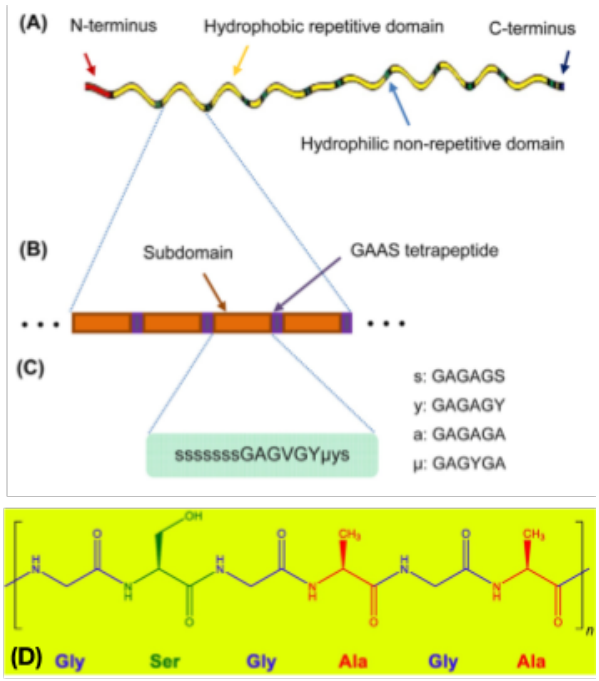

Figure 2.14. (A) Each fibroin heavy chain (H-chain) consists of hydrophobic repetitive domains interspersed between hydrophilic non-repetitive domains (Foo et al., 2005) (B) Each repetitive domain consists of subdomains separated by GAAS tetrapeptides. (C) Each repetitive domain consists of subdomains separated by GAAS tetrapeptides (Koh et al., 2015, p. 90; C. Z. Zhou et al., 2001) (D) Fibroin amino acid repeat units (peptide) (Pereira et al., 2015). Reproduced with permission.[14, 15, 16, 17]

[14] Reprinted by permission from CCC RightsLink: [Springer Nature] [Applied Physics A: Materials Science & Processing] (Role of pH and charge on silk protein assembly in insects and spiders: C. Wong Po Foo et al), [COPYRIGHT] (2005)

[15] Copyright (2014) Wiley. Used with permission from Rui F. P. Pereira, Maria M. Silva, Verónica de Zea Bermudez, *Bombyx mori* silk fibers: An outstanding family of materials, Macromolecular Materials and Engineering, John Wiley and Sons. Copyright © 1999-2020 John Wiley & Sons, Inc. All rights reserved.

[16] Reprinted by permission from CCC RightsLink: [John Wiley and Sons] [Proteins: Structure, Function and Bioinformatics] (Silk fibroin: Structural implications of a remarkable amino acid sequence: Joel Janin, Zhen-Gang Li, Roland Perasso, et al), [COPYRIGHT] (2001)

[17] Reprinted from Progress in Polymer Science, Vol 46, Leng-Duei Koh, Yuan Cheng, Choon-Peng Teng, Yin-Win Khin, Xian-Jun Loh, Si-Yin Tee, Michelle Low, Enyi Ye, Hai-Dong Yu, Yong-Wei Zhang, Ming-Yong Han, Structures, mechanical properties and application of silk fibroin materials, Pages No. 86-110, Copyright (2015), with permission from Elsevier.

For this study, it is important to understand the protein structure. Proteins are polymers formed by a sequence of amino acids. By convention, small chains are often identified as peptides, like it was seen in *Figure 2.14*. In contrast, proteins are longer chains that have more than 100 amino acids that are formed by peptide bonds (Foo et al., 2005; C. Z. Zhou et al., 2001).

Since proteins are polymers formed by amino acids, their spatial architecture is well understood. *Figure 2.15* shows the different protein structures. The primary structure is the chemical formula or sequence of amino acids; the secondary structure is made of three-dimensional construction of protein segments; the tertiary structure refers to the complete protein shape; and the quaternary is the structured formed by multiple proteins (Heim, Romer, & Scheibel, 2010).

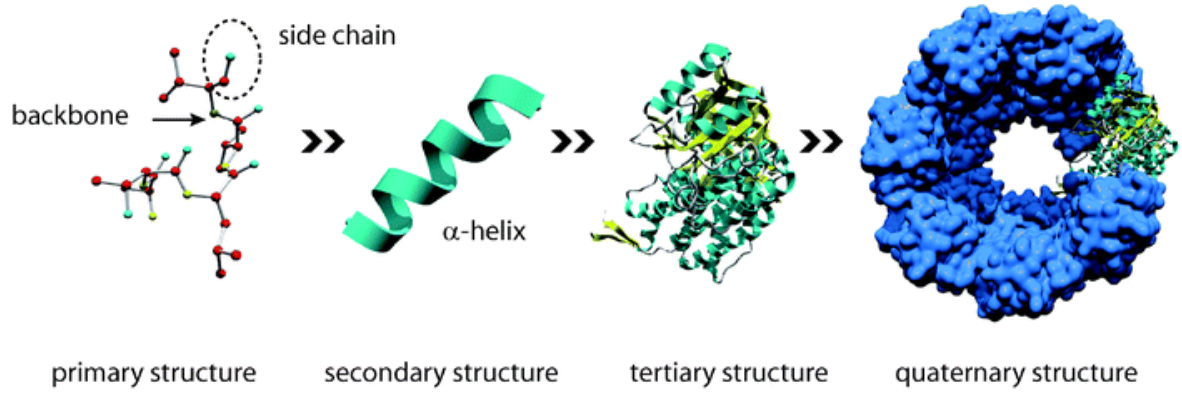

Figure 2.15. The hierarchical structure of proteins. Reproduced with permission.[18]

As this study focuses on one protein (silk fibroin), it is important that we understand its primary (1-dimensional) and secondary (3 dimensional) structure. Even though the primary structure of silk has been well understood since a decade ago, the three-dimensional structure and the assembling of protein is still being studied. Particularly, the effect of the structure in the mechanical properties of silk fibres.

[18] Reprinted with permission from Chem. Soc. Rev. 2010, 110, 6, 3479–3500 Publication Date: March 4, 2010 https://doi.org/10.1021/cr900339w. Copyright 2021 American Chemical Society

To further study this polymer, the protein materials of silk "are semi-crystalline polymers consisting of ordered domains containing crystallites with precise secondary structures and high H-bonding density, interspersed with disordered amorphous domains with a lower H-bonding density" (Walker et al., 2015). This is an important point, as we do not have a long unique chain, but a mix of amorphous and crystal phases, which together give silk its main properties as shown in *Figure 2.16 (Y. Wang et al., 2019).*

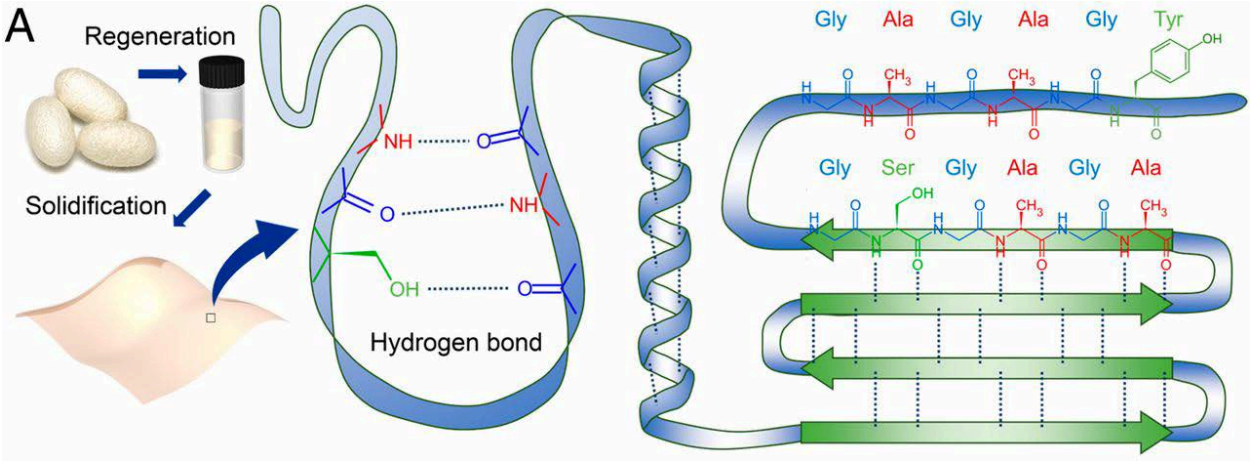

Figure 2.16. Structure of silk fibroin. Schematic of reconstituted silk-fibroin molecular chain showing the hydrogen bonding and secondary structures (random coil, β-sheet, helix). Reproduced with permission.[19]

Several models to describe silk protein 3D folding have been proposed in the review by Fu C., which go in depth to illustrate silk structure defined by hydrogen bonds. Also, Nguyen has a new and extensive review of silk structure (Fu, Shao, & Fritz, 2009; Nguyen et al., 2015).

There has been effort to comprehend the correlation that the formation and the behaviour silk fibrous elements have. One of the first models was a semi-crystallite one. Silk fibres were seen as composite elements, where β-crystallites fixed firmly in the protein matrix, as seen in *Figure 2.17*. Highly oriented β-crystals and feeble oriented β-sheets are part of the

[19] Proceedings of the National Academy of Sciences, Controlling silk fibroin conformation for dynamic, responsive, multifunctional, micropatterned surfaces, Yu Wang, Beom Joon Kim, Berney Peng, Wenyi Li, Yuqi Wang, Meng Li, Fiorenzo G. Omenetto, Published under Creative Commons licence (2019)

crystalline regions. It is believed β-crystals work as molecule cross-links, while giving toughness, and the non-crystallite regions give the silk its elasticity (Nguyen et al., 2015).

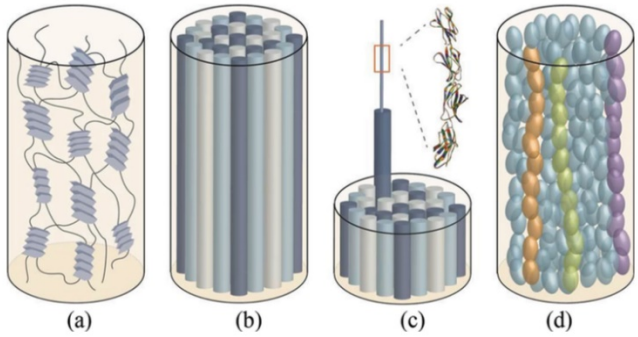

Figure 2.17. Proposed models for spider silk and silkworm silk: a) bulk network model, b) fibrillar structure model, c) string bean model, d) micelle model. Reproduced with permission.[20]

It does not matter how many models there have been since then, all of them agree that the key to understand the structural and mechanical properties is hidden in the relation between the β-sheets and the amorphous region. In *Figure 2.18* we can observe a three-phase model where the protein is folded in crystalline, interphase and amorphous regions. The difference in size and connections between phases will change the inherent properties of the silk (Paquet-Mercier, Lefèvre, Auger, & Pézolet, 2013).

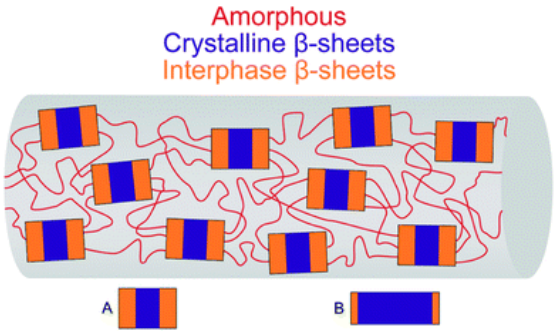

Figure 2.18. Three-phase silk model. For *Nephila p.*clavipes silk (A) and *B. mori* silk (B), the areas of the blue (crystals) and orange (interphase) rectangles are scaled with respect to the proportion of crystalline and interphase β-sheets, respectively. Reproduced with permission.[21]

Following the previous example, we could also predict the differences in crystalline fragmentation between spider and worm silk. It has been found that spider silk is stronger than the one from silkworm as shown in *Figure 2.19* (left), even though the chemical configurations are very similar (Holland, Terry, Porter, & Vollrath, 2007; Vollrath et al., 2013). The

[20] Copyright (2014) Wiley. Used with permission from Anh Tuan Nguyen, Qiao-Ling Huang, Zhen Yang, Naibo Lin, Gangqin Xu, Xiang Yang Liu, Crystal networks in silk fibrous materials: from hierarchical structure to ultra performance, Nano Micro Small, John Wiley and Sons. Copyright © 1999-2020 John Wiley & Sons, Inc. All rights reserved.

[21] Reprinted from Soft Matter, Vol 9/Issue 1, Paquet-Mercier, François; Lefèvre, Thierry; Auger, Michèle; Pézolet, Michel, Evidence by infrared spectroscopy of the presence of two types of β-sheets in major ampullate spider silk and silkworm silk, Pages No. 208-215, Copyright (2015), with permission from The Royal Society of Chemistry.

explanation will be found in higher interconnection of regions in spider silk, which avoids crystallite fragmentation, as shown in *Figure 2.19* (right) (Du, Yang, Liu, Li, & Xu, 2011; Nguyen et al., 2015).

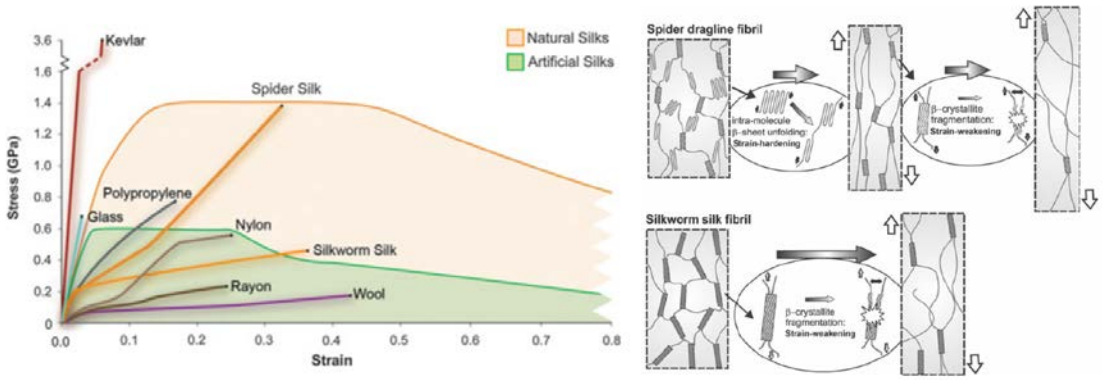

Figure 2.19. Silk mechanical properties (left) Silk tensile properties in comparison to other industrial and natural fibres and artificial silks. Colored backgrounds indicate the impressive toughness of silk and vast range of properties achievable by varying spinning conditions (right) A schematic model demonstrating how the silkworm and spider dragline fibres respond when they are subjected to stretching. There are two components in the alanine-rich regions of spider dragline silk: β-crystallites and intra-molecular β-sheets. Reproduced with permission.[22, 23]

2.3.3 Hierarchical Structure

The molecular structure is not the only parameter that will prompt the mechanical characteristics of silk, as there the hierarchical structure is present as well. It has been revealed that the uncommon conduct of the silk fibres comes from the disposition at the mesoscale. To see how the hierarchical structures of silk look like, it is seen in *Figure 2.20*. Silk from both a spider and a silkworm is composed of nanofibrils which measure 30-35nm in diameter. These nanofibrils are made of nano β-crystallites joined by amorphous peptide chains (Xu, Gong, Yang, & Liu, 2014).

[22] Reprinted by permission from [Springer Nature]: [MRS Bulletin [The science of silks], F. Vollrath et al] Copyright 2013.
[23] Copyright (2010) Wiley. Used with permission from Ning Du, Zhen Yang, Xiang Yang Liu, et al, Structural Origin of the Strain-Hardening of Spider Silk, Advanced Functional Materials, John Wiley and Sons. Copyright © 1999-2021 John Wiley & Sons, Inc. All rights reserved.

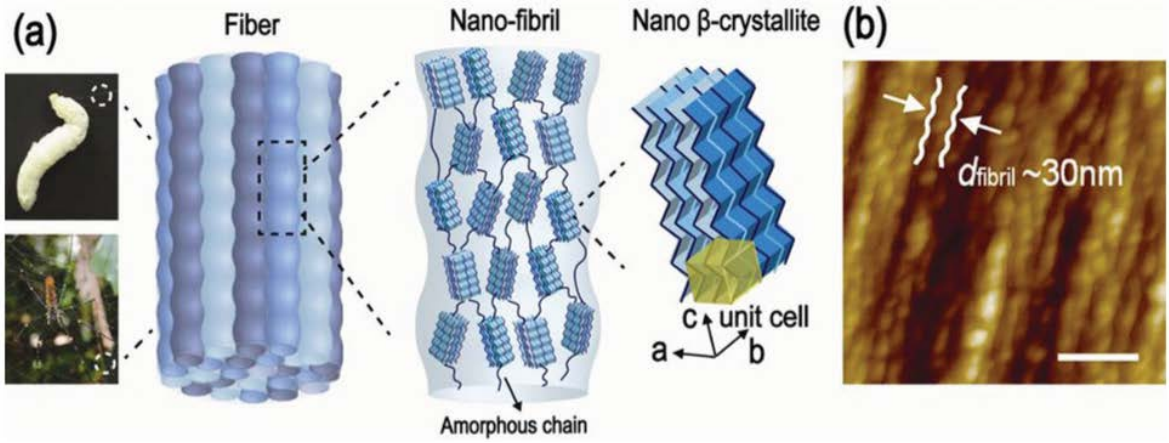

Figure 2.20. The hierarchical structure of *Bombyx mori* silkworm and *Nephila pilipes* spider dragline silk fibers. (a) Both the silkworm silk and spider dragline fiber are composed of numerous interlocking nano-fibrils. Inside the nano-fibrils, the β-crystallites are connected by the amorphous chains to form a network. The β-crystallite is composed of stacked β-sheets with the peptide chains connected by the hydrogen bonds in each sheet. The yellow box indicates the unit cell of the β-crystallites and the coordinate indicates a (inter-sheet), b (inter- chain) and c directions. (b) AFM image of nano-fibrillar structure in *B. mori* silkworm silk with a sequence of associated segments (scale bar: 100nm) Reproduced with permission.[24]

Overall, it is possible that in a primarily single phase or a multiphase, crystal networks have permanent junctions. In the multiphase the crystallite networks work to enmesh liquid. This is how soft materials that act as self-supporting soft solids are formed (Nguyen et al., 2015). *Figure 2.21* shows three characteristic hierarchical structures that belong to silk compounds. It has been observed that the silk fibres form not a single molecule but complex networks, and these in turn create crystals which link across domains. Each silk crystal interrelate with adjacent domain, and the mechanical properties will depend on the strength of the aggregate of links across the network. Single silk fibers will have limited mechanical strength than multiple fibers interacting together in the same direction (Nguyen et al., 2015, p. 1041).

[24] Reproduced from Soft Matter, What makes spider silk fibers so strong? From molecular-crystallite network to hierarchical network structures, Copyright 2014, with permission from the Royal Society of Chemistry.

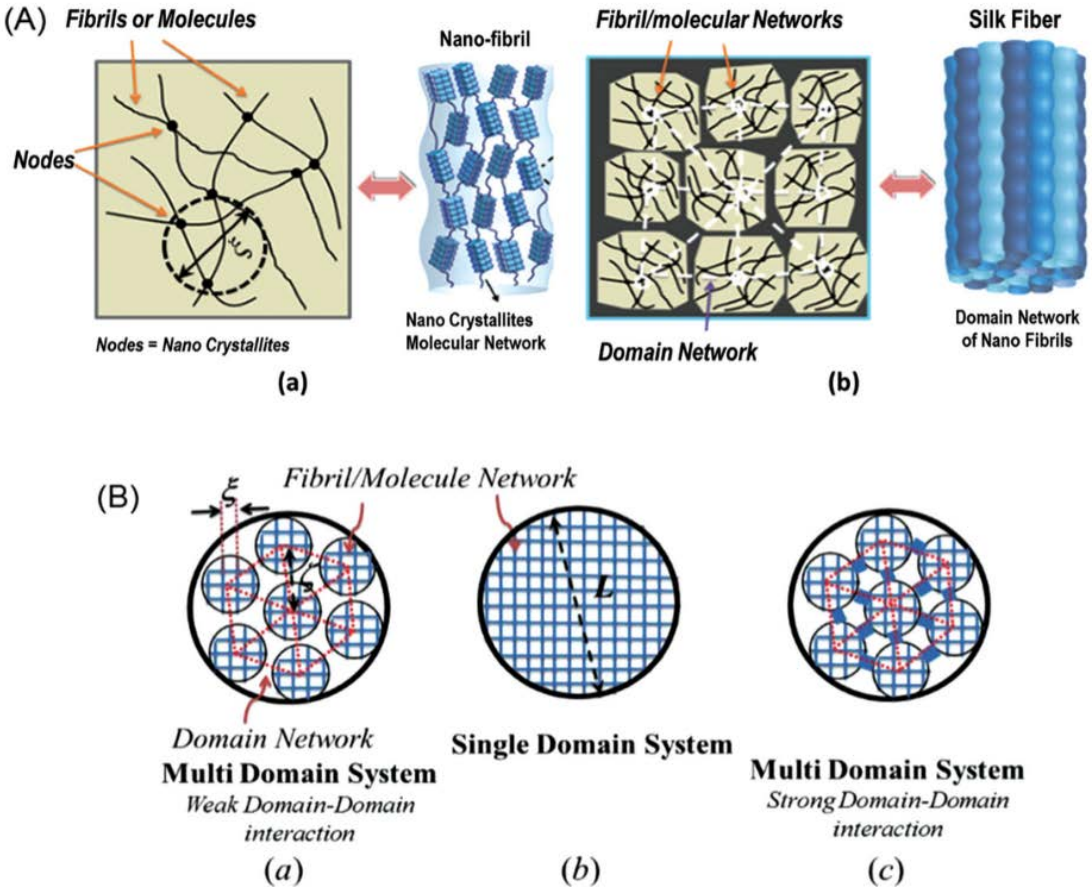

Figure 2.21. (A) Comparison between the hierarchical network of soft fibrous materials and the silk fiber (a) "single" fiber network and nano-fibril in silk; (b) multi-domain fiber network and fibril bundle. (B) Schematic illustration of three typical hierarchical structures: (a) a multi domain system, the domain-domain interaction is weak or zero; (b) a single domain system; (c) a multi domain system, the domain-domain interaction is strong or infinite. Reproduced with permission.[25, 26, 27]

Most systems that can be found in nature are of multi-domains. The weak-interacting of these networks (*Figure 2.21*B-a) usually possess lower mechanical properties. When there are strong inter-domain interactions, there might be steadier hierarchical networks (*Figure 2.21*B-c) and more durable components (Nguyen et al., 2015).

[25] Reproduced from Soft Matter, What makes spider silk fibers so strong? From molecular-crystallite network to hierarchical network structures, Copyright 2014, with permission from the Royal Society of Chemistry.
[26] Copyright (2014) Wiley. Used with permission from Anh Tuan Nguyen, Qiao-Ling Huang, Zhen Yang, Naibo Lin, Gangqin Xu, Xiang Yang Liu, Crystal networks in silk fibrous materials: from hierarchical structure to ultra performance, Nano Micro Small, John Wiley and Sons. Copyright © 1999-2020 John Wiley & Sons, Inc. All rights reserved.
[27] Copyright (2010) Wiley. Used with permission from Xiang-Yang Liu, Jing-Liang Li, Architecture of Supramolecular Soft Functional Materials: From Understanding to Micro-/Nanoscale Engineering, Advanced Functional Materials, John Wiley and Sons. Copyright © 1999-2021 John Wiley & Sons, Inc. All rights reserved.

Figure 2.21B-c shows us the multi-domain structure formation of silkworm silk and spider silk fibres. The fibre of both types of silk is made of nanofibrils that measure 30nm for *B. mori* fibres and 35nm for *Nephila pilipes* spider fibres. β-crystallites (crystalline domains) are joined by non-β-structures (non-crystalline domains) in the interior of the nanofibrils. Distinct silk protein molecules work like the intersections of the molecular structure and they make up each β-crystallite (Nguyen et al., 2015).

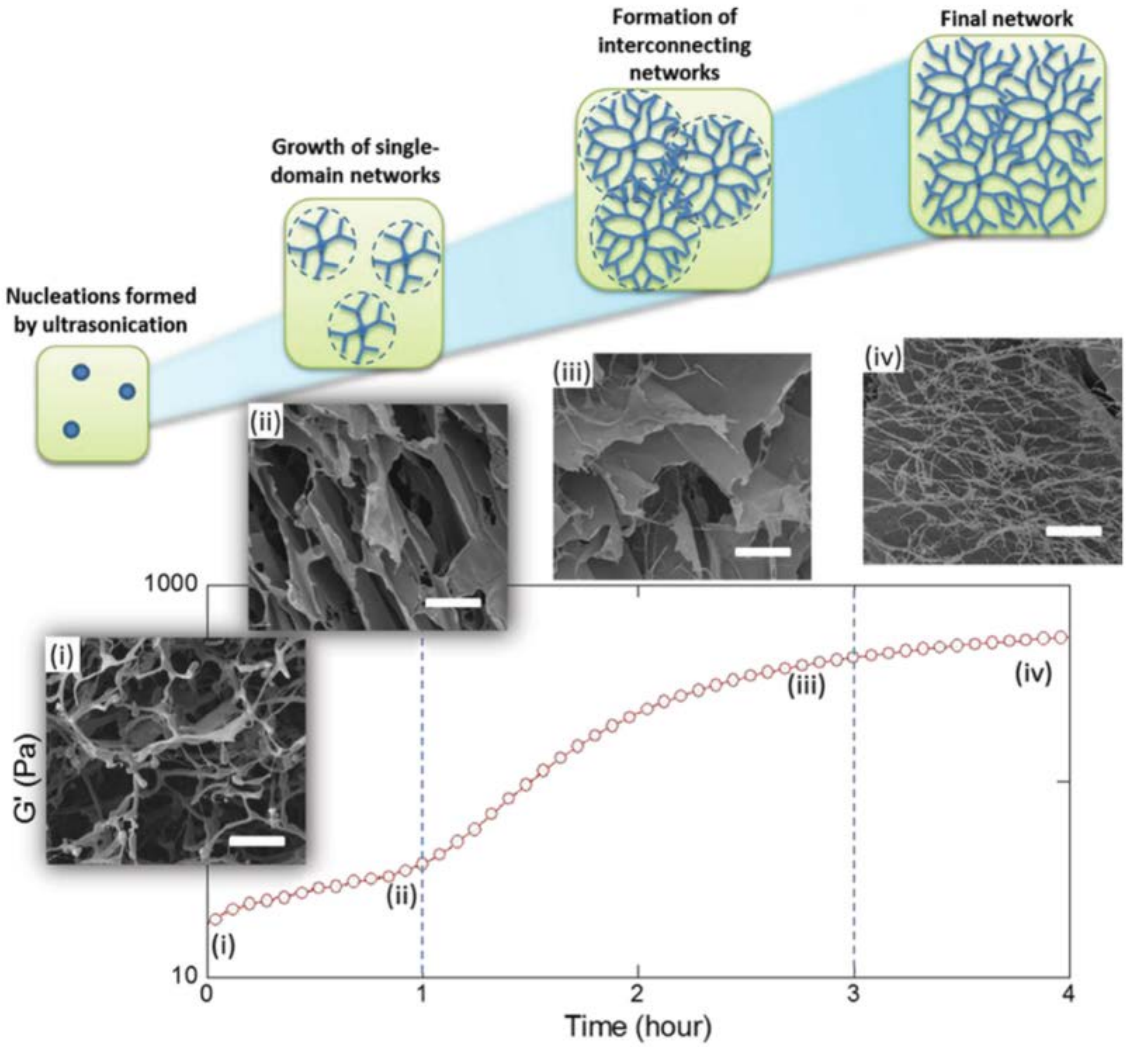

Figure 2.22. Illustration of the formation of nanofibrillar network at different gelation stages. Inserted SEM images represent freeze-dried RSF hydrogel at different gelation states: (i) 0 h, 1 h, (iii) 3 h, (iv) 20 h after ultrasonication. The scale bar presents 500 μm. Reproduced with permission.[28]

[28] Copyright (2014) Wiley. Used with permission from Anh Tuan Nguyen, Qiao-Ling Huang, Zhen Yang, Naibo Lin, Gangqin Xu, Xiang Yang Liu, Crystal networks in silk fibrous materials: from hierarchical structure to ultra performance, Nano Micro Small, John Wiley and Sons. Copyright © 1999-2020 John Wiley & Sons, Inc. All rights reserved.

2.3.4 Mechanical and Rheological Properties

Soft fibrous materials in their typical macroscopic conduct are governed by rheological and mechanical characteristics. For the rheological feature, the characterization comes from $G^* = [(G')^2 + (G'')^2]^{1/2}$. In here G' refers to the storage modulus, which describes the elasticity, while G'' describes the viscosity (J.-L. Li & Liu, 2010).

The intersections of the crystallites in crystal networks may be divided into two kinds: transient and permanent, it depends on the type of the attaching forces. As mentioned before, lower rheological and mechanical properties often derive from weak connections; this is when transient networks occur as shown in *Figure 2.23*(left). On the contrary, when crystal networks have permanent connections comprised of fibre branching and strong entanglement as in *Figure 2.23*(right), they usually have higher performance (J.-L. Li & Liu, 2010).

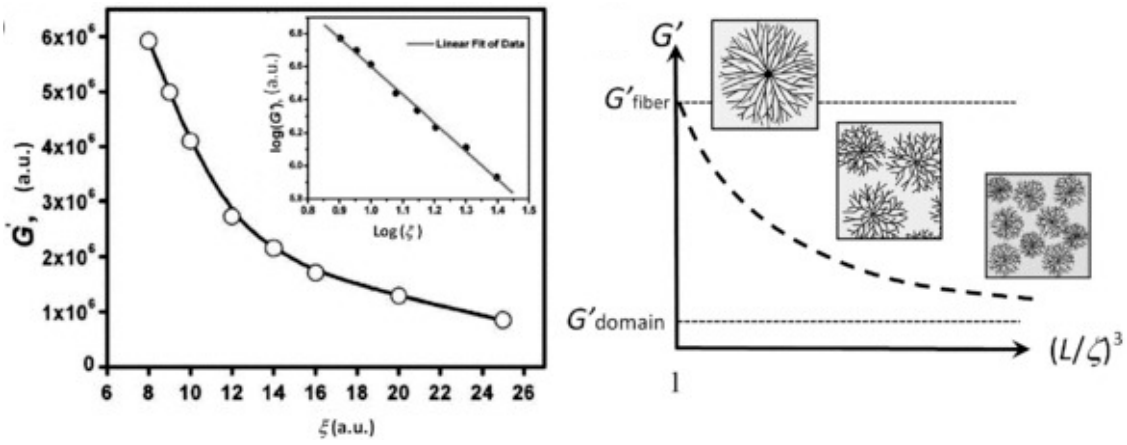

Figure 2.23. Correlation between length ξ on G′ and domain transition. (left) The simulation data showing the effect of the correlation length ξ on G′. The inset is the log-log plot of G′ vs. ξ. (right) Illustration of transition of the G′ of a material from G'_{fiber} to G'_{domain}. Reproduced with permission.[29]

The storage modulus G is linked straight with the secondary network structure. G' is calculated by the correlation length ξ. This can be described as the standard mesh extent of the

[29] Copyright (2010) Wiley. Used with permission from Xiang-Yang Liu, Jing-Liang Li, Architecture of Supramolecular Soft Functional Materials: From Understanding to Micro-/Nanoscale Engineering, Advanced Functional Materials, John Wiley and Sons. Copyright © 1999-2021 John Wiley & Sons, Inc. All rights reserved.

system. For the usual networks, G' decreases when ξ increases in a power law $G' \sim \xi$. This can be seen in *Figure 2.23* (left) (J.-L. Li & Liu, 2010).

The silk fibres that come from spiders are fascinating; they are environmentally friendly, have biocompatibility, and great mechanical properties. They also have shown to have a mixture of higher strength and elasticity. For example, *Nephila p.* dragline silk fibres generally present a maximum stress-strain of 1.3 GPa and an extensibility of 40%, which amounts to a tensile strength of 160 kJ kg^{-1} (Nguyen et al., 2015). This means it is 5 times tougher over synthetic fibres. Moreover, this silk fibres have the ability to take in considerable impact energy along low impact force when hit. Silkworm silk fibres, however, possess weaker mechanical properties (N. Lin & Liu, 2015). Stretching is performed differently by both, due to hierarchical network structures (N. Lin & Liu, 2015; Nguyen et al., 2015).

2.3.5 Induced and Self-assembling of Silk

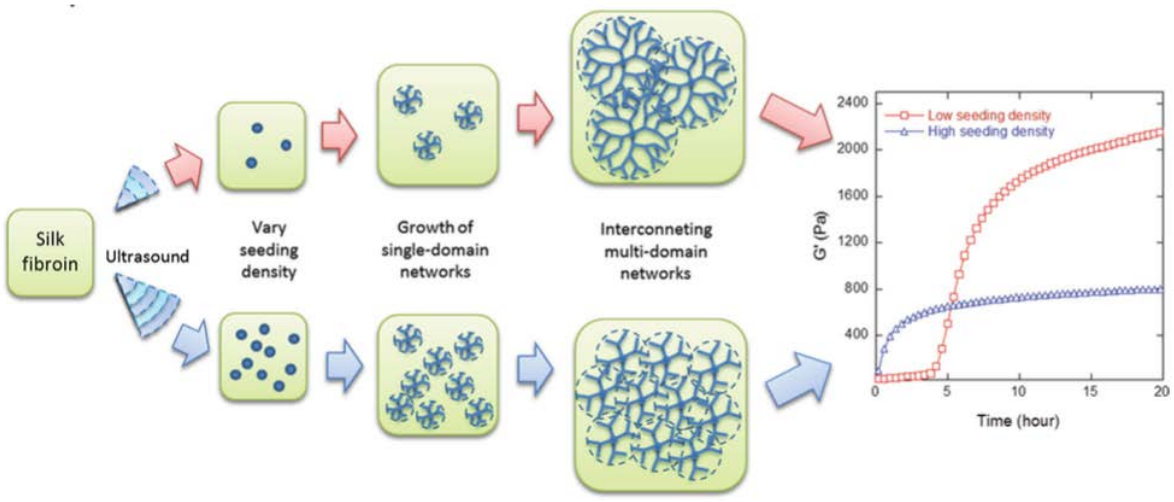

Figure 2.24. Strategy to control the mechanical property of silk fibroin hydrogels by controlling the hierarchical network structures, i.e. varying the density of nucleation centers. Reproduced with permission.[30]

[30] Copyright (2014) Wiley. Used with permission from Anh Tuan Nguyen, Qiao-Ling Huang, Zhen Yang, Naibo Lin, Gangqin Xu, Xiang Yang Liu, Crystal networks in silk fibrous materials: from hierarchical structure to ultra performance, Nano Micro Small, John Wiley and Sons. Copyright © 1999-2020 John Wiley & Sons, Inc. All rights reserved.

Following the previous analysis of mesh formation, the key to assembling is the formation of silk fibroin particles, which in turn will form multi-domain networks. The speed of the assembling, as well as the use of external stimulus, will influence in the final structure of the domain. *Figure 2.24* illustrates how ultrasound influences the assembling process improving the multi domain network formation.

Non-contact mode AFM has been used to study silkworm silk self-assembling by protein shearing. It is feasible to assess the morphologic distinctions of one protein molecule, and determine protein accumulation. It was found that concentration leads to morphological changes on the structure of the protein assemblies following shearing. Depending on protein concentration, fibrillar structures of two distinct types were acquired (*Figure 2.25 and Figure 2.26*) (Greving, Cai, Vollrath, & Schniepp, 2012; Pereira et al., 2015) .

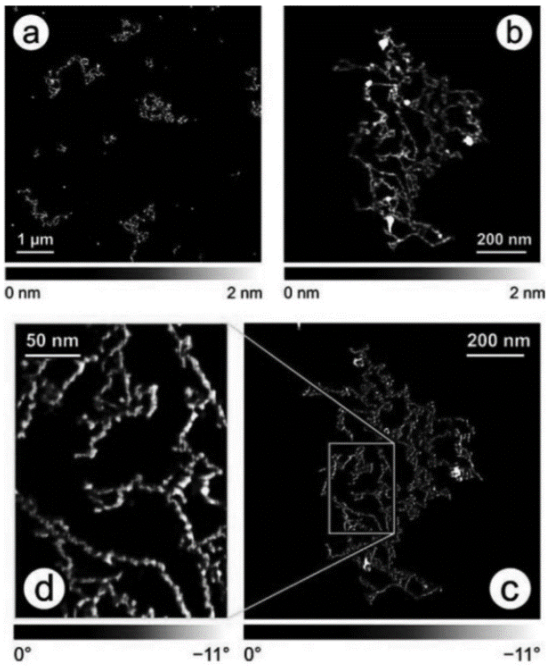

Figure 2.26. Noncontact AFM images of silk deposited from an aqueous1:1000 solution by spin-coating, which induced shear in the solution:(a, b) topography image; (c, d) phase images Reproduced with permission.[31]

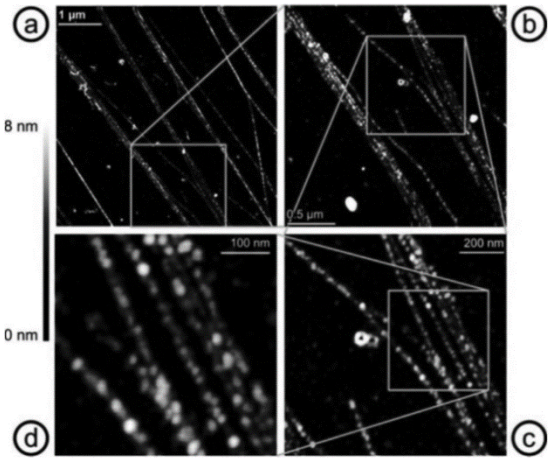

Figure 2.25. Noncontact mode AFM topography images showing a sample that was prepared by spin-coating a 1:10 silk solution. The images show self-assembly of silk protein into linear, thread-like structures Reproduced with permission.[31]

[31] Reprinted with permission from Imke Greving, Minzhen Cai, Fritz Vollrath et al., Shear Induced Self-Assembly if Native Silk Proteins into Fibrils Studied by Atomic Force Microscopy, Biomacromolecules, Copyright (2012). American Chemical Society.

We mentioned earlier that "silk materials are semi-crystalline polymers consisting of ordered domains containing crystallites with precise secondary structures and high H-bonding density, interspersed with disordered amorphous domains with a lower H-bonding density" (Walker et al., 2015, p. 1). The formation of the ordered crystallites can consist of "β-sheets, α-helical coiled-coils, collagen helices or the polyglycine II structure" (Walker et al., 2015, p. 1). Crystallite orientation is a characteristic that differentiates the extended β-sheet structure from the cross- β-sheet structure; from this, more structural variation is derived (Walker et al., 2015).

Silk that is produced by the cocoon fibres of silkworms as well as the dragline silks of orb-spiders hold crystallites of the extended β-sheet kind. Non-canonical silks, which carry crystallites of other kinds, are fabricated by a minimum of 9 groups of insects (Walker et al., 2015).

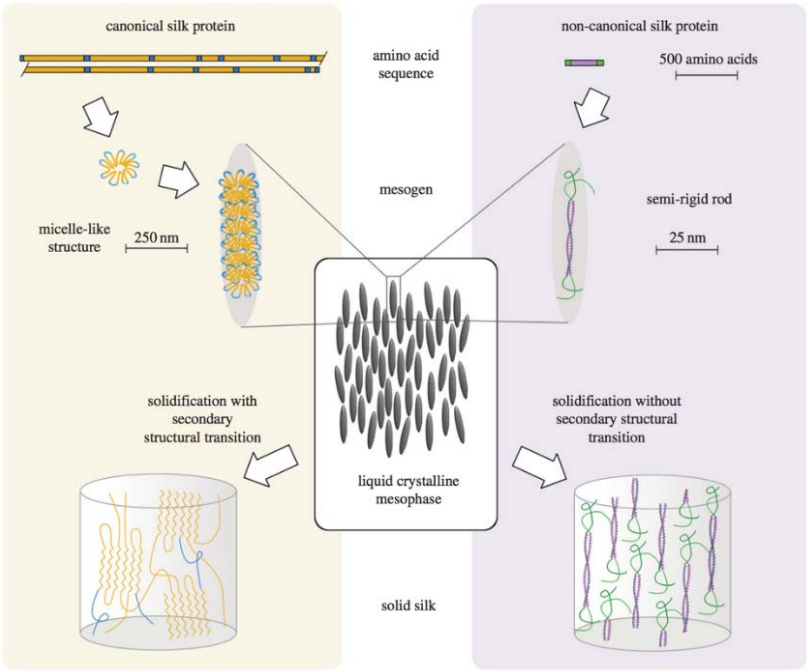

Figure 2.27. Comparison of liquid crystalline processing of canonical and non-canonical silk protein. Canonical silk proteins from silkworms and spiders (left) assemble into large, micelle-like mesogens by virtue of their flexibility and amphiphilicity, while non-canonical silk proteins (right) fold into comparatively small rod or lath-like mesogens with well-defined secondary structure. Liquid crystalline intermediates reduce flow viscosity, assist solubility and participate in the formation of supramolecular structure. Solidification occurs concurrently with a structural transition to the final extended-b-sheet structure for canonical silk proteins, whereas non-canonical silk proteins do not change structure markedly during solidification. Reproduced with permission.[32]

[32] Reprinted from Proceedings Biological Sciences, Vol 282/Issue 1809, Andrew A. Walker, Chris Holland, Tara D. Sutherland, More than one way to spin a crystallite: multiple trajectories through liquid crystallinity to solid silk, Pages No. 1-9, Copyright (2015), with permission from The Author(s) Published by the Royal Society.

Figure 2.27 is important, as it summarizes the different stages of silk from protein, micelle, mesophase (liquid crystalline), and finally a solid structure. It is thought that the flexible essence of H-fibroin in the silk network is convenient for the arrangement of lyotropic mesophases that are shaped like micelle. This structure is made of lengthy areas of hydrophobic repeats interspersed with hydrophilic ties. Thus, the low degree of birefringence displayed by mesophasic silk dope is improbable to happen because of orientation birefringence ensuing from the long-range location of polarizable bonds; however, it depicts pattern birefringence. It arises from the anisotropic allocation of two coinciding stages, that prove to be also isotropic (Walker et al., 2015). The phases could be recounted as first, a hydrophobic one made up of the dominant repeats of the silk protein, and second, a hydrophilic one made up of ions water, and the hydrophilic ties belonging to the silk protein. If the environment innately prefer anisotropic lyotropic formations, like hexagonal pillars, or if isotropic formations, like micelles, aggregates between head to tail polymerization (as it has happened when shearing), anisotropy might emerge (Greving et al., 2012; Walker et al., 2015). The mesogen will likely be similar to micelles seen in native and reconstituted silk, and will have an extra feature of elongation as shown in *Figure 2.28* (H. J. Jin & Kaplan, 2003).

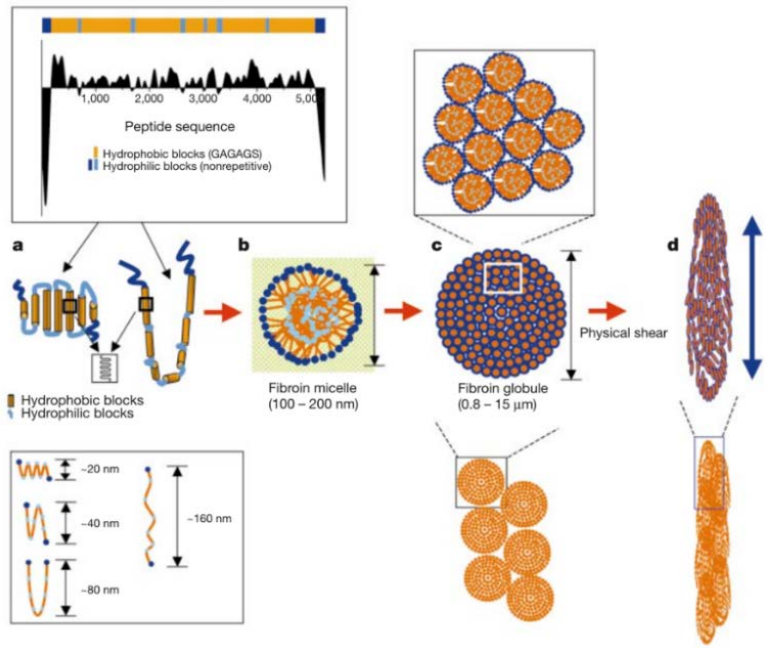

Figure 2.28. An schematic of silk assembly into micelles and macrostructures. Reproduced with permission.[33]

[33] Reprinted by permission from Springer Nature, [Springer Nature] [Nature] [(Mechanism of silk processing in insects and spiders, Hyoung-Joon Jin, David L. Kaplan)], [Copyright 2003]

There are a few studies that have compared silk and synthetic raw material staples. Due to the growth of shear-induced polarized light imagery, it was found, by comparing it with a common polymer, that silk feedstock required 1000 times less energy to be able to produce fibrils. It is thought that this incredible energy saving is done because of a particular element: an aquamelt. This element is a normally hydrated polymeric that can become solid at normal temperatures because of a controlled stress absorption. This might be due to a subtle chemical contribution (*Figure 2.29*). The solidification is caused by a very distinctive interplay of the elements with their shell of moisture. Moreover, the shell vanishes and there is a separation between solvent water and solid polymer. Since all new proteins have a peptide-based chemistry, the process is thought to be part of all of them (Vollrath et al., 2013). This way, this is the mechanism that would enclose any fibrillation that happens in spinning, which, as mentioned before, is irreversible. The understanding of aquamelts could help answer problems about reconstitution to finally make biomimetic silks. It might also help the discovery of new forms of handling hydrogen bonding in biological and synthetic polymers (Vollrath et al., 2013).

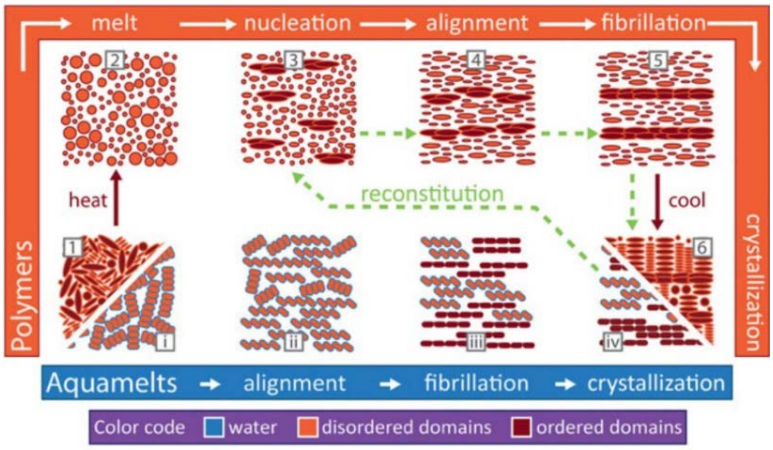

Figure 2.29. Scheme for fibre formation in polymers (orange box, numbers) and their proposed subclass aquamelts (blue box, Roman numerals). Horizontal arrows depict stages that require sample shearing, with aquamelts requiring one-tenth the work required in order to bring about fibrillation (as represented by arrow length). Colored objects in the drawings represent components responsible for the formation of fibres in the systems: long chain molecules (their radius of gyration or shape) in polymers and proteins (secondary and tertiary structures) in aquamelts. These are color-coded to represent ordered, disordered, and hydrated domains. Green dotted arrows represent the path reconstituted (artificial) silk currently follows in order to be reprocessed into a fibre (Vollrath et al., 2013, p. 76). Reproduced with permission. [34]

[34] Reprinted from MRS Bulletin, Vol 38, F. Vollrath, D. Porter, C. Holland, The Science of Silks, Pages No. 73-80, Copyright (2013), with permission from Materials Research Society 2013

The hierarchical structure of silk proteins can be found as well in other elements that have been prepared by regenerated silk protein solution; one example is hydrogels. The gelation process occurs slowly at environmental temperatures, but can be accelerated in other ways, such as changing pH, protein concentration, temperature, or also by utilizing other stimuli, like electric fields, shear force, surfactant, alcohols and ultrasound. Even though it is thought that in gelation β-crystallites were assembled with inter and intramolecular silk fibroins because of hydrophobic interactions and hydrogen bonds, there is not yet an understanding of the interrelation between mechanical properties and hierarchical network (Nguyen et al., 2015).

2.3.6 Self-assembly in Silk

The use of different solvents to achieve silk self-assembly has been proposed with a focus on the preparation of silk films. In particular, ethanol, as it is a very important element in the $CaCl_2/H_2O/C_2H_5OH$ ternary solution, plays an substantial role in the disintegration of silk fibroins through causing their enlargement. The same moment, the presence of ethanol can perhaps cause the β-sheet change of silk fibroin (Krens & Heisenberg) molecules. Globule-like nanostructures has been noted in regenerated SF films, and if the ethanol content was reduced in the solvent, the size also diminished (J. Zhou et al., 2014). Other solvents can lead to the formation of silk aggregates, and these are unloaded into a specific surface *Figure 2.31* and *Figure 2.32*.

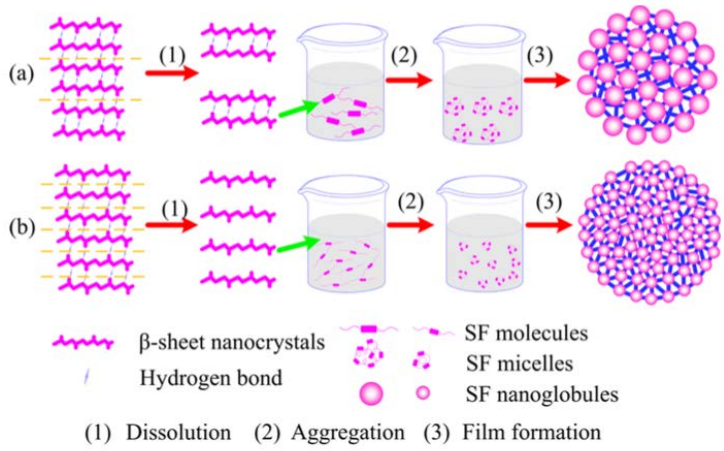

Figure 2.30. Mechanism of the regenerated SF films prepared by changing ethanol concentration in a CaCl2/H2O/C2H5OH solution. (a) Solvent A; (b) solvent B (J. Zhou et al., 2014). Reproduced with permission.[35]

[35] Reprinted with permission from Juan Zhou, Bin Zhang, Lijun Shi, et al., Regenerated silk fibroin films with controllable nanostructure size and secondary structure for drug delivery, Applied Materials, Copyright (2014) American Chemical Society.

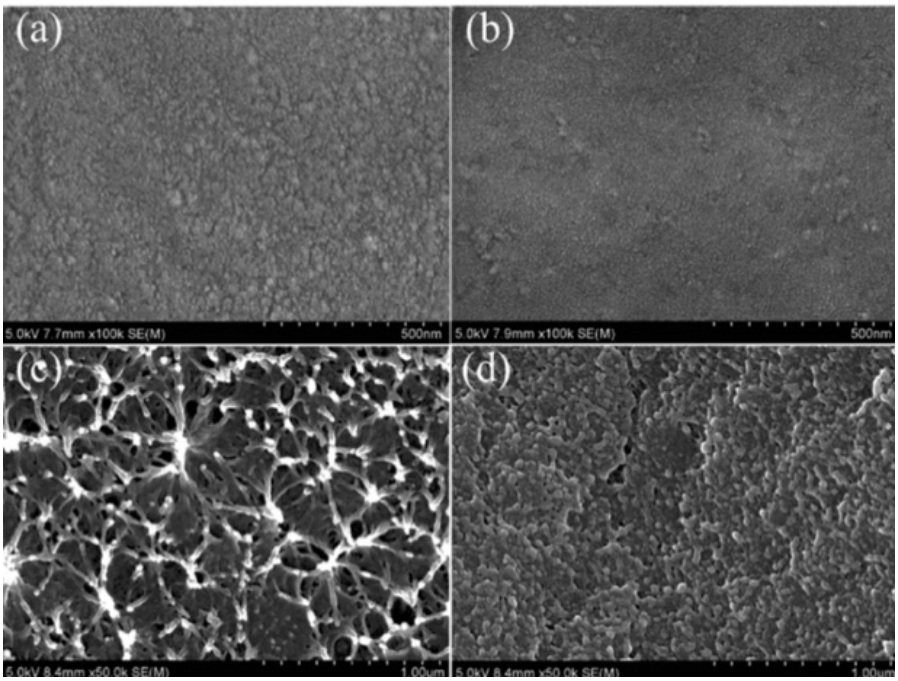

Figure 2.31. SEM of the cross-sectional mor-phology of the re-generated SF films A5 and B5. (a) SF films A5, by breaking off in liquid nitrogen; (b) SF films B5, by breaking off in liquid nitrogen; (c, d) represented different section of the SF films B5 fractured at room temperature. Scale bars are (a, b) 500 nm and (c, d) 1 μm. Reproduced with permission.[36]

Several studies have explored silk self-assembly in a controlled setting to understand the formation of microspheres and nanofilaments. A relevant study by Lu et al. (2012) explores the thermodynamics and kinetics of the self-assembly process. The authors use slow dry silk I hydrogels at room temperature. When the hydrated silk fibroins are stretched, the resulting film has elastic properties as the silk transitions from into silk II. Further examination showed that silk was initially self-assembled into micelles, which then aggregated into nanofilaments. Further research has shown that the mechanical strength of silk could arise by the formation of silk II β-sheets. However, the steps from micelles to nanofibrils have not been fully elucidated yet (Keten, Xu, Ihle, & Buehler, 2010; Q. Lu et al., 2012).

Silk molecules present hydrophobic and hydrophilic sections. When micelles are formed, the edges are formed by the larger terminal hydrophilic blocks, while the hydrophilic

[36] Reprinted with permission from Juan Zhou, Bin Zhang, Lijun Shi, et al., Regenerated silk fibroin films with controllable nanostructure size and secondary structure for drug delivery, Applied Materials, Copyright (2014) American Chemical Society.

blocks are enclosed inside. Since the micellar formations in water can be rearranged, this structure is thermodynamically unstable. Therefore, the self-assembly process is controlled by the molecules movement and the hydrophilic/hydrophobic interaction. This is confirmed by results in other studies, in which it is shown that increasing the temperature, and hydrogen bonding speeds up the transition from isotropic mesophase to crystalline structures (S. Lu et al., 2010; Lv, Cao, Zhang, Ma, & Zhu, 2005).

Quite interestingly, Lu (2012) also observed that micelles aggregated into nanofibrils instead of bigger globules as the concentration of silk increased. This is due to the rise of the hydrophilic interplay of silk fibroin and water. Thus, the repulsion forces due to negative charges on the silk fibroin molecules play a crucial role in managing micelle aggregation. Additionally, the process also gave insights into the silk transition's metastable equilibrium between its I and II forms. It was found that hydrophilic interactions by silk I limit the formation of crystal at early stages, while these interactions disappear in silk II structures. Thus, the thermodynamic processes supported the transition of silk fibroin from random coils into silk II β-sheet formation. However, it is important to note that due to the energy barrier between silk I and II, some random coils will form silk I as an intermediate, after which it will change to silk II (Q. Lu et al., 2012).

2.3.7 Applications of silk self-assembly

Different investigations have analyzed the efficacy of silk as a device for delivering drugs utilizing self-assembled elements (Z. Zhao, Li, & Xie, 2015). Therefore, most of the research has focused in developing a high throughput system for the formation of the given spheres. An extensive review was developed recently by Zhao Z.(2015), where it summarize more than 10 distinct techniques for particle structuring as salting out agent in water, desolvation/ coacervation, supercritical fluid technologies and electrospraying, micro emulsion and others.

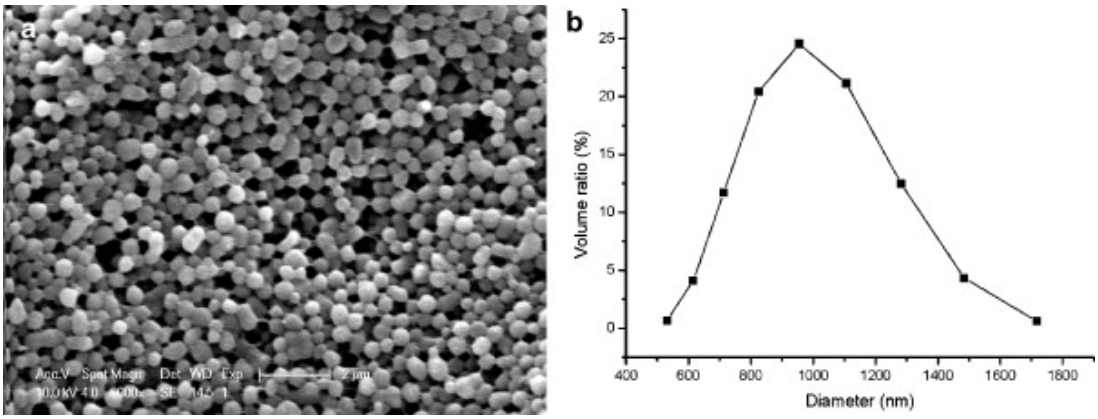

Figure 2.32. (a) SEM image of silk fibroin particles, and, (b) their size distribution. Reproduced with permission.[37]

We would like to mention a particularly similar method to the one used in current research. Silk fibroin particles (*Figure 2.32*) have been processed by utilizing ethanol and polyvinyl alcohol solution (PVA). The procedure consists in preparing a solution of silk fibroin and ethanol 28%, mix and then 1.5 PVA%v/v is added and centrifuged. The ternary solution is then set into a freezer during 24 h to form silk fibroin elements, and the resulting spheres are shown in *Figure 2.32* (Shi & Goh, 2012).

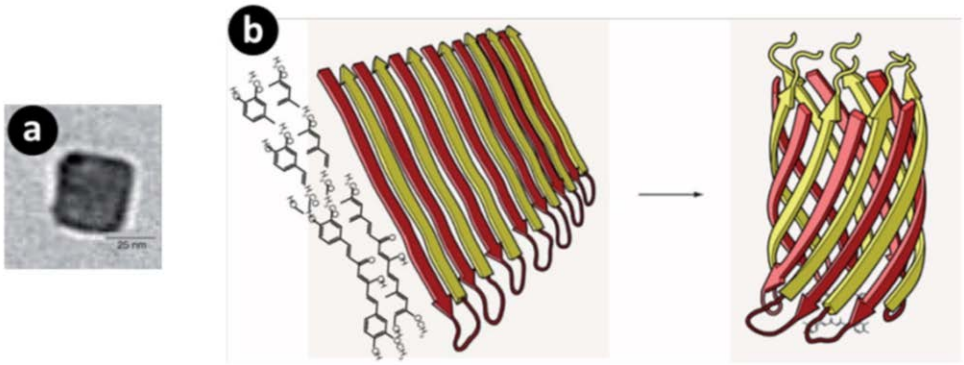

Figure 2.33. TEM image of curcumin molecule encapsulation in the SF cylindrical barrel structure (a). Schematic representation of molecule and SF b-sheets self-assembly (b) (Mathur & Gupta, 2010, p. 817) Reproduced with permission.[38]

Silk self-assembly has also been utilized in encapsulation. For the improvement of drug bioavailability, the particles were fabricated utilizing silk fibroins. The molecule was encapsulated in the silk fibroin cylindrical barrel structure (Figure 2.33). Thus, when using

[37] Reprinted from International Journal of Pharmaceutics, Vol 420, Pujiang Shi,James C.H. Goh,. Release and cellular acceptance of multiple drugs loaded silk fibroin particles, Copyright 2011 with permission from Elsevier.

[38] Reproduced from Nanomedicine (Lond). (2010) 5(5), 807-820 with permission of Future Medicine Ltd.

curcumin, the curcumin was encapsulated in a silk fibroin cylindrical barrel structure (Pereira et al., 2015).

Furthermore, silk fibroin has been presented as a potential bioink for biomedical applications. To produce the bioink from silkworm silk, the fibroin is re-engineered into a solution by separating the hydrogen bonding and hydrophobic domains that control the intra- and inter-chain interaction inside the silk fibroin chain. When it is ready in a solution, it can induce the formation of β-crystallization, which is used to create 3D shapes. Additionally, when the cells are not enclosed in the bioink, it can also be used for standard 3D printing. Several studies have been explored the use of silk for bioink with silkworm and recombinant spider silk (Chawla, Midha, Sharma, & Ghosh, 2018).

Silk-based composite scaffolds also have applications in tissue engineering. Porous scaffolds are used as the 3D templates, which degrade slowly as the extracellular matrix develops. Therefore, these scaffolds play a vital role as a starter matrix for "cell attachment, proliferation, and maintenance of their functions *in vivo* and *in vitro* tissue engineering" (P. X. Ma, 2004). Silk scaffolds have been used in skin regeneration and wound dressing (Q. Lu, Zhang, Hu, & Kaplan, 2010; Zarrintaj et al., 2018), skeletal tissue engineering (He et al., 2016; Nematollahi et al., 2017), vascular tissue engineering (Ding et al., 2019; Ravi & Chaikof, 2010) and others (Tandon, Kandasubramanian, & Ibrahim, 2020).

2.4 Cells

2.4.1 Introduction

We have previously defined self-assembly as the autonomous alignment of elements from a beginning state towards structures or constructions, with no foreign interference (Boncheva et al., 2005; Jakab et al., 2010; G. M. Whitesides & Boncheva, 2002; George M. Whitesides & Grzybowski, 2002). Self-assembly is also found inside the human body. One example is histogenesis, which can be seen when the structure of an embryo differentiates and

develops organs and cells from common tissue (Bignold, 2015; "Histogenesis," 1998). The basis of cellular self-assembly could, then, brighten the path for constructing living structures. Although the building of, for example, organs, has not been completely successful yet, there are some cases which have obtained good results (Macchiarini et al., 2008; Nakamura & Sato, 2018). Nevertheless, to further understand cells self-assembly, methods must take into consideration the way the body can innately regenerate. As the Hoshin process describes, to advance the field, it is necessary to focus on angiogenesis and molecular and systems biology, amongst others (Hellman & Nerem, 2007).

We'll discuss cells cultured in 3 dimensions, such as organoids and spheroids, in the following sections. Spheroids are simple structures formed by the aggregation of a single type of cells in ultra-low attachment plates. Although organoids can also be cultured by cell aggregation, they are more commonly derived from stem cells that grow in a supporting matrix. Regardless of these differences, the literature uses the term "cell-aggregates" to refer to both spheroids and organoids. In the present thesis, we will follow this convention by using the word "spheroids" for cell-aggregates made of a single cell type and "organoids" for complex cell-aggregates with multiple types of cells.

2.4.2 History of cell aggregates

It has been years since modified aggregates of animal cells started to be used in research. For example, there was a technique to create stable aggregates of embryonic cells in amphibian embryos. To obtain the aggregates, embryonic transfers or single cells on agar as an underlying layer were utilized to keep away the cells from adhering to the ground of the culture dishes (Johannes Holtfreter, 1944). When there was a need to reduce the cells interaction with the substratum, the samples were mechanically shaken (J. Holtfreter, 1947; Mueller-Klieser, 1987).

Another study worked on the reaggregation of independent cells sourced from chick embryos on plasma clots. To make the suspensions, trypsin and hyaluronidase were used to disaggregate the embryonic organ elements (Aron Moscona, 1952; Mueller-Klieser, 1987). Later, it was proven *in vitro* the intrusive ability that melanoma cells possess (A. Moscona, 1957). With Dabrowska Piaskowska, (1959) it was discovered that there exists an impressive similarity in the form of the tumor cell aggregates and the original tumor tissue. "Moscona's method" was brought to the public in 1961; this technique consists in the induction and growth of multicellular aggregates kept in suspension cultures utilizing Erlenmeyer flasks that were placed in a gyratory shaker. It was then used in further research (Mueller-Klieser, 1987). An example of this is when Halpern et al. (1966) showed that malignant cells can form aggregates at a much higher rate than normal cells. Also, Schelich (1967) discovered the better ability to structural formation in aggregates of malignant and dedifferentiated ascites cells from humans. Another important finding was that only quantitative distinctions might occur in malignant and non-malignant cells, according to their ability to aggregate inside agitated liquid media (Mueller-Klieser, 1987).

Sutherland and others (Inch, McCredie, & Sutherland, 1970; Sutherland, Inch, McCredie, & Kruuv, 1970; Sutherland, McCredie, & Inch, 1971) were the first to utilize multicellular tumor spheroids for cell response to therapy. Spheroids have also been used for therapeutic studies.

2.4.3 Organoids

Organoids are multicellular 3D constructs, which mirror the architecture of organs. Although they are simplified versions of organs, they have multicellular intricacy and present organ functionality (de Souza, 2018; Hofer & Lutolf, 2021; Takebe & Wells, 2019). Organoids can be derived from primary tissue, embryonic stem cell or induced pluripotent stem cells (Meina Li & Stewart, 2021). As they are tractable models which can also be genetically manipulated,

they are commonly used to study pathophysiology and organ development *in vitro* (Takebe & Wells, 2019). Organoids are used in a broad number of applications, such disease modelling, the study of pathogens that affect humans, personalized drugs, cell therapy, and drug screening (Hofer & Lutolf, 2021; Takebe & Wells, 2019). Furthermore, organoids can mimic gene and protein expression and metabolic behaviour (Hofer & Lutolf, 2021).

Cell aggregates have been used in biomedical research for several decades. Still, it is only recently that the study of organoids has become a crucial part of biomedical and tissue engineering research. It was the revolutionary work by Sasai et al (2011) and Clevers et al (2009) changed this research field. The study from Clevers proved that intestinal organoids could be constructed from adult stem cells. At the same time, Sasai and co-workers used embryonic or pluripotent stem cells (PSCs) to recount the development of cortical tissues and the optic cup (Rossi, Manfrin, & Lutolf, 2018). More importantly, their research showed the intrinsic ability of stem cells to self-assemble into 3D structures which mimic *in vivo* organs.

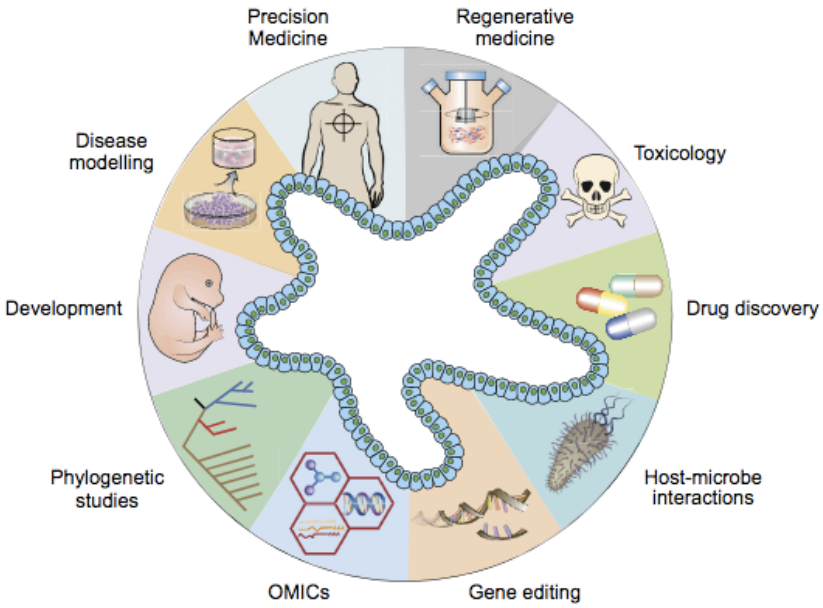

Figure 2.34. Applications of organoid technology. Reproduced with permission.[39]

[39] Reprinted under Creative Commons Attribution CC-BY 4.0: © the American Physiological Society.

Organoids have varied functionality, like muscle contractility, gastric acid secretion, neuronal activity, epithelial barrier, etc. However, PSC-derived organoids do not display the maturity of their *in vivo* counterparts. This is partially caused by oxygen and nutrient diffusion restriction, limiting the organoid size to a few millimetres (Takebe & Wells, 2019). For this reason, vascularization remains one of the biggest challenges to resolve if we want to promote organoid growth and achieve tissue maturity (Grebenyuk & Ranga, 2019). Regardless of these limitations, organoids research continues to give us insight into tissue development and has a great potential for clinical translational research.

2.4.3.1 Applications of Organoid Technologies

Figure 2.34 gives us an overview of the wide variety of applications of organoid technologies. One of the primary uses of organoid models is in disease modelling, which in turn can be used for "drug screening, genotype-phenotype testing and even biobanking for specific diseases and future personalized treatments" (Grebenyuk & Ranga, 2019). Organoids have been used to study congenital conditions and acquired diseases. One of the first conditions to be modelled was cystic fibrosis. Dekkers et al. (2013) generated CF-patient-derived intestinal organoids that could recapitulate the disease *in vitro* and used to evaluate the effectiveness of CFTR modulators (Berkers et al., 2019). Organoids have also been used in other congenital conditions as: microcephaly caused by genetic mutations (Lancaster et al., 2013), idiopathic autism spectrum disorder (Eiraku et al., 2008; Mariani et al., 2015) and Leber congenital amaurosis (Parfitt et al., 2016).

Organoids are also used to model acquired diseases, and in fact, they have become a well-established model in cancer research. Healthy and tumor tissues from patients can be efficiently grown into organoids, and the derived tumor resembles phenotypically and genetically (Pauli et al., 2017). This similarity can enable tailored drug testing and personalized treatment (Drost & Clevers, 2018). Emerging technologies have also allowed the organoids to

keep the heterogeneity of the original tumors, which can significantly support fundamental and clinical cancer research (Fatehullah, Tan, & Barker, 2016). Furthermore, organoids model cancer dynamics. Some authors have built phylogenetic trees by observing the genetic mutations to construe the lineage connections that exist amid cells in a specific tumor (Kuo & Curtis, 2018).

2.4.3.2 Necrosis

Cell aggregates lack of vascular system have important consequences to the viability of the cells. Variations in oxygenation and nutrient deliver can damage the cell causing necrosis. Cells in the center of the organoid are more affected, creating a "necrotic core' (Daster et al., 2017). Although this characteristic of the organoids might limit their usage, it is well-regarded in cancer research. Similarly, to *in vivo* tumors, a tumor spheroid will develop hypoxic and necrotic regions. Chemical gradients concerning catabolites, oxygen and nutrients occur in the tumor samples, and cells close to the edge of the spheroid vigorously cycle tumor cells next to capillaries. The cells in the core, meanwhile, turn inactive and start to die due to necrosis, as seen in *Figure 2.35*. The probability of finding necrotic cells increase wiiiiii09ith organoid growth. A necrotic core can be usually found in multicellular tumor spheroids when they are bigger than 500µm (Hirschhaeuser et al., 2010).

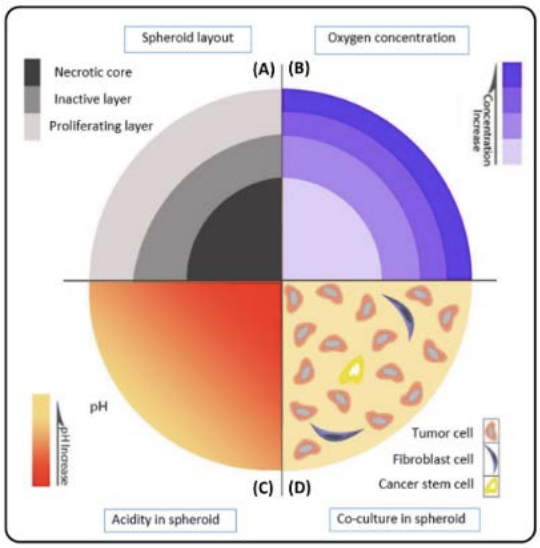

Figure 2.35. Tumor spheroid characteristics. (A) The three cell layers, distinguished by the rate of proliferation; (B) oxygen concentration gradient in tumor spheroid; (C) the pH gradient shows the existence of an acidic environment in the core as a result of anaerobic activities; (D) shows cells and the surrounding ECM in a co-cultured tumor spheroid (Moshksayan et al., 2018). Reproduced with permission.[40]

[40] Reprinted from Sensors and Actuators B: Chemical, Vol 263, Moshksayan et al. Spheroids on a chip: Recent advances and design considerations in microfluidic platform for spheroid formation and culture, Pages 151-176., Copyright 20108 with permission from Elsevier.

Since it's difficult to use spheroids with necrosis in regenerative medicine, one study (Anada, Fukuda, Sai, & Suzuki, 2012) used 3D culture chips in order to build spheroids. These chips allow direct oxygen flow to the cells since it is built with only gas-pearmeable polydimethylsiloxane mold. There are two theories of how to control the formation of necrosis, the first one is the control of the size of the spheroids, while the other one is what this study did, which is to control the direct oxygenation of the spheroid. The chip allowed the prevention of necrosis in the cells, even in comparative larger cell aggregates.

2.4.3.3 Organoid engineering

For the structuring of an organoid, there is usually the self-organization from continuous local interplay amongst cells that came from a disorganized arrangement, augmented by positive feedback. Generally, homogenous PSCs is used for tissue self-organization for eyecup, blood vessel and brain organoids. Here, aggregation size regulates tissue patterning, and this modifies consequent self-organization programs. Heterogeneous aggregates are also used, which come from different progenitor types. These are usually occupied in the unification of accessory structure into the organoids to obtain higher-order behaviour (Takebe & Wells, 2019).

However, self-organizing is not enough for mature organs. To promote the features of an organoid, an extracellular matrix that backs up cell growth needs to be used (Hofer & Lutolf, 2021; Rossi et al., 2018). As EMC "is the basis of virtually all organoid culture systems" (Hofer & Lutolf, 2021, p. 409) common alternatives as Matrigel are generally used for this purpose, as shown in brain organoids (de Souza, 2018). Also, cultures with Matrigel help the research of branching morphogenesis. Working the matrix composition has been seen to better fused intestinal organoid formation, amongst other things (Takebe & Wells, 2019). To engineer more complex organoids with higher order functions, it is important to continue with advancements in spatiotemporal ECM manipulation (Murrow, Weber, & Gartner, 2017; Takebe & Wells,

2019). Spatiotemporal regulation can be obtained by direct patterning of the growth matrix. It helps the spatial delivery of cues and to reproducibly generate organoids that have a higher level of maturation (Hofer & Lutolf, 2021). Another way to recapitulate the procedure organogenesis are soluble factors, which have been used to construct sophisticated pattering that occurs at the tissue edge. Here, there is a time and dose variation of signalling pathways that generate pattern structuring that gets stabilized due to the calculated inter-cellular interplay (Takebe & Wells, 2019).

There are also synthetic biology-inspired methods that have been seen to manipulate symmetry breaking and help programmed sorting. With perfusion, engineering procedures allow the exact regulation of the geometry input and output flow settings, the reserve of nutrients, shear stress stimulation, and the local mechanical properties of the developing filaments (Sontheimer-Phelps, Hassell, & Ingber, 2019; Takebe & Wells, 2019). Moreover, mechanical forces like fluid shear stress or hydrostatic pressure can direct a signalling dimension to control tissue self-organization (Takebe & Wells, 2019).

2.4.4 Spheroids

When there is the necessity to reconstruct or change injured or lost organs and tissues, tissue engineering is what will help with the building of a biological stand-in (Katari, Peloso, & Orlando, 2014; Laschke & Menger, 2017). To do this, “isolated cells are seeded on biodegradable scaffold, which serve as matrices for cell attachment and determine the 3D shape of the tissue substitutes” (Laschke & Menger, 2017, p. 133). Nevertheless, even with this tissue substitutes, there is the problem of biocompatibility. Also, as life is 3 dimensional, and the interplay of cells with setting is 2D, this is an artificial condition (Laschke & Menger, 2017).

As mentioned before, when the embryo grows, cells self-assembly and structure tissues that are 3D, while there is thorough cell to cell contact. The contact is essential, as it preserves intracellular operations (Fitzgerald, Malhotra, Curtin, FJ, & CM, 2015; Laschke & Menger,

2017). These cells are enveloped in an extracellular cast that delivers important biochemical and biomechanical indications; it also establishes cell differentiation, homeostasis, and proliferation (Kinney, Hookway, Wang, & McDevitt, 2014). Moreover, the cells get diffusively transported, which results in a heterogeneous spatial dispersion of nutrients, signalling molecules, oxygen and metabolites (Kinney et al., 2014; Laschke & Menger, 2017). As it is a complex process to try and copy these settings, researchers have tried using spheroids to assemble them for tissue engineering (see *Figure 2.36*).

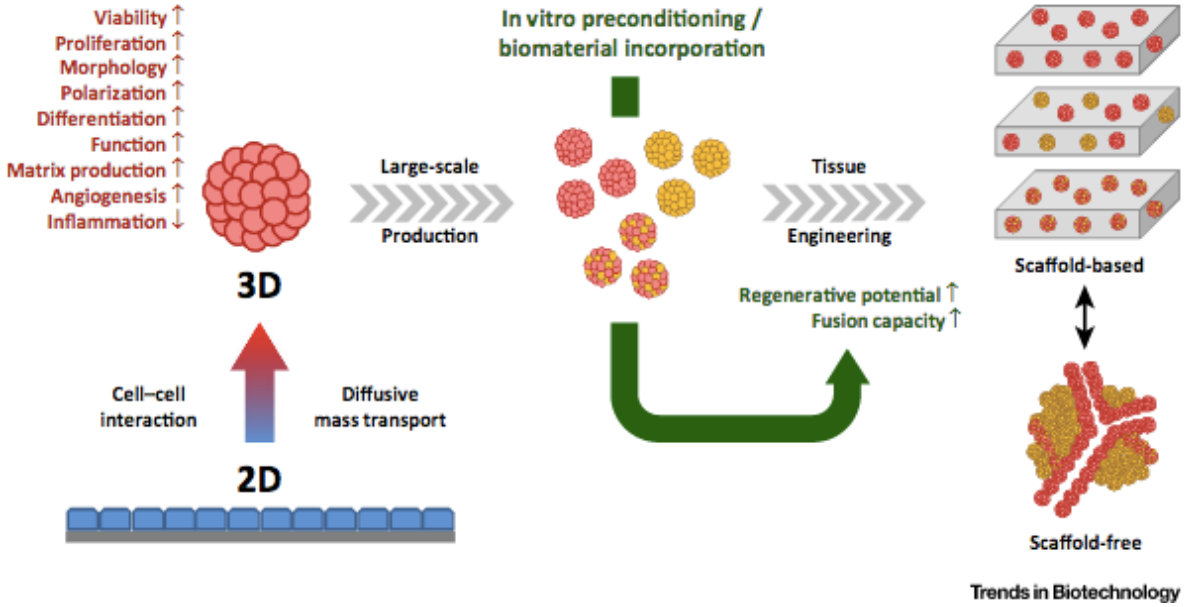

Figure 2.36. As a result of their 3D structure, intensive cell-cell interactions and diffusive mass transport, spheroids exhibit a panel of biological and regenerative properties, which are markedly improved when compared to 2D cell monolayers. Accordingly, they are increasingly used for tissue engineering. For this purpose, sophisticated technologies have been developed, which allow the large-scale production of spheroids. For the generation of complex tissues, monoculture spheroids of different cellular origin (marked in red and orange) are combined or multiple cell types are incorporated in coculture spheroids. *In vitro* preconditioning under different culture condition sand biomaterial incorporation improve the regenerative potential of spheroids and their fusion capacity. Subsequently, the spheroids are seeded on scaffolds to generate scaffold-based tissue substitutes or are fused to scaffold-free macro-tissues. Reproduced with permission.[41]

[41] Reprinted from Trends in Biotechnology, Vol 35 /Issue 2, Matthias W. Laschke, Michael D. Menger, Life is 3D: Boosting spheroid function for tissue engineering, Pages No. 133-144, Copyright (2017), with permission from Elsevier.

2.4.5 Generation of Spheroids

Spheroids are generated through the basic laws of self-assembly (George M. Whitesides & Grzybowski, 2002). *In vitro*, it has also been seen that when self-assembly happens, cells cannot adhere to any surface, and will be forced to interact with themselves. To reach this result, there have been several spheroid construction methods (Achilli, Meyer, & Morgan, 2012; Fennema, Rivron, Rouwkema, van Blitterswijk, & de Boer, 2013; J. H. Kim et al., 2015; Yoon, Bhang, Shin, Shin, & Kim, 2012). It is a matter of deciding which method is better for each enterprise. First, there should be a large construction of spheroids of a determined size and configuration. This is done as to not cause necrotic damage in the spheroid core, as the cells inside spheroids present diffusive oxygen supply (Groebe & Mueller-Klieser, 1996). The amount of spheroids should be in the thousands to millions to effectively create tissue substitutes. Thus, the methods should be efficient and adaptable for scaling-up and automatization (Laschke & Menger, 2017).

2.4.5.1 Spinner culture

Among the most common methods, the spinner culture one generates spheroids with cell-to-cell collisions in the midst of constant stirring (Achilli et al., 2012; Castaneda & Kinne, 2000; J. B. Kim, 2005). In this technique spinner flasks are implanted alongside a homogeneous single cell suspension, and convective forces created by an impeller control the mass transfer in the sample. It is important to keep a consistent rotation speed. The fluid action helps mass transport between the spheroids. Spinner culture may be adjusted to generate a large number of spheroids. Because of shear forces, this technique is not as convenient for cells that present low cohesiveness, or are delicate where there are shear forces, or for adherent cells that could endure apoptosis while in the suspension (Achilli et al., 2012).

2.4.5.2 *Forced Floating*

This is one method to block the attachment of 3D spheroids to the vessel surface, and thus generate them. This is done by altering the surface. The surface can be altered, for example, by using poly-HEMA, so that there is enforced floating of the cells (Breslin & O'Driscoll, 2013). There is cell to cell contact, and multicellular sphere structuring (R. Z. Lin & Chang, 2008). Other coatings used for this method are agarose, and poly (*N*-*p*-vinlbenzyl-d-lactonamide) (Cui, Hartanto, & Zhang, 2017).

This technique has various benefits. It is simple and can be easily duplicated, since equivalent numbers of cells can be implanted in each well to create steady spheroids. The measurements of spheroids can be adjusted, and if bigger spheroids are needed, larger numbers of cells should be seeded. This method is suitable for high-throughput drug testing as the spheroids created can be accessed for experimentation (Ivascu & Kubbies, 2006). It has an inexpensive cost, and it is a simple procedure (Cui et al., 2017). Also, because they are generated in a 96-well plate, large quantities of morphologically spheroids can be created (Breslin & O'Driscoll, 2013). The main disadvantages would be the variations in size and shape in the spheroids, as well as the intensive labour needed for the production (Cui et al., 2017).

2.4.5.3 *Liquid Overlay*

Another technique is liquid overlay. This method restricts the cells from adhering to the culture plates and boosts cell aggregation (Enmon Jr, O'Connor, Lacks, Schwartz, & Dotson, 2001; Ivascu & Kubbies, 2006; H.-l. Ma et al., 2012). To avoid cell attachment, the cell culture plate needs to be of a low-adhesive material such as agarose (Napolitano, Chai, Dean, & Morgan, 2007), polydimethylsiloxane (PDMS) (Lopa et al., 2015), poly(2-hydroxethyl methacrylate) / poly-HEMA (Lopa et al., 2015), or polyethylene glycol (PEG) hydrogels (Cha et al., 2018).

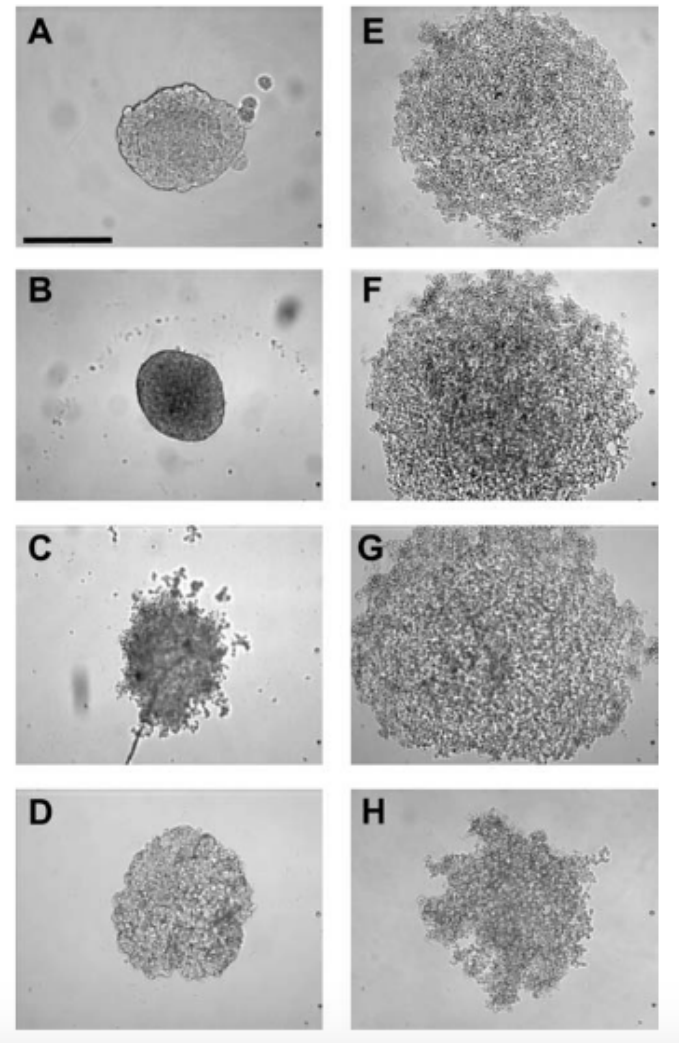

Figure 2.37. Rapid formation of spheroids or aggregates of different breast cancer cell lines using poly-HEMA–coated 96-well, round-bottom plates (5000 cells/well, 24-h culture period; exception: 48 h forMCF7-ADR) (A) MCF7, (B) T-47D, (C) MDA-MB-435 (might be of melanoma origin in case that trans differentiation event can be excluded), (D) MCF7-ADR, (E) MDA-MB-231, (F) MDA-MB-468,(G) SK-BR-3, and (H) MDA-MB-361. Size of black bar =500 μm. Reproduced with permission.[42]

In the present dissertation, we use poly-HEMA as the coating method for culturing 3D spheroids. Over four decades ago, Folkman et al. (1978) established a coating method to reduce cell adherence with poly (2-hydroxethyl methacrylate), also known as "poly-HEMA". They showed that as the coating layer thickness increase, cell adhesion is reduced, and spheroids are formed. Ivascu, A. et al. (2006) explored spheroid formation and toxicity across different cancer cell lines. They found no changes in cell viability, results which have been replicated in other studies. (Achilli et al., 2012; Enmon Jr et al., 2001; Landry, Bernier, Ouellet, Goyette, & Marceau, 1985; Metzger et al., 2011; Turksen, 2018). Therefore, poly-HEMA coating is a well-established technique for the culture of 3D spheroids.

[42] Reprinted from SLAS Discovery, Vol 11/Issue 8, Andrea Ivascu, Kubbies Manfred, Rapid generation of single-tumor spheroids for high throughput cell function and toxicity analysis, Pages No. 922-932, Copyright (2006), with permission from Sage Publications.

2.4.5.4 Hanging Drop

The hanging drop method consist in the generation of multicellular spheroids due to single spheroids forming in hanging drops dangling from a microtiter plate, as seen in *Figure 2.38* (Kelm, Timmins, Brown, Fussenegger, & Nielsen, 2003). The main benefits of this method are that the spheroids will have a uniform-size, that the operation is easy and the controlled environment. While, the troubles found are that the multicellular spheroids are small, and with this classic method, there was not a way for mass production (Cui et al., 2017).

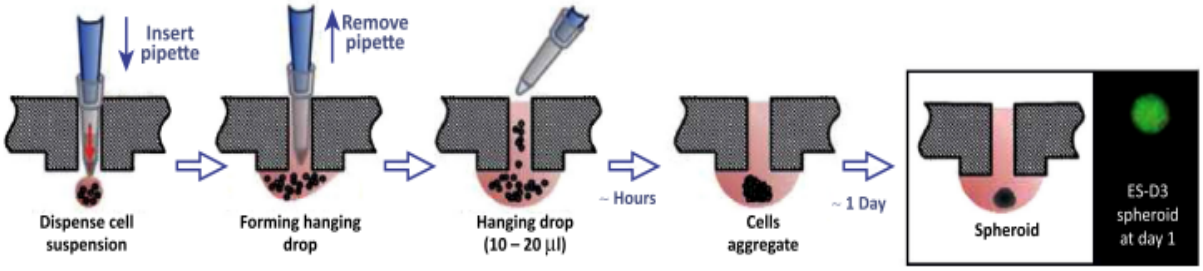

Figure 2.38. Spheroids formation by hanging droplet. Reproduced with permission.[43]

In 2011 there was a major breakthrough when a robot-assisted hanging-drop culture was created; this helped with the production of a maximum of 384 spheroids in a single batch (Tung et al., 2011). This improves the classical hanging drop method, which builds on imposed gravity for the production of spheroids. For the spheroid to be constructed, it is gravity that makes cells to concentrate at the base of the drop (Achilli et al., 2012; Kelm et al., 2003). In 2011, with patterned superhydrophobic biomimetic outer layers, it was confirmed that high-throughput hanging-drop cultures can be created at a lesser cost (Neto et al., 2015). This way there is an ordered nutrient delivery, interspheroid metabolic interaction, and this gives a result of particularized quality evaluations (Frey, Misun, Fluri, Hengstler, & Hierlemann, 2014). To scale up and reach thousands of spheroids per well, there is the arrangement of spheroids on non-adhesive hydrogels (Z. Zhao et al., 2014). This method facilitates the formation of more

[43] Reprinted from Trends in Biotechnology, Vol 35 /Issue 2, Matthias W. Laschke, Michael D. Menger, Life is 3D: Boosting spheroid function for tissue engineering, Pages No. 133-144, Copyright (2017), with permission from Elsevier.

complex cell aggregates, like honeycombs, tori and rods (Dean, Napolitano, Youssef, & Morgan, 2007). As of late, there is a new platform for extensive manufacturing of clinical-grade human cardiomyocyte spheroids; these are made from pluripotent stem cells. This new technique might help in the regeneration or replacement of damaged heart tissue (Fonoudi et al., 2015; Laschke & Menger, 2017).

2.4.5.5 Bioreactor

For this method, first, cells in a liquid medium are grown in spinner flasks. These are basically stirred tank bioreactors, where impeller mixing preserves the suspended cells. The liquid movement might help in mass transport of nutrients going to the spheroids, and waste coming from them. The cells do not touch any substrates (J. B. Kim, 2005). Other than working this method with spinner flasks, there is also a NASA bioreactor called HARV (high aspect ratio vessel), see *Figure 2.39*.

First, the culture system was created in order to simulate microgravity; moreover, this kept cells in suspension beneath low-shear stress all through culture. The generation of spheroids happened hardly any hours after culture started, spheroids became larger through cell division and fusion, until they reached 0.5 mm. There were complex and epithelial-like constructions produced with cellular interaction (Ingram et al., 1997).

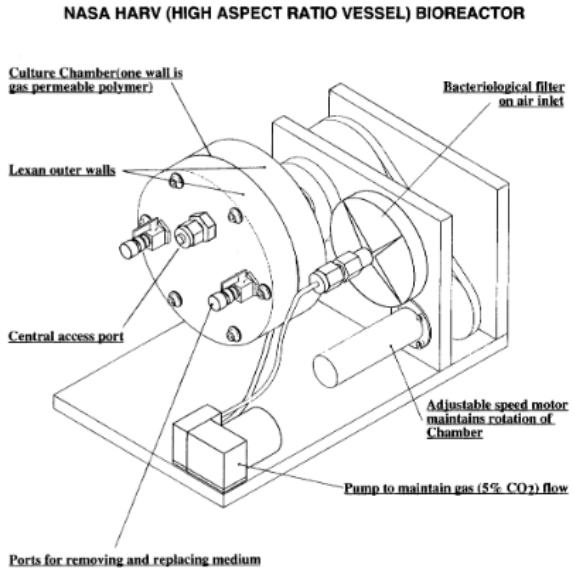

Figure 2.39. The NASA HARV (high aspect ratio vessel) bioreactor used in culturing a variety of cell lines. Reproduced with permission.[44]

[44] Reprinted by permission from [Springer Nature]: [Springer Nature] [*In Vitro* Cellular and Developmental Biology] [(Three dimensional growth patterns of various human tumor cell lines in simulated microgravity of a nasa bioreactor, M. Ingram, G. B. Techy et al.), [COPYRIGHT] (1997).

Among the benefits, it is a simple culture method, which can be mass produced. It also has good mixing for nutrient delivery and waste removal. However, there are variations in the size and shape, as well as shear damage in the spinner flask technique (Cui et al., 2017).

2.4.5.6 Force Driven

The methods that are considered to be force driven are classified into: magnetic force, electric force and acoustic force. In a study (Ino, Ito, & Honda, 2007) to create a multicellular spheroids in a simple way with magnetite nanoparticles and magnetic force, magnetite cationic liposomes were utilized to magnetically tag the marked cells. After that, steel plates that were arranged in a magnet were put below a cell culture surface, and the magnetically tagged cells lined on the edge depending where the steel plates were. Intricate cell patterns were generated (Ino et al., 2007).

Electric manipulation techniques have shown some benefits against others, like having a better resolution than ultrasound methods, and it is easier to handle numerous cells (Markx & Buckle, 2008). Electric techniques divide in two: direct current and alternating current methods, and both have been used for forming masses with living cells (Alp et al., 2003; Ozkan et al., 2003; Pohl, 1972). Electrophoresis, a direct current, is “motion produced by the action of an electric field (whether uniform or nonuniform) upon a charged object” (Pohl, 1972, p. 437), and dielectrophoresis, the alternative current, is very similar to electrophoresis, except the electric field is nonuniform and the movement is caused by the action upon a neutral object (Pohl, 1972). Sebastian, Buckle & Markx (2006) used DEP force to form multicellular aggregates of mammalian cells, and they demonstrated that by applying a consistent limited stream of new sorbitol iso-osmotic buffer to eliminate ions spilling from the cells, they could keep a large positive DEP force during the whole generation of the aggregates. It was confirmed that DEP force can be used to generate aggregates with 3 dimensional structures.

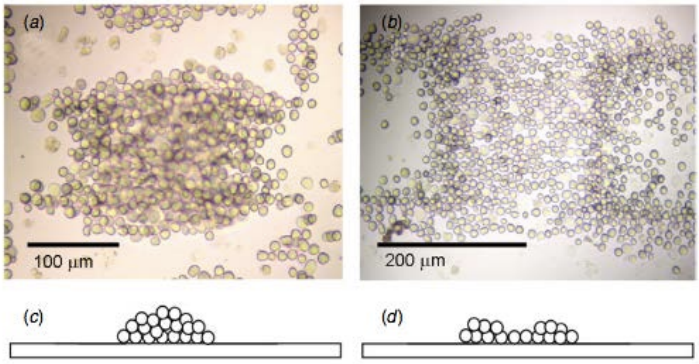

Figure 2.40. Aggregation patterns between interdigitated oppositely castellated electrodes at different electric field strengths: (a) aggregation of Jurkat cells at 100µm electrode regions at 20 Vpk–pk;(b) aggregation of Jurkat cells in 200µm electrode regions at 8 Vpk–pk; (c) schematic representation of the cells distribution at high field strength; (d)idem at low field strengths (Sebastian et al., 2006).
Reproduced with permission.[45]

Acoustic force has been seen with microcentrifugation (Alhasan et al., 2016) but also with acoustic tweezers. Chen et al. (2016) indicated the effectiveness of building multicellular spheroids in the 3 dimensional acoustic tweezers stage. They utilized drag force from microstreaming and, thus, levitated cells vertically. Also, they utilized radiation from Gor'kov potential for cells to structure horizontally. It was also proved it is an effective and high-throughput technique as it continuously generated more than 150 spheroids, that could have their size controlled; they were relocated to Petri dishes at a 30 minutes mark. The spheroids that resulted from this technique could be utilized for drug testing, as they had a particular drug resistance.

2.4.5.7 Multicellular Spheroid Chip

A fairly recent method includes a multicellular spheroid chip that is able to structure and remove 3D spheroids while utilizing removable cell trapping blockades. This technique forms smaller spheroids that present better uniformity. The research also included the fabrication of a spheroid chip where the trapping barriers are swollen for spheroid formation, and they diminish in size for a secure extraction of the new spheroids. This method is efficient

[45] Reprinted from Journal of Micromechanics and Microengineering, Vol 16 /Number 9, Anil Sebastian, Anne-Marie Buckle, Gerard H Markx, Formation of multilayer aggregates of mammalian cells by dielectrophoresis, Pages No. 1769-1777, Copyright (2006), with permission from IOP.

to obtain homogeneous, small 3D spheroids, which can help in gene expression analysis (H. J. Jin, Cho, Gu, Kim, & Oh, 2011).

Even if the production of spheroids has leaped, the application of tissue or organs in clinical operations seems to be far from us. Organs display intricate hierarchical formations and vasculature (Guven et al., 2015). Thus, it is not only a matter of spheroid production, but also of new methods to see the blending of distinct kinds of spheroids resulting in the organs or tissues needed (Laschke & Menger, 2017).

2.4.6 The Mechanical Properties of Individual Cell Spheroids

The mechanical properties present in tissues arise more complex, deriving from the single elements that build the system, and the interaction that these elements have through the various length scales (Brasch, Harrison, Honig, & Shapiro, 2012). Single cells' properties in isolation are ruled by the biophysical traits of the cytoskeleton and cell membrane. On the contrary, the physical traits of tissue derive from complex unions of cell adhesion molecules with themselves, the extracellular matrix and the cytoskeleton (Blumlein, Williams, & McManus, 2017; Schiele et al., 2015).

For the cause of tissue surface tension, two theories have been introduced: the differential adhesion hypothesis (R. A. Foty & Steinberg, 2005; Steinberg, 1963) and the differential interfacial tension hypothesis. (Brodland, 2003; Graner, 1993; Manning, Foty, Steinberg, & Schoetz, 2010). The differential adhesion hypothesis acknowledges the connection there is with adhesive energy and surface tension. Meanwhile, the differential interfacial tension hypothesis contemplates as well an input from cortical tension; it would be the percentage of adhesion tension to cortical tension, which regulates the total surface tension (Blumlein et al., 2017). Each individual cell has cortical tensions that have an scope of 10^{-3}–10^{-5} mN m^{-1} (Cartagena-Rivera, Logue, Waterman, & Chadwick, 2016; E. Evans & Yeung, 1989). Meanwhile, tissue interfacial tension has been established between 1.6 to 20 mN m^{-1}

(Ramsey A Foty, Pfleger, Forgacs, & Steinberg, 1996; Guevorkian, Colbert, Durth, Dufour, & Brochard-Wyart, 2010; Manning et al., 2010; Mgharbel, Delanoe-Ayari, & Rieu, 2009).

2.4.7 Experimental Techniques Used to Quantify Mechanical Properties of Model Tissues.

To determine the aforementioned mechanical properties of cells, there have been several methods to measure them. Tissue surface tension is an important criterion to define lasting equilibrium conditions. Moreover, rheological parameters are necessary in order to identify the dynamic development of a tissue going through the action of forces (Gonzalez-Rodriguez, Guevorkian, Douezan, & Brochard-Wyart, 2012). Previous research has illustrated that soft tissues operate like elastic solids in seconds or minutes, since their momentary disfigurement is proportional to the enforced weight, in addition to the tissue rapidly recovering its original form when the weight is released. When there is lengthier time periods, tissues experience cellular rearrangement, and this prompts other continued deformations, which are called viscoelastic behaviour (Forgacs, Foty, Shafrir, & Steinberg, 1998; Guevorkian et al., 2010; H. Phillips & Steinberg, 1978).

There are two patterns to determine tissue rheology that have emerged as a result of the experiments that have been made. The first model theorizes that tissues act like a viscoelastic fluid that has a surface stress; this way a standard tissue is defined by its Young's modulus of elasticity, surface tension, and dynamic viscosity to seize that in a lengthy period of time, tissues slide like viscous fluids (Forgacs et al., 1998; Gonzalez-Rodriguez et al., 2012; Guevorkian et al., 2010; H. Phillips & Steinberg, 1978). The second model depicts a tissue as an elasto-visco-plastic solid, defined by a dynamic viscosity, a Young's modulus, and a yield stress (Ambrosi & Preziosi, 2009; Gonzalez-Rodriguez et al., 2012). "The yield stress is a threshold of stress below which the tissue can elastically recover its initial shape after the load is released" (Gonzalez-Rodriguez et al., 2012, p. 912). Furthermore, in accordance with this, if

the used stress is bigger than the yield stress, then the tissue will obtain lasting plastic disfigurations, even when the stress is released (Gonzalez-Rodriguez et al., 2012). Now, we will discuss the methods that have helped understand the mechanical properties of the spheroids.

2.4.7.1 Micropipette Aspiration

A cell suspended in a saline blend is partly aspirated inside the entrance of the pipette. The spherical form of the cells can happen naturally, for example in white blood cells, or instinctively if cells are isolated from the edges. A hemispherical estimation is structured in the pipette (Hochmuth, 2000). If the suction were to continue, it would generate a liquid-like cell that would slide into the pipette due to a constant cortical tension (E. Evans & Yeung, 1989). The outer layer of a solid cell would move inside the pipette to reach a new equilibrium (Hochmuth, 2000; Theret, Levesque, Sato, Nerem, & Wheeler, 1988). In *Figure 2.41* we can observe a more complex setup with two micropipettes in a single cell. This method will be described in detail in later chapters.

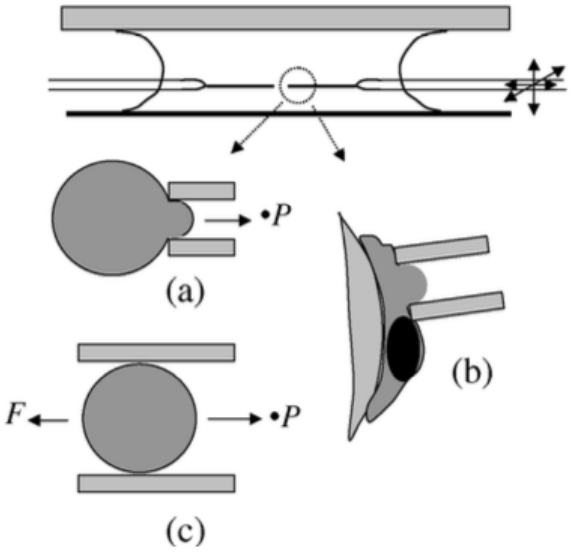

Figure 2.41. Two micropipettes in a chamber. A pneumatic micromanipulator controls the movement of a micropipette along three orthogonal axes. (a) A spherical cell being aspirated into a micropipette with a suction pressure ΔP. (b) An attached cell being aspirated into a pipette. (c) A closely fitting cell or bead moving freely in a pipette like a piston in a cylinder. When static, the suction pressure times the cross-sectional area of the pipette equals the attachment force F (Hochmuth, 2000, p. 17). Reproduced with permission.[46]

[46] Reprinted from Journal of Biomechanics, Vol 33/Issue 1, Robert M Hochmuth, Micropipette aspiration of living cells, Pages No. 15-22, Copyright (200), with permission from Elsevier.

2.4.7.2 Atomic Force Microscopy

The atomic force microscope uses force fields in the middle of the probe and the sample to help the probe navigate above the surface (Radmacher, Tillamnn, Fritz, & Gaub, 1992). It is actually established on the discovery of repulsive and/or attractive surface forces. There is interplay amidst the surface, and a probe that is near correlates to the force of the atoms in the sample and the atoms in the tip that scan the surface. To create image contrast, there should be control of the forces of interplay in the tip and the surface. The tip is generated at the bottom of a flexible cantilever, which is accountable for the signal transduction. When there is interplay with the sample and the tip, there is bending or curling of the cantilever, depending of the interaction force. These physical changes are caught by a small laser, whose reflection is centered on a photodiode detector. A shift of the cantilever, if there is communication with characteristics on the sample surface, is controlled while scanning and adapted to a 3D image of the surface (Kuznetsova, Starodubtseva, Yegorenkov, Chizhik, & Zhdanov, 2007; Mozafari, Reed, Rostron, & Hasirci, 2005).

Atomic force microscopy is capable to unveil the differences of mechanical properties of the surface at nano level and, also, the subsurface layers of cells (Kuznetsova et al., 2007).

2.4.7.3 Aggregate Centrifugation

When Phillips and Steinberg (1969) experimented with centrifugal fields, they used chick cells. First, a cell suspension was set in fresh culture medium; it was then split in two 15-ml roller tubes and incubated at 37°C for a period of 1-2 hours. The cells were rotating to structure thick sheets at the base of the tubes, and again incubated at 37°C for an extent of 1-2 hours; this would allow the building of intercellular adhesions. While one tube was clutched at 12°C, the sheet of cells in the other tube was detached and sliced into fragments of 0.08 × 0.4 × 0.4 mm, which were then rotated at 140 rpm on a gyratory shaker, at 37°C. The tube that was kept at 12°C was, the next day, incubated at 37°C for 1-2 hours and cut similarly to the other

tube. The spherical aggregates, along with the new slices were centrifugated at 37°C for 24-48 hours. The centrifugal accelerations ranged cf 2000 – 12000 *g*. When this was about to finish, a blend of formalin and ethanol was injected into the spinning centrifuge tubes in a volume equivalent to one third of the amount of the culture medium in the individual tubes. After 30 minutes, the centrifugation was finished (H. M. Phillips & Steinberg, 1969).

This showed that after 24-48 hours of centrifugation, aggregates that had been originally spherical and flat achieved akin final shapes, meaning that they maintain shape equilibrium (H. M. Phillips & Steinberg, 1969).

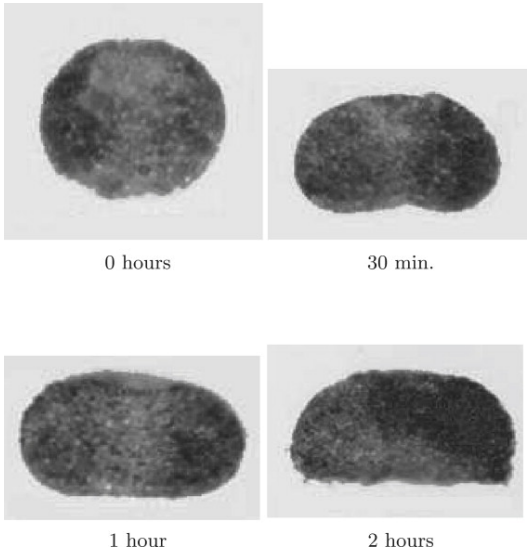

Figure 2.42. Ectodermal cell aggregates after different durations of centrifugation at 100 ×g. Reproduced with permission.[47]

When Kalantarian et al. (2009) experimented centrifugation with *Xenopus laevis*, equilibrium was attained faster than in the first study, as *X. laevis* aggregates have a lower viscosity. *Figure 2.42* shows the original and final shape of the aggregates.

[47] Reprinted from Biophysical Journal, Vol. 96 /Issue 4, Ali Kalantarian, Hiromasa Ninomiya, Sameh M. I. Saad, et al., Axisymmetric drop shape analysis for estimating the surface tension of cell aggregates by centrifugation , Pages No. 1606-1616, Copyright (2009), with permission from Elsevier.

2.4.7.4 *Parallel-plate Compression*

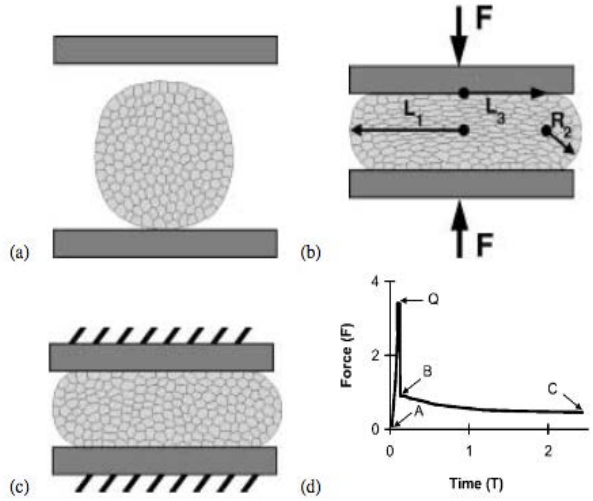

Figure 2.43. A parallel plate compression test of a cell aggregate. (a) The initial configuration, with cells in an annealed state.(b) Immediately following a rapid compression, the cell mass and individual cells are flattened normal to the compression plates. (c) With time, the cells re-anneal, but the profile of the cell mass changes little. (d) The corresponding force versus time curve. The letter Q denotes the end of the compression process while the letters A through C indicate points on the curve corresponding to the configurations shown in the other parts of this figure Reproduced with permission.[48]

This is one of the best techniques to assess the surface tension of a cell aggregate. When the compression test starts, the cells are thought to be in an annealed phase and forming a compact homotypic mass. When compression happens, it is fast and the cells flatten individually, along with the mass (*Figure 2.43*). Large forces will be created as abundant force is needed to quickly distort the cytoplasm of the cells. Subsequent to compression, the spacing between the plate continues to be the same in expectation of the anneal of the cells (Brodland, 2003).

2.4.8 Applications to Physiology and Bioengineering

Analogies with soft matter have given new information on tissue mechanics, and this has been enforced for the understanding certain aspects in physiology. This way, it was determined there was an opposite correlation with the surface tension of a tumor and its intrusive capacity. The *in vitro* surface stress of malignant astrocytoma cell lines was demonstrated with the parallel-plate compression method and how intrusive they were in a cell by employing a Matrigel trans filter invasion assay. They reached the conclusion that to establish tumor intrusiveness the important parameter is the surface tension and not only

[48] Reprinted from Biorheology, Vol. 40, G Wayne Broadland, New information from cell aggregate compression tests and its implications for theories of cell sorting, 273-277, with permission from IOS Press. The publication is available at IOS Press through https://content.iospress.com/articles/biorheology/bir189

cadherin expression (Gonzalez-Rodriguez et al., 2012; Winters, Shepard, & Foty, 2005). It was later determined that the invasiveness of a tumor relies on an equilibrium among cell-cell interactions and cell-matrix interactions (Hegedus, Marga, Jakab, Sharpe-Timms, & Forgacs, 2006). It was also demonstrated that the forming of a fibronectin cellular matrix delays or even restrains the spreading of an aggregate made of brain tumor cells (Gonzalez-Rodriguez et al., 2012; Sabari et al., 2011).

Moreover, tissue wetting analogies have wide ramifications in embryonic expansion. Krens and Heisenberg (2011) showed how cell sorting is part of mouse blastocyst formation, among others. Sorting patterns of embryonic tissues seen *in vivo* can be duplicated *in vitro* with cell aggregates, as done with the arrangement of brain cortical layers in mice; however, the applicability of the behaviours of *in vitro* cell sorting to analyze embryonic tissue coating has not been settled (Gonzalez-Rodriguez et al., 2012; Ogawa et al., 1995). There is also aggregate fusion that has been seen in initial chick heart growth, where septa and valves are generated by fusion of cardiac cushions (Jakab et al., 2008). A phenomenon found everywhere is viscous tissue spreading; it specifically occurs when tissue layers reorganize their relative positions, as it happens in the embryonic epiboly (Luu, David, Ninomiya, & Winklbauer, 2011). The competence of analogies to liquid systems can be seen in the retinal epithelium of Drosophila, where cone cells organize between each other, continuing the energy-minimization precepts also found in soap bubbles in two-dimension liquid film. Furthermore, global energy minimization also explains the development of the model of cells that structure the wing disc epithelial covering in Drosophila (Farhadifar, Roper, Aigouy, Eaton, & Julicher, 2007; Gonzalez-Rodriguez et al., 2012). Finally, new 3D cell culture methods bring different *in vitro* structures to research tissue mechanics. As systems improve to replicate *in vivo* conditions, , we will be able to better understand physiological behaviour (Gonzalez-Rodriguez et al., 2012).

Chapter 3: Methods and Materials

3.1 Materials and Reagents

3.1.1 Hydrophobic Substrate Preparation

To make the surface hydrophobic, silane coated silicon substrate was employed. To better the condition of the external area, the silicon substrate was provided with a cover of an initial oxide layer. After this, silicon was dissected in small portions and doused in hot piranha solution 7:3 (v/v) H2SO4 (95%), and H2O2 (30%) during 30 min. This way, if there were water molecules in the model, they would have been eliminated, and it would reveal the -OH groups. The resulting sample was flushed with Mili-Q water and distilled ethanol, to then be dried using nitrogen gas. Finally, to create the octadecyltrichlorosilane-coated silicon substrates, the sample was immersed in an OTS solution that was produced using 0.25 mL of android OTS (90% purity, Aldrich), dispersed in 50 mL of bicyclohexyl (≥99% purity, Sigma-Aldrich). The substrate was under the liquid for 24 h. It was then flushed with anhydrous chloroform (99% pure, Sigma-Aldrich). The resulting OTS substrates underwent sonication for 15 min using chloroform, ethanol and toluene. Previous to its use, they were rinsed with ethanol 98% and dried with nitrogen gas. To store the substrates, petri dishes were used.

3.2 Droplet Dissolution

3.2.1 Reagents

The solvents utilized were toluene (99.9 vol %, Sigma-Aldrich) and ethanol (98 vol %, Sigma-Aldrich, without changes from the received formula. The water used was processed from a Milli-Q unit (18.2 MΩ·cm, Millipore, Merck Australia).

3.2.2 Experimental Set-up

A glass vial was was washed with a sodium hydroxide solution, and rinsed using water and ethanol; the drying was done in an oven at 60 °C (Jativa, Schutz, Bergstrom, Zhang, & Wicklein, 2015). The mix of ethanol and toluene was set in the glass vial. The substrate of

OTS−Si was put at the base of the container. A small drop of silk or cellulose was then put on top of the substrate. After this, the upper part of the vial was closed with a film to evade solvent evaporation. A contact angle measurement system (OCA20, DataPhysics Instruments GmbH, Germany) was utilized to control and record view sized images of the droplet with time. The resulting video was examined utilizing shape recognition software (SCA202, DataPhysics Instruments) to acquire volume, the radius, and contact angle (Jativa & Zhang, 2017). For cellulose, real-time polarized video microscopy of the crystal structuring in the diminishing droplets was made with a Nikon Eclipse FN1 light microscope (Japan). The droplet was put in a specially made aluminium holder with a lid that had a glass window for the imaging. The container was placed between cross-polarizers and the videos were recorded using an inline camera with 2 megapixel CCD sensor (Kappa Zelos-02150CGV, Kappa Optronics GmbH, Germany). The frame rate was adjusted depending the shrinkage rate of the droplets. When the droplet dissolution was finished, the solution was taken out with care and the spheres were removed to characterize them after they dried (Jativa et al., 2015).

3.3 Silk

3.3.1 Silk Fibroin

The silk used was shipped from Advanced BioMatrix (San Francisco USA) and it was a partly hydrolyzed silk fibroin II protein at the concentration of 5% (w/v) in a liquid solution. For the solution, domesticated *Bombyx mori* from China were harvested, and treated into the solution we have with the use of heavy inorganic salts. After, it was desalted, tested, and stored. Its shipment was made on dry ice. One important characteristics of this silk fibroin solution is the maintenance of the fibroin light chain at around 25 kDa. Even though it is not treated to be sterile, it has low bioburden (Jativa & Zhang, 2017).

3.3.2 Silk Dissolution Rate

The droplet started the dissolution process after reaching a crest in volume. This also gave into the second phase. The dissolute rate is faster with expansion in the amount of ethanol in the solution. The dissolution rate grew by ~8 times, when the amount of ethanol expanded from 0.5 to 5%; this advocates that the dissolution rate of the droplet can be tuned according to the concentration of ethanol in the bulk phase. There was also a thin layer that continuously spread from the bottom of the droplet, and the droplet became black. However, by the end of the shrinkage, the droplet turned transparent. The volume of the droplet expanded quickly attained 1.7 times the first volume. The increase advocates fast consumption of a considerable volume of liquid from the surrounding phase. A thin shell of the protein structured at the droplet surface, and then wrinkled when the volume diminished. When the dissolution finished, the bulk liquids were detached and the spheres dried naturally (Jativa & Zhang, 2017).

3.3.3 Microstructural Characterization of Silk Microspheres

To establish the microstructure of the silk spheres, a field-emission scanning electron microscope (FESEM) was used. For this, dry silk sphere samplings were attached to 12 mm aluminium stubs with doublesided carbon taps. After this, the samples were covered with gold by means of a Xenosput sputter coater (Dynavac, Wantirna South, Australia). The imaging was done with a Philips XL30 field-emission scanning electron microscope (Philips, Eindhoven, Netherlands) at a voltage of 2.0− 15 kV. In order to dissect one sphere, it was set in the SEM stub adhesive surface, and then pressured against a blade. It was discovered that the dissecting of the spheres did not influence the morpholofy of the sectional surface, as several spheres were cut and they displayed similar characteristics in their structure, indicating that the nanostructures were not harmed. There were, however, some fissures on the sphere that were produced by the dissecting. For the absorbance and transmittance spectra of the silk, a microspectrophotometer (CRAIC Technologies, USA) armed with a 15× objective and a xenon

lamp was used. The spectra were seen in the range of 400 and 700 nm, at 50 scans per measurement. The data were analyzed with proprietary spectral software. The surface pore (porosity) area fraction was determined from SEM images by using image analysis software (ImageJ). Images from different areas of the sphere were analyzed to determine the averaged surface porosity area fraction on the silk sphere (Jativa & Zhang, 2017).

3.4 Cellulose

3.4.1 Cellulose Nanocrystals

Cellulose nanocrystals (CNC) were processed from softwood pulp by continuous delivery of hydrochloric acid hydrolysis of Tempo (2,2,6,6-tetramethylpiperidine-1-oxyl)-mediated oxidized cellulose nanofibres (CNF) featuring surface –COOH associations. For this, hydrochloric acid was combined dropwise to 1 g of CNF to arrive to the end concentration of 2.5 M, and this blend was put into heat of 130°C during 6 h. The effect was diluted with de-ionized water. The suspension was then washed, the precipitation was gathered and dialyzed with de-ionized water. After this, the suspension underwent sonication during 10 m with Sonics Vibracell (USA), and centrifugation to acquire isolated nanocrystals. Finally, the concentration of the CNC diffusion was 0.75 vol% and a surface charge of 0.31 mmol g−1 was unveiled by polyelectrolyte titration. The crystals have a length distribution of 264 ± 118 nm and a thickness distribution of 2.9 ± 1.3 nm as ascertained with findings of AFM images. The crystals are comprised of solidly packed β(1–4) linked d-glucose chains adhered collectively by broad hydrogen bonding and van der Waals forces; these forces adequately obstruct water filtration and the ensuing physical growth (Jativa et al., 2015).

3.4.2 Cellulose Dissolution Rate

For the dissolution of liquid droplets comprised of 0.3 or 0.75 vol% CNC, 20 ml of various compositions that consist of toluene and ethanol with containing 0.5, 1, 5, 10, and 15 vol% of ethanol were utilized. Droplets measuring 1–10 μl were put on the

octadecyltrichlorosilane substrates; these were already submerged in the solution. For the process, the glass vial was washed with a sodium hydroxide solution (10 g ml−1) for 30 min, flushed with Milli-Q® water and ethanol, and dried in the oven at 60 °C. To evaluate the dissolution dynamics, the droplet was monitored. Furthermore, to record side-view photos of the shrinking droplet at various time, and in a closed glass container, a contact measurement (OCA20, Dataphysics Instruments GmbH, Germany) system was used. For the analysis of each image, an automated shape recognition software was utilized SCA202, DataPhysics Instruments); this system analyzed the shape of the droplet and computed the volume, and the radius of a sphere (Jativa et al., 2015).

3.4.3 Cellulose Tactoids Imaging

The liquid droplet that had CNC was put in a custom-built container made out of aluminium with a lid that has a glass window that permits reflection polarized microscopy imaging. This holder was set in the middle of cross-polarizers and an inline camera with 2 megapixel CCD sensor (Kappa Zelos-02150C GV, Kappa Optronics GmbH, Germany) was used to record videos. The frame rate was adapted depending the shrinkage proportion the droplets presented (Jativa et al., 2015).

3.4.4 Microstructural Characterization of Cellulose Microspheres.

For cellulose spheres TEM, they were incubated in 100% LR white resin during 24 h at room temperature. After this, there was another incubation again in 100% resin during 6 h, where the spheres got fixed in the fresh resin in gelatine capsules and thus, quietly fell into the bottom. The capsules were sealed to avoid air, and the resin polymerized in an oven at 60°C during 24 h.

The engrained spheres in blocks were cut using a diamond knife on a Leica Ultracut S microtome and we gathered ultra-thin sections (90 nm) onto formvar-coated 100 mesh hexagonal copper grids. The sections that were on grids were consecutively stained using

saturated uranyl acetate for 10 min and Triple Lead Stain for 5 min (Sato, T., 1968, J. Electron Microscopy, 17: 158.), and to observe it, a FEI Tecnai Spirit transmission electron microscope at 120 kV was used. The images were obtained with a Gatan Eagle digital camera at a resolution of 2K x 2K pixels.

For SEM, cellulose was spheres were set on top of 12 mm aluminium stubs with double-sided carbon tabs. Then, they were coated with gold utilizing a Xenosput sputter coater (Dynavac, Wantirna South, Australia). For the images, a Philips XL30 field-emission scanning electron microscope (Philips, Eindhoven, Netherlands) was used at a voltage of 2.0 kV and spot size of 2 (Jativa et al., 2015).

3.5 Cellular Self-assembling

3.5.1 Cell Culture

The human pulmonary fibroblast cell cultures were established following Schuliga et al. as follow: “parenchymal fibroblast (PFb) and cultures were established from macroscopically normal biopsies of lung resections derived from patients undergoing either lung lobectomy or transplant. Each resection specimen generated a primary culture, and a minimum of three such cultures was used for each experimental design. Pleura-free parenchyma was chopped into 1–2 mm3 pieces that were allowed to adhere to uncoated plastic culture plates to generate explant cultures. Cells were grown to confluence over 1–2 weeks, and then passaged weekly at a 1:4 split ratio”(M. J. Schuliga et al., 2009).

Human airways smooth muscle cultures were established as follow: “Smooth muscle bundles of muscle bronchi were dissected from the surrounding connective tissue. The smooth muscle strips were then immersed in medium and partially digested in the presence of collagenase (3 mg·mL^{-1}, 30 min). The strips were then chopped using a scalpel (~2 mm^3), and digested in medium containing elastase (0.5 mg·mL^{-1}, 2 h), then collagenase (1 mg·mL^{-1}, 12 h). Examination of the tissue upon completion of the digestion revealed a high proportion of

single cells. The resulting cell suspension was pelleted and washed twice with PBS before being resuspended in DMEM supplemented with 10% v v^{-1} heat-inactivated fetal calf serum (FCS), L-glutamine (2 mM), sodium pyruvate (1 mM), non-essential amino acids (1% v v^{-1}, Sigma, St Louis, MO, USA), penicillin-G (100 U·mL^{-1}), streptomycin (100 μg·mL^{-1}) and amphotericin B (2 μg·mL^{-1}). The cells were then seeded into a 25 cm^2 tissue culture flask and grown until a confluent monolayer was formed" (M. Schuliga et al., 2013; A. G. Stewart et al., 2013). To determine the identity of the cultures, we used a monoclonal antibody against alpha-smooth muscle actin using immunofluorescence. The cultures show uniform staining for smooth muscle specific α-actin, a mesenchymal cell marker but not CD31, an endothelial marker (Skalli et al., 1986).

The tissues used were from IPF patients and non-IPF donors. The cells used in all the tests were human airways smooth muscle and fibroblast cells between passages 3-10. Cells were passaged in Dulbercco's Modified Eagle's Media (DMEM); they consisted of 10% (v/v) heat-inactivated fetal calf serum (FCS), 15mM HEPES, 0.2% (v/v) sodium bicarbonate, 2 mM L-glutamine, 1% (v/v) non-essential amino acids, 1% (v/v) sodium pyruvate, 2.5 μg/mL amphotericin, 5 IU/mL penicillin and 50μg/mL streptomycin.

Confluent culture flasks were serum deprived for 24h prior to the generation of 3D spheroids. The cells were displaced with trypsin followed by resuspension in incomplete DMEM at a cell density of 250 x 10^3 cells mL^{-1}. Two hundred μL of this cell suspension was added into 96 well round bottom plates coated with 0.5% poly(2-hydroxyethyl methacrylate) (poly-HEMA) (Santa Cruz, sc-253284), to decrease cellular adhesion to plastic, and by incubating cells to permit aggregation into cellular spheroids for 48 h. Cells were also seeded at 125 x 10^3 and 62.5 x 10^3 cells mL^{-1} to study the effect of initial cell numbers in the final size of spheroids.

Where indicated, cells were treated first with 100 pM TGF-β1 (R&D Systems, Minneapolis, MN). Also PF670462 (3μM) (Abcam, Australia) prior to 100 pM TGF-β1 (R&D Systems, Minneapolis, MN).

3.5.2 Cell count

Cells were incubated in 2D plates and 3D spheroids with FCS (5 % v/v). After 48 hours, cells were washed with PBS and mixed for 10 min in a solution with trypsin (0.125% w/v) /EDTA (0.02% w/v) in PBS containing 0.1% collagenase. For spheroids, we additionally used 21 gauge needles to ensure cell separation. Cells were then re-suspended in 2%FCS in PBS containing 0.2% Trypan blue (Sigma, USA). An haemocytometer was used for cell count, and live and death cell were noted.

3.5.3 Real Time Quantitative Polymerase Chain Reaction (RT-qPCR)

Total RNA was removed from cultured cells using RNAspin Mini RNA Isolation Kit (GE Healthcare). RNA extracts were reverse transcribed into cDNA using High-Capacity RNA-to-cDNA Kit (Applied Biosystems). Real-time PCR was then performed using a QuantStudio 6 Flex Real-Time PCR System using iTaq Universal SYBR green supermix and the following thermal protocol: 50°C (2 min), 95°C (10 min), then 40 cycles of 95°C (15 sec), 60°C (1 min). The threshold cycle (CT) values obtained for target genes were normalized against those obtained for 18S ribosomal RNA (18S rRNA), which was contained as internal control. The generation of specific PCR products was settled by dissociation curve assay. Primer sequences used are shown in Chapter 7.

3.5.4 Human Lung Fibroblast Donor Characteristics

Samples used came from 16 IPF patients and 14 non-IPF donors that experienced lung transplant or resection. The majority of the patients were male. The standard age of IPF and non-IPF donors was 60.6 years and 48.0 years. If smokers, the information is classified in *Table 3.1*. There is no other information of the donors.

Table 3.1 List of Donors Health Details

IPF				Non-IPF			
ID	Sex	Age	Smoking	ID	Sex	Age	Smoking
ALF001	M	62	Unknown	ALF009	unknown	39	Ex-smoker
ALF004	M	45	Unknown	ALF010	M	69	Ex-smoker
ALF008	M	65	Unknown	ALF012	F	60	Current
ALF016	M	69	Ex-smoker	ALF013	F	28	Ex-smoker
ALF018	M	63	Unknown	ALF017	unknown	unknown	Unknown
ALF019	F	56	Never	ALF020	M	41	Ex-smoker
ALF023	M	61	Never	ALF024	F	44	Unknown
ALF027	M	57	Ex-smoker	ALF025	unknown	unknown	Unknown
ALF028	F	59	Ex-smoker	ALF026	M	28	Unknown
ALF029	M	61	Ex-smoker	ALF030	unknown	35	Unknown
ALF035	F	61	Ex-smoker	ALF034	F	67	Unknown
ALF037	M	43	Ex-smoker	ALF044	F	61	Unknown
ALF039	M	67	Never	ALF049	Unknown	Unknown	Unknown
ALF040	F	71	Never	ALF050	M	42	Unknown
ALF041	F	66	Never				
ALF045	F	64	Never				

3.5.5 Preparation of Low Adherence Plates

A 0.5% Poly (2-hydroxyethyl methacrylate) (Poly-HEMA; Santa Cruz, sc-253284) solution was prepared by dissolving it in 95% ethanol in sterile Milli-Q water (Merck, Millipore, Kilsythe, VIC, Australia). The mixing of poly(HEMA) with solution was facilitated by the use of a shaker during 24 hours to ensure complete mixing. Ninety six-well round-bottomed plates were coated with 50 µL 0.5% poly(Hema) solution to inhibit cell adhesion to

plastic, and they were left in incubator for 3 days until the solution had concentrated to dryness. Prepared plates were stored at 4 degrees for a period of no longer than 3 weeks to ensure plate coating quality.

3.5.6 Immunohistochemistry

Paraffin-embedded IPF and non IPF lung tissue was obtained from Alfred Health from the Alfred Tissue Biobank for Interstitial Lung Disease (HREC#336/13, Alfred Hospital, Melbourne, Vic, Australia). Idiopathic pulmonary fibrosis was pathologically diagnosed by multidisciplinary review as previously described (M. Schuliga et al., 2017; M. J. Schuliga et al., 2009). Sections were counterstained with haematoxylin (Grale Scientific, Australia). Donor characteristics are provided in Table 3.1.

On serial sections, a Masson's Trichrome stain was also performed to provide indicative levels of fibrosis in IPF and non-IPF sections the reagents required include Bouin's fixative solution Scott's tap water, Mayer's Haematoxylin, Trajan Scientific; Celestine Blue, Biebrich Scarlet/Acid Fuchsin; Phosphotungstic acid, Sigma; Aniline blue solution (aust biostain)

Spheroids were fixed in 10% neutral buffered formalin (Grale Scientific) for 10 min and washed twice by PBS. After fixation, spheroids were embedded into a 3% agarose solution and processed overnight into paraffin. Sequential 3 µm sections were stained with Mayer's Haematoxylin and Eosin (Trajan Scientific, Australia). A Masson's Trichrome stain was also performed.

3.5.7 Immunofluorescence

For F- and G-actin staining, cells were rinsed twice with PBS. Then they were fixed in 10% (v/v) neutral buffered formalin (NBF) during 15 minutes and permeabilized with 0.2% (v/v) Triton X-100 during 5 minutes. After rinsing in PBS, cells were blocked with 0.1% Triton X-100 in 1% BSA/PBS solution for 15 minutes, and then stained with Oregon green 488 (green) phalloidin (1:50, Invitrogen Molecular Probes, #O7466) and Alex-Fluor 594 (red)

deoxyribonuclease I (DNase I)-texas red conjugate (10mg/ml, Invotrogen Molecular Probes, #D12372) during 20 minutes at environmental temperature. In these circumstances, phalloidin and DNase I bind F- and G-actin were used. We stained the nuclei with DAPI (1:100 in PBS) during 10 minutes. Spheroids were mounted in slides using DAKO fluorescent mounting media, while 2D cultures were kept in media. They were analyzed utilizing a Zeiss fluorescence microscope-live cell imaging system.

3.5.8 SEM and TEM Analysis

Samples were fixed in 2.5% glutaraldehyde in PBS for 1h, and then fixed in osmium tetraoxide 1% for 30min. These were then rinsed with PBS and serially transferred from 0% to 100% ethanol, in 20% increments and an incubation period of 10min each.

The surface of spheroids was imaged by scanning electron microscopy. Samples in 100% ethanol were critical point dried and then left for 24h for further evaporation of solvent. The microspheres were deposited on double-sided carbon tape and coated with gold. The SEM images were acquired using a Philips XL30 field-emission (FE)-SEM and a JEOL JSM-7401F FE microscope for high-resolution SEM images.

The internal structure of spheroids was characterized by transmission electron microscopy (TEM) of ultramicrotome-sectioned samples. CNC spheres in 100% were incubated twice in 100% LR-white resin and subsequently embedded in capped gelatine capsules. After a polymerization step at 60°C for 24h, the embedded spheres were sectioned with a diamond knife on a Leica Ultracut S microtome, and ultra-thin sections (90nm) were collected onto formvar-coated TEM grids. The sections were sequentially stained with saturated uranyl acetate for 10min and triple lead stained for 5min and viewed in an FEI Tecnai Spirit transmission electron microscope at 120 kV. Images were captured with a Gatan Eagle digital camera at a resolution of 2k pixels.

3.5.9 Live Cell Imaging of HASM and pFB Spheroids

Whole spheroid aggregates were imaged with the Olympus IX51 (Olympus America Inc., Center Valley, PA, USA) brightfield microscope at 4x objective to allow for comparison to size of spheroid. Images were collected using the ImagePro Plus Software (Media Cybernetics, Rockville, MD, USA). Areas of spheroids were quantified using ImageJ.

3.5.10 Cell Stiffness and Viscosity Measurements

To measure the Young's tensile modulus (E) of 3D spheroids, the micropipette aspiration technique was utilized, as seen before (Guevorkian et al., 2010; Michael Schuliga et al., 2013). The stiffness present in each fibroblast was determined from plastic culture vessels utilizing trypsin. A temperature control chamber (Warner Instrument CL-100) was used for the micropipette aspiration to keep the cells at 3737°C. To avoid cell adhesion, the tips of the custom-made glass micropipettes (8 µm diameter) were pre-coated using silicone Sigmacote (Sigma, UK). By regulating the water level of a water reservoir, suction pressure was applied to the cell/cell aggregate. The suction pressure was enforced applied in 1 cm H_2O (0.098kPa) increments and maintained stability for 60s at each increment. The highest suction pressure was 6cm H_2O (0.588kPa). At the finishing point of every pressure increment, the aspirated length in the micropipette was determined from a brightfield image recorded by a Leica DMI6000B microscope. The probable Young's modulus in the cell was determined by means of a model that accepts the cell is an homogeneous, isotropic, elastic and incompressible half-space medium (Theret et al., 1988). For the calculation, Young's Modulus E was found with Equation 3.1, where Dp is the inner diameter of the micropipette and L the aspiration length. ΔP represents the aspiration pressure and ϕ is the wall function with a typical value of 2.1, as described previously (Hochmuth, 2000).

$$\text{Equation 3.1: } E = \frac{3\ Dp\Delta P}{4\ \pi\ L\ \phi}$$

3.6 Image Data Analysis and Validation

While researching and doing the study of the mechanical properties of spheroids by means of micropipette aspiration, due to the viscoelastic experiments, there were images amounting to the hundreds. As we failed to manually examine these images, we realized it was a restricting factor in data analysis. Other stated image tracking software for single cells, have not been easy to accommodate for tracking experimental images in spheroids aspiration. This happens because spheroids are 3D structures, and single cells are “semi-flat structures” with negligible height. When the spheroid micropipette aspiration has started, the non-aspirated areas in the outer edge of the spheroid cover the tip of the micropipette, thus making the image examination with standard software complex. It became more difficult because of the opaque image created by 3D spheroid structure when compared to a translucent individual cell. Another restraint is that usually single most single cell aspiration image software are made better in order to disclose the complete cell and the micropipette. Because spheroids are bigger than individual cells, only a part of the complete spheroid volume can be seen in a common image. It will only focus on the micropipette and the aspirated part in the spheroid.

Taking into account these limitations, an analysis program was developed for a faster analysis of the mechanical properties of spheroids. The software interface was developed in Matlab (R2015b) and permitted the automated calculation of viscosity and stiffness as it analyzes images of micropipette aspiration experiments. To reach these values, a region of interest (ROI) is chosen to produce a template; after this, the software tracks the pipette location and recognizes the place where the pipette is. It also facilitates measurement of alterations in the aspiration length for all the images in an experiment.

3.6.1 Image Detection Optimization

For a faster processing of the images, some guidelines were included in the sofware to permit the user to diminish the image analysis of time, and better the software image

examination. Spheroid aspiration images have a greater magnification where the pipette uses most of the image area. The whole image could be used as a template, but this would increase the image analysis time since all the pixels in every image need to be examined. In order to resolve this, the user can choose a smaller ROI for the software to use like a template. The user can select a well-defined area that looks similar in all the aspiration images (i.e., the pipette edge), and then the software will match this place in every image. Furthermore, to guarantee the accuracy of image processing, the user should always select two ROIs as a template. This way the likelihood that a small contrast variance affects measurements will be diminished.

The user is also able to better the image tracking system if they alter the relative contrast and pixel dot recognition of the template. Fine-tuning the image contrast permits an improved identification of the micropipette and spheroids in the background. It is possible that the comparative intensities of images could differ from experiment to experiment, hence this adaptation is useful. Smoothness, the second parameter, permits the diminishing of roughness and alterations in contrast amidst adjacent pixels. These two parameters efficiently adjust the image to be used as a template for analysis.

3.6.2 Aspiration Length and Optimization

The last step is about determining the aspiration length of the spheroid inside the micropipette. The software for single cell aspiration depends on the recognition of the micropipette ROI. This, nevertheless, demands high processing power due to the size of each spheroid image. Also, the recognition of the micropipette first aspiration point can be hard since the spheroids at that point present an opaque structure. This way, another addition was included in the software in order to ascertain two main guidelines: micropipette entrance and aspiration point. The micropipette entrance can be found without difficulty by the user, and is determined by appointing both edges of the pipette. A vector is drawn which permits the user to validate if the vector is parallel to the micropipette entrance. The user will be inquired where

is the aspiration point, that is the highest point of the meniscus of the aspiration. Then, a new vector will be set with the distance from the micropipette entrance to the aspiration point as shown in *Figure 3.1*.

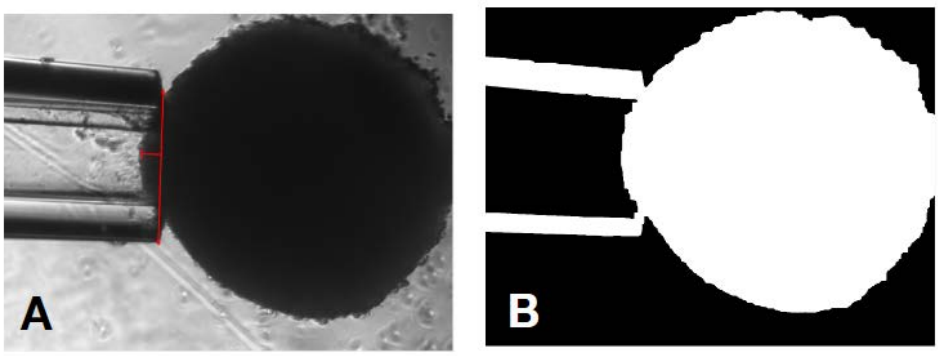

Figure 3.1. Image analysis during spheroid micropipette aspiration. (A) Original aspiration image, and red line show the aspiration length in relation to the micropipette tip. (B) Shows the ROI generated image recognition software.

The user can manually add the micropipette in diameter in every experiment. This is a constant value if the same pipette was utilized. Nevertheless, the software can also determine it. To diminish any margin of error in the aspirated and the user, the user will choose the wall and the other wall, and the software can then determine the average distance.

3.6.3 Results Validation

When the parameters have been set, the image analysis will be automatic. As it continues to process each image, the software will exhibit progressive binary images. This will permit the user to validate errors at each level. A value for viscosity will be given when all the images have been examined. Moreover, for step-by-step aspiration the software supplies a dot plot with a linear regression and the value of R2. This permits the user to ratify if the stiffness outcome fits the expected linear plot of an elastic material and visibly check if an image was not accurately identified giving an incorrect result. If the result does not fit the expected linear plot, the user can reformulate the parameters and reiterate the image analysis. If not all the images have been detected, the user can erase the images from the linear regression calculation and display a new Young's modulus value.

3.7 Statistical Analysis of Data

Statistical analysis was done with GraphPad Prism 7.0 (Graphpad, San Diego, CA) software. Data were examined as group data and seen in figures as interquartile ranges (box and whisker plots) or mean ± SE (dot plots and line graphs) from n donors. For one factor analysis one-way ANOVA or unpaired t test was used; and for two factor analysis two-way ANOVA were utilized with the Bonferroni's post-hoc test. P values less than or equal to 0.05 (after correction for multiple comparisons) were considered to be statistically significant.

Chapter 4: Transparent Silk Fibroin Microspheres from Controlled Droplet Dissolution in a Binary Solution

4.1 Foreword

This chapter describes the utilization of the droplet dissolution technique to generate and study customisable spheres constructed from silk fibroin that can span hundred micrometers in diameter. Silk has an array of distinct characteristics in many fields, ranging from the textile to the biomedical. One way to promote the construction of materials made out of silk is to be able to regulate the structure of silk fibroin, which is explored in this chapter. The results of this study indicate that the morphology of the constructed silk spheres could be tailored and that it is feasible to control the surface microstructures by manipulating the ratio of ethanol and toluene in the surrounding phase. The findings described in this chapter could have significant applications in the fields of optics and biomedicine. This paper was originally published according to the following citation:

Jativa, F., & Zhang, X. (2017). Transparent silk fibroin microspheres from controlled droplet dissolution in a binary solution. *Langmuir*, *33*(31), 7780-7787.

4.2 Abstract

Silk is a natural polymer with a broad range of potential applications in textiles, advanced materials, biomedical devices, and drug delivery. The ability to control the morphology and assembly of silk fibroin is essential for the fabrication of silk-based structured materials. Here, we report an effective and simple approach based on droplet dissolution for weaving silk fibroin into spheres of several hundred micrometers in diameter. The spheres possess regular wrinkled microstructures on the surface and switchable transparency for visible light. To produce these silk spheres, we immersed a sessile micro-drop of the silk fibroin aqueous solution in a surrounding phase of ethanol in toluene at low concentration (<10%). The droplet experienced a two-phase process: the first phase of volume expansion due to the

intake of organic solvents from the surrounding phase and the second phase of droplet dissolution. The dissolution rate is closely related to the dynamics of the droplet, while the resulting microstructure of the silk microsphere is simply adjusted by the composition of the surrounding solution. At high concentrations of ethanol, silk fibroin formed a thin shell around the droplet during the initial expansion of the droplet in volume. As the droplet shrank at a later stage, the shell around the droplet wrinkled and crumpled, leading to regular ridges and crevices on the microsphere surface. This work demonstrates that controlled droplet dissolution may be explored as a novel and effective way to tailor microstructures of silk assemblies. The as-prepared silk microspheres may be potentially used as optical units or microcarriers.

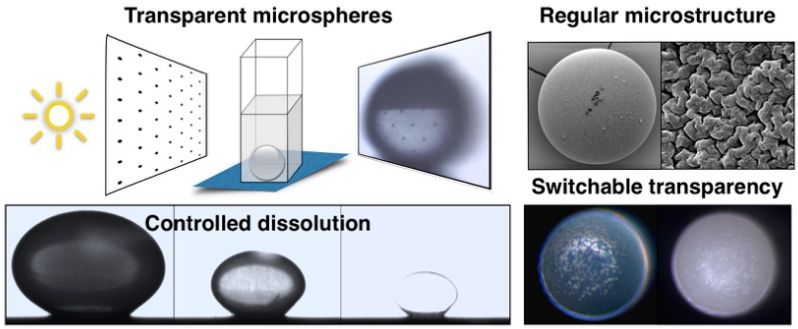

Figure 4.1. Visual abstract

4.1 Introduction

As a unique natural polymer, silk possesses biocompatibility and excellent mechanical and wetting properties, promising important applications in advanced materials, biomedical devices, and drug delivery (Koh et al., 2015; Qi et al., 2017; Volkov, Ferreira, & Cavaco-Paulo, 2015; Zheng et al., 2010). The ability to control the morphology and assembly of the silk fibroin is essential for the structure and functionality of silk-based materials. Several studies have evaluated the effectiveness of silk as a tool for drug delivery using self-assembled particles (Kundu, Chung, Kim, Tae, & Kundu, 2010; Lozano-Perez et al., 2017; Mottaghitalab, Farokhi, Shokrgozar, Atyabi, & Hosseinkhani, 2015; Mwangi et al., 2015; Numata & Kaplan, 2010; X. Wang, Yucel, Lu, Hu, & Kaplan, 2010; Wenk, Merkle, & Meinel, 2011), while others have

focused on the development of effective protocols for the formation of the silk spheres (Wongpinyochit, Johnston, & Seib, 2016; Xiao, Lu, Lu, & Kaplan, 2016; Z. Zhao et al., 2015). Because it became possible to suspend regenerated silk fibroin in water with different concentrations, flexible solution-based methods have been developed to process silk. A recent review has summarized more than ten different methods for particle formation, including desolvation/coacervation, salting out from water, supercritical fluid technologies, electrospraying, microemulsion, and polymer blend (Z. Zhao et al., 2015).

As an important step in many methods, an organic solvent, such as acetone or ethanol, is often used as an antisolvent, added directly into a bulk suspension of silk fibroin to induce the formation of nanoparticles. This process of dissolution consists of reducing the solubility of the protein leading to phase separation. For instance, silk fibroin nanoparticles have been prepared by using dimethyl sulfoxide (Kundu et al., 2010), ethanol (Reis, Neufeld, Ribeiro, & Veiga, 2006), and polyvinyl alcohol (Shi & Goh, 2012). In a different configuration, the dissolution of a sessile droplet of a colloidal suspension may be potentially utilized to assemble the colloids into regular assemblies with desirable microstructures. This process based on droplet dissolution is particularly flexible when the surrounding phase consists of a cosolvent and an antisolvent of the droplet liquid. It is possible to achieve a vast range of shrinkage rate by simply varying the combination and ratio of the two solvents in the surrounding phase, highly complementary to droplet evaporation-driven self-assembly and pattern formation (Brutin, 2015; Cazabat & Guéna, 2010; Deegan et al., 1997; Erbil, 2012; Hu & Larson, 2002; Z. Lin, 2013; Marin et al., 2012; X. Zhang, Wang, Watanabe, Uddin, & Li, 2011). The solubility of the solvents is analogical to a ternary mixture in the phenomenon named Ouzo effect (Aschenbrenner et al., 2013; Lepeltier, Bourgaux, & Couvreur, 2014; Vitale & Katz, 2003), solvent shifting, or nanoprecipitation (Aubry, Ganachaud, Cohen Addad, & Cabane, 2009; Schubert, Delaney, & Schubert, 2011; Yan et al., 2014). Our recent work has

demonstrated the possibility of droplet dissolution for assembling graphene oxide (GO) snowballs and nanocellulose microspheres (Jativa et al., 2015; H. Yang et al., 2015; H. Yang et al., 2012).

It is known that a pure liquid droplet on a substrate may dissolve rapidly, shrink at different rates, or even self-propel or split in the binary solution with different ratios of the cosolvent and the antisolvent (Takahiko Ban, Aoyama, & Matsumoto, 2010; Dietrich et al., 2016; Poesio, Beretta, & Thorsen, 2009). For a droplet comprising colloidal particle suspension, the droplet behaviours are expected to be also influenced by the properties and interactions of the colloids dispersed within the droplet. In a similar process of solubility reduction, it has been observed that silica nanoparticles in the suspension could form a thin layer upon contact with an immiscible solvent (Grauzinyte, Forth, Rumble, & Clegg, 2015; Haase, Stebe, & Lee, 2015). Considering the large size and slow diffusion of silk fibroin, we also expect that interfacial enrichment of the silk fibroin may have a significant implication for the solvent transport across the droplet and the formation of the microstructure on the superficial layer of the assembled silk.

In this work, we investigate the behaviours of a silk solution droplet on a substrate immersed in a binary solution and explore the possibility of controlling the morphology and assembly of silk proteins by the controlled droplet dissolution. The binary liquid phase consists of ethanol as the cosolvent and toluene as the antisolvent. The *in situ* images revealed interfacial enrichment of silk fibroins and initial volume expansion of the droplet from the intake of the surrounding phase. By the end of droplet dissolution, we obtained silk microspheres that possess regular microstructures controllable by the ratio of solvents in the surrounding phase. Interestingly, the transparency of the silk spheres to visible light is switchable by hydration and dehydration processes. We will first present the final microstructures of the silk microspheres and then the two-phase behaviours of the droplet

immersed in the binary solution that led to the formation of these silk spheres. The main factor for varying the sphere morphology will be the ratio of the cosolvent and antisolvent in the surrounding phase, while other conditions (i.e., temperature, liquid volume, and initial droplet size) are constant in all experiments. We will also briefly show the effect of other antisolvents on the interfacial precipitation of silk. This work clearly demonstrates that the droplet dissolution process provides new opportunities for making silk spheres with regular and tuneable surface microstructures and desirable optical properties.

4.2 Results

4.2.1 Switchable Transparency of Silk Protein Microspheres.

We examined the transparency of silk spheres obtained by varying the concentration of ethanol in the binary solution. Representative optical images in *Figure 4.2* show the top view of two silk protein spheres obtained in 1 and 5% ethanol solutions. The former is transparent with some small white patches on the surface, whereas the latter is entirely white. The micro-spectrophotometry measurements of the as-prepared spheres show that the transmittance increases in the visible spectrum between 400 and 700 nm for both spheres. For the sphere prepared in 1% ethanol, the transmittance is above 75% at a wavelength longer than 500 nm, whereas the white sphere from 5% ethanol solution remains below 20% transmittance within the visible spectrum.

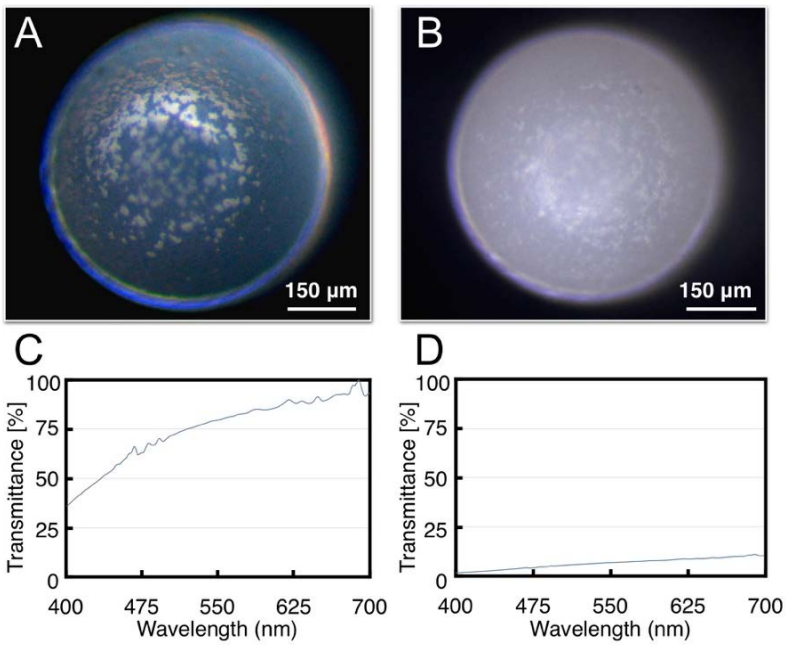

Figure 4.2. Optical images of two silk microspheres in air. (A) Transparent silk protein sphere prepared in 1% ethanol solution. (B) Opaque silk protein sphere prepared in 5% ethanol solution. Transmittance spectrum for the spheres obtained in 1% (C) and 5% (D) ethanol solution.

The sphere was stable and remained transparent for an extended period under ambient condition and became opaque only after drying for several days in air. The loss of transparency was possibly attributed to removal of the moisture from the sphere surface with time. When exposed to water, however, the sphere became transparent again in less than 1 min.

To reveal the recovered transparency of the sphere in water, we tried to see through the sphere immersed in water and were able to obtain a clear image of a pattern of regular dots printed on a piece of white paper. The dot pattern in *Figure 4.3A* was placed in front of the sphere that was submerged in water in *Figure 4.3B*. Light was illuminated first through the white paper with the pattern, then through the sphere, and finally reached the camera. The image recorded by the camera (*Figure 4.3C*) shows the dot pattern with the alignment matching the one printed on the paper, exactly similar to an image obtained through a transparent glass marble. This test confirmed the underwater transparency of the assembled silk sphere. When the hydrated sphere was taken out from water, it remained transparent, and once dried after a long period, it turned into white color again. This process of hydration and dehydration could be repeated to make the sphere transparent and opaque correspondingly. For comparison, the spheres prepared in 0.5% ethanol solution showed similar optical properties. However, the dry sphere prepared in 5% ethanol solution was opaque all of the time both in air and in water.

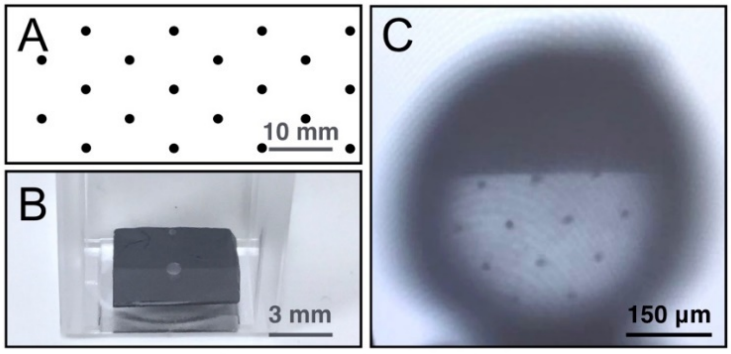

Figure 4.3. Transparency of the hydrated sphere. (A) Dotted pattern printed on a piece of paper that was placed behind the silk sphere. (B) Transparent silk sphere immersed in water. Before immersion in water, the sphere was obtained from droplet dissolution in 1% ethanol solution and then dried in air for several days. (C) Optical image of the dotted pattern observed through the sphere.

4.2.2 Surface Microstructures of Transparent and Opaque Silk Spheres

The detailed morphology of the prepared silk spheres was characterized by a scanning electronic microscope as shown in *Figure 4.4* and Figure 4.5. We observed submicron bumps over the surface of the sphere obtained from the droplet dissolution in 1% ethanol solution. Similar morphological structures were also observed for spheres prepared from a lower ethanol concentration. *Figure 4.4* shows a smoother surface covered with sub-micrometer bumps when 0.5% ethanol solution was used as the surrounding phase. Careful examination of the inner structure by cutting through the sphere shows that the inside is solid and uniform.

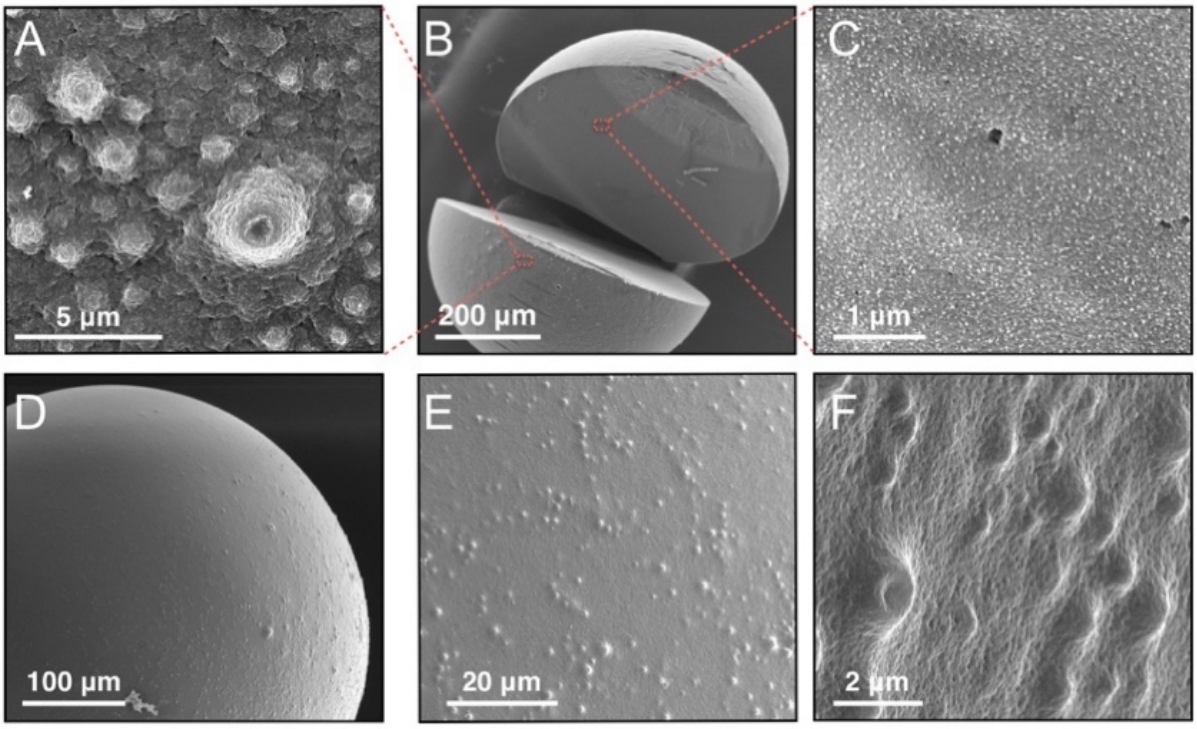

Figure 4.4. SEM images of two transparent silk spheres formed in (A−C) 1% ethanol solution and (D−F) 0.5% ethanol solution. (A) Outer surface of 1% ethanol spheres presents small truncated cones. (B,C) Inside of the spheres is highly regular with only slight imperfections. (D−F) Sphere obtained by 0.5% ethanol solution shows similar truncated microcones on the surface but with lower numbers and a smoother surrounding area. The inset in (E) shows the optical image of the transparent sphere that is cut in half.

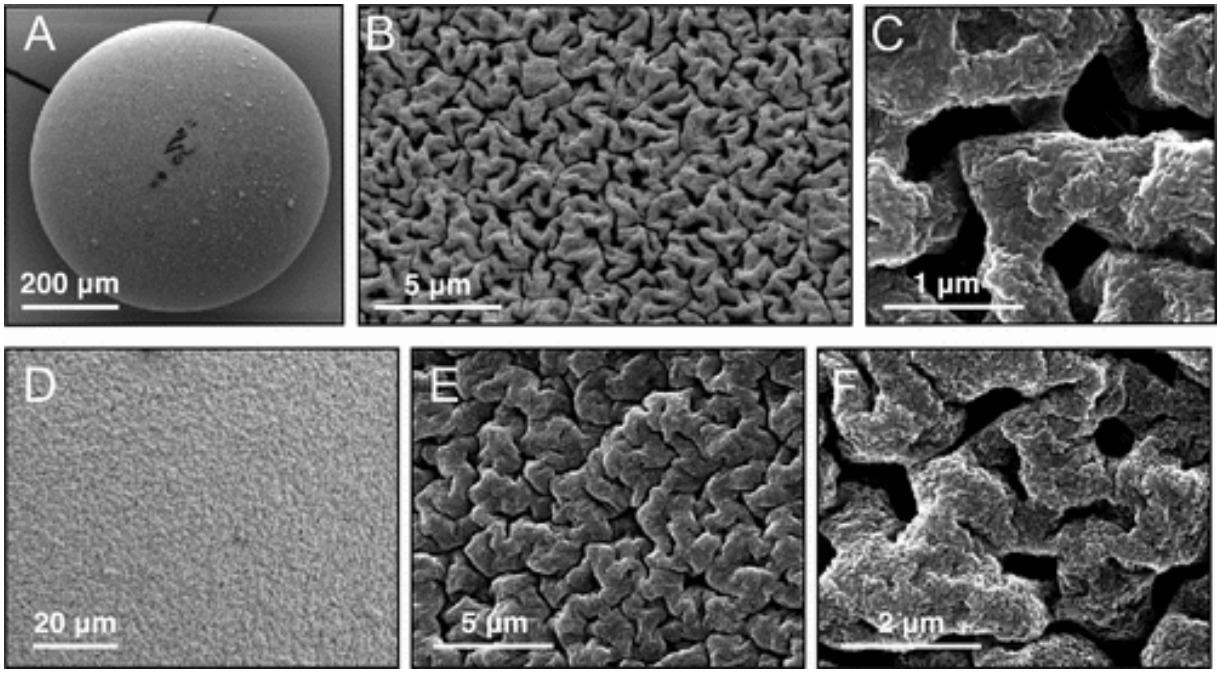

Figure 4.5. SEM images of white silk spheres. SEM image of the sphere formed in toluene solutions containing 5 vol % (A−C) and 7% (D−F) ethanol solution.

The images in *Figure 4.5* and *Figure 4.6* show the sectional and superficial surface microstructures of the spheres obtained in 5 and 7% ethanol solutions. These spheres are non-transparent with morphological structures that are significantly different from transparent silk spheres prepared from the solution with low concentration of ethanol. There are ridges and crevices on the sphere surface, like the morphology of a walnut. The image analysis reveals that the ridges are ~500 nm on average in width. They are uniform and are present over the entire sphere surface. The ridges are more densely packed on the sphere obtained in 7% ethanol solution. There are some clear imperfections, and nonuniform layers cross the sectional surfaces. From the solution with the concentration of ethanol above 10%, we could not obtain spherical silk structures anymore because the droplet dissolved rapidly upon contact with the surrounding phase.

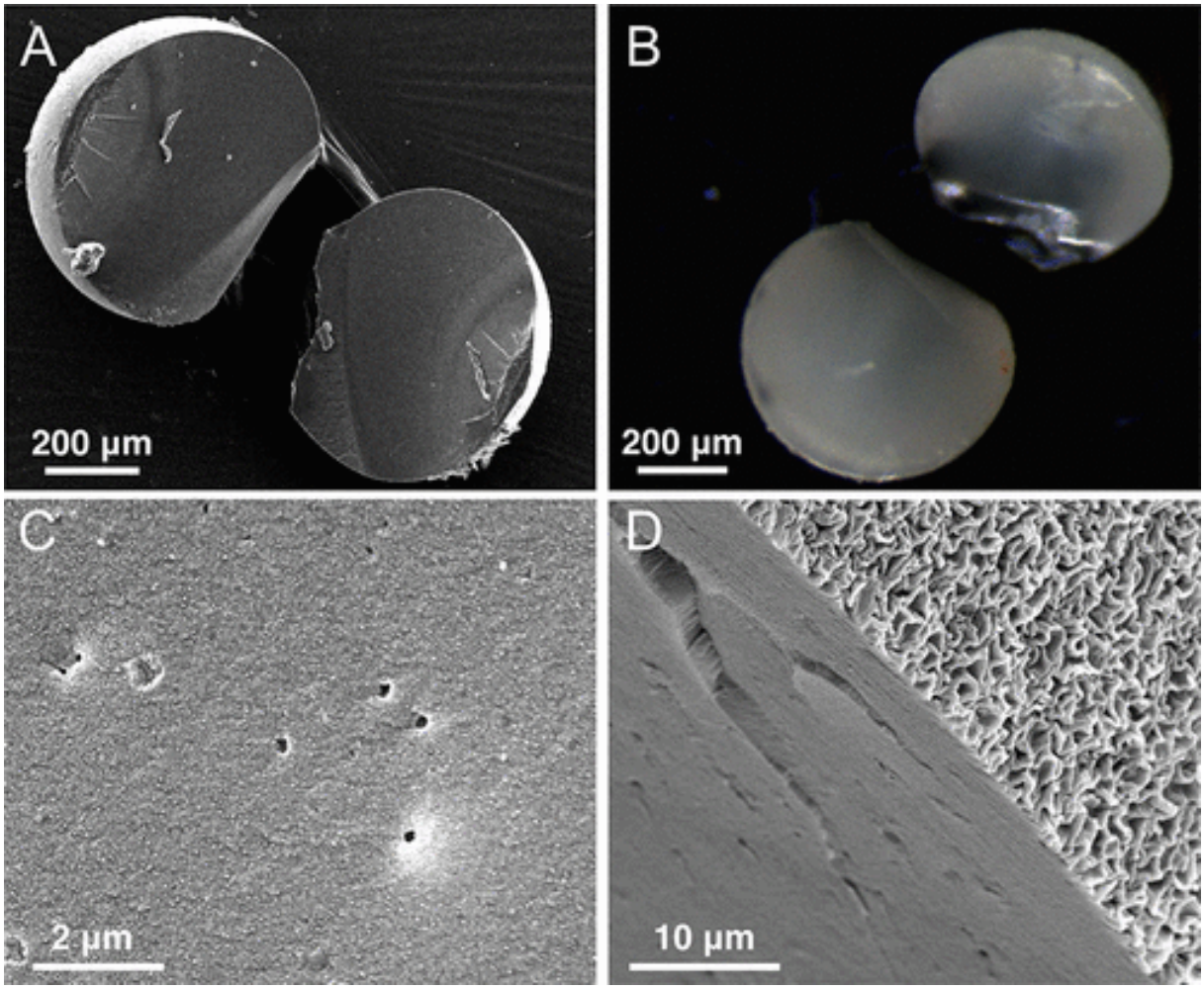

Figure 4.6. Inner structures of non-transparent silk spheres prepared in 5% ethanol solution. (A) SEM and (B) optical images of non- transparent sphere after being cut through. (C,D) Image of the sectional surface of the cut sphere. There are some imperfections and several nonuniform layers cross the surface.

We took several SEM images of the surface of each sphere and analyzed the surface porosity of the spheres. The plot in *Figure 4.7* shows that the surface porosity of the silk surface increases with the increase in the ethanol concentration in the solution up to 5%.

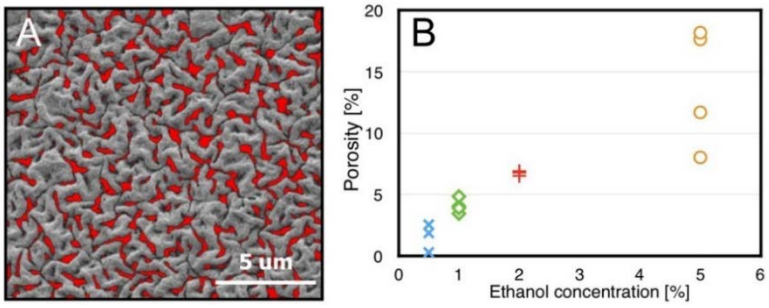

Figure 4.7. Surface porosity calculation. (A) Example of a threshold for a given surface image. (B) Surface porosity of the silk microspheres as a function of ethanol concentration in the surrounding phase. As the ethanol concentration is lower, the spheres are more smoothened.

4.2.3 Dynamical Behaviors of the Silk Solution Droplet in the Binary Solution.

To understand the dependence of the morphological features of the silk spheres on the composition of the binary solution, we followed the evolution of a silk droplet upon immersion into the surrounding phase with different concentrations of ethanol. The initial concentration of ethanol in the solution was set from 0.5 to 10%. The drop shrinkage was recorded for the entire duration of the dissolution. The representative time course snapshots of the droplet in 2% ethanol solution at different dissolution times are shown in *Figure 4.8A*. The videos are provided in the Supporting Information of the online published version of this paper.

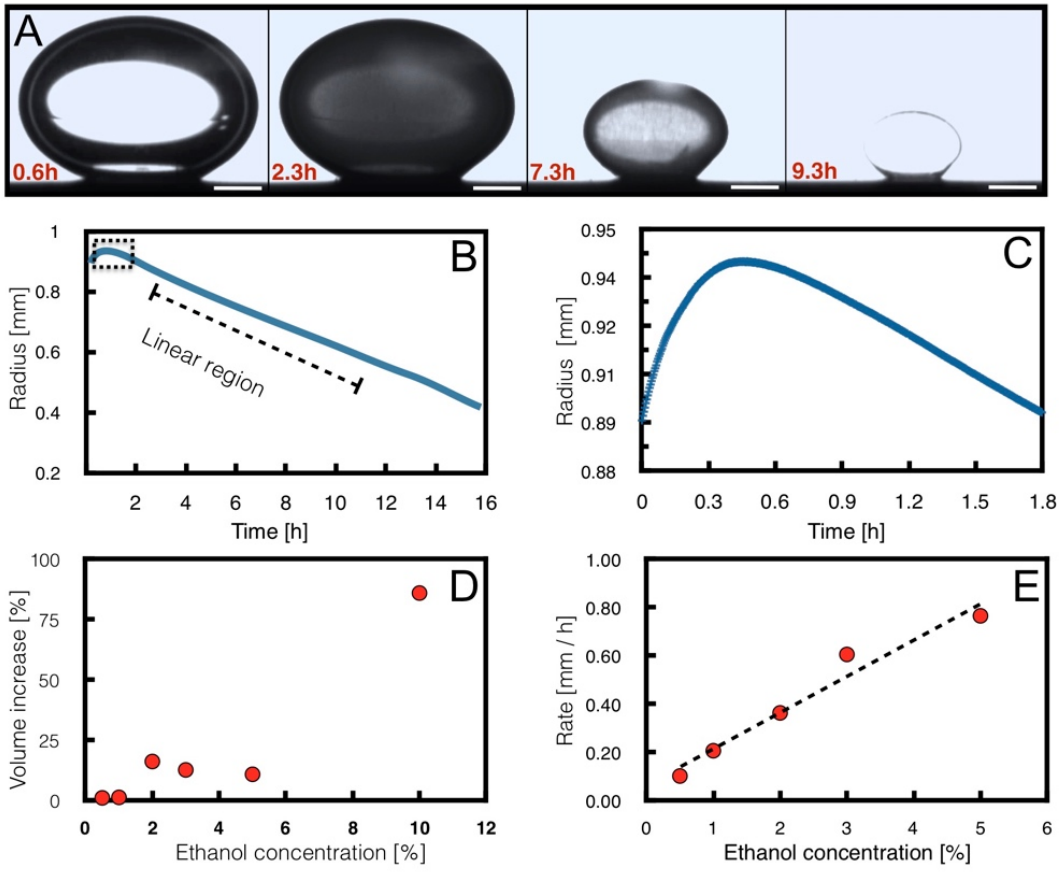

Figure 4.8. Silk fibroin 3 µL droplet in 2% ethanol solution. (A) Time-course snapshots of the droplet. Initially precipitation of fibroin proteins makes the droplet opaque. As the droplet shrank, it became transparent again, resulting in a transparent 3D silk sphere by the end. The length of scale bars in the images is 400 µm. (B) Plot of the radius of silk fibroin droplet as a function of time. Here, the radius is equivalent to a half of the maximal lateral extension of the droplet. (C) At the beginning, there is an increase in the drop volume as organic solvents diffuse in the droplet to achieve equilibrium. (D) Volume increase from the first phase of the droplet immersed in the solution of different ethanol concentrations. (E) Plot of silk dissolution rates as a function of the ethanol concentration.

The plots of the droplet radius as a function of time in *Figure 4.8B,*C show typical two-phase dynamics. The initial phase is marked by an increase in the droplet size. Compared with the initial droplet volume, a substantial increase in the droplet volume by 16% was observed for the first half an hour after immersion of the droplet in the binary solution at 2% ethanol concentration. The most significant droplet expansion was observed in 10% ethanol solution, reaching ~80% volume increase. By contrast, negligible volume expansion was observed at the concentration of ethanol below 1%. The results suggest that the volume expansion is influenced by the concentration of ethanol in the surrounding phase. After a peak in the volume, the droplet gradually transited to dissolution, and the second phase commenced. The most important feature in the second phase is the approximate linear relationship between the droplet radius and dissolution time as shown in *Figure 4.8 C*.

To quantify the dissolution rate of the silk droplet in the second phase, we fit the linear region in the plot of droplet radius versus time with a line as shown in *Figure 4.8 B*. The shrinkage rate of the droplet radius at the second phase is represented by the slope of the linear fitting in the second phase. The plot of the dissolution rate as a function of the ethanol concentration in *Figure 4.8E* shows that the dissolution rate is faster with increase in the concentration of ethanol in the solution. The dissolution rate increased by ~8 times as the concentration of ethanol in the surrounding phase increased from 0.5 to 5%, suggesting that the dissolution rate of the droplet is finely tuneable by the concentration of ethanol in the bulk phase.

We also noticed that a thin layer gradually spread from the bottom of the droplet, and then, the entire droplet becomes black in the video. Interestingly, near the end of the shrinkage, the droplet slowly became transparent again as shown in *Figure 4.8A*. The initial volume expansion and the shell formation are particularly pronounced in the solution with a high concentration of ethanol. *Figure 4.9* shows some representative snapshots of droplets in 10%

ethanol solutions. The droplet volume increased rapidly and reached 1.7 times the initial volume in the first half hour. Such rapid expansion in the droplet volume clearly suggests quick intake of a large volume of liquid from the surrounding phase. It is evident that a thin shell of the protein formed at the droplet surface and wrinkled as the droplet volume reduced. Such initial volume expansion and shell formation were also observed for the binary solution of ethanol and decane, where all of the silk precipitated very quickly, and the aqueous droplet even moved away from the empty silk shell in *Figure 4.9B*.

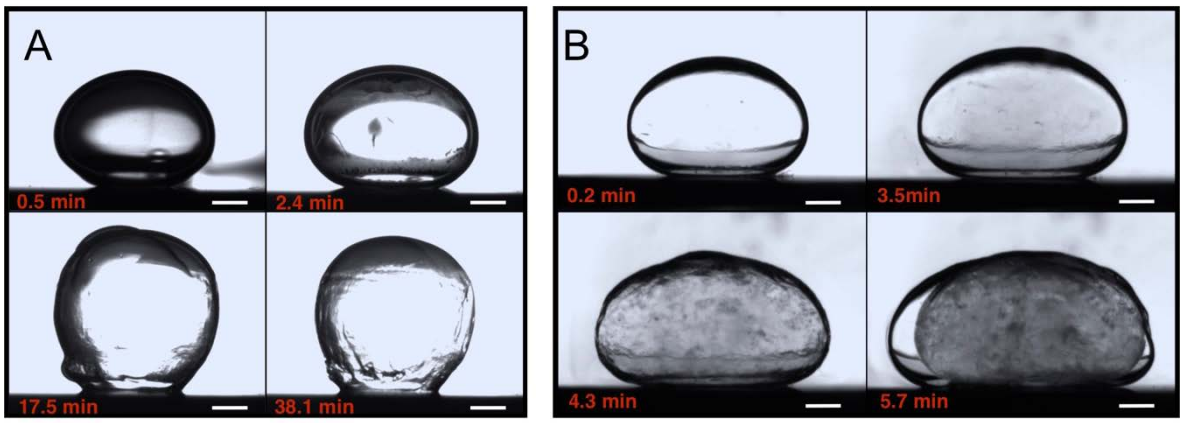

Figure 4.9. Snapshots of silk solution droplet in (A) 10% ethanol in toluene and (B) decane solutions. At the beginning, there is an increase in the drop volume as the ethanol diffuse in the droplet. Initial precipitation of fibroin proteins makes the droplet opaque. The fibroin forms a skin around the droplet. Length of the scale bar: 400 μm.

Once the dissolution process was complete, all bulk liquids were carefully removed from the system and the spheres were left in air to dry naturally. Depending on the binary solution which the droplet was immersed in, the spheres shrank to a different extent from drying. Following a solution of 2% ethanol, no sphere compression was observed. However, after the solution of 10% ethanol, the sphere size decreased by 40% after drying. The extent of the sphere shrinkage lay in between for intermediate ethanol concentrations. This compression may further alter the microstructures of the spheres and hence their optical properties. Consequently, the spheres prepared in 5% ethanol solution were not transparent in air, although they were by the end of the droplet dissolution.

4.3 Discussion

The above two-phase behaviour of a silk droplet in the binary solution is similar to that reported for a droplet consisting of other nano-colloids, such as GO or nanocellulose (Jativa et al., 2015; Song, Lu, Yang, Zhang, & Zhang, 2016; H. Yang et al., 2012), which also exhibited an initial growth phase and then a dissolution phase upon immersion in a binary solution. The dissolution rate in the second phase generally increased with the concentration of the cosolvent in the surrounding phase. However, compared with these colloidal suspensions, the duration of the initial expansion phase is approximately 10 times longer for a silk droplet. On the other hand, a droplet of pure water or electrolyte solutions in the binary solution did not experience the first phase of expansion; instead, it dissolved much faster in the first phase than in the second phase (Song et al., 2016). The substantial intake of organic solvents from the binary solution may be due to gel-like structures of silk fibroin at the interface (Y. Yang et al., 2012), which delays the establishment of an interfacial zone around the droplet and the transition to the dissolution phase. In our view, the duration of the initial expansion is influenced most significantly by the concentration of the cosolvent in the surrounding phase and the interfacial behaviours of the dispersed colloids in the droplet. Compared with the interfacial properties of the dispersed colloids or molecules, how strong they bind water molecules in the bulk may be less important, given that their initial concentration is so low in the droplet. Therefore, we did not observe an initial expansion for an electrolyte solution droplet. The expansion of GO suspension droplet was not as significant as silk, although GO was also well-dispersed in water.

The intake of organic solvents from the surrounding phase may have significant implications on the stability and behaviours of the protein in the droplet. It is expected that mixing the organic solvents in the droplet may lead to changes in protein spatial structures and formation of the aggregates. In several relevant systems, Chen et al. have extensively studied silk protein stability when ethanol is added to a silk 2D film or aqueous solution (X. Chen,

Knight, Shao, & Vollrath, 2002; X. Chen, Shao, Knight, & Vollrath, 2007). They showed that adding ethanol to a silk solution created a phase in which β-sheets formed. The rate of β-sheet nucleation was proportional to the ethanol concentration in the solution. Furthermore, they also showed that β-sheet formation follows three steps: slow β-sheet nucleation, fast aggregation, and finally slow perfection (X. Chen et al., 2007). The presence of β-sheet in assembled structures may contribute to the transparency of the spheres prepared under the conditions with low ethanol concentration.

When a droplet is in contact with the solution at high concentration of ethanol (i.e., 10% in toluene or in decane), the rapid intake of organic solvents and the mixing between water and organic solvent in the interfacial zone of the droplet contribute to interfacial precipitation of proteins and the formation of a shell around the droplet. Later on, this shell became crumpled and wrinkled from compression owing to droplet dissolution, and therefore, the as-prepared silk spheres acquired such a distinct surface morphology full of crevices and ridges. When the concentration of ethanol is reduced to 2% or even less, the slow intake of organic solvents into the droplet may not induce a large amount of aggregation at an initial stage, which explains the initial transparency of the droplet. However, as the droplet dissolved with time, more aggregates formed, and consequently, the droplet became opaque. The transparency acquired by the droplet at the late stage may be attributed to the rearrangement of the silk with droplet dissolution. The slow dissolution rate at low concentration of ethanol may also explain the absence of strong shell formation and less rough surface of the final silk sphere.

The transparency of the silk spheres could be preserved for a few days in air, suggesting its prolonged stability. The moisture on the sphere surface layer appears to be important for the high transparency. As the sphere becomes completely dehydrated in air, it becomes opaque. The dehydrated microspheres are rehydrated in short time upon immersion in water, suggesting possibly that the hydration of only the interfacial layer is essential. The mechanism for this

switchable transparency of the silk microsphere may be different from the well-known optical properties of Japanese skeleton flowers (Yong et al., 2015). The color of this white flower originates from the reflection of light from the structures of the dry petals. The wet petals become transparent when it rains because of the refractive index matching between water trapped in the petals and the cellular interface (Yong et al., 2015). Although water is essential for the transparency of both the flower and the silk sphere, the former turns white as soon as the surrounding medium changes to air. However, the silk spheres are transparent under water and remain so even after being taken out into air, as long as the top layer remains moisturized. Furthermore, the silk spheres can remain transparent after being cut into half (see the images in Supporting Information).

Intake of organic solvents may also lead to the oversaturation of toluene and the nucleation of toluene nanodroplets in the interfacial zone of the droplet. This phenomenon of the spontaneous formation of nanodroplets is analogous to Ouzo effect (Aschenbrenner et al., 2013; Lepeltier et al., 2014; Vitale & Katz, 2003), solvent shifting, or nanoprecipitation in a bulk ternary mixture (Aubry et al., 2009; Schubert et al., 2011; Yan et al., 2014); surface nanodroplets by solvent exchange (X. Zhang et al., 2015); or the formation of nanodroplets in an Ouzo droplet owing to preferential evaporation of the cosolvent (Tan et al., 2016). These toluene microdroplets may be coated and stabilized by the fibroin as the droplet shrank at the second phase, leading to the submicrometer bumps on the silk spheres. Elimination of these microbumps in future work may be a way to further improve the transparency of the silk spheres.

4.4 Conclusions

In summary, we demonstrate that controlled droplet dissolution in a binary surrounding phase may be an effective approach to obtain silk spheres with tunable surface microstructures. The ratio of the cosolvent and the antisolvent in the surrounding phase is essential for adjusting

the surface morphology and transparency of the assembled silk spheres. Upon immersion in the solution, the droplet intakes the organic phase, which showed significant influence on the stability and arrangement of the silk in the later phase of the droplet dissolution. At low concentrations of the cosolvent, the initial volume expansion from solvent intake is less and the subsequent dissolution rate is also slower. The as-prepared sphere acquired less rough surface and exhibited switchable transparency. At high concentrations of the cosolvent and fast expansion−dissolution rates, a thin shell of the precipitated protein formed, wrapping around the droplet. Wrinkling and crumpling of the shell with droplet dissolution gave rise to the ridges and crevices on the surface of the assembled silk spheres. The process based on the droplet dissolution is simple, versatile, and effective in tuning the detailed surface microstructures of a silk sphere. The transparent spheres may be used as an optical element under water. Although not transparent, the silk spheres with a rough surface may be potentially used as microcarriers owing to their tuneable porosity.

4.5 Experimental Section

4.5.1 Materials and Chemicals.

The silk from the supplier (Advanced BioMatrix, San Francisco USA) was a partially hydrolyzed silk fibroin II solution at the concentration of 5% (w/v). Toluene (99.9 vol %, Sigma-Aldrich) and ethanol (98 vol %, Sigma-Aldrich) were used as received. Water was prepared from a Milli-Q unit (18.2 MΩ·cm, Millipore, Merck Australia). A glass vial was used as the container for the droplet dissolution. The vial was cleaned with a sodium hydroxide solution, rinsed with water and ethanol, and dried in an oven at 60 °C before use. The hydrophobic substrates were octadecyltrichlorosilane (Enmon Jr et al.)-coated silicon substrates, which were prepared by following the protocols in literature (Lessel et al., 2015; M. Wang, Liechti, Wang, & White, 2005; X. H. Zhang, Maeda, & Craig, 2006).

The silk from the supplier (Advanced BioMatrix, San Francisco USA) was a partially hydrolyzed silk fibroin II at the concentration of 5% (w/v) in an aqueous solution. To prepare the solution, whole cocoons, harvested from domesticated *Bombyx mori* in China, were degummed and processed into a liquid protein solution using heavy inorganic salts. The solution was then desalted, tested, and packaged. One of the key features of the silk fibroin solution is the preservation of the fibroin light chain at around 25 kDa.

4.5.2 Setup for the Droplet Dissolution.

The binary solution of ethanol and toluene of different concentrations was put inside of the glass vial. The substrate of OTS−Si was placed at the bottom of the vial. A droplet of 3 μL of silk solution was placed above the substrate, and then, the top of the vial was sealed by a film to avoid solvent evaporation. A contact angle measurement system (OCA20, DataPhysics Instruments GmbH, Germany) was used to monitor and record the droplet with time. The side-view video of the droplet was analyzed using shape recognition software (SCA202, DataPhysics Instruments) to obtain droplet height, volume, and contact angle. At the end of the droplet dissolution, the solution was removed carefully, and the silk spheres were taken out for characterization. For comparison, we tested the process of drying a drop of silk fibroin solution on the same substrate in air. In this way, we did not obtain a silk sphere, but a spherical cap, due to the smaller contact angle of the drop in air and the pinned boundary of the evaporating drop.

4.5.3 Characterization of the Microstructure of Silk Microspheres.

The microstructure of the silk spheres was examined using a field-emission scanning electron microscope (FESEM). Dry silk sphere samples were mounted onto 12 mm aluminium stubs with double- sided carbon tabs. The samples were then coated with gold using a Xenosput sputter coater (Dynavac, Wantirna South, Australia) and imaged with a Philips XL30 field-

emission scanning electron microscope (Philips, Eindhoven, Netherlands) at a voltage of 2.0−15 kV.

To cut a sphere, we first placed it in the SEM stub adhesive surface and proceeded to cut it by pressing against a blade. To examine whether the cutting process might influence the morphology of the sectional surface, we cut several spheres and found that sectioned spheres exhibit similar features in their internal structure, suggesting the nanostructures in the inner area of the sphere were not affected. We also observed some fractures and cracks on the sphere caused by cutting, for example, as shown in the top panels of *Figure 4.4*.

The silk absorbance and transmittance spectra were obtained using a microspectrophotometer (CRAIC Technologies, USA) equipped with a 15× objective and a xenon lamp. The spectra were recorded in the visible range of 400 and 700 nm, at 50 scans per measurement.

The data were analyzed with proprietary spectral software. The surface pore (porosity) area fraction was determined from SEM images by using image analysis software (ImageJ). Images from different areas of the sphere were analyzed to determine the averaged surface porosity area fraction on the silk sphere.

Chapter 5: Confined Self-Assembly of Cellulose

5.1 Foreword

The self-assembly of cellulose nanocrystals was investigated in isolated shrinking droplets. Our results indicate that the morphology of the resulting assembled structure can be controlled by manipulating the percentage of the binary liquid phase composed of ethanol and toluene. This phenomenon offers the opportunity to produce customizable microbeads with clear-cut nanostructures that may be utilized for photonic, nano-technological, and biomedical applications. The overall results of the study provided fundamental insights into the structural evolution of liquid crystalline CNC phases. This chapter has originally been published in the following citation, and was revised for this thesis:

Jativa, F., Schütz, C., Bergström, L., Zhang, X., & Wicklein, B. (2015). Confined self-assembly of cellulose nanocrystals in a shrinking droplet. *Soft Matter*, *11*(26), 5374-5380.

5.2 Abstract

With the use of shrinking isolated droplets, we have analysed the way in which cellulose nanocrystals (CNC) assemble into liquid crystalline phases. In order to regulate the final structure of the complete microbead, we fine-tuned the water dissolution rate of a liquid CNC droplet submerged in a toluene-ethanol solution. We found out that when there is a low ethanol concentration in the enclosing fluid, dense sphere-shaped microbeads are formed; whilst when the ethanol concentration is high, we achieved collapsed core-shell particles. We utilized polarized light microscopy was in order to follow the spatial development and coalescence of birefringent spheroids during droplet shrinkage; whereas the final nematic assembly was observed through electron microscopy. This technique of enclosed CNC structuring provides the opportunity to generate ordered microbeads, which can then be advantageous as templates for their optical characteristics.

5.3 Introduction

Cellulose has an array of mechanical characteristics, which when combined with its good chemical durability, make it a unique component in the assemblage of materials for use in technical and biomedical processes (Wicklein & Salazar-Alvarez, 2013) This has been demonstrated in studies involving rod-like cellulose nanocrystals (CNC) which can self-assemble in liquid crystalline phases (Y. Habibi et al., 2010; J. F. Revol et al., 1992; J. F. Revol, Godbout, Dong, & Gray, 1994). Some other studies have demonstrated that high-performance materials can be constructed via biomimetic self-assemblage (Dumanli et al., 2014; Wicklein & Salazar-Alvarez, 2013). Thus this paves the way for the preparation of chiral nematic films with important optical characteristics such as iridescence or birefringence (Kelly, Giese, Shopsowitz, Hamad, & MacLachlan, 2014; Park et al., 2014).

The structuring of the chiral nematic phase primarily depends on particle interplay, CNC concentration and on the solvent aspect ratio (Lagerwall et al., 2014; J. F. Revol et al., 1994). Gelation and/or glass assembly compete with liquid crystal self-assembly at elevated CNC concentrations. During this process, the motion of the CNC rods becomes limited which leads to the shutting of the system into a “frozen” condition (Lagerwall et al., 2014).

There are very few studies that demonstrate the process by which complex CNC elements are constructed, including those that have a chiral nematic structure other than films, such as micro-spheres. More studies on this field is therefore necessary since structured nanocellulose microspheres could be used as a technique to deliver drugs and even fragrances (Nypelo, Rodriguez-Abreu, Kolen'ko, Rivas, & Rojas, 2014). Moreover, optically active colloidal particles can also be utilized to generate discrete colloidal crystals with photonic characteristics, as well as work as templates for the synthesis of inverted opals (F. Li, Josephson, & Stein, 2011; Shopsowitz, Qi, Hamad, & Maclachlan, 2010). It is important to note that with shape anisotropic colloids like the rod-like cellulose nanocrystals, it is more likely to create

microspheres with various microstructures and diverse textures (Dugyala, Daware, & Basavaraj, 2013; S. Y. Zhang, Regulacio, & Han, 2014).

Although the equilibrium stage of CNC at low and reasonable concentrations is well-studied (Lagerwall et al., 2014), its assembly at much higher concentrations and under limited circumstances has not been fully understood. A relatively recent study proposed that adjusting the onset of gelling, by adding glucose for instance, can regulate the helicoidal structure of CNC rods in dried films (Mu & Gray, 2014) proposed that adjusting the onset of gelling, by adding glucose for instance,, can regulate the helicoidal structure of CNC rods in dried films.

The most common method of generating spherical colloidal aggregates is evaporation-induced self-assembly of colloidal dispersion droplets (Marin et al., 2012; Pauchard & Allain, 2003; Uetani & Yano, 2013; S. Y. Zhang et al., 2014). However, the control over the drying rate is not feasible at low rates, and it affects the condition of the finished structure (Uetani & Yano, 2013). There is another form that has of late shown the way in which two-dimensional nanosheets can organize into microspheres via an isolated droplet dissolution immersed in a 2-phase liquid stage (Song et al., 2013; H. Yang et al., 2012); similarly, toroidal microstructores of nanocolloidal assemblies have obtained with this method (Z. Lu, Rezk, Jativa, Yeo, & Zhang, 2017). This method allows the dissolution rate to be regulated by the configuration of the surrounding binary liquid stage as well as generate structures in the form of microbeads.

In this study, we observe shrinking droplets of aqueous cellulose nanocrystal dispersions utilizing real-time polarized microscopy of the liquid crystalline stage in combination with electron microscopy of the surface and internal structure of the spheres. We were able to demonstrate that there are liquid crystalline tactoids which assemble at low shrinkage rates, which first appear close to the outer edge of the droplet; ultimately they fuse with each other and assemble into organized domains while the CNC accumulation increases. The CNC assembly stops at high shrinkage rates and it shifts to a formation of a stiff shell at

the droplet's outer edge which ultimately ends in collapsed dry spheres as they have an empty interior structure.

5.4 Experimental section

A detailed description of the methodology can be found in Chapter 3 of this thesis. This includes cellulose nanocrystals preparation (3.4.1); reagents, materials and hydrophobic substrate (3.1 and 3.1.1); dissolution rate set-up, dissolution rate experiments (3.2.2 and 3.4.2); tactoid imaging (3.4.3); microstructural characterization of cellulose (3.4.4). Schematics of the setup for droplet dissolution can be found in *Figure 5.1*.

5.5 Results and Discussion

5.5.1 Liquid Crystalline Phase Formation in a Shrinking Droplet

We tracked the development of a liquid crystalline phase in the enclosed space of an isolated shrinking a droplet that contained CNC, while being submerged in a binary toluene-ethanol solution (*Figure 5.2*). The spherical form of the droplet is maintained all throughout the dissolution process since the contact angle of the shrinking droplet located on the hydrophobized substrate is very high (~155°) (*Figure 5.5a*).

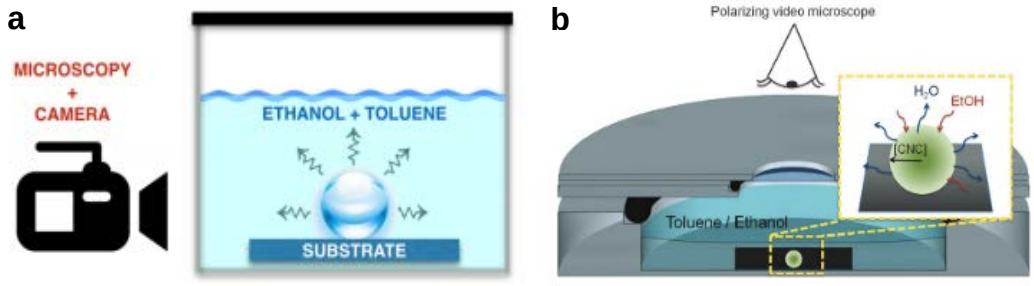

Figure 5.1. Schematic of the setup used for (a) water dissolution dynamics of aqueous CNC droplets in toluene/ethanol solutions and (b) polarized video microscopy imaging of the shrinking droplets placed on a hydrophobized OTS-silicon substrate. (a) Side-view images of the shrinking droplet were recorded with a contact angle measurement equipment.. The glass vial was sealed to prevent solvent evaporation. (b) The CNC droplet (light green) is placed on a hydrophobic OTS-silicon substrate (black) and recorded in reflection mode. The diffusion of water and ethanol as well as the resultant radial CNC concentration gradient are illustrated.

The shrinkage of the droplets is depicted by a linear diminishing of the droplet radius, R, as a function of time as shown in *Figure 5.2*. The shrinkage curves demonstrate that the droplets expand initially in *Figure 5.2a*; this could be because of the absorption of ethanol into the CNC droplet. It can be seen in *Figure 5.2b* that the droplet shrinkage rate expands with the ethanol uptake from the surrounding toluene mixture. Following this, the diameter of the droplet decreases in a linear manner until the shrinkage is slowed down by the structured CNC rods. This type of shrinkage rate dependency has already been observed before and connected to the non-ideal blending of multi-component droplets in partially immiscible liquids (T. Ban, Yamada, Aoyama, Takagi, & Okano, 2012; H. Yang et al., 2012).

Moreover, convective effects are to be anticipated from what was observed in the droplet vibration during the dissolution process. These movements can efficiently agitate the boundary layer encircling the droplet, and, as a consequence, encourage water diffusion into the surrounding medium (Poesio et al., 2009; Zhu et al., 2009). When there is a high ethanol concentration (10 vol%), an alteration in the curvature of the shrinkage curve is observed (*Figure 5.2*b). This is possibly caused by the self-propelled droplet motion on the hydrophobic substrate (Takahiko Ban et al., 2010; Poesio et al., 2009) when the first stage of the shrinkage process occurs.

The shrinkage rates vary by more than one order of magnitude, and this supports the probability of being able to control the assembly kinetics and particle packing. *Table 5.1* classifies the shrinkage rates for the area where the shrinking droplet radius is in the middle of 40 and 80% of the original radius, equivalent to CNC concentrations between 1 and 13 vol%.

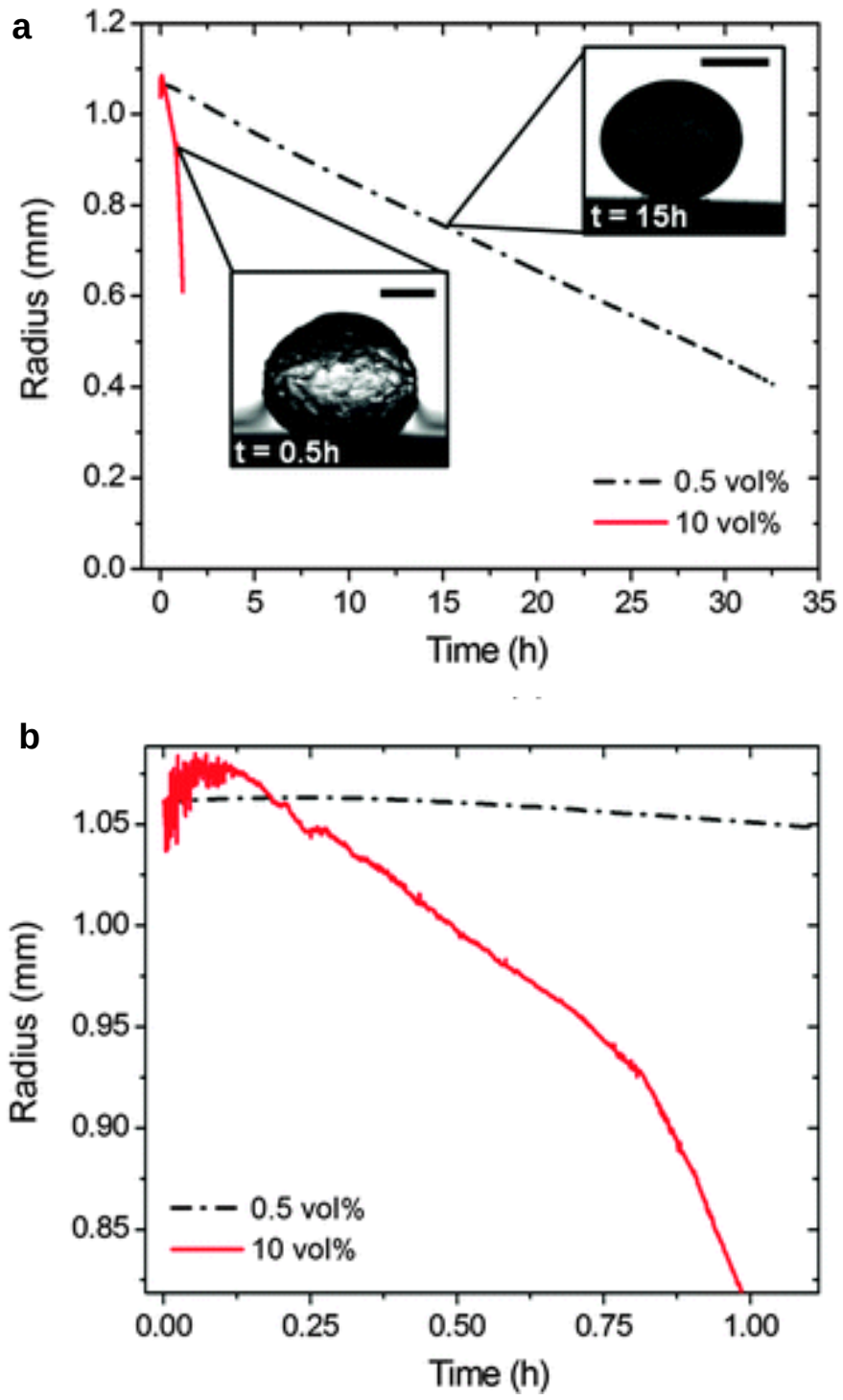

Figure 5.2. Shrinkage curves of CNC-containing droplets in EtOH–toluene solu-tions containing 0.5 vol% EtOH (dashed line) and 10 vol% EtOH (solid line). (a). The inset photographs show side views of the shrinking droplets in the respective solutions (scale bars are 600µm). The initial droplet volume was 5µl and the initial CNC concentration was 0.75 vol%. The curves show the entire shrinkage process until the droplet is solidified. (b) Magnification of the shrinkage curves at the initial stage, showing the droplet expansion in 10 vol% EtOH due to the intake of the liquid from the surrounding phase and a change of slope at 0.8 h.

Table 5.1. Shrinkage rates for CNC droplets in different toluene–ethanol solutions. The shrinkage rate was averaged by a minimum of 3 experiments for each ethanol concentration.

Ethanol [%]	Shrinkage rate of the droplet [10^{-3} µm s^{-1}]	Standard Deviation
0.5	5.6	0.9
1	8.3	1.3
5	33	9
10	58-23	-

Polarized video microscopy was used to follow the structuring and development of birefringent ordered domains as shown in *Figure 5.3a*. It has been conclusively proved that colloidally stable CNC dispersions endure an isotropic-to-nematic stage conversion as the CNC concentration expands and birefringent, liquid crystalline domains appear under cross-polarized light (Park et al., 2014; J. F. Revol et al., 1992). The carboxylated CNC system depicts a biphasic area from an initial aggregation of 0.4 vol% CNC up to 0.75 vol% for the fully evolved aqueous crystalline phase (*Figure 5.3b*). At the same time when the CNC dispersion droplets shrink and the CNC aggregation inside the droplet grows, mobile spherical aqueous crystalline domains, that is, tactoids, are generated as seen in *Figure 5.3a* (Bouligand & Livolant, 1984; J. F. Revol et al., 1992).

The lack of black extinction lines in the polarized photographs of the tactoids indicate that the carboxylated cellulose nanocrystals utilized here do not evolve a helical structure under the dynamic conditions of this investigation. However, the phase separation and structuring of the helical pitch in the nanocrystal dispersions was found out to be time-dependent (Castro-Guerrero & Gray, 2014) and was only visible after a few months in equilibrium (*Figure 5.3c*).

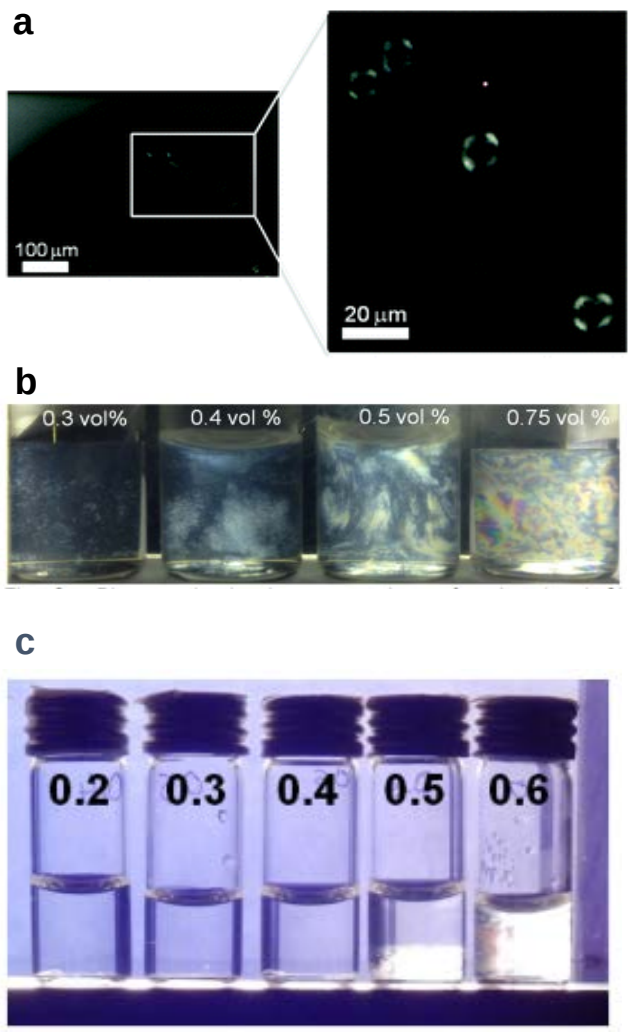

Figure 5.3. (a)Birefringent domains in the interphase region of a shrinking CNC dispersion droplet observed under polarized light. The droplet contained 0.3 vol% CNC and was immersed in a toluene/5 vol% ethanol solution. The image was taken 1.4 h after immersion. The tactoids display a Maltese cross indicating the orientation of the crossed polarisers. (b-c) Photograph showing suspensions of carboxylated CNC positioned between crossed polarizers. The image indicates the biphase region between the isotropic and liquid crystalline phase with an onset concentration of 0.3 vol% and the 100 % liquid crystalline phase at (a) 0.75 vol%, and (b) 0.6 vol%. (b) The image was taken 48 h after sample preparation and no phase separation occurred until then. (c) The image was taken 6 months after sample preparation. The numbers in the photograph indicate the vol% of CNC. The chiral nematic order was confirmed by laser diffraction.

The observation that tactoids initially appear near the interface with the surrounding toluene/ethanol binary mixture shows a radial CNC concentration gradient inside the shrinking droplet. Early work on self-assembling particles with evaporation-induced structuring has depicted that the competition with the diffusion rate and the droplet shrinkage rate can develop in substantial aggregation rates near the interface (Bigioni et al., 2006). Based on the Stoke–Einstein relation to $D = 8.1 \times 10^{-13}$ m2 s^{-1}, we were able to predict the diffusion constant for freely rotating CNC rods and infinite dilution, which can then be compared to values for CNC that was observed prior (Sim et al., 2015). Upon comparison of the diffusion distances calculated from $(2Dt)^{1/233}$ with the droplet shrinkage rate, it was shown that diffusion is not capable of keeping up with the shrinking liquid-liquid interface when the ethanol aggregation in the enclosing liquid is 5% or higher. These approximate calculations hence confirm the observations of tactoids structuring near the liquid-liquid interface. Comparable

solute concentration gradients were also reported in evaporating colloidal droplets which sometimes lead to the skin effect (Duggal, Hussain, & Pasquali, 2006; Pauchard & Allain, 2003).

A significant difference was observed between the 5 and 15% EtOH concentration in the surrounding liquid with regards to the time-dependent development of the liquid crystalline phase. We can see in *Figure 5.4a* that discrete tactoids in CNC dispersion droplets submerged in a solution containing 5% EtOH rise after about 1-2 h post submerging. The tactoids progressively become larger and then consolidate to form a complete birefringent microbead. On the other hand, rapid droplet shrinkage at 15% EtOH in the surrounding solution exhibit a different consolidation course whereby large birefringent, halo- shaped regions immediately arise at the interface of the droplet *Figure 5.4b.* These metastable birefringent areas occur only for a short time before they are completely replaced by large tactoids (*Figure 5.4b*, 0.75 h) which gradually combine to form a stable birefringent shell.

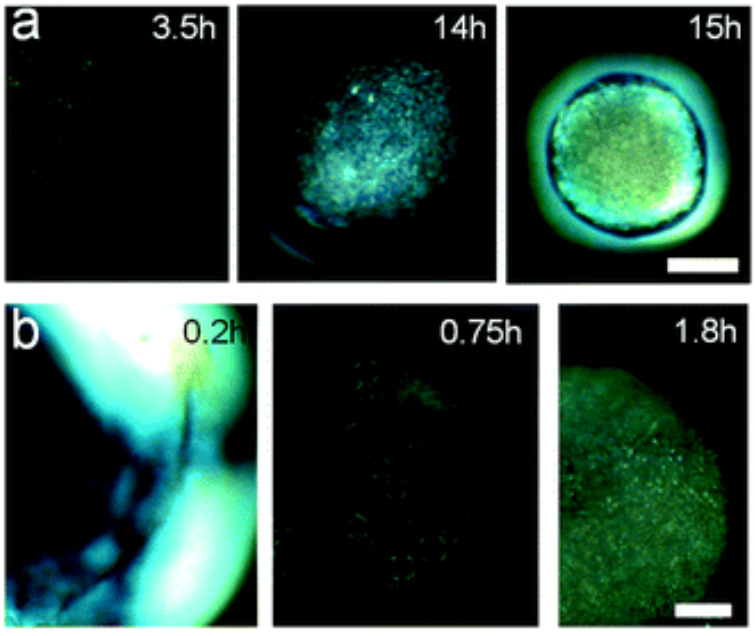

Figure 5.4. The time evolution of liquid crystalline phase in shrinking CNC droplets. Reflection polarized microscopy images of a droplet in: (a) toluene/5 vol% ethanol (a) and (b) toluene/15 vol% ethanol, taken at different times during the shrinking process. The initial CNC concentration of the droplets was 0.3 vol%. Birefringent domains appear bright under cross polarized light. The scale bar is 100 µm.

The high ethanol concentration correlate with the large droplet shrinkage rate and this seems to result in a very rapid growth of CNC aggregation at the interface. This triggered the formation of a thin aqueous crystalline “skin” at the surface of the droplet. Nonetheless, the consecutive dissolution of the skin implies that the convection within the rapidly shrinking and

moving droplet might diminish the CNC concentration below the phase boundary. When this initial phase was over, the erratic motion of the droplet stopped and it appears like the rapid droplet shrinkage builds a stable supersaturation of CNC at the interface, which in turn generates large tactoids. This very concentrated CNC aggregations can generate a rigid shell-like structure, that could resist more droplet shrinkage (*Figure 5.5b*). The shell buckling could have been caused by the mechanical instability due to droplet shrinkage (Sacanna, Irvine, Chaikin, & Pine, 2010). It is noteworthy that the whole droplet shrinkage process is completed after less than 2 h at 15% EtOH, and the compaction of the spheres can last as long as 37 h at 0.5% EtOH.

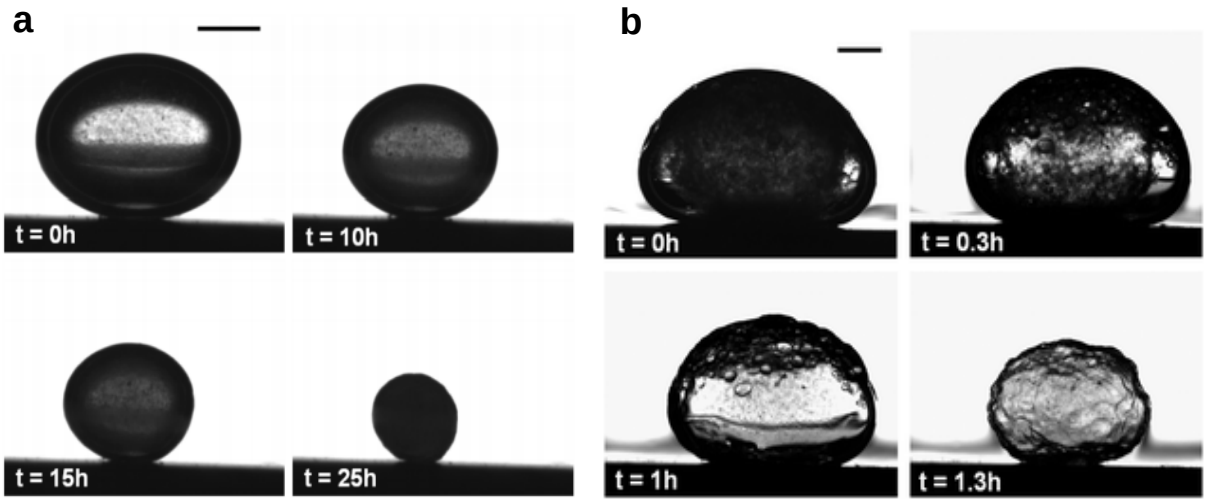

Figure 5.5. Side view images of a shrinking CNC droplet with an initial volume of (a) 0.5 µl and (b) 10 µl in a toluene/10 vol% ethanol solution. These exemplifying images show that the spherical shape of the droplet is maintained throughout the dissolution process owing to the hydrophobized substrate on which it resides. (b) The images show the formation of a shell-like structure during rapid droplet shrinkage. The scale bar is 600 µm.

5.5.2 Microstructure of CNC Microspheres

The final size of the microbead relies upon the initially dispensed droplet volume and on the ethanol concentration, which results in smaller microbeads at low shrinkage rates (i.e. low vol% EtOH). SEM imaging of CNC assemblies structured in <5 vol% ethanol show an oblate, ellipsoid-like shape (*Figure 5.6a*). Whereas, the assemblies generated at higher ethanol concentrations (>10 vol%) have a collapsed, discoidal shape (*Figure 5.6b*). The average size

of the oblate, dry microbeads is around 300–800 mm, and this correlates to a final volume of 1–10% of the original droplet volume. *Figure 5.7a* shows multiple folded cellulose sheets crumpled in the surface. Quite interestingly, *Figure 5.7b* shows that the droplet shrinkage rate does not affect the nematic structure, which is consistent with the tactoids formation process

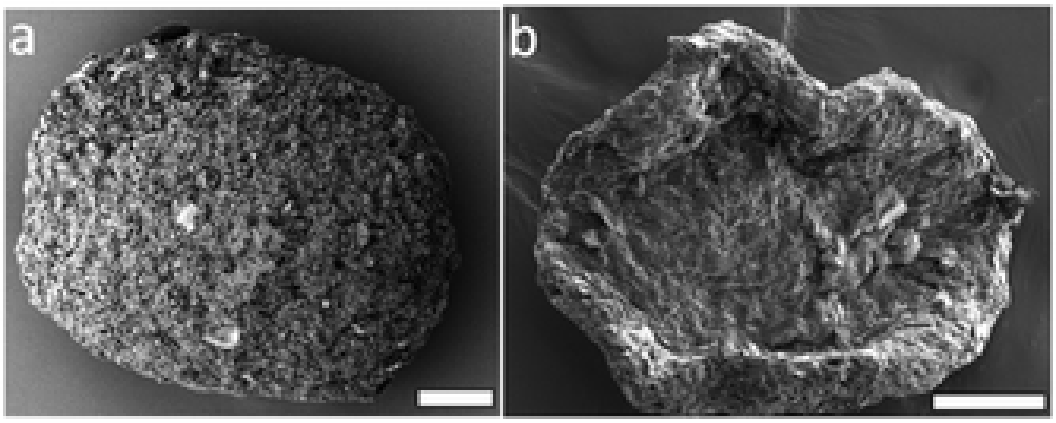

Figure 5.6. SEM images of dried CNC microbeads formed in toluene solutions containing (a) 0.5 vol% and (b) 10 vol% ethanol. The scale bars are 100 µm.

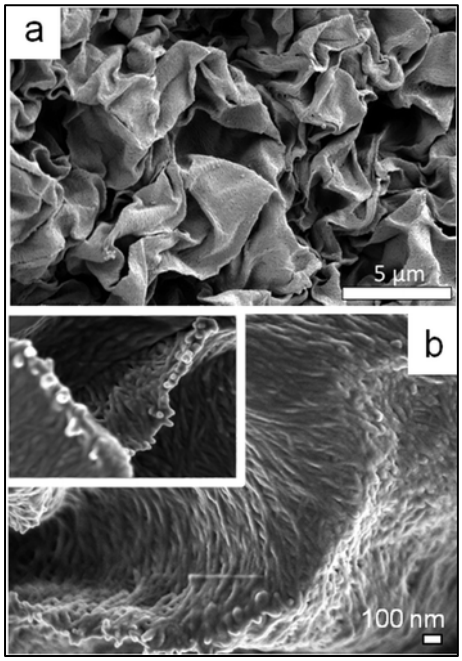

Figure 5.7. SEM image of the surface of a CNC microbead formed in toluene/0.5 vol% EtOH (a). A high resolution (HR)-SEM micrograph of the surface of a microbead formed in toluene/5 vol% EtOH (b). The inset shows a magnified view on twisted CNC rods. The scale bar is for both images the same.

The spheres internal configuration was observed by TEM of spheres sections. *Figure 5.8* shows a very organized structure in which the distance between CNC is less than 5nm. The CNC rods show nematic organization inside discrete domains of distinct prevalent orientations that evidences to a local helical organization (*Figure 5.8b* and *c*). Contrarily, no pitch lines or reflection colours were seen in the assembled structures, and this is different to thin CNC films usually formed from slow evaporation of CNC suspensions (Dumanli et al., 2014; Mu & Gray, 2014; Park et al., 2014). Those films generally depict iridescent colours that come from the helicoidal organization of the

nanocrystals and pitch lines that happened in solvent evaporation. One of the causes for this difference might be related to the rapid, non-equilibrium structure of the nanocrystals within the shrinking droplets. As a matter of fact, this CNC dispersion needs some months of equilibrium in order for a chiral nematic phase separation to happen (*Figure 5.3c*). This result works as the basis of the dynamic cellulose nanocrystal self-assembly (Schutz et al., 2015).

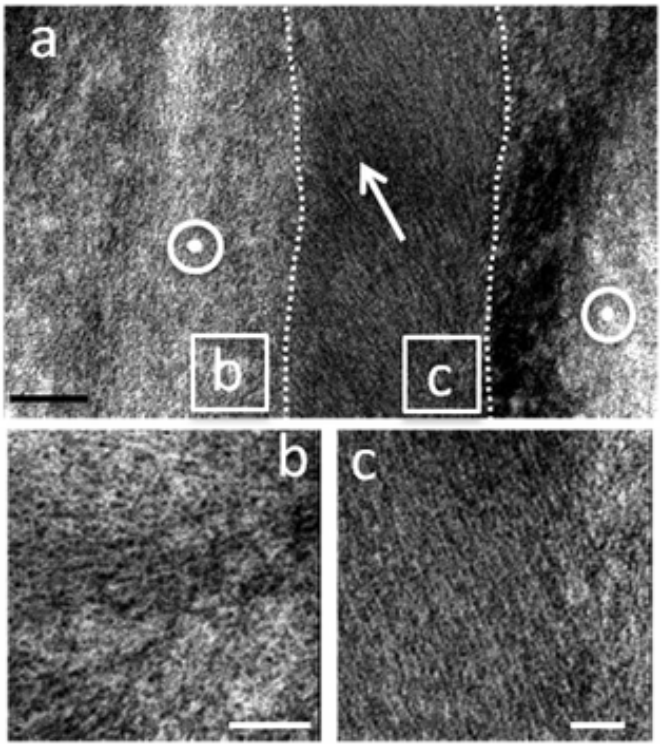

Figure 5.8. The internal microstructure of a dried CNC microbead formed in toluene/1 vol% ethanol. The bead was ultramicrotome-sectioned through the center of the particle and transmission electron microscopy reveals zones of different CNC rod orientation (separated by dotted lines) (a). The rods are aligned normal to the plane of the section (b) or in the plane (c).The circles in (a) indicate the normal orientation and the arrow the in-plane orientation. Scale bares are 100 nm (a) and 50 nm (b, c).

5.5.3 Model for Issolution-driven CNC Self-assembly

A summary of this self-assembling process is showed in *Figure 5.9* for high and low ethanol concentration. The results show that for ethanol concentrations under 5 vol%, the droplet shrinkage rate is small enough to lead to a gradual and radial growth of the CNC concentration. This leads to a restructuring of liquid crystalline tactoids in the interphase area, that aggregate together in the nematic phase across the droplet in an ordered way (*Figure 5.9a*). For large droplet shrinkage rates as observed in *Figure 5.9b*, a “skin” is immediately formed in the interface which is thin, flexible and birefringent (See *Figure 5.4b, panel 0.2 h*). This is caused as the droplet dissolves very fast and the concentration in the droplet surface jumps above the critical concentration for the isotropic-to-nematic transformation. This birefringent skin can be easily disturbed as shown by the disappearance of bright areas (see *Figure 5.4b,*

panel 0.75 h.) when the droplet keeps on shrinking. With time, a shell enclosing a depleted, hollow sphere is created, which crumples and breaks down when it dries. These mechanical instability have formerly been attributed to the structuring of permeable rigid "skins" when the drying of colloidal sessile droplets occurs (Pauchard & Allain, 2003), or the dissolving of microdroplets of nanosheet suspensions (Song et al., 2013).

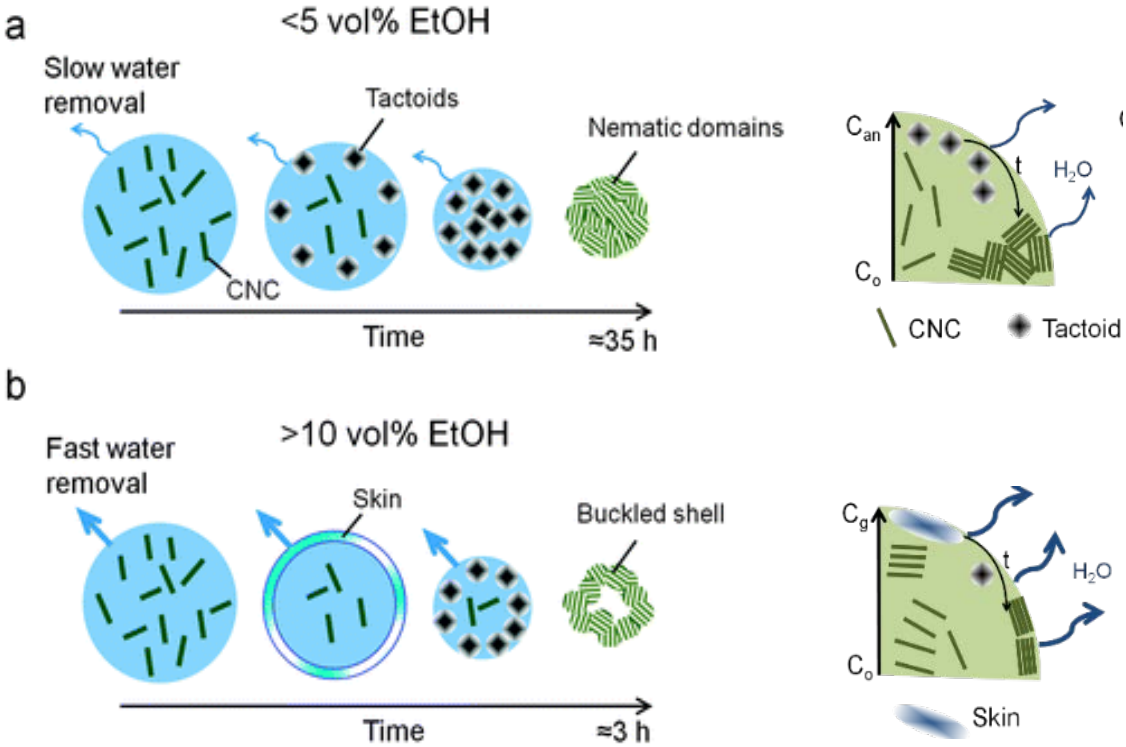

Figure 5.9. Schematic description of the CNC assembly process as function of the ethanol concentration. (a) Slow water dissolution rates at <5vol%ethanol lead to a gradual CNC concentration increase until an anisotropic CNC phase (tactoids) is formed. Over time, these tactoids merge to a solid spheroid. (b) High water dissolution rates at >10 vol% ethanol causes a rapid increase of the CNC concentration and a birefringent ''skin'' is formed at the interface. This layer undergoes tactoid transformation and subsequent formation of a shell covering a depleted and hollow droplet.

5.6 Conclusions

We investigated the relationship of CNC self-assembly in shrinking droplets along with the water dissolution rate of the droplet submerged in a binary toluene-ethanol solution. The dissolution rate of the CNC droplet heavily relies on the solvent ratio. Thick spheroid beads were formed at low dissolution rates while collapsed discoidal particles were formed at high water expulsion rates. This permits for the efficient management of the morphology of the final

colloidal assemblies by fine-tuning the ratio of the two liquids in the bulk phase. The nematic microstructure of the assemblies seems to be autonomous of the dissolution rate, possibly due to the tactoid structuring in the initial phases of the dissolution process. The self-assembly of CNCs in the enclosed space of isolated droplets contributes significant insights into the structural development of liquid crystalline CNC stages, and presents accurate nanostructures which can be helpful for photonic or nano-technological applications.

Chapter 6: Modeling the Mechanical Properties of Human Lung Mesenchymal Cell Aggregates

6.1 Foreword

A great challenge in the study of lung diseases is the difficulty in recreating *in vivo* models. This study explores cell aggregates from primary mesenchymal cells and their mechanical properties. There are previous reports of mesenchymal cell aggregates in the literature, however the remodelling process, as well as key properties such as stiffness and viscosity have not been previously characterized. A medium-throughput method to establish the mechanical properties of mesenchymal spheroids was developed, and this study is the first to report that mesenchymal spheroids present elastic properties which are easy to measure and with high reproducibility.

The study in which this chapter is based will be submitted for publication soon.

6.2 Abstract

Development of effective *in vitro* models that fully recapitulate the *in vivo* environment remains a major challenge in the study of lung diseases. Cell aggregates present, as a distinctive model to study, the effect of tissue remodelling, extracellular matrix formation, cell-cell interaction, and tissue-like biomechanical properties. More recently, it has been observed that 3D structures also allow comparison of mechanical properties such as stiffness and viscosity, with disease. While there are increasing reports on the properties of cell aggregates that present a viscous liquid-like structure, these rely on complex methodologies and techniques. Furthermore, the mechanical properties of elastic solid-like spheroids have not yet been explored.

This study proposes a medium-throughput model to determine the mechanical properties and the characterization of mesenchymal 3D spheroids. Self-assembling of spheroids with a different initial number of cells was observed in a period of 48h. Spheroid external structure was characterized by scanning electron microscopy, while the internal structure was studied by immunostaining and transmission electron microscopy on spheroid sections. Micropipette step-by-step aspiration methods used in single cells were validated and adapted for spheroids to determine the Young's modulus. A software was developed to determine stiffness as well as viscosity coefficient during creep tests based on fast image analysis. Additionally, we also applied micropipette step-by-step aspiration to determine the Young's modulus of small lung tissue samples.

The results show mesenchymal cells assemble into spheroids with distinctive smooth surfaces. Spheroid characterization shows that cells in the outer-most layers are significantly elongated, while those inside the spheroid have irregular non-directional assembly. Micropipette aspiration of different sides of the spheroid generate similar Young's modulus which confirms that cells on the spheroid periphery contribute to form a mechanical uniform elastic shell. This elastic form keeps the structure cohesive and distributes the mechanical load when spheroids are aspirated, thus validating the step-by-step aspiration model.

We conclude that mesenchymal spheroids present an elastic solid-like structure, and that step-by-step micropipette aspiration is an effective medium-throughput method to characterize their mechanical properties.

6.3 Introduction

The respiratory system comprises a conducting region that allows the transmission of air and a respiratory region in which the air exchange of gases occur. The conducting airways are composed of epithelial cells which form branches and alveolar structures. The conducting airways are composed of epithelial cells which form branches and alveolar structures. The

airways are surrounded by mesenchyme and vascular tissue (Fang et al., 2019). The mesenchyme is the source of complex and diverse cell types as endothelial cells, fibroblasts and myofibroblasts, cartilage-forming cells, lymphatics, smooth muscle cells and mesothelial cells (Morimoto et al., 2010). The interaction between the epithelium layer and mesenchyma is critical for lung development and function (McCulley, Wienhold, & Sun, 2015).

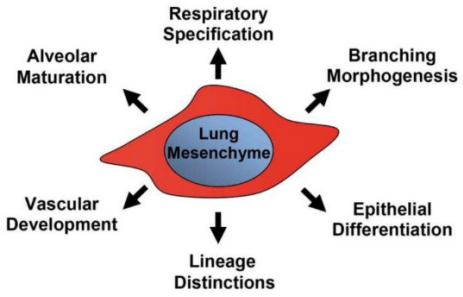

Figure 6.1. The lung mesenchyme holds a central position in the formation of a functional lung. Reproduced with permission.[49]

Despite extensive efforts by researchers in developing effective *in vitro* models to study lung diseases, there are still big challenges to fully recapitulate established *in vivo* properties of lung cells (Bosquillon, 2010; Petersen et al., 2010; Sporty, Horalkova, & Ehrhardt, 2008) Standard two-dimensional (2D) monolayer culture has been proven to be a valuable setting for cell-based studies. However, the use of a traditional flat and rigid plates fails to replicate *in vivo* conditions where cells are surrounded in extracellular matrix (ECM) and exposed to cyclical mechanical stresses (Edmondson, Broglie, Adcock, & Yang, 2014). These differences become even more critical considering 2D cell culture tests may provide false positive data which can lead to misleading and erroneous results for *in vivo* responses, making drug screening increasingly expensive (Edmondson et al., 2014). The current standard procedure of screening compounds for drug discovery proceeds as follows: I. 2D cell culture-based tests, II. animal model tests, and finally, III. clinical trials. Unfortunately, many of the test drugs fail in the last step, which happens to be the most expensive phase (DiMasi & Grabowski, 2007;

[49] "The pulmonary mesenchyme directs lung development" https://doi.org/10.1016/j.gde.2015.01.011 © 2015 Elsevier Ltd. All rights reserved.

Edmondson et al., 2014). Only about 10% of the test drugs are successful in progressing through clinical development, which can be mainly attributed to lack of clinical efficacy and/or unacceptable toxicity levels (Hopkins, 2008; Kola, 2008).

This had led to an increased interest in culture models which can better replicate the three-dimensional (3D) structure found in *in vivo* conditions (Edmondson et al., 2014; Fennema et al., 2013; Huh, Hamilton, & Ingber, 2011; Nam, Smith, Lone, Kwon, & Kim, 2015; Peng, Unutmaz, & Ozbolat, 2016; Rimann & Graf-Hausner, 2012; Skardal, Shupe, & Atala, 2016). It has been shown that cell aggregates present a distinctive model to study the effect of tissue remodelling, extracellular matrix formation, cell-cell interaction and tissue-like biomechanical properties (Shamir & Ewald, 2014; Skardal et al., 2016). Furthermore, these macro-structural systems allow for the comparison of mechanical properties such as stiffness and viscosity at the onset, with disease progression, and in response to pharmacological treatments (G. Cheng, Tse, Jain, & Munn, 2009; Guevorkian & Maître, 2017; Khalilgharibi, Fouchard, Recho, Charras, & Kabla, 2016; Kopanska, Alcheikh, Staneva, Vignjevic, & Betz, 2016; Alastair G. Stewart et al., 2015).

As work with spheroids is becoming more predominant, several tools are available to mechanically characterize spheroids such as centrifugation (Kalantarian et al., 2009; Ninomiya & Winklbauer, 2008), parallel-plate compression (Forgacs et al., 1998; Ramsey A Foty et al., 1996), micro-pipette aspiration (Gonzalez-Rodriguez et al., 2012; Guevorkian et al., 2010; Guevorkian, Gonzalez-Rodriguez, Carlier, Dufour, & Brochard-Wyart, 2011; Guevorkian & Maître, 2017) and more recently, cavitation rheology (Blumlein et al., 2017). These mechanical methods are mostly configured for cell aggregate models of limited elasticity where a load will lead to permanent viscoelastic deformation. While this liquid-like behaviour is commonly observed in cell aggregates that are structurally non-cohesive, there has been no study on spheroids with elastic solid-like structure.

Additionally, these methods rely on complex experimental setups, and require long periods of time to determine the mechanical properties of a single spheroid. Quite surprisingly, the use of elastic models, such as step-by-step micropipette aspiration, have not been explored in spheroids.

Although it has been several decades since the establishment of 3D cell culture techniques (Sutherland, 1988; Sutherland et al., 1971), the use of cell spheroids of mesenchymal origin such as fibroblast, myofibroblast and smooth muscle has been limited to the studies of cancer disease and tumors (Bizik et al., 2004; Salmenpera, Karhemo, Rasanen, Laakkonen, & Vaheri, 2016; Vaheri, Enzerink, Rasanen, & Salmenpera, 2009). No mechanical characterization of these aggregates has been attempted, even though mesenchymal cells play a key role in the biomechanics of the lung.

This study evaluates the mechanical properties of mesenchymal 3D spheroids from human airways smooth muscle cells (HASM) and parenchymal fibroblasts (pFb). Given the exceptional elasticity of mesenchymal spheroids, we propose a medium-throughput method to determine their elastic modulus by using step-by-step micropipette aspiration. This method has been traditionally used for single cells but never explored in spheroids. We further validated this result using the proposed technique to determine the stiffness of lung tissue sample. Finally, to facilitate easy access and establish step-by-step aspiration as a medium-throughput method to determine spheroids elastic modulus, by using an image analysis software for the aspiration process.

6.4 Material and Methods

6.4.1 Preparation of Poly(HEMA) Non-adhesive Plates

A 0.5% Poly (2-hydroxyethyl methacrylate) (Poly(HEMA)) solution was prepared by dissolving it in 95% ethanol in sterile Milli-Q water (Merck, Millipore, Kilsythe, VIC, Australia). The mixing of poly(HEMA) with solution was facilitated by the use of a shaker

during 24 hours to ensure complete mixing. Ninety six-well round-bottomed plates were coated with 50 μL 0.5% poly(HEMA) solution to inhibit cell adhesion to plastic, and they were left in incubator for 3 days until the solution had concentrated to dryness. Prepared plates were stored at 4 degrees for a period of no longer than 3 weeks to ensure plate coating quality.

6.4.2 Cell Culture and 3-dimensional Multicellular Spheroids

Human airway smooth muscle (HASM) and parenchymal fibroblast (pFb) cultures were established from macroscopically normal airways of lung resections as previously described in the methods chapter. Confluent culture flasks were serum deprived for 24h prior to the generation of spheroids. The cells were displaced with trypsin followed by resuspension in incomplete DMEM at a cell density of 250 x 10^3 cells mL^{-1}. Two hundred μL of this cell suspension was added to each well of the pre-coated poly(HEMA) (Santa Cruz, sc-253284) plate. The plate was then subjected to centrifugation at 1000g for 10min at room temperature to generate multicellular spheroids. Cells were also seeded at 125 x 10^3 and 62.5 x 10^3 cells mL^{-1} to study the effect of initial cell numbers in the final size of spheroids.

6.4.3 Cell counting

Cells were incubated in 2D plates and 3D spheroids with FCS (5 % v/v). After 48 hours, cells were washed with PBS and mixed for 10 min in a solution with trypsin (0.125% w/v) /EDTA (0.02% w/v) in PBS containing 0.1% collagenase. For spheroids, we additionally used 21 gauge needles to ensure cell separation. Cells were then re-suspended in 2%FCS in PBS containing 0.2% Trypan blue (Sigma, USA). An haemocytometer was used for cell count, and live and death cell were noted."

6.4.4 SEM and TEM Analysis

Samples were fixed in 2.5% glutaraldehyde in PBS for 1h, and then fixed in osmium tetraoxide 1% for 30min. These were then rinsed with PBS and serially transferred from 0% to 100% ethanol, in 20% increments and an incubation period of 10min each.

The surface of spheroids was imaged by scanning electron microscopy. Samples in 100% ethanol were critical point dried and then left for 24h for further evaporation of solvent. The microspheres were deposited on double-sided carbon tape and coated with gold. The SEM images were acquired using a Philips XL30 field-emission (FE)-SEM and a JEOL JSM-7401F FE microscope for high-resolution SEM images.

The internal structure of spheroids was characterized by transmission electron microscopy (TEM) of ultramicrotome-sectioned samples. Spheroids were incubated twice in 100% LR-white resin and subsequently embedded in capped gelatine capsules. After a polymerization step at 60°C for 24h, the embedded spheres were sectioned with a diamond knife on a Leica Ultracut S microtome, and ultra-thin sections (90nm) were collected onto formvar-coated TEM grids. The sections were sequentially stained with saturated uranyl acetate for 10min and triple lead stained for 5min and viewed in an FEI Tecnai Spirit transmission electron microscope at 120 kV. Images were captured with a Gatan Eagle digital camera at a resolution of 2k pixels.

6.4.5 Live Cell Imaging of HASM and pFB Spheroids

Whole spheroid aggregates were imaged with the Olympus IX51 (Olympus America Inc., Center Valley, PA, USA) brightfield microscope at 4x objective to allow for comparison to size of spheroid. Images were collected using the ImagePro Plus Software (Media Cybernetics, Rockville, MD, USA). Areas of spheroids were quantified using ImageJ.

6.4.6 Micropipette Aspiration Method

The micropipette aspiration technique is a well-established method for measuring the mechanical properties of single cells (Hochmuth, 2000), and the protocol was adapted for the aspiration of cell aggregates. A micromanipulator was used to carefully position the micropipette in contact with a single spheroid suspended in PBS at 37°C. The micropipette was attached to an adjustable water reservoir to finely regulate suction pressure, while images of

the aspirated spheroid were taken in real time by a digital camera–fitted microscope (Zeiss Axioshop, Germany). The relation between cell elongation, applied pressure and time allowed us to determine the mechanical properties of the spheroids. The glass micropipettes were custom-made with an internal diameter of approximately 40 µm and the tip coated with a silicone solution (Sigmacote, Sigma-Aldrich, Australia) to prevent cell adhesion. Suction pressure was applied to each cell by controlling the height of the water reservoir.

For measuring the Young's modulus of spheroids, the suction pressure was applied in five increments of 1cm H_2O (0.098kPa) and kept stable for 60s. The maximum suction pressure applied was therefore 5cm H_2O (0.490kPa). The aspirated length of the cell into the micropipette was measured from the bright field image at the end of each pressure increment as seen in *Figure 6.4* b-c. The Young's modulus of the spheroid stiffness can be calculated based on the model as shown in the schematic. This model assumes that the spheroid is a homogeneous, isotropic, elastic and incompressible half-space medium, where Young's Modulus *E* is given by,

$$E = \frac{3\,\Delta P\,R_i}{2\,\pi\,L\,\Phi_{(\eta)}}, \text{ with } \quad \eta = \frac{R_o - R_i}{R_i} \qquad \text{(Eq.6.1)}$$

where R_i and R_o is the inner and outer radii of the micropipette respectively, L is the aspiration length, ΔP represents the aspiration pressure and Φ refers to the wall function and is generally taken as 2.1 for single cell micropipette aspiration experiments (Theret et al., 1988).

For measuring the viscoelastic properties of spheroids, a constant pressure of 4cm H_2O was applied and kept stable. In response to the high pressure, spheroids exhibited a viscoelastic solid creep behaviour characterized by a rapid jump in displacement and generally reached an equilibrium deformation after four minutes (*Figure 6.4*c). The standard linear solid model (*Figure 6.4*d) was used to compute the viscoelastic parameters of the spheroids (M. Sato, Theret, Wheeler, Ohshima, & Nerem, 1990) which is used via the following equations:

$$L = \frac{\Phi R_i \Delta P}{\pi k_1}\left(1 - \frac{k_2}{k_1 + k_2} e^{-t/\tau}\right) \quad \text{(Eq.6.22)}$$

$$\mu = \frac{\tau\, k_1 k_2}{k_1 + k_2} \quad \text{(Eq.6.3)}$$

The viscoelastic parameters k_1, k_2 and time constant, τ, were determined from non-linear regressions of the aspiration length versus time plots. The apparent viscosity, μ, was calculated from Eq. 6.3.

To determine the average coefficient of variation CV(%) across donors, four technical replicates were carried on four different donors (biological replicates). Additionally, to determine the CV(%) for the same spheroid, we repeated the aspiration of a given spheroid in the opposite site and we compared these values.

6.4.7 Image Analysis

Image analysis software was used for streamline calculations of the spheroid mechanical properties as described in detail in Chapter 2. Aspiration images are loaded in the software which determine the aspiration length of the spheroid inside the micropipette. The software template is defined by the user, after which images are quickly analyzed to determine either spheroid's Young's modulus or viscosity.

6.4.8 Fixing and Immunohistochemistry

Spheroids were fixed in 10% neutral buffered formalin (Grale Scientific) for 10 min and washed twice by PBS. After fixation, spheroids were embedded into a 3% agarose solution and processed overnight into paraffin. Sequential 3 μm sections were stained with Mayer's Haematoxylin and Eosin (Trajan Scientific, Australia).

6.5 Results

6.5.1 Spheroid Self-assembling Properties

Previous studies of mesenchymal cells have reported the formation of cell aggregates with spherical shape when cultured in low adhesion surfaces. These studies provide relevant insights into the changes we observe in mesenchymal aggregates during cell proliferation, gene expression and even response to different treatments (Murray & Spector, 1999; Salmenpera et al., 2008; Salmenpera et al., 2016; Wirz et al., 2008). However, a detailed study of the self-assembling process, as well as the characterization of the mechanical properties of the final cell aggregates have not been fully explored. Furthermore, previously reported methods in the formation of mesenchymal spheroids are for small spheroids (~100 µm in diameter), where the final spheroids final sizes are around 30 times of a single cell. Meanwhile the present study evaluates spheroids of larger diameters (~300 µm in diameter).

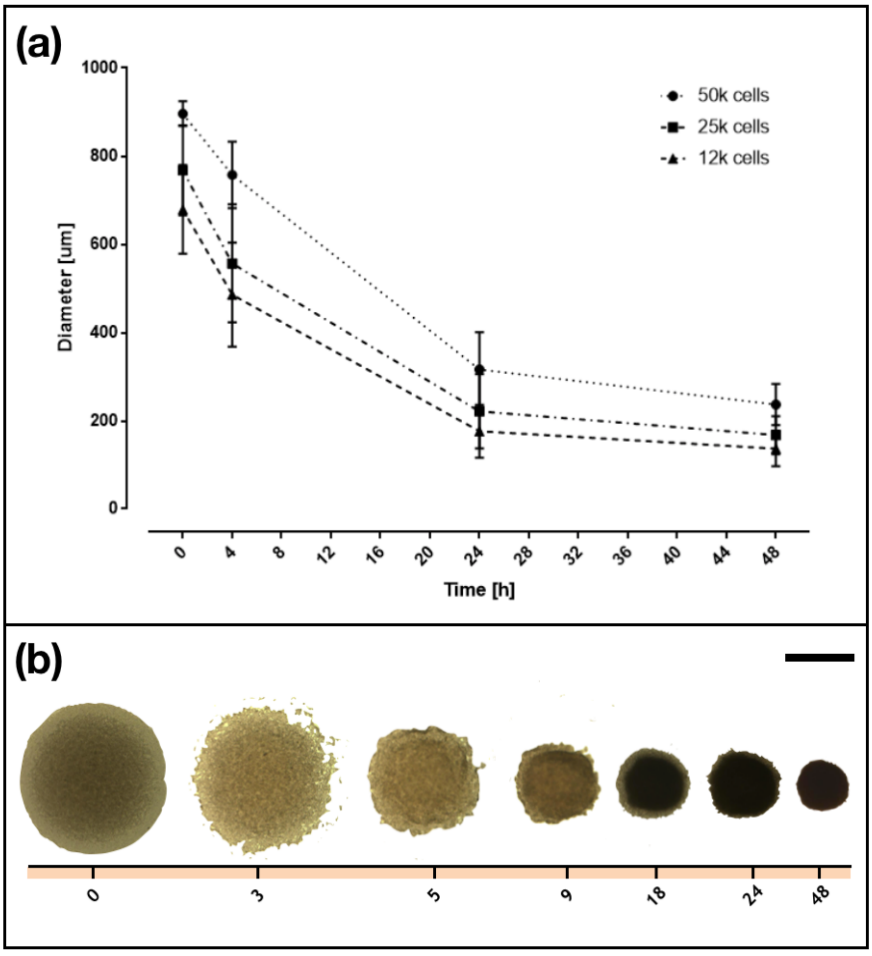

Figure 6.2. Spheroids remodelling over time. (a) Changes in diameter of fibroblast spheroids with an initial cell number of 50k, 25k and 12k cells.(b) Remodelling of a hASM spheroid com-posed of 50k cells. The spheroid compaction occurs fast in the first 24h. Scale bar = 400 µm.

Initial experiments in cell size were carried out with pFb cells to determine a suitable cell number for the purposes of this study. Results show that the spheroids assemble over a certain period of time as shown in *Figure 6.2*. The rate of assemblage was evaluated by changing the initial number of cells and looking at its relationship with the compaction rate. *Figure 6.2* shows the change in diameter of the spheroids from cell seeding to 48 hours. It has also been observed that self-assembling can be divided in three different stages based on the assembling rate at which the spheroid diameter decreases: I) First, we observed a constant rate remodelling phase characterized by a fast assembling of cells into a cohesive smaller spherical structure in between 0h to 4h. The fast assembling rate is due to the depletion of empty spaces between cells during aggregation; II) Once most of the cells have aggregated into a small volume, we started to observe a decrease in the cell compaction rate. This is a transition stage, where self-assembling rate is defined by the change from 2D into 3D structure. It is in this stage that the spheroids form a cohesive structure; III) Once the cell migration has finished forming a compact structure, we observe spheroids at a much slower assembling rate. In this stage cells are pushing each other and creating a compact final structure.

6.5.2 Characterization of Mesenchymal Cell Spheroids

Scanning electron microscope shows spheroid external structure in detail. *Figure 6.3*(a) shows the regular round structure of the spheroid with all the cells assembled in a spherical structure. This suggests a remodelling mechanism which not only leads to the formation of cell aggregates, but also creates a cohesive structure Furthermore, it was also observed that the cells were not only clustered together by the assembling, but they were also elongated parallel to the surface of the spheroid. This arrangement of “stretched cells” can be seen in *Figure 6.3* (b), and it is similar to *in vivo* conditions, such as where muscle cells are stretched to generate tension.

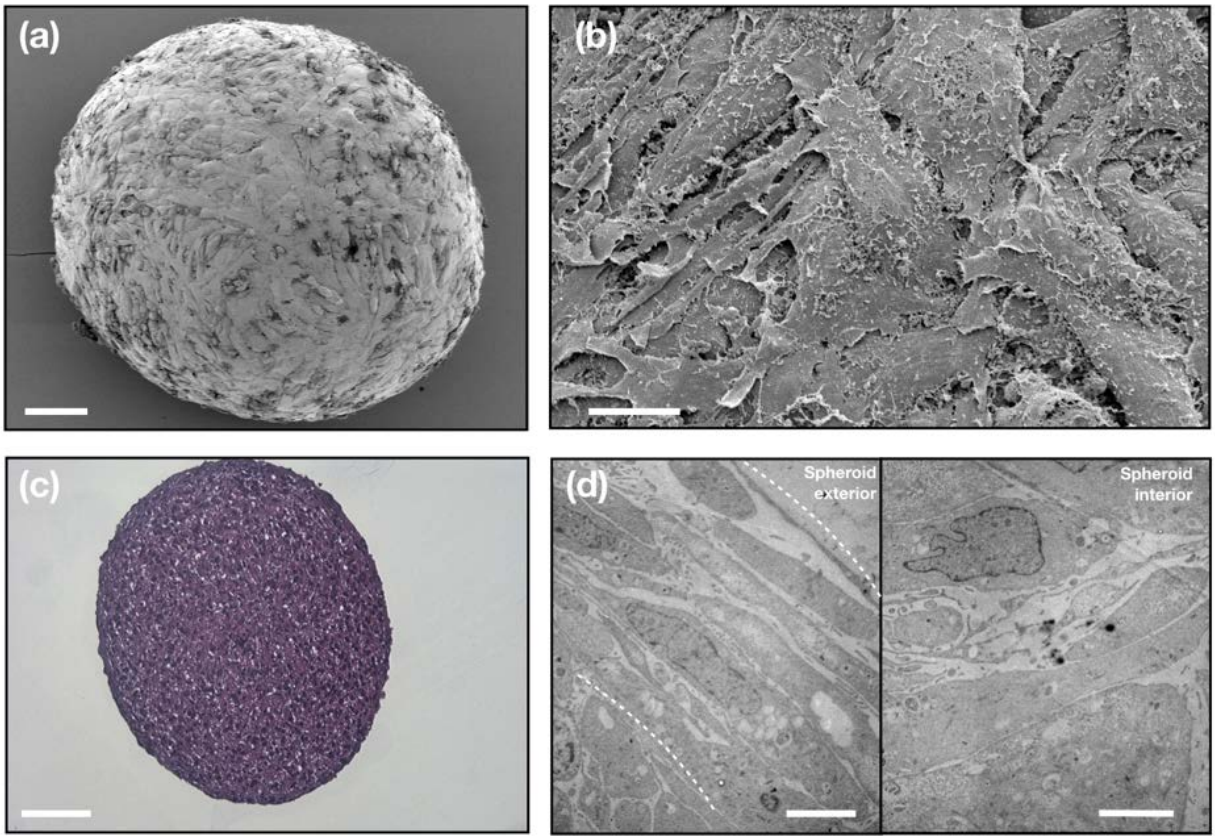

Figure 6.3. Spheroid external and internal characterization (a) SEM image of hASM spheroid after 48h. Scale bar=50 µm (b) Close up image of the spheroid surface which shows cells fully stretched creating a loaded surface. Scale bar=10 µm. (c) Histology image of spheroid section with H&E staining. It's observed that cell density is evenly distributed inside the spheroid. Scale bar = 50 µm. (d) TEM images of a spheroid on the surface (left) and center (right). Spheroid topmost layer is highlighted in between dotted lines showing several stretched cells. Cells inside of the spheroids show an irregular assembly pattern. Scale bar=5 µm.

A further insight of spheroid internal structure can be observed in *Figure 6.3* (c-d). Histology section shows an even distribution of cell density throughout the spheroid. A closer look into the spheroids structure by TEM confirms that a layer of stretched cells can be found on the spheroid periphery. These layers of cells might be hypothesized to influence the overall stiffness properties of the spheroid. TEM images from the spheroid center revealed cells inside the spheroid have an irregular non-directional assembly and are not as stretched as the ones found in the surface.

6.5.3 Evaluation of Half-space Model in Spheroids and Test Variability

To determine the mechanical properties of the cell aggregates by micropipette aspiration, we evaluated well-established models which have been used for single cells in the last decades. The half-space models developed by Theret et al. to determine Young's modulus and apparent viscosity were described in detail in the methods section (Hochmuth, 2000; M. Sato et al., 1990; Theret et al., 1988), however its validity on spheroids needs to be scrutinized.

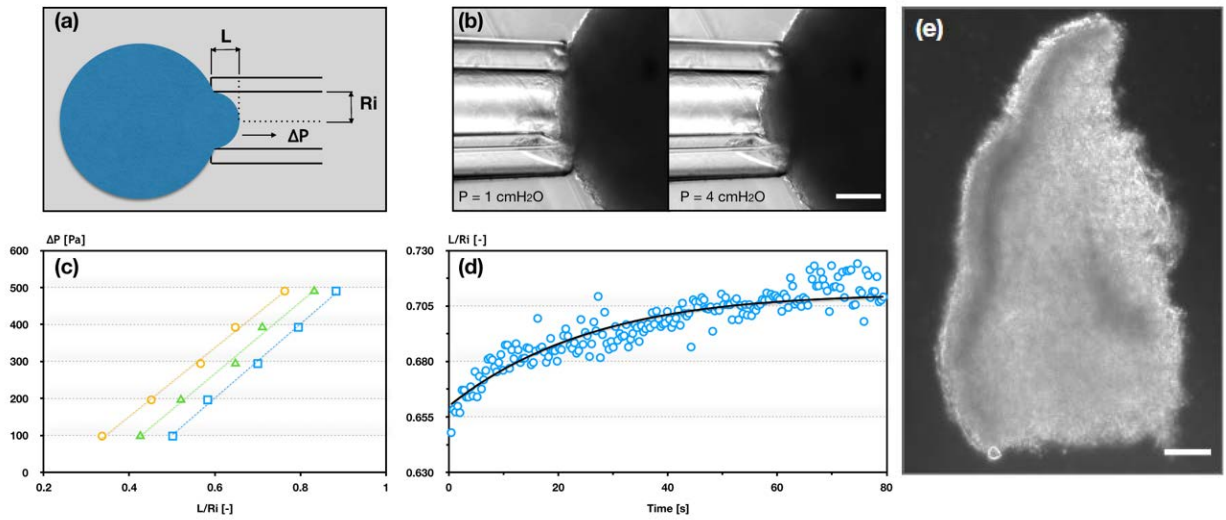

Figure 6.4. Aspiration schematic and viscoelastic experiments (a) Schematic of spheroid aspiration into a micropipette. (b) Images of a spheroids at different pressures. Scale bar = 50 µm. (c) Step-by-step aspiration experiment which shows data from 3 spheroids from the same passage and donor. (d) Creeping test at constant pressure of 4 Pa with images taken every 10th of a second. (e) Native parenchymal tissue section sample.

Previous studies on cell aggregate viscoelastic properties by micropipette have been limited to time-dependent deformation (Guevorkian et al., 2010; Guevorkian & Maître, 2017), due to the liquid-like behaviour of the aggregates. In such aggregates, a constant pressure leads to creep time dependent deformation, which is incompatible with an elastic model (Bidhendi & Korhonen, 2012). And even though micropipette aspiration elastic models have been used for the aspiration of soft tissue (Argatov & Mishuris, 2016), to the best of our knowledge there are no reports of micropipette aspiration elastic models for spheroids.

An effective application of the half-space model developed by Theret et al. (1988) to measure the Young's modulus, requires a correlation between the pressure difference and the aspirated lens. The model assumes a linear and incompressible, homogeneous and elastic half-space, that has been applied to several studies (Baaijens, Trickey, Laursen, & Guilak, 2005), and has been thoroughly described in the methodology.

To determine the reliability of the step-by-step aspiration technique, variations in the Young's modulus numerical value were assessed in three different conditions: a) aspiration of the same spheroid twice in opposite sides, b) aspiration of spheroids from the same donor and passage (also known as technical replicates), and c) aspiration of spheroids from different donors, also known as biological replicate.

The first experimental condition allows us to determine if the stiffness is consistent in the periphery of the spheroid, otherwise, additional replicates will be required. The second condition, technical replicates, allows us to determine the accuracy of the method. It is common in most biological techniques, such as PCR, to have several technical replicates to reduce uncertainty.

It was found that the average coefficient of variation CV(%) of the elastic Young's modulus for the same spheroid was $\leq 3\%$. The small variation confirms that the spheroid not only has a top layer which is flat, but the load is evenly distributed keeping a constant elasticity throughout the surface. This isotropic surface is analogous to what is observed in single cells in which their mechanical properties are uniform all around the cell wall and is consistent with structural findings of the previous section, in which the top layer of the spheroid holds a constant load.

Even more interesting is the low variability of technical replicates (inter-test variation), between spheroids of the same donor and passage. This is shown in *Figure 6.5*, in which CV(%) measurements of four technical replicates each on four different donors (biological replicates).

It can be observed that not only the CV is similar in between donors, but furthermore it can detect changes of >5.81%~6%. This high reproducibility validates step-by-step aspiration as method to determine the mechanical properties of spheroids.

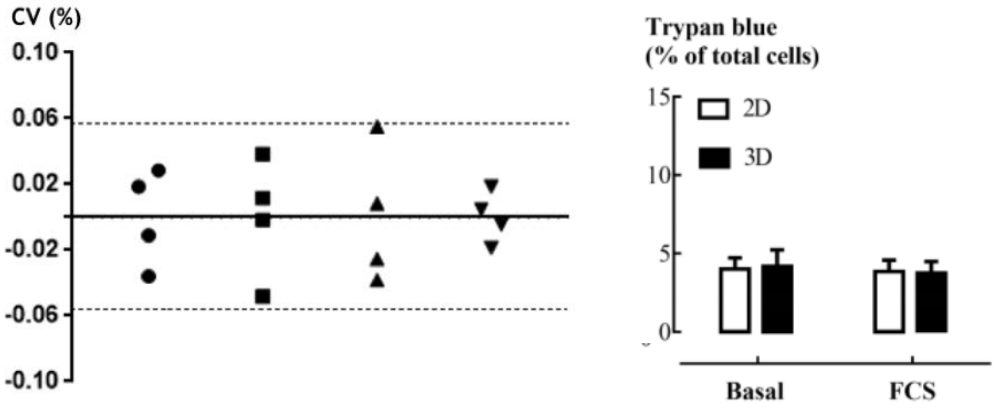

Figure 6.5. (left) Coefficient of Variation CV(%), on four different donors. Each data point represents the aspiration of a single spheroid. (Right) Cell viability does not change between 2D and 3D cultures (A. Mitke et al., 2017).

6.5.4 Stiffness and Viscosity of Mesenchymal Cell Spheroids

From the previous section, we can conclude that step-by-step aspiration of mesenchymal cells is not only a much faster method of characterization, but the results showed high reproducibility and low variation of the numerical values. Using this methodology, we proceed to evaluate the average stiffness of HASM and pFb spheroids. *Table 6.1* and *Table 6.2* present the values of the mechanical properties of HASM and pFb aggregates. The Young's Modulus was determined by the average results from four different experiments using cells from different donors (biological replicates). It is quite interesting to observe they are quite soft with an average stiffness of 0.21 ± 0.03 kPa for pFb and 0.17 ± 0.02 kPa for HASM spheroids. The stiffness values are in the same order of magnitude as single cells, and approximately one order of magnitude softer than lung tissue. These soft environments represent *in vivo* tissue, as standard 2D plates can reach stiffness of 1GPa, which are a thousand orders of magnitude stiffer.

Table 6.1. Elastic properties of single cells, spheroids and lung tissue by micropipette aspiration.

	Single cell [kPa]	Spheroid [kPa]	Aspirated lung tissue stiffness	Average stiffness native normal lung by AFM
Parenchymal fibroblast	0.13 ± 0.02 (Keenan et al., 2018)	0.21 ± 0.03	1.33 ± 0.25	1.96 ± 0.13 kPa (Booth et al., 2012)
Airways smooth muscle	0.11 ± 0.02	0.17 ± 0.02		

Table 6.2. Viscoelastic properties of single cells, spheroids and lung tissue by micropipette aspiration.

	Spheroid viscosity coefficient (μ) [Pa s]	Time constant (τ) [s]	Native normal lung viscosity (τ) [Pa s]
Parenchymal fibroblast	0.6211 ± 0.23	33 ± 8.6	3.0 [Saini et al. 2010]
Airways smooth muscle	0.9318 ± 0.17	26 ± 7.1	

6.6 Discussion

In contrast to the liquid-like behaviour observed in spheroids from other cell types, we have found that mesenchymal cells form spheroids of regular spherical shape with elastic surface. Cell aggregates under low adhesion conditions form a structure in which the stress is evenly distributed around the spheroid. Such elastic structure is mechanically sustained by the cells on the outer shell of the spheroids that are organized into layers. These cells are largely stretched, a morphology mostly observed in 2D cultures but not in spheroids. This is schematically shown in *Figure 6.6*.

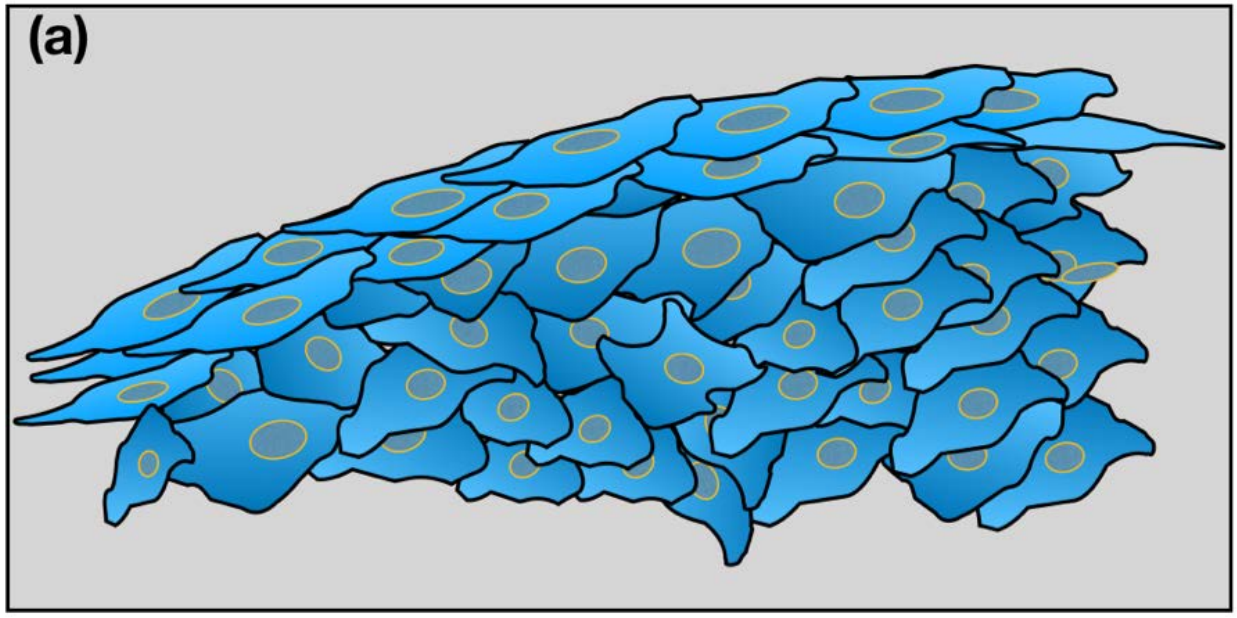

Figure 6.6. Schematic of a spheroid cross-section. Cells in the top layer (light blue) are fully stretched, while cells inside show asymmetrical assembly, but still form a cohesive structure. As observed by SEM and TEM, the top-most layers show stretched cells.

These unique characteristics makes mesenchymal spheroids an ideal model for the study of mechanical properties of cell aggregates. Previous studies have shown the creep and stress relaxation test can be used to determine the viscosity and infer the Young's modulus in liquid-like viscoelastic spheroids (Guevorkian et al., 2010; Guevorkian & Maître, 2017). However, the relaxation test requires extensive amounts of time, and limiting the number of samples that can be evaluated.

Our results show that the measured Young's modulus using step-by-step aspiration is highly reproducible between spheroid replicates. Repeated aspiration of the same spheroid in different sections will give Young's modulus with a variation of less than 3%, which confirms the uniform elastic behaviour around the spheroid. Technical replicates obtained by aspirating spheroids from the same donor and passage show a variation of Young's modulus of less than 5%, which is particularly remarkable as other standard biological techniques, like PCR, can have amplification variances from 60% to 100% (Rao, Huang, Zhou, & Lin, 2013). Furthermore, the technical replicates showed a high reproducibility, allowing us to determine

changes in Young's modulus with more precision. This is important as we compare Young's modulus of spheroids from different donors, thus keeping the biological replicates as minimum as possible.

6.7 Conclusions

This study demonstrates a reliable method to characterize the stiffness and viscoelastic properties of mesenchymal cell spheroids. Although micropipette aspiration is commonly used to determine the mechanical properties of a single cells, to the best of our knowledge, this is the first study which presents an accurate and efficient method to determine the Young's modulus of cell aggregates with step-by-step aspiration. Mesenchymal spheroids are observed to assemble into highly regular spherical shapes with cells stretched on the outer layers, creating a surface that evenly bears the mechanical load given their exceptional elasticity

Additionally, to establish the micropipette aspiration assay as a medium-throughput method for spheroids, Young's modulus determination (step-by-step) and viscoelastic characterization (creep tests), have been developed to automate and optimize the image analysis.

Chapter 7: Applications of 3D Spheroids in the Study of Idiopathic Pulmonary Fibrosis

7.1 Foreword

In Chapter 6, we have shown that the study of spheroids helped analyze the characteristics of fibroblasts and potential in drug testing assays. Idiopathic Pulmonary Fibrosis is a disease that has not had an effective treatment for the past 80 years, hence the significance of this study. The novel compound PF670462 was tested, and our results demonstrate that it is a promising treatment for IPF, since, for example, it softens the fibroblast spheroids. This chapter includes rewritten parts of the published study below:

Keenan, C. R., Langenbach, S. Y., **Jativa, F.**, Harris, T., Li, M., Chen, Q., ... & Prodanovic, D. (2018). Casein kinase 1δ/ε inhibitor, PF670462 attenuates the fibrogenic effects of Transforming Growth Factor-β in pulmonary fibrosis. *Frontiers in Pharmacology*, *9*, 738.

7.2 Abstract

Idiopathic Pulmonary fibrosis (IPF) is a devastating fibrotic disease with few treatment options and still not well understood. In this study, we aimed to evaluate the use of three-dimensional parenchymal fibroblast aggregates for the study of IPF disease. It was found that spheroids that came from IPF donors presented an increase in stiffness, and showed structural changes as collagen deposition. PF670462 was evaluated as potential treatment for IPF disease and it was found it caused a softening in IPF spheroids, as well as inhibit the fibrogenic gene expression in 2D and 3D culture systems. This research also show that micropipette aspiration of cell aggregates is an effective medium-throughput tool for drug screening.

7.3 Introduction

For over 80 years idiopathic pulmonary fibrosis (IPF) has challenged the medical community by the lack of an effective pharmacologic treatment. For decades, standard therapy was based on the disproved hypothesis that IPF is an inflammatory disorder (G. Raghu et al., 2011) Therefore corticosteroids and other drugs that have anti-inflammatory and immunosuppressive actions were commonly used (Alastair G. Stewart et al., 2017). Standard treatment just a decade ago would have included a mix of prednisone, azathioprine and acetylcysteine. Clinical trials would now show that this combined therapy only increases mortality rates. Further trials of other potential treatments including "interferon gamma, endothelin receptor antagonists, warfarin, etanercept, imatinib, and N-acetyl-cysteine monotherapy" (Ganesh Raghu & Selman, 2015, p. 253) would also give negative results (Idiopathic Pulmonary Fibrosis Clinical Research et al., 2012; Ganesh Raghu & Selman, 2015).

It was only in 1999 when the first reports emerged of a new drug, pirfenidone, which has potential beneficial effects on IPF treatment (Idiopathic Pulmonary Fibrosis Clinical Research et al., 2014). Positive results of subsequent clinical trials led to its authorization as a therapeutic treatment a decade later (Noble et al., 2011; Taniguchi et al., 2010). At the same time another drug, Nintedanib, also passed clinical trials and by 2014 both pharmacologic agents became an available option for the treatment of IPF (Richeldi et al., 2011; Richeldi et al., 2014).

Although there is a lot of interest in these two antifibrotic agents, IPF disease biology is still poorly understood. Pirfenidone shows suppression of both TGF-β production and over-expression of collagen I and II genes, while Nintedanib is a tyrosine kinase inhibitor which interferes with fibroblast proliferation, migration and differentiation, and the secretion of extracellular matrix (ECM). Both drugs exhibit inflammatory and antifibrotic effects, but their

exact mechanism of action is unknown. Lastly, although these drugs slow the progress of the disease, there is still no available cure for IPF.

Thus, the development of new methods for the study of IPF disease is critical, as it will ultimately lead to a more effective drug discovery (Berhan et al., 2020; A. B. Mitke, Harris, Schuliga, et al., 2018). Traditional 2D *in vitro* settings have proved to be limited only in exploring key markers of the disease such as collagen deposition and tissue stiffening (A. B. Mitke, Harris, Langenbach, et al., 2018; A. Stewart et al., 2019; Alastair G. Stewart et al., 2016). The aim of this chapter is to ascertain the comparative use of 3D fibroblast aggregates as a tool for the study of IPF disease and in drug screening. These micro-tissue structures may provide better modelling of disease processes than animal models or conventional 2D plastic culture because of their innate similarities (A. Mitke et al., 2017). Furthermore, the mechanical properties, *i.e.* stiffness, are also evaluated for spheroids derived from different donors and treatments.

7.4 Material and Methods

7.4.1 Cell Culture

We cultured primary human parenchymal fibroblast cells (pFbs) that came from parenchyma of lung resection specimens from non-transplanted lungs of donors that had no chronic respiratory disease and those of IPF patients diagnosed by multidisciplinary review (HREC #336/13; Alfred Hospital, Melbourne 106 VIC, Australia), as previously described (M. Schuliga et al., 2017; M. J. Schuliga et al., 2009).

Table 7.1 describes donor characteristics of specimens used for cell culture. pFbs were passaged in Dulbercco's Modified Eagle's Media (DMEM); they consisted of 10% (v/v) heat-inactivated fetal calf serum (FCS), 15mM HEPES, 0.2% (v/v) sodium bicarbonate, 2 mM L-glutamine, 1% (v/v) non-essential amino acids, 1% (v/v) sodium pyruvate, 2.5 μg/mL amphotericin, 5 IU/mL penicillin and 50μg/mL streptomycin. Primary fibroblast 3D spheroids

were created by seeding cells into 96 well round bottom plates coated with 0.5% poly(2-hydroxyethyl methacrylate) (poly(HEMA)) to decrease cellular adhesion to plastic, and by incubating cells to permit aggregation into cellular spheroids for 24-48 h.

Before the experiment, we incubated pFb cells in serum-free DMEM that consisted of 0.25% bovine serum albumin (BSA) and insulin-transferrin-selenium–containing supplement (Monomed A; CSL, Parkville, Melbourne, Australia). Where indicated, cells were treated first with PF670462 (3μM) (Abcam, Australia) prior to 100 pM TGF-β1 (R&D Systems, Minneapolis, MN).

Table 7.1. Donor characteristics for human primary fibroblast cultures

Age	**Sex**	**Forced expiratory volume (FEV1) (% pred)**	**Forced vital capacity (FVC) (%pred)**	**Transfer factor for carbon monoxide (TLCO) (% pred)**	**Smoking History (pack yrs)**
50.2 ± 14.6 (mean ± SD)	7M/5F/1 unknown	*unknown*	*unknown*	*unknown*	*7 unknown; 5 ex; 1 current*
58.0 ± 8.2 (mean ± SD)	7M/1F	53.8 ± 16.2 (mean ± SD)	48.7 ± 18.6 (mean ± SD)	22.0 ± 9.4 (mean ± SD)	2 Never/4 ex/2 unknown

7.4.2 Single Cell and Spheroids Stiffness Measurement

As in previous chapters, to calculate the Young's tensile modulus (E) of spheroids, the micropipette aspiration method was utilized, as seen in literature (Guevorkian et al., 2010; Michael Schuliga et al., 2013). For the evaluation of the stiffness of each fibroblast cell, this was done with the ensuing detachment from plastic culture vessels utilizing trypsin. The method itself of micropipette aspiration was carried out in a temperature control chamber (Warner Instrument CL-100) so that cells would be kept at 37°C. To avert cell attachment, the tips of the custom-tailored glass micropipettes (8 μm diameter), were pre-coated using silicone Sigmacote (Sigma, UK). By regulating the water elevation in a water repository, suction pressure was enforced to the aggregate. This suction pressure was enforced in 1cm H_2O (0.098kPa) additions while also maintaining it constant for 60s at every addition. The highest suction pressure was 6cm H_2O (0.588kPa). To calculate the aspirated length in the micropipette, a brightfield image made with a Leica DMI6000B microscope at the stop of every pressure

addition was used. The cell stiffness was computed with a model that accepts the cells as a consistent, isotropic, flexible, and incompressible half-space medium (Theret et al., 1988). To obtain the Young's Modulus E, Equation 7.1 was used, where Ri is the inner radius of the micropipette and L the aspiration length. ΔP illustrates the aspiration pressure and ϕ is the wall function with a usual value of 2.1 (Hochmuth, 2000).

$$E = \frac{3\,\Delta P\,R_i}{2\,\pi\,L\,\Phi_{(\eta)}}, \text{ with } \quad \eta = \frac{R_o - R_i}{R_i} \qquad \text{(Equations 7.1 \& 7.2)}$$

7.4.3 Immunohistochemistry

Paraffin-embedded IPF and non IPF lung tissue was obtained from Alfred Health from the Alfred Tissue Biobank for Interstitial Lung Disease (HREC#336/13, Alfred Hospital, Melbourne, Vic, Australia). Idiopathic pulmonary fibrosis was pathologically diagnosed by multidisciplinary review as previously described (M. Schuliga et al., 2017; M. J. Schuliga et al., 2009). Sections were counterstained with haematoxylin (Grale Scientific, Australia).

On serial sections, a Masson's Trichrome stain was also performed to provide indicative levels of fibrosis in IPF and non-IPF sections the reagents required contain Bouin's fixative solution Scott's tap water, Mayer's Haematoxylin, Trajan Scientific; Celestine Blue, Biebrich Scarlet/Acid Fuchsin; Phosphotungstic acid, Sigma; Aniline blue solution (aust biostain)

Spheroids were fixed in 10% neutral buffered formalin (Grale Scientific) during 10 min and rinsed twice by PBS. After fixation, spheroids were embedded into a 3% agarose solution and processed overnight into paraffin. Sequential 3 µm sections were stained with Mayer's Haematoxylin and Eosin (Trajan Scientific, Australia). A Masson's Trichrome stain was also performed.

7.4.4 Immunofluorescence

pFB cells for immunofluorescence staining were seeded in 96 well plates (conning) and left to adhere overnight. Cells were then serum-starved for 16 h prior to pre-incubation with

TGF-β (100 pM) for 48 h. Spheroids were cultured for 48 hours as described previously. For F- and G-actin staining, cells were rinsed twice with PBS. Then they were fixed in 10% (v/v) neutral buffered formalin (NBF) during 15 minutes and permeabilized with 0.2% (v/v) Triton X-100 during 5 minutes. After rinsing in PBS, cells were blocked with 0.1% Triton X-100 in 1% BSA/PBS solution for 15 minutes, and then stained with Oregon green 488 (green) phalloidin (1:50, Invitrogen Molecular Probes, #O7466) and Alex-Fluor 594 (red) deoxyribonuclease I (DNase I)-texas red conjugate (10mg/ml, Invotrogen Molecular Probes, #D12372) during 20 minutes at environmental temperature. In these circumstances, phalloidin and DNase I bind F- and G-actin were used. We stained the nuclei with DAPI (1:100 in PBS) during 10 minutes. Spheroids were mounted using DAKO fluorescent mounting media, while cells and analyzed utilizing a Zeiss fluorescence microscope-live cell imaging system.

7.4.5 Gene Expression

Total RNA was removed from cultured cells using RNAspin Mini RNA Isolation Kit (GE Healthcare). RNA extracts were reverse transcribed into cDNA using High-Capacity RNA-to-cDNA Kit (Applied Biosystems). Real-time PCR was then performed using a QuantStudio 6 Flex Real-Time PCR System using iTaq Universal SYBR green supermix and the following thermal protocol: 50°C (2 min), 95°C (10 min), then 40 cycles of 95°C (15 sec), 60°C (1 min). The threshold cycle (CT) values obtained for target genes were normalized against those obtained for 18S ribosomal RNA (18S rRNA), which was contained as internal control. The generation of specific PCR products was settled by dissociation curve assay. Primer sequences used are shown in Table 7.2 (Keenan et al., 2018).

Table 7.2 *Human primer sequences for RT-qPCR*

Gene	Forward Primer	Reverse Primer
18S rRNA	CGC CGC TAG AGG TGA AAT TC	TTG GCA AAT GCT TTC GCT C
COL1A	GTG CTA AAG GTG CCA ATG GT	ACC AGG TTC ACC GCT GTT AC
CTGF	TGT GTG ACG AGC CCA AGG A	TCT GGG CCA AAC GTG TCT TC
IL-6	AGCTCTATCTCGCCTCCAGGA	CGCTTGTGGAGAAGGAGTTCA

7.5 Results and Discussion

7.5.1 The Stiffness of IPF Spheroids

A 3D *in vitro* model was grown from primary cells that came from IPF donors and non-diseased controls. The cells formed spheroids and were incubated for 48 h. Most restructuring happened in the first 24 h, and there was the least amount of change in the volume of the spheroid in the next 24 h. The size of spheroids from both IPF and non-diseased control donors was the same all throughout the process of spheroid remodelling.

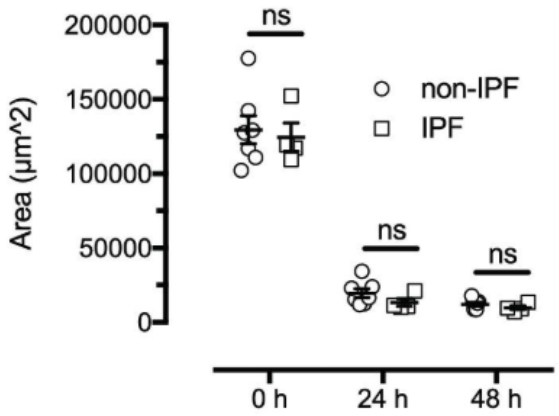

Figure 7.1. Formation and morphology of fibroblast spheroids. The spheroids remodel over the first 24 h since formation assuming a smaller and consistent volume by 48 h. (A) The IPF derived spheroids (n = 4) remodel and assume a similar volume to fibroblast spheroids from non-IPF donors. Adapted from Christine R. Keenat et al., (2018).

Fibroblasts that come from non-diseased and IPF patients are reactive to the stiffness of their mechanical microenvironment, particularly in the contractile and proliferative phenotype seen the moment cells touch stiffer extracellular matrix (Marinkovic, Liu, & Tschumperlin, 2013). To calculate stiffness, cells and spheroids was aspirated into the barrel of a micropipette with a pressure gradient as shown in Fig 7.2. When there is less displacement into the barrel for a specific amount of pressure, the material is considered stiffer. No difference was found in the mechanical stiffness of each cell that came from either IPF or non-IPF donors. However quite interestingly, cell spheroids that were derived from IPF donors displayed significantly higher stiffness than those from non-IPF donors; this suggests that the stiffness is an emerged characteristic that could improve the pro-fibrotic phenotype of these cells if cultured as spheroids. Additionally, since TGF-β induces fibrosis through both the activation of fibroblasts and the expression of ECM genes (Leask & Abraham, 2004), we next sought to establish whether spheroids will show similar changes. Exposure to the fibrogen TGF-β for 48 h increased the stiffness of non-IPF spheroids ($P < 0.05$, $n = 5$), but the stiffness is still not as high as that of the IPF spheroids.

Pre-treatment with the drug PF670462 (3 μM) 30 min prior to TGF-β exposure diminished the amount of stiffness in IPF spheroids ($P < 0.05$, $n = 6$). Hence, PF670462 softens IPF fibroblast spheroids and by that conceivably intervenes with the positive-feedback cycle of stiffness-induced stiffening (Keenan et al., 2018).

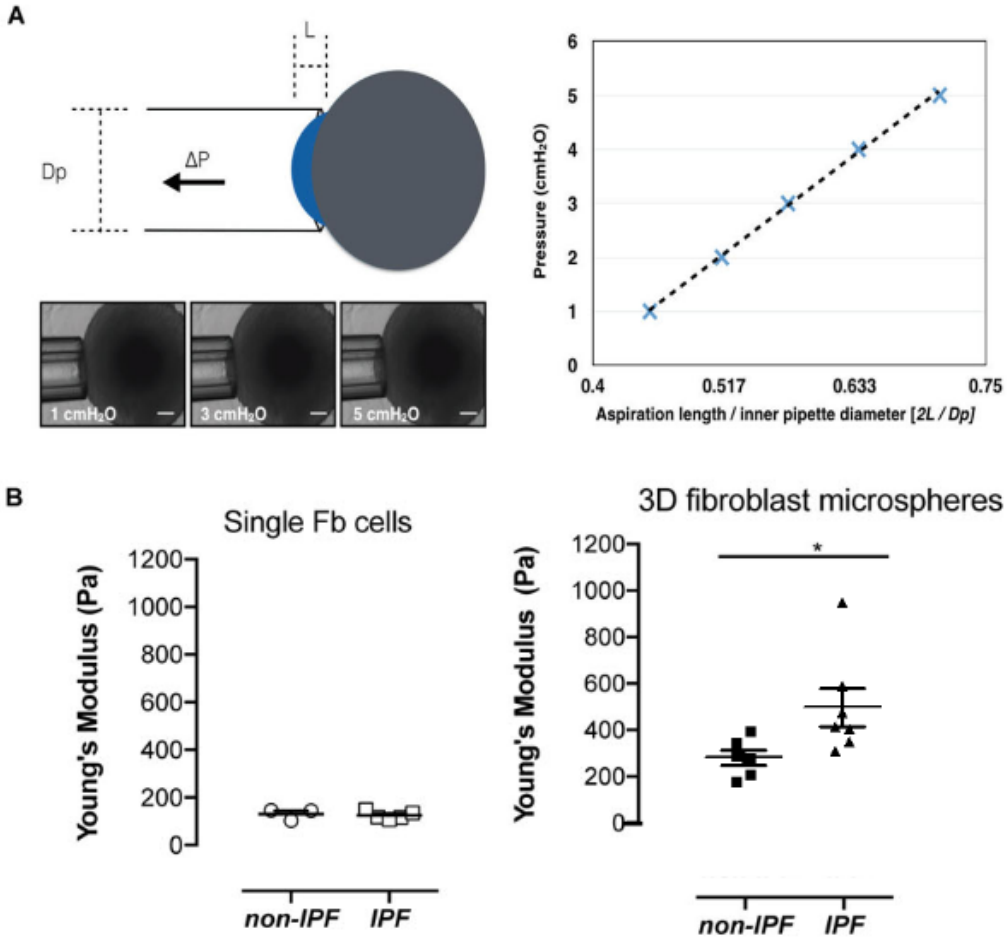

Figure 7.2. (A) Measurement of Young's modulus. With increasing pressure (P) the spheroid travels a distance (L) through the micropipette barrel of inner diameter (Dp). A representative spheroid is shown with aspiration at 3 different pressures. The normalized distance (2L/Dp) is linearly related to the applied pressure and the slope of the linear regression defines the Young's modulus. Scale bars indicate 100 µm. (B) Spheroid stiffness was measured by micropipette aspiration and quantified to measure the Young's Modulus of stiffness in single cells (non-IPF, n = 3; IPF, n = 5) and in spheroids (non-IPF, n = 6; IPF, n = 6) Adapted from Keenan, C et *al.*, (Keenan et al., 2018).

7.5.2 Morphology of Human Fibroblast Spheroids from IPF and non-IPF patients

Spheroids and 2D cultures were stained to observe their internal structure. Haematoxylin and eosin staining showed differences in morphology, whereby IPF spheroids had an increased interstitial area in between cells, similar to the scarring found in in IPF patients. Massons's Trichrome staining was also performed in both IPF and non-IPF spheroids and lung parenchyma. The preliminary results show that IPF spheroids show an increase in collagen, similarly to those found in IPF patients as seen in *Figure 7.3*. This increase in collagen

production might also explain the increase in IPF spheroid stiffness shown in the previous section.

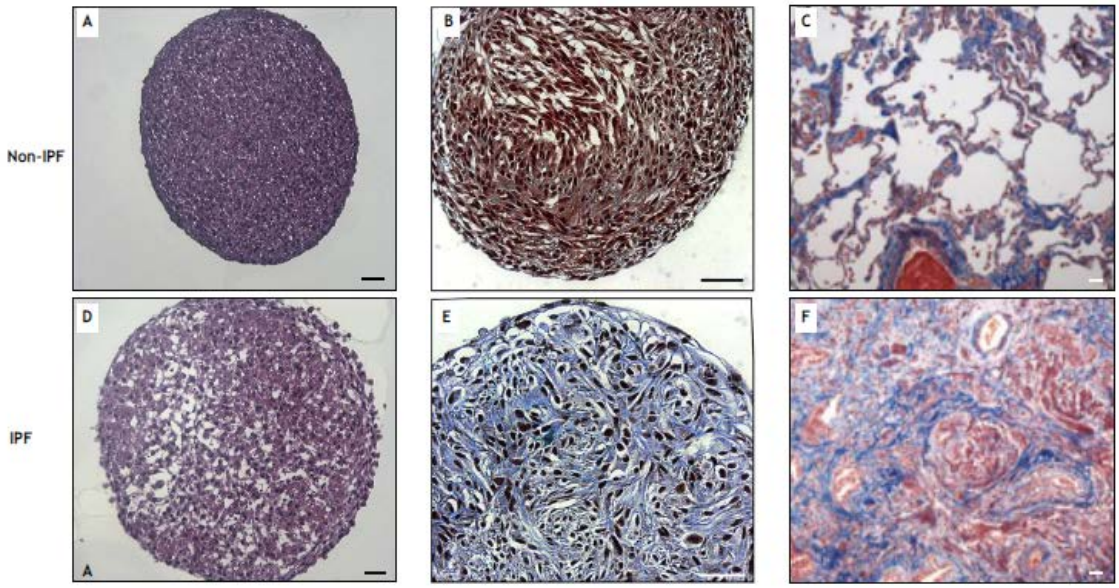

Figure 7.3. Collagen deposition in spheroids and parenchymal tissue from non-IPF and IPF donors (A-D) Histology image of spheroid sections with H&E staining. Scale bar = 20 µm. (B-E) Masson's Trichrome stain in both IPF and non-IPF spheroids and (C-F) lung parenchyma. Increased blue color signifies increased collagen production. Scale bar=20 µm.

Spheroids and 2D cultures were stained with fluorescence dyes to observe F/G actin as well as the nucleus following the protocol as described in the methodology. *Figure 7.4* show IPF and non-IPF actin distribution. Preliminary results exhibited similar distributions of actin in 2D cultures, whereas spheroids show an increase of fibrillar actin (*Figure 7.4*). The presence of a network formation inside the spheroids was also observed. These imply that actin, in addition to collagen, plays a role in the increased stiffness observed in the IPF

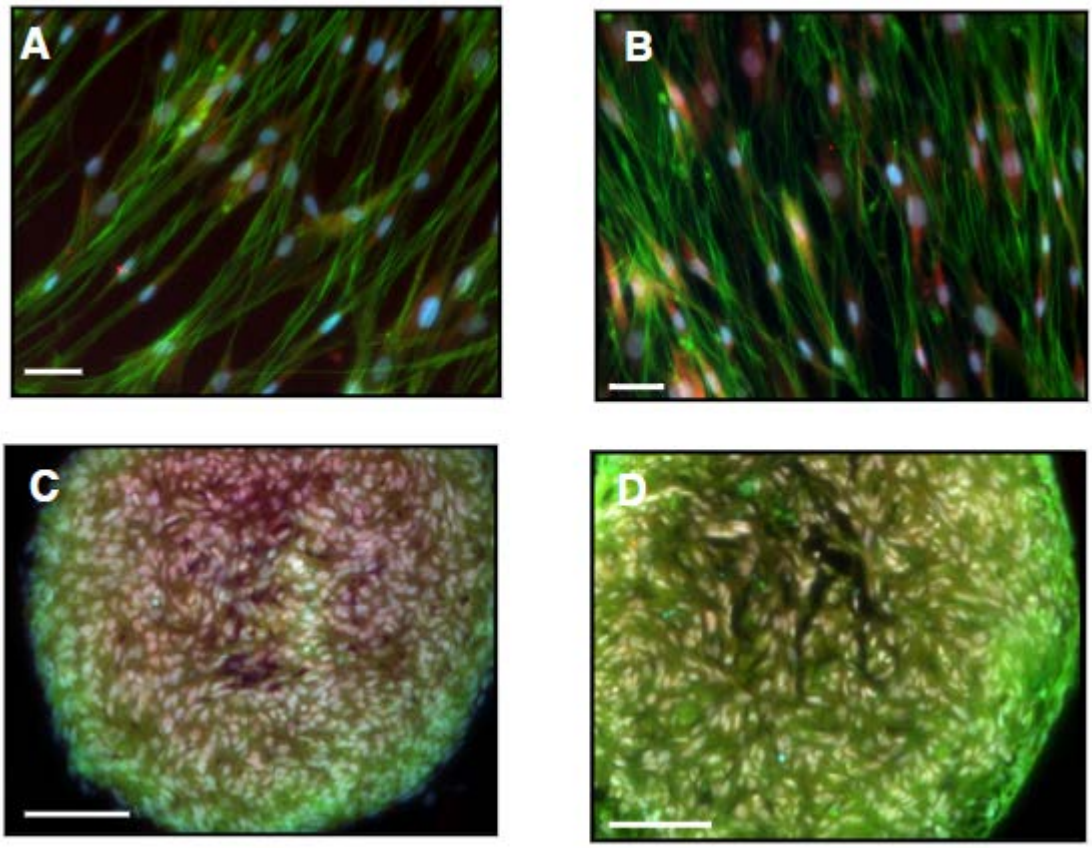

Figure 7.4. F-G actin fluorescence staining of non-IPF and IPF cells in (A-B) 2D culture, and (C-D) spheroids. Scale bar 10 µm and 50 µm respectively. Filamentous Actin Green, Globular Actin Red and Nuclei blue.

7.5.3 Softening of Fibrotic Spheroids Using Drug Treatment

In the previous sections, we showed that exposure to the fibrogen TGF-β for 48 h increased the stiffness of non-IPF spheroids ($P<0.05$, $n=6$) but not to the level of stiffness of IPF spheroids. In contrast, single cells of IPF and non-IPF donors showed no differences in stiffness. Pre-treatment of primary pFb spheroids with PF670462 (3 µM) for 30 minutes prior to TGF-β exposure reduced the level of stiffness in non-IPF spheroids ($P<0.05$, $n=7$) (*Figure 7.5A*).

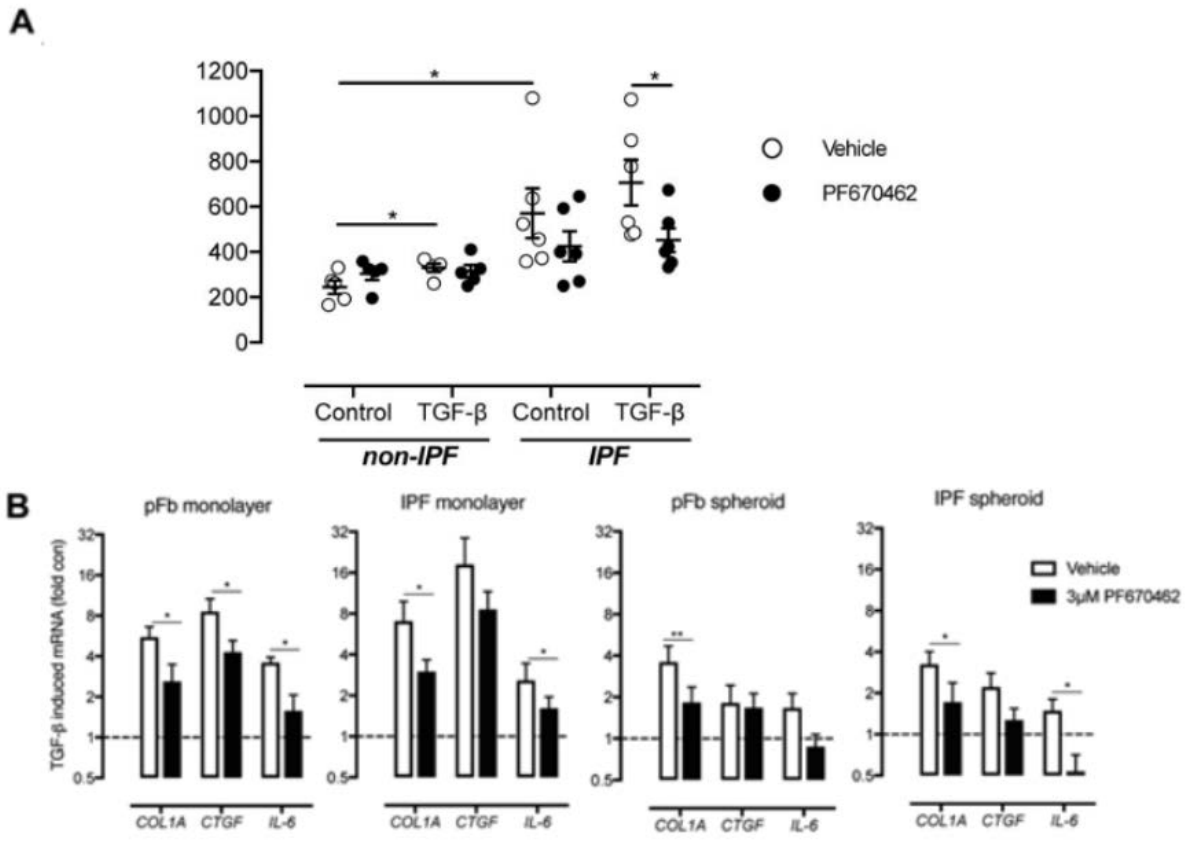

Figure 7.5. Effect of PF670462 stiffness and fibrogenic gene expression of primary human parenchymal fibroblasts (pFb) cells. (A) Spheroids were generated from IPF and non-IPF pFbs and incubated with PF670462 for 30 min prior to TGF-β stimulation for 24 h. Spheroid stiffness was measured by micropipette aspiration. (B) Gene expression of pFb monolayers and spheroids was measured by RT-qPCR after 24 h TGF-β. Adapted from Christine R. Keenat et al., (Keenan et al., 2018)

It was also found that TGF-β increased mRNA expression of the fibrogenic genes COL1A, CTGF and IL-6 in pFb monolayers and spheroids from IPF and non-IPF donors (*Figure 7.5 B*). However, the spheroids showed lower levels of TGF-β induction of fibrogenic genes compared with fibroblast cell monolayers. IPF cultures showed enhanced induction of the genes COL1A and CTGF, whereas IL-6 induction was comparable with non-diseased controls (*Figure 7.5* B). Pre-treatment with PF670462 inhibited the TGF-β-induced increase in COL1A and IL-6 mRNA in fibroblast monolayers and spheroids from both IPF and non-diseased control donors (*Figure 7.5* B). CTGF induction was attenuated in fibroblast monolayers from non-diseased controls but was not markedly altered by PF670462 treatment in IPF cultures or control spheroids (*Figure 7.5* B).

Fibroblasts from normal and IPF patients are known to be responsive to the stiffness of their mechanical microenvironment, with increases in contractile and proliferative phenotype observed when cells are in contact with stiffer extracellular matrix (Jaffar et al., 2018). More importantly, whilst we saw no difference in mechanical stiffness in individual cells derived from IPF or non-IPF donors, cell spheroids generated from IPF fibroblasts showed significantly higher stiffness compared to non-IPF donors, suggesting that the stiffening is an emergent property that may enhance the pro-fibrotic phenotype of these cells. PF670462 softened the spheroids from IPF donors, suggesting that this compound may interrupt the positive-feedback cycle. The effect of a stiff microenvironment may also explain the greater TGF-β-induced fibrogenic gene levels in fibroblast monolayers on supra-physiologically stiff plastic, compared with that in spheroids. PF670462 consistently inhibited gene activation, regardless of the environmental stiffness.

7.6 Conclusion

In conclusion, we found that 3D parenchymal fibroblast spheroids are a useful tool to study Idiopathic Pulmonary Fibrosis. Fibroblast spheroids mimic a few of the significant properties of fibrotic tissues within IPF lungs (*i.e.*, higher levels of active TGF-β, incremented collagen and actin production, and increased stiffness). Furthermore, stiffness analysis allowed the drug screening of both commercially available and novel compounds. Specifically, this was explored in a new compound, PF670462, as a potential target for disease treatment. It was found that PF670462 softens primary human fibroblast spheroids from IPF donors and inhibits the TGF-β-induced gene expression of fibrotic genes. Therefore, fibrotic fibroblast spheroids might serve as a new analysis system for pre-clinical drug testing, and warrants further investigation.

Chapter 8: Conclusions

Self-assembly has certainly proven to be the basis in pattern structuring in several fields. This research aimed to assess the self-assembling mechanism of cellulose and silk through droplet diffusion; to measure the self-assembling of mesenchymal cells and with this to design a testing procedure to characterize cell aggregates; and to evaluate the functions of cell aggregates as a tool in diseases and drugs discovery.

8.1 Evaluating the Self-assembling Process of Silk and Characterizing the Obtained Structures.

Silk is a natural polymer that presents a wide range of properties, which applies to many fields other than the textile industry. For instance, it is used in the biomedical field for drug delivery. Controlled droplet diffusion was discovered to be an efficient way to obtain silk spheres with customizable surface microstructures. The key to fine-tune the morphology and transparency of the surface is in the ratio of the cosolvent and antisolvent in the surrounding phase. All in all, there were two phases, one of volume expansion and the other of droplet dissolution. The volume expansion was influenced by the percentage of ethanol in the surrounding phase. Upon immersion in the solution, the droplet intakes the organic phase, which showed significant influence on the stability and arrangement of the silk in the later phase of the droplet dissolution. A substantial increase in the droplet volume by 16% was observed at 2% ethanol concentration. The most significant droplet expansion was observed in 10% ethanol solution, reaching up to ~80% volume increase. However, at ethanol concentrations below 1%, there was no significant expansion observed. That is, at low concentrations of the cosolvent, the initial volume expansion from solvent intake is less and the subsequent dissolution rate is also slower. The as-prepared sphere acquired less rough surface and exhibited switchable transparency. It is important to note that when the dissolution started, there was a linear relationship between the droplet radius and the dissolution time. The

dissolution rate increased by ~8 times as the concentration of ethanol in the surrounding phase increased from 0.5 to 5%. These results suggest that both the expansion and dissolution rate of the droplet is finely tuneable by the concentration of ethanol in the bulk phase. At high concentrations of the antisolvent and fast expansion–dissolution rates, a thin shell of the precipitated protein formed, wrapping around the droplet. Wrinkling and crumpling of the shell with droplet dissolution gave rise to the ridges and crevices on the surface of the assembled silk spheres. The process based on the droplet dissolution is simple, versatile, and effective in tuning the detailed surface microstructures of a silk sphere.

We have also shown the transparency of the obtained silk spheres by varying the concentration of ethanol in the binary solution. The micro-spectrophotometry measurements of the as-prepared spheres show that the transmittance increases in the visible spectrum between 400 and 700 nm for both spheres. For the sphere prepared in 1% ethanol, the transmittance is above 75% at a wavelength longer than 500 nm and has a transparent appearance, whereas the sphere from 5% ethanol solution remained below 20% transmittance within the visible spectrum and has a white color. The interior of the sphere displayed a solid, uniform architecture when sectioned. Spheres prepared in 5% and 7% ethanol are non-transparent and their morphological formations are distinct. The sphere surface presented uniformly-distributed crevices and ridges which were about ~500 nm. Both spheres prepared under varying ethanol concentrations could have significant applications. The transparent spheres may be used as an optical element while the opaque spheres may be potentially used as microcarriers owing to their customizable porosity.

8.2 Evaluating the Self-assembling Process of Cellulose and Characterizing the Obtained Structures.

Cellulose is the most common renewable organic matter on Earth. There is a myriad of by-products from cellulose that can be used in different fields but in particular, nanocellulose is amongst the derivatives that has shown a variety of mechanical properties with important applications. In this study, the self-assembly of cellulose nanocrystals (CNC) in shrinking droplets was analyzed in relation to the water dissolution rate while immersed in a binary toluene-ethanol mixture. The dissolution rate of the CNC droplet strongly depends on the composition of the bulk liquid. We have demonstrated that the droplet shrinkage rate greatly increases with the ethanol concentration in the surrounding toluene solution. The droplets initially expand due to the active uptake of ethanol into the aqueous CNC dispersion. After the initial expansion, the size of the droplet decreases steadily until the shrinkage is hindered by the assembled CNC rods. As to the obtained structures; the nanocrystals had a length dispersion of 264 ± 118 nm and a width distribution of 2.9 ± 1.3 nm. The crystals were comprised of tightly arranged β (1-4) linked D-glucose chains. The rate of the dissolution relies on the ratio of the liquids in the mixture, thus if the ratio of the liquids is regulated, the morphology of the spheres can also be controlled. The shrinkage of the droplets was observed as a function of the linear decline of its radii.

Electron microscopy images revealed the morphology of the assembled structures. Dense spheroid beads were produced at low dissolution rate or collapsed discoidal particles at high water removal rates. That is, CNC assemblies formed in <5 vol% ethanol have an oblate, ellipsoid-like shape while the assemblies formed at higher ethanol concentrations (>10 vol%) have a collapsed, discoidal shape. The average diameter of the dry, oblate microbeads is ~300–800 μm, which corresponds to a final volume about 1–10% of the initial droplet volume. The final microbead size depends on the initially dispensed droplet volume and on the ethanol

concentration, generally resulting in smaller microbeads at low shrinkage rates (*i.e.* low vol% EtOH). This process offers the opportunity to study the self-assembly in liquid crystalline CNC phases and create controlled microbeads in a confined space of isolated droplets. The ability to control the microbeads has to do with how the shrinkage rates vary by more than one order of magnitude. As to the microbeads, they had a final diameter that relied upon the starting allocated droplet volume and on the percentage of ethanol. If the shrinkage rates were low, the resulting microbeads were smaller.

It is noteworthy that the nematic microstructure of the assemblies seemed to be autonomous of the dissolution rate, presumably as a consequence of tactoids formation at the beginning of the dissolution phase. Self-assembling of CNCs in the confined space of isolated droplets not only provides fundamental insights in the structural evolution of liquid crystalline CNC phases but also offers precise nanostructures that can be advantageous for photonic or nano-technological applications, as well as for use as templates for scaffolds for tissue engineering.

8.3 Evaluating the Self-assembling Process of Mesenchymal Cells and Designing a Methodology for the Characterization of Cell Aggregates.

Cell aggregates are effective for determining cell-cell interaction, amongst others, that could help in the analysis of lung diseases. Prior to this research, the mechanical properties of mesenchymal cell spheroids had not been studied to date. We observed the self-assembling of cells into three stages. First, a fast assembling rate, followed by a transition stage with a lessening in the cell compressing pace, and where the spheroids assembled into a cohesive structure. In the final stage, there was an even slower assembling rate, which resulted in an elastic spheroid. Micropipette aspiration on mesenchymal cells also proved to be an effective technique to identify the characteristics of mesenchymal cell spheroids. Besides being compressed together, the cells were also stretched, which is close to an *in vivo* setting where

muscle cells stretch to produce tension. It is hypothesized that these cells regulate the elastic characteristics of the spheroid. Other cells within the spheroid were more circular and not as stretched. Moreover, the study on mesenchymal cells is the first of its kind that demonstrates an effective technique in which the Young's modulus can be easily determined with step-by-step aspiration. The standard coefficient of variation of the Young's modulus was very reproducible, with changes below ≥ 3% in elasticity all through the spheroid surface. The spheroids were seen assembling into highly consistent spherical forms. Image analysis was simplified by developing a custom software for micropipette aspiration, and establishing the assay as a medium-throughput technique for the determination of Young's modulus, and viscoelastic properties.

8.4 Potential Applications of Cell Aggregates as a Characterization Tool for Disease and Drug Discovery

It was discovered that 3D parenchymal fibroblast aggregates are helpful in the way we analyze Idiopathic Pulmonary Fibrosis. These spheroids mimic some of the mechanical properties of the fibroblasts present in IPF lungs. These include higher stiffness, increased levels of active TGF-β, and more attenuated collagen production. We found that spheroids from IPF donors exhibited an increase in stiffness as compared to non-IPF spheroids. The increased stiffness of IPF-derived spheroids was not evident when the stiffness of individual fibroblasts was compared, suggesting that intercellular interactions and ECM formation contribute to this emergent property of the IPF spheroid. In addition to stiffness changes, we also characterized changes in the ECM of 2D vs 3D cultures. Masson's trichrome of 2D culture plates show no increase in collagen deposition between non-IPF and IPF donors, while staining of some fixed sections of the spheroids showed a clear increase in collagen deposition in IPF spheroids. It was also observed that non-IPF spheroids seeded with low concentrations of collagen showed an increase in stiffness. Similarly, intensity phalloidin staining of F-actin in

2D plates showed no difference in intensity, while 3D sections showed an increase in F-actin for IPF spheroids.

Lastly, stiffness assay permits drug testing of new and commercially accessible compounds. The effect of novel casein kinase inhibitor, PF670462, for TGF- β modulation was evaluated and has shown to be a promising treatment for the illness. Exposure to the fibrogen TGF-β for 24 h incremented the stiffness of non-IPF spheroids; however, not to the level of stiffness of IPF spheroids. Spheroids were then treated with PF670462 (3 μM) for 30 minutes prior to TGF-β exposure. PF670462 was shown soften IPF fibroblast aggregates and also inhibit the stiffness increase in non-IPF spheroids. It also hindered the TGF-β-induced gene expression of fibrotic genes. Hence, fibrotic fibroblast spheroids might serve as a new analysis system for pre-clinical drug testing, and warrants further investigation.

Chapter 9: References

Achilli, T. M., Meyer, J., & Morgan, J. R. (2012). Advances in the formation, use and understanding of multi-cellular spheroids. *Expert Opin Biol Ther, 12*(10), 1347-1360. doi:10.1517/14712598.2012.707181

Aizenberg, J., Muller, D. A., Grazul, J. L., & Hamann, D. R. (2003). Direct fabrication of large micropatterned single crystals. *Science, 299*(5610), 1205-1208. doi:10.1126/science.1079204

Alhasan, L., Qi, A., Al-Abboodi, A., Rezk, A., Chan, P. P. Y., Iliescu, C., & Yeo, L. Y. (2016). Rapid Enhancement of Cellular Spheroid Assembly by Acoustically Driven Microcentrifugation. *ACS Biomater Sci Eng, 2*(6), 1013-1022. doi:10.1021/acsbiomaterials.6b00144

Alp, B., Andrews, J. S., Mason, V. P., Thompson, I. P., Wolowacz, R., & Markx, G. H. (2003). Building structured biomaterials using AC electrokinetics. *IEEE Eng Med Biol Mag, 22*(6), 91-97. doi:10.1109/memb.2003.1266052

Ambrosi, D., & Preziosi, L. (2009). Cell adhesion mechanisms and stress relaxation in the mechanics of tumours. *Biomech Model Mechanobiol, 8*(5), 397-413. doi:10.1007/s10237-008-0145-y

Anada, T., Fukuda, J., Sai, Y., & Suzuki, O. (2012). An oxygen-permeable spheroid culture system for the prevention of central hypoxia and necrosis of spheroids. *Biomaterials, 33*(33), 8430-8441. doi:10.1016/j.biomaterials.2012.08.040

Andrienko, D. (2018). Introduction to liquid crystals. *Journal of Molecular Liquids, 267*, 520-541. doi:10.1016/j.molliq.2018.01.175

Argatov, I., & Mishuris, G. (2016). Pipette aspiration testing of soft tissues: the elastic half-space model revisited. *Proc Math Phys Eng Sci, 472*(2193), 20160559. doi:10.1098/rspa.2016.0559

Aschenbrenner, E., Bley, K., Koynov, K., Makowski, M., Kappl, M., Landfester, K., & Weiss, C. K. (2013). Using the polymeric ouzo effect for the preparation of polysaccharide-based nanoparticles. *Langmuir, 29*(28), 8845-8855. doi:10.1021/la4017867

Aubry, J., Ganachaud, F., Cohen Addad, J. P., & Cabane, B. (2009). Nanoprecipitation of polymethylmethacrylate by solvent shifting: 1. Boundaries. *Langmuir, 25*(4), 1970-1979. doi:10.1021/la803000e

Baaijens, F. P., Trickey, W. R., Laursen, T. A., & Guilak, F. (2005). Large deformation finite element analysis of micropipette aspiration to determine the mechanical properties of the chondrocyte. *Ann Biomed Eng, 33*(4), 494-501. doi:10.1007/s10439-005-2506-3

Ban, T., Aoyama, A., & Matsumoto, T. (2010). Self-generated Motion of Droplets Induced by Korteweg Force. *Chemistry Letters, 39*(12), 1294-1296. doi:10.1246/cl.2010.1294

Ban, T., Yamada, T., Aoyama, A., Takagi, Y., & Okano, Y. (2012). Composition-dependent shape changes of self-propelled droplets in a phase-separating system. *Soft Matter, 8*(14), 3908 - 3916.

Battista, O. A., & Smith, P. A. (2002). Microcrystalline Cellulose. *Industrial & Engineering Chemistry, 54*(9), 20-29. doi:10.1021/ie50633a003

Behera, B. K., & Varma, A. (2019). Gasoline-Like Biofuel. In *Bioenergy for Sustainability and Security* (pp. 79-158): Springer.

Benkirane, M., Meignen, J. M., Boyer, J., & Verine, A. (1989). Lipoprotein lipase in rat heart--I. Characterization of tri-, di- and monoacylglycerol lipase activities in post-heparin effluents. *Comp Biochem Physiol B, 94*(1), 13-18. doi:10.1016/0305-0491(89)90003-5

Berhan, A., Harris, T., Jaffar, J., Jativa, F., Langenbach, S., Lönnstedt, I., . . . Stewart, A. G. (2020). Cellular Microenvironment Stiffness Regulates Eicosanoid Production and Signaling Pathways. *American journal of respiratory cell and molecular biology, 63*(6), 819-830. doi:10.1165/rcmb.2020-0227OC

Berkers, G., van Mourik, P., Vonk, A. M., Kruisselbrink, E., Dekkers, J. F., de Winter-de Groot, K. M., . . . van der Ent, C. K. (2019). Rectal Organoids Enable Personalized Treatment of Cystic Fibrosis. *Cell Rep, 26*(7), 1701-1708 e1703. doi:10.1016/j.celrep.2019.01.068

Bidhendi, A. J., & Korhonen, R. K. (2012). A finite element study of micropipette aspiration of single cells: effect of compressibility. *Comput Math Methods Med, 2012*, 192618. doi:10.1155/2012/192618

Bigioni, T. P., Lin, X. M., Nguyen, T. T., Corwin, E. I., Witten, T. A., & Jaeger, H. M. (2006). Kinetically driven self assembly of highly ordered nanoparticle monolayers. *Nat Mater, 5*(4), 265-270. doi:10.1038/nmat1611

Bignold, L. P. (2015). *Principles of Tumors*: Elsevier Science & Technology.

Bizik, J., Kankuri, E., Ristimaki, A., Taieb, A., Vapaatalo, H., Lubitz, W., & Vaheri, A. (2004). Cell-cell contacts trigger programmed necrosis and induce cyclooxygenase-2 expression. *Cell Death Differ, 11*(2), 183-195. doi:10.1038/sj.cdd.4401317

Blake, A. J., Champness, N. R., Hubberstey, P., Li, W.-S., Withersby, M. A., & Schröder, M. (1999). Inorganic crystal engineering using self-assembly of tailored building-blocks. *Coordination Chemistry Reviews, 183*(1), 117-138. doi:10.1016/s0010-8545(98)00173-8

Blumlein, A., Williams, N., & McManus, J. J. (2017). The mechanical properties of individual cell spheroids. *Sci Rep, 7*(1), 7346. doi:10.1038/s41598-017-07813-5

Boden, N. (2003). *Molecular Self Assembly: The Future*: IOSS Press.

Boles, M. A., Engel, M., & Talapin, D. V. (2016). Self-Assembly of Colloidal Nanocrystals: From Intricate Structures to Functional Materials. *Chem Rev, 116*(18), 11220-11289. doi:10.1021/acs.chemrev.6b00196

Boncheva, M., Andreev, S. A., Mahadevan, L., Winkleman, A., Reichman, D. R., Prentiss, M. G., . . . Whitesides, G. M. (2005). Magnetic self-assembly of three-dimensional surfaces from planar sheets. *Proc Natl Acad Sci U S A, 102*(11), 3924-3929. doi:10.1073/pnas.0500807102

Booth, A. J., Hadley, R., Cornett, A. M., Dreffs, A. A., Matthes, S. A., Tsui, J. L., . . . White, E. S. (2012). Acellular normal and fibrotic human lung matrices as a culture system for in vitro investigation. *Am J Respir Crit Care Med, 186*(9), 866-876. doi:10.1164/rccm.201204-0754OC

Bosquillon, C. (2010). Drug transporters in the lung--do they play a role in the biopharmaceutics of inhaled drugs? (1520-6017 (Electronic)).

Bouligand, Y., & Livolant, F. (1984). The organization of cholesteric spherulites. *J. Phys. France, 45*(12), 1899-1923.

Brasch, J., Harrison, O. J., Honig, B., & Shapiro, L. (2012). Thinking outside the cell: how cadherins drive adhesion. *Trends Cell Biol, 22*(6), 299-310. doi:10.1016/j.tcb.2012.03.004

Breslin, S., & O'Driscoll, L. (2013). Three-dimensional cell culture: the missing link in drug discovery. *Drug Discov Today, 18*(5-6), 240-249. doi:10.1016/j.drudis.2012.10.003

Brezesinski, T., Groenewolt, M., Gibaud, A., Pinna, N., Antonietti, M., & Smarsly, B. (2006). Evaporation-Induced Self-Assembly (EISA) at Its Limit: Ultrathin, Crystalline Patterns by Templating of Micellar Monolayers. *Advanced Materials, 18*(17), 2260-2263. doi:10.1002/adma.200600258

Brodland, G. W. (2003). New information from cell aggregate compression tests and its implications for theories of cell sorting. *Biorheology, 40*(1-3), 273-277.

Brown, C. P., Whaite, A. D., MacLeod, J. M., Macdonald, J., & Rosei, F. (2014). With great structure comes great functionality: Understanding and emulating spider silk. *Journal of Materials Research, 30*(1), 108-120. doi:10.1557/jmr.2014.365

Brown, R. M., & Saxena, I. M. (2007). Preface. In R. M. Brown & I. M. Saxena (Eds.), *Cellulose: molecular and structural biology* Springer.

Bruce, D. W., Deschenaux, R., Donnio, B., & Guillon, D. (2007). Metallomesogens. In D. M. P. Mingos & R. H. Crabtree (Eds.), *Comprehensive Organometallic Chemistry III* (pp. 195-293). Oxford: Elsevier.

Brutin, D. (2015). *Droplet Wetting and Evaporation: From Pure to Complex Fluids* (D. Brutin Ed.): Elsevier.

Capadona, J. R., Shanmuganathan, K., Trittschuh, S., Seidel, S., Rowan, S. J., & Weder, C. (2009). Polymer nanocomposites with nanowhiskers isolated from microcrystalline cellulose. *Biomacromolecules, 10*(4), 712-716. doi:10.1021/bm8010903

Carlescu, I. (2020). Introductory Chapter: Nematic Liquid Crystals. In *Liquid Crystals and Display Technology*: IntechOpen.

Carlton, R. A. (2011). Polarized Light Microscopy. In *Pharmaceutical Microscopy* (pp. 7-64). New York, NY: Springer New York.

Cartagena-Rivera, A. X., Logue, J. S., Waterman, C. M., & Chadwick, R. S. (2016). Actomyosin Cortical Mechanical Properties in Nonadherent Cells Determined by Atomic Force Microscopy. *Biophysical journal, 110*(11), 2528-2539. doi:10.1016/j.bpj.2016.04.034

Castaneda, F., & Kinne, R. K. (2000). Short exposure to millimolar concentrations of ethanol induces apoptotic cell death in multicellular HepG2 spheroids. *J Cancer Res Clin Oncol, 126*(6), 305-310. doi:10.1007/s004320050348

Castro-Guerrero, C. F., & Gray, D. G. (2014). Chiral nematic phase formation by aqueous suspensions of cellulose nanocrystals prepared by oxidation with ammonium persulfate. *Cellulose, 21*(4), 2567-2577. doi:10.1007/s10570-014-0308-1

Cazabat, A.-M., & Guéna, G. (2010). Evaporation of macroscopic sessile droplets. *Soft Matter, 6*(12), 2591-2612. doi:10.1039/b924477h

Cha, J. M., Shin, E. K., Sung, J. H., Moon, G. J., Kim, E. H., Cho, Y. H., . . . Bang, O. Y. (2018). Efficient scalable production of therapeutic microvesicles derived from human mesenchymal stem cells. *Sci Rep, 8*(1), 1171. doi:10.1038/s41598-018-19211-6

Chawla, S., Midha, S., Sharma, A., & Ghosh, S. (2018). Silk-Based Bioinks for 3D Bioprinting. *Adv Healthc Mater, 7*(8), e1701204. doi:10.1002/adhm.201701204

Chen, I. A., & Walde, P. (2010). From self-assembled vesicles to protocells. *Cold Spring Harb Perspect Biol, 2*(7), a002170. doi:10.1101/cshperspect.a002170

Chen, K., Wu, M., Guo, F., Li, P., Chan, C. Y., Mao, Z., . . . Huang, T. J. (2016). Rapid formation of size-controllable multicellular spheroids via 3D acoustic tweezers. *Lab Chip, 16*(14), 2636-2643. doi:10.1039/c6lc00444j

Chen, W., Yu, H., Liu, Y., Chen, P., Zhang, M., & Hai, Y. (2011). Individualization of cellulose nanofibers from wood using high-intensity ultrasonication combined with chemical pretreatments. *Carbohydrate Polymers, 83*(4), 1804-1811. doi:10.1016/j.carbpol.2010.10.040

Chen, X., Knight, D. P., Shao, Z., & Vollrath, F. (2002). Conformation transition in silk protein films monitored by time-resolved Fourier transform infrared spectroscopy: effect of potassium ions on Nephila spidroin films. *Biochemistry, 41*(50), 14944-14950. doi:10.1021/bi026550m

Chen, X., Shao, Z., Knight, D. P., & Vollrath, F. (2007). Conformation transition kinetics of Bombyx mori silk protein. *Proteins, 68*(1), 223-231. doi:10.1002/prot.21414

Cheng, G., Tse, J., Jain, R. K., & Munn, L. L. (2009). Micro-environmental mechanical stress controls tumor spheroid size and morphology by suppressing proliferation and inducing apoptosis in cancer cells. *PLOS ONE, 4*(2), e4632. doi:10.1371/journal.pone.0004632

Cheng, Q., Wang, S., & Rials, T. G. (2009). Poly(vinyl alcohol) nanocomposites reinforced with cellulose fibrils isolated by high intensity ultrasonication. *Composites Part A: Applied Science and Manufacturing, 40*(2), 218-224. doi:10.1016/j.compositesa.2008.11.009

Choi, I., Yang, S., & Choi, T. L. (2018). Preparing Semiconducting Nanoribbons with Tunable Length and Width via Crystallization-Driven Self-Assembly of a Simple Conjugated Homopolymer. *J Am Chem Soc, 140*(49), 17218-17225. doi:10.1021/jacs.8b10406

Comrie, J. P. (2011). *Molecular self-assembly: advances in chemistry, biology, and nanotechnology* (J. P. Comrie Ed.): Nova Science Publishers.

Cui, X., Hartanto, Y., & Zhang, H. (2017). Advances in multicellular spheroids formation. *J R Soc Interface, 14*(127), 1-15. doi:10.1098/rsif.2016.0877

da Silva Perez, D., Montanari, S., & Vignon, M. R. (2003). TEMPO-mediated oxidation of cellulose III. *Biomacromolecules, 4*(5), 1417-1425. doi:10.1021/bm034144s

Dabrowska-Piaskowska, K. (1959). Observations on the histoformative capacities of tumor cells dissociated by digestion with trypsin. *Exp Cell Res, 16*(2), 315-323. doi:10.1016/0014-4827(59)90259-9

Dadi, A. P., Varanasi, S., & Schall, C. A. (2006). Enhancement of cellulose saccharification kinetics using an ionic liquid pretreatment step. *Biotechnol Bioeng, 95*(5), 904-910. doi:10.1002/bit.21047

Daster, S., Amatruda, N., Calabrese, D., Ivanek, R., Turrini, E., Droeser, R. A., . . . Muraro, M. G. (2017). Induction of hypoxia and necrosis in multicellular tumor spheroids is associated with resistance to chemotherapy treatment. *Oncotarget, 8*(1), 1725-1736. doi:10.18632/oncotarget.13857

Datta, S., Saha, M. L., & Stang, P. J. (2018). Hierarchical Assemblies of Supramolecular Coordination Complexes. *Acc Chem Res, 51*(9), 2047-2063. doi:10.1021/acs.accounts.8b00233

de Souza, N. (2018). Organoids. *Nature Methods, 15*(1), 23-23. doi:10.1038/nmeth.4576

Dean, D. M., Napolitano, A. P., Youssef, J., & Morgan, J. R. (2007). Rods, tori, and honeycombs: the directed self-assembly of microtissues with prescribed microscale geometries. *FASEB J, 21*(14), 4005-4012. doi:10.1096/fj.07-8710com

Deegan, R. D., Bakajin, O., Dupont, T. F., Huber, G., Nagel, S. R., & Witten, T. A. (1997). Capillary flow as the cause of ring stains from dried liquid drops. *Nature, 389*(6653), 827-829. doi:10.1038/39827

Dekkers, J. F., Wiegerinck, C. L., de Jonge, H. R., Bronsveld, I., Janssens, H. M., de Winter-de Groot, K. M., . . . Beekman, J. M. (2013). A functional CFTR assay using primary cystic fibrosis intestinal organoids. *Nat Med, 19*(7), 939-945. doi:10.1038/nm.3201

Desiraju, G. R. (1995). Supramolecular Synthons in Crystal Engineering—A New Organic Synthesis. *Angewandte Chemie International Edition in English, 34*(21), 2311-2327. doi:10.1002/anie.199523111

Dietrich, E., Wildeman, S., Visser, C. W., Hofhuis, K., Kooij, E. S., Zandvliet, H. J. W., & Lohse, D. (2016). Role of natural convection in the dissolution of sessile droplets. *arXiv preprint*.

Dill, K. A., & MacCallum, J. L. (2012). The protein-folding problem, 50 years on. *Science, 338*(6110), 1042-1046. doi:10.1126/science.1219021

DiMasi, J. A., & Grabowski, H. G. (2007). Economics of new oncology drug development. *J Clin Oncol, 25*(2), 209-216. doi:10.1200/JCO.2006.09.0803

Ding, Z., Zhou, M., Zhou, Z., Zhang, W., Jiang, X., Lu, X., . . . Kaplan, D. L. (2019). Injectable Silk Nanofiber Hydrogels for Sustained Release of Small-Molecule Drugs and Vascularization. *ACS Biomater Sci Eng, 5*(8), 4077-4088. doi:10.1021/acsbiomaterials.9b00621

DLS. (2021). XRR: X-ray Reflectivity. Retrieved from https://www.diamond.ac.uk/Instruments/Techniques/Diffraction/XRR.html

Dourdain, S., Colas, M., Bardeau, J. F., Gang, O., Ocko, B., & Gibaud, A. (2011). Time-Resolved in Situ Gisaxs Experiment of Evaporation-Induced Self-Assembly of Ctab Templated Silica Thin Films under Controlled Humidity. *International Journal of Nanoscience, 04*(05n06), 873-878. doi:10.1142/s0219581x05003826

Drost, J., & Clevers, H. (2018). Organoids in cancer research. *Nat Rev Cancer, 18*(7), 407-418. doi:10.1038/s41568-018-0007-6

Du, N., Yang, Z., Liu, X. Y., Li, Y., & Xu, H. Y. (2011). Structural Origin of the Strain-Hardening of Spider Silk. *Advanced Functional Materials, 21*(4), 772-778. doi:10.1002/adfm.201001397

Dufresne, A. (2013). *Nanocellulose*: De Gruyter.

Dufresne, A. (2017). *Nanocellulose: from nature to high performance tailored materials* (Second edition. ed.): De Gruyter.

Duggal, R., Hussain, F., & Pasquali, M. (2006). Self-Assembly of Single-Walled Carbon Nanotubes into a Sheet by Drop Drying*(1)*, 29.

Dugyala, V., Daware, S., & Basavaraj, M. (2013). Shape anisotropic colloids: synthesis, packing behavior, evaporation driven assembly, and their application in emulsion stabilization. (29), 6711.

Dumanli, A. G., Kamita, G., Landman, J., van der Kooij, H., Glover, B. J., Baumberg, J. J., . . . Vignolini, S. (2014). Controlled, Bio-inspired Self-Assembly of Cellulose-Based Chiral Reflectors. *Adv Opt Mater, 2*(7), 646-650. doi:10.1002/adom.201400112

Edmondson, R., Broglie, J. J., Adcock, A. F., & Yang, L. (2014). Three-dimensional cell culture systems and their applications in drug discovery and cell-based biosensors. *Assay Drug Dev Technol, 12*(4), 207-218. doi:10.1089/adt.2014.573

Eichhorn, S. J., Hearle, J. W. S., Jaffe, M., & Kikutani, T. (Eds.). (2009). *Handbook of Textile Fibre Structure, Volume 1 - Fundamentals and Manufactured Polymer Fibres*: Woodhead Publishing.

Eiraku, M., Takata, N., Ishibashi, H., Kawada, M., Sakakura, E., Okuda, S., . . . Sasai, Y. (2011). Self-organizing optic-cup morphogenesis in three-dimensional culture. *Nature, 472*(7341), 51-56. doi:10.1038/nature09941

Eiraku, M., Watanabe, K., Matsuo-Takasaki, M., Kawada, M., Yonemura, S., Matsumura, M., . . . Sasai, Y. (2008). Self-organized formation of polarized cortical tissues from ESCs and its active manipulation by extrinsic signals. *Cell Stem Cell, 3*(5), 519-532. doi:10.1016/j.stem.2008.09.002

Engström, J., Asem, H., Brismar, H., Zhang, Y., Malkoch, M., & Malmström, E. (2020). In Situ Encapsulation of Nile Red or Doxorubicin during RAFT-Mediated Emulsion Polymerization via Polymerization-Induced Self-Assembly for Biomedical Applications. *Macromolecular Chemistry and Physics, 221*(5), 1900443. doi:10.1002/macp.201900443

Enmon Jr, R. M., O'Connor, K. C., Lacks, D. J., Schwartz, D. K., & Dotson, R. S. (2001). Dynamics of spheroid self-assembly in liquid-overlay culture of DU 145 human prostate cancer cells. *Biotechnology and Bioengineering, 72*(6), 579-591.

Erbil, H. Y. (2012). Evaporation of pure liquid sessile and spherical suspended drops: a review. *Adv Colloid Interface Sci, 170*(1-2), 67-86. doi:10.1016/j.cis.2011.12.006

Evans, D., & Wennerström, H. (1999). *The colloidal domain: where physics, chemistry, biology, and technology meet.* .

Evans, E., & Yeung, A. (1989). Apparent viscosity and cortical tension of blood granulocytes determined by micropipet aspiration. *Biophysical journal, 56*(1), 151-160. doi:10.1016/S0006-3495(89)82660-8

Fang, S., Zhang, S., Dai, H., Hu, X., Li, C., & Xing, Y. (2019). The role of pulmonary mesenchymal cells in airway epithelium regeneration during injury repair. *Stem Cell Res Ther, 10*(1), 366. doi:10.1186/s13287-019-1452-1

Farhadifar, R., Roper, J. C., Aigouy, B., Eaton, S., & Julicher, F. (2007). The influence of cell mechanics, cell-cell interactions, and proliferation on epithelial packing. *Curr Biol, 17*(24), 2095-2104. doi:10.1016/j.cub.2007.11.049

Fatehullah, A., Tan, S. H., & Barker, N. (2016). Organoids as an in vitro model of human development and disease. *Nat Cell Biol, 18*(3), 246-254. doi:10.1038/ncb3312

Fennema, E., Rivron, N., Rouwkema, J., van Blitterswijk, C., & de Boer, J. (2013). Spheroid culture as a tool for creating 3D complex tissues. *Trends Biotechnol, 31*(2), 108-115. doi:10.1016/j.tibtech.2012.12.003

Fitzgerald, K. A., Malhotra, M., Curtin, C. M., FJ, O. B., & CM, O. D. (2015). Life in 3D is never flat: 3D models to optimise drug delivery. *J Control Release, 215*, 39-54. doi:10.1016/j.jconrel.2015.07.020

Folda, T., Hoffmann, H., Chanzy, H., & Smith, P. (1988). Liquid crystalline suspensions of poly(tetrafluoroethylene) 'whiskers'. *Nature, 333*(6168), 55-56. doi:10.1038/333055a0

Folkman, J., & Moscona, A. (1978). Role of cell shape in growth control. *Nature, 273*(5661), 345-349. doi:10.1038/273345a0

Fonoudi, H., Ansari, H., Abbasalizadeh, S., Larijani, M. R., Kiani, S., Hashemizadeh, S., . . . Baharvand, H. (2015). A Universal and Robust Integrated Platform for the Scalable Production of Human Cardiomyocytes From Pluripotent Stem Cells. *Stem Cells Transl Med, 4*(12), 1482-1494. doi:10.5966/sctm.2014-0275

Foo, C. W. P., Bini, E., Hensman, J., Knight, D. P., Lewis, R. V., & Kaplan, D. L. (2005). Role of pH and charge on silk protein assembly in insects and spiders. *Applied Physics A, 82*(2), 223-233. doi:10.1007/s00339-005-3426-7

Forgacs, G., Foty, R. A., Shafrir, Y., & Steinberg, M. S. (1998). Viscoelastic properties of living embryonic tissues: a quantitative study. *Biophysical journal, 74*(5), 2227-2234. doi:10.1016/S0006-3495(98)77932-9

Foty, R. A., Pfleger, C. M., Forgacs, G., & Steinberg, M. S. (1996). Surface tensions of embryonic tissues predict their mutual envelopment behavior. *Development, 122*(5), 1611-1620.

Foty, R. A., & Steinberg, M. S. (2005). The differential adhesion hypothesis: a direct evaluation. *Dev Biol, 278*(1), 255-263. doi:10.1016/j.ydbio.2004.11.012

Frey, O., Misun, P. M., Fluri, D. A., Hengstler, J. G., & Hierlemann, A. (2014). Reconfigurable microfluidic hanging drop network for multi-tissue interaction and analysis. *Nat Commun, 5*(1), 4250. doi:10.1038/ncomms5250

Fu, C., Shao, Z., & Fritz, V. (2009). Animal silks: their structures, properties and artificial production. *Chemical Communications*(43), 6515-6529.

Garmann, R. F., Goldfain, A. M., & Manoharan, V. N. (2018). Measuring the self-assembly kinetics of individual viral capsids. *bioRxiv*, 265330. doi:10.1101/265330

Gonzalez-Rodriguez, D., Guevorkian, K., Douezan, S., & Brochard-Wyart, F. (2012). Soft matter models of developing tissues and tumors. *Science, 338*(6109), 910-917. doi:10.1126/science.1226418

Graner, F. (1993). Can Surface Adhesion Drive Cell-rearrangement? Part I: Biological Cell-sorting. *Journal of Theoretical Biology, 164*(4), 455-476. doi:10.1006/jtbi.1993.1167

Grauzinyte, M., Forth, J., Rumble, K. A., & Clegg, P. S. (2015). Particle-stabilized water droplets that sprout millimeter-scale tubes. *Angew Chem Int Ed Engl, 54*(5), 1456-1460. doi:10.1002/anie.201408365

Grebenyuk, S., & Ranga, A. (2019). Engineering Organoid Vascularization. *Front Bioeng Biotechnol, 7*, 39. doi:10.3389/fbioe.2019.00039

Greving, I., Cai, M., Vollrath, F., & Schniepp, H. C. (2012). Shear-induced self-assembly of native silk proteins into fibrils studied by atomic force microscopy. *Biomacromolecules, 13*(3), 676-682. doi:10.1021/bm201509b

Groebe, K., & Mueller-Klieser, W. (1996). On the relation between size of necrosis and diameter of tumor spheroids. *International Journal of Radiation Oncology*Biology*Physics, 34*(2), 395-401. doi:10.1016/0360-3016(95)02065-9

Grzybowski, B. A., Wilmer, C. E., Kim, J., Browne, K. P., & Bishop, K. J. M. (2009). Self-assembly: from crystals to cells. *Soft Matter, 5*(6), 1110-1128. doi:10.1039/b819321p

Guevorkian, K., Colbert, M. J., Durth, M., Dufour, S., & Brochard-Wyart, F. (2010). Aspiration of biological viscoelastic drops. *Phys Rev Lett, 104*(21), 218101. doi:10.1103/PhysRevLett.104.218101

Guevorkian, K., Gonzalez-Rodriguez, D., Carlier, C., Dufour, S., & Brochard-Wyart, F. (2011). Mechanosensitive shivering of model tissues under controlled aspiration. *Proc Natl Acad Sci U S A, 108*(33), 13387-13392. doi:10.1073/pnas.1105741108

Guevorkian, K., & Maître, J. L. (2017). Chapter 10 - Micropipette aspiration: A unique tool for exploring cell and tissue mechanics in vivo. In T. Lecuit (Ed.), *Methods in Cell Biology* (Vol. 139, pp. 187-201): Academic Press.

Guven, S., Chen, P., Inci, F., Tasoglu, S., Erkmen, B., & Demirci, U. (2015). Multiscale assembly for tissue engineering and regenerative medicine. *Trends Biotechnol, 33*(5), 269-279. doi:10.1016/j.tibtech.2015.02.003

Haase, M. F., Stebe, K. J., & Lee, D. (2015). Microparticles: Continuous Fabrication of Hierarchical and Asymmetric Bijel Microparticles, Fibers, and Membranes by Solvent Transfer-Induced Phase Separation (STRIPS) (Adv. Mater. 44/2015). *Advanced Materials, 27*(44), 7013.

Habibi, Y., Chanzy, H., & Vignon, M. R. (2006). TEMPO-mediated surface oxidation of cellulose whiskers. *Cellulose, 13*(6), 679-687. doi:10.1007/s10570-006-9075-y

Habibi, Y., Lucia, L. A., & Rojas, O. J. (2010). Cellulose Nanocrystals: Chemistry, Self-Assembly, and Applications*(6)*, 3479.

Halpern, B., Pejsachowicz, B., Febvre, H. L., & Barski, G. (1966). Differences in patterns of aggregation of malignant and non-malignant mammalian cells. *Nature, 209*(5019), 157-159. doi:10.1038/209157a0

Hanamura, M., Sawada, T., & Serizawa, T. (2021). In-Paper Self-Assembly of Cellulose Oligomers for the Preparation of All-Cellulose Functional Paper. *ACS Sustainable Chemistry & Engineering, 9*(16), 5684-5692. doi:10.1021/acssuschemeng.1c00815

Hata, Y., & Serizawa, T. (2021). Self-assembly of cellulose for creating green materials with tailor-made nanostructures. *J Mater Chem B, 9*(19), 3944-3966. doi:10.1039/d1tb00339a

He, J.-X., Tan, W.-L., Han, Q.-M., Cui, S.-Z., Shao, W., & Sang, F. (2016). Fabrication of silk fibroin/cellulose whiskers–chitosan composite porous scaffolds by layer-by-layer

assembly for application in bone tissue engineering. *Journal of Materials Science, 51*(9), 4399-4410. doi:10.1007/s10853-016-9752-7

Hegedus, B., Marga, F., Jakab, K., Sharpe-Timms, K. L., & Forgacs, G. (2006). The interplay of cell-cell and cell-matrix interactions in the invasive properties of brain tumors. *Biophysical journal, 91*(7), 2708-2716. doi:10.1529/biophysj.105.077834

Heim, M., Romer, L., & Scheibel, T. (2010). Hierarchical structures made of proteins. The complex architecture of spider webs and their constituent silk proteins. *Chem Soc Rev, 39*(1), 156-164. doi:10.1039/b813273a

Hellman, K. B., & Nerem, R. M. (2007). Editorial: advancing tissue engineering and regenerative medicine. *Tissue Eng, 13*(12), 2823-2824. doi:10.1089/ten.2007.1504

Henriksson, M., Henriksson, G., Berglund, L., & Lindström, T. (2007). An environmentally friendly method for enzyme-assisted preparation of microfibrillated cellulose (MFC) nanofibers. *European polymer journal, 43*(8), 3434-3441.

Hirschhaeuser, F., Menne, H., Dittfeld, C., West, J., Mueller-Klieser, W., & Kunz-Schughart, L. A. (2010). Multicellular tumor spheroids: an underestimated tool is catching up again. *J Biotechnol, 148*(1), 3-15. doi:10.1016/j.jbiotec.2010.01.012

Histogenesis. (1998). In *Encyclopædia Britannica*: Encyclopædia Britannica, inc. .

Hochmuth, R. M. (2000). Micropipette aspiration of living cells. *J Biomech, 33*(1), 15-22. doi:10.1016/s0021-9290(99)00175-x

Hofer, M., & Lutolf, M. P. (2021). Engineering organoids. *Nat Rev Mater, 6*(5), 1-19. doi:10.1038/s41578-021-00279-y

Holland, C., Terry, A. E., Porter, D., & Vollrath, F. (2007). Natural and unnatural silks. *Polymer, 48*(12), 3388-3392. doi:10.1016/j.polymer.2007.04.019

Holliday, B. J., & Mirkin, C. A. (2001). Strategies for the Construction of Supramolecular Compounds through Coordination Chemistry. *Angewandte Chemie International Edition, 40*(11), 2022-2043. doi:10.1002/1521-3773(20010601)40:11<2022::Aid-anie2022>3.0.Co;2-d

Holtfreter, J. (1944). A study of the mechanics of gastrulation. *Journal of Experimental Zoology, 95*(2), 171-212. doi:10.1002/jez.1400950203

Holtfreter, J. (1947). Changes of structure and the kinetics of differentiating embryonic cells. *J Morphol, 80*(1), 57-91. doi:10.1002/jmor.1050800104

Hopkins, A. L. (2008). Network pharmacology: the next paradigm in drug discovery. *Nat Chem Biol, 4*(11), 682-690. doi:10.1038/nchembio.118

Hu, H., & Larson, R. G. (2002). Evaporation of a Sessile Droplet on a Substrate. *The Journal of Physical Chemistry - Part B, 106*(6), 1334.

Huh, D., Hamilton, G. A., & Ingber, D. E. (2011). From 3D cell culture to organs-on-chips. *Trends Cell Biol, 21*(12), 745-754. doi:10.1016/j.tcb.2011.09.005

Idiopathic Pulmonary Fibrosis Clinical Research, N., Martinez, F. J., de Andrade, J. A., Anstrom, K. J., King, T. E., Jr., & Raghu, G. (2014). Randomized trial of acetylcysteine in idiopathic pulmonary fibrosis. *N Engl J Med, 370*(22), 2093-2101. doi:10.1056/NEJMoa1401739

Idiopathic Pulmonary Fibrosis Clinical Research, N., Raghu, G., Anstrom, K. J., King, T. E., Jr., Lasky, J. A., & Martinez, F. J. (2012). Prednisone, azathioprine, and N-acetylcysteine for pulmonary fibrosis. *N Engl J Med, 366*(21), 1968-1977. doi:10.1056/NEJMoa1113354

Inam, M., Jones, J. R., Perez-Madrigal, M. M., Arno, M. C., Dove, A. P., & O'Reilly, R. K. (2018). Controlling the Size of Two-Dimensional Polymer Platelets for Water-in-Water Emulsifiers. *ACS Cent Sci, 4*(1), 63-70. doi:10.1021/acscentsci.7b00436

Inch, W. R., McCredie, J. A., & Sutherland, R. M. (1970). Growth of nodular carcinomas in rodents compared with multi-cell spheroids in tissue culture. *Growth, 34*(3), 271-282.

Ingram, M., Techy, G. B., Saroufeem, R., Yazan, O., Narayan, K. S., Goodwin, T. J., & Spaulding, G. F. (1997). Three-Dimensional Growth Patterns of Various Human Tumor Cell Lines in Simulated Microgravity of a NASA Bioreactor*(6)*, 459.

Ino, K., Ito, A., & Honda, H. (2007). Cell patterning using magnetite nanoparticles and magnetic force. *Biotechnology and Bioengineering, 97*(5), 1309-1317.

Ivascu, A., & Kubbies, M. (2006). Rapid generation of single-tumor spheroids for high-throughput cell function and toxicity analysis. *J Biomol Screen, 11*(8), 922-932. doi:10.1177/1087057106292763

Jaffar, J., Yang, S. H., Kim, S. Y., Kim, H. W., Faiz, A., Chrzanowski, W., & Burgess, J. K. (2018). Greater cellular stiffness in fibroblasts from patients with idiopathic pulmonary fibrosis. *Am J Physiol Lung Cell Mol Physiol, 315*(1), L59-L65. doi:10.1152/ajplung.00030.2018

Jakab, K., Damon, B., Marga, F., Doaga, O., Mironov, V., Kosztin, I., . . . Forgacs, G. (2008). Relating cell and tissue mechanics: implications and applications. *Dev Dyn, 237*(9), 2438-2449. doi:10.1002/dvdy.21684

Jakab, K., Norotte, C., Marga, F., Murphy, K., Vunjak-Novakovic, G., & Forgacs, G. (2010). Tissue engineering by self-assembly and bio-printing of living cells. *Biofabrication, 2*(2), 022001. doi:10.1088/1758-5082/2/2/022001

Jang, M., & Ahn, H. J. (2017). Rolling Circle Transcription for the Self-Assembly of Multimeric RNAi Structures and Its Applications in Nanomedicine. *Methods Mol Biol, 1632*, 65-74. doi:10.1007/978-1-4939-7138-1_4

Jativa, F., Schutz, C., Bergstrom, L., Zhang, X., & Wicklein, B. (2015). Confined self-assembly of cellulose nanocrystals in a shrinking droplet. *Soft Matter, 11*(26), 5374-5380. doi:10.1039/c5sm00886g

Jativa, F., & Zhang, X. (2017). Transparent Silk Fibroin Microspheres from Controlled Droplet Dissolution in a Binary Solution. *Langmuir, 33*(31), 7780-7787. doi:10.1021/acs.langmuir.7b01579

Jin, H. J., Cho, Y. H., Gu, J. M., Kim, J., & Oh, Y. S. (2011). A multicellular spheroid formation and extraction chip using removable cell trapping barriers. *Lab Chip, 11*(1), 115-119. doi:10.1039/c0lc00134a

Jin, H. J., & Kaplan, D. L. (2003). Mechanism of silk processing in insects and spiders. *Nature, 424*(6952), 1057-1061. doi:10.1038/nature01809

Jin, X. H., Price, M. B., Finnegan, J. R., Boott, C. E., Richter, J. M., Rao, A., . . . Manners, I. (2018). Long-range exciton transport in conjugated polymer nanofibers prepared by seeded growth. *Science, 360*(6391), 897-900. doi:10.1126/science.aar8104

John, V. T., McPherson, G., & Bose, A. (2003). Self-Assembly of Surfactants to Organogels. In B. H. Robinson (Ed.), *Self-assembly*: IOSS Press.

Josten, E., Wetterskog, E., Glavic, A., Boesecke, P., Feoktystov, A., Brauweiler-Reuters, E., . . . Bergstrom, L. (2017). Superlattice growth and rearrangement during evaporation-induced nanoparticle self-assembly. *Sci Rep, 7*(1), 2802. doi:10.1038/s41598-017-02121-4

Kalantarian, A., Ninomiya, H., Saad, S. M., David, R., Winklbauer, R., & Neumann, A. W. (2009). Axisymmetric drop shape analysis for estimating the surface tension of cell aggregates by centrifugation. *Biophysical journal, 96*(4), 1606-1616. doi:10.1016/j.bpj.2008.10.064

Katari, R. S., Peloso, A., & Orlando, G. (2014). Tissue engineering. *Adv Surg, 48*(1), 137-154. doi:10.1016/j.yasu.2014.05.007

Keenan, C. R., Langenbach, S. Y., Jativa, F., Harris, T., Li, M., Chen, Q., . . . Stewart, A. G. (2018). Casein Kinase 1delta/epsilon Inhibitor, PF670462 Attenuates the Fibrogenic

Effects of Transforming Growth Factor-beta in Pulmonary Fibrosis. *Front Pharmacol, 9*(738), 738. doi:10.3389/fphar.2018.00738

Kelly, J. A., Giese, M., Shopsowitz, K. E., Hamad, W. Y., & MacLachlan, M. J. (2014). The Development of ChiralNematic Mesoporous Materials. *Accounts of Chemical Research, 47*(4), 1088.

Kelm, J. M., Timmins, N. E., Brown, C. J., Fussenegger, M., & Nielsen, L. K. (2003). Method for generation of homogeneous multicellular tumor spheroids applicable to a wide variety of cell types. *Biotechnol Bioeng, 83*(2), 173-180. doi:10.1002/bit.10655

Keten, S., Xu, Z., Ihle, B., & Buehler, M. J. (2010). Nanoconfinement controls stiffness, strength and mechanical toughness of beta-sheet crystals in silk. *Nat Mater, 9*(4), 359-367. doi:10.1038/nmat2704

Khalilgharibi, N., Fouchard, J., Recho, P., Charras, G., & Kabla, A. (2016). The dynamic mechanical properties of cellularised aggregates. *Curr Opin Cell Biol, 42*, 113-120. doi:10.1016/j.ceb.2016.06.003

Kim, J. B. (2005). *Three-dimensional tissue culture models in cancer biology.* Paper presented at the Seminars in cancer biology.

Kim, J. H., Lim, I. R., Joo, H. J., Choi, S. C., Choi, J. H., Cui, L. H., . . . Lim, D. S. (2015). Sphere formation of adipose stem cell engineered by poly-2-hydroxyethyl methacrylate induces in vitro angiogenesis through fibroblast growth factor 2. *Biochem Biophys Res Commun, 468*(1-2), 372-379. doi:10.1016/j.bbrc.2015.10.083

Kim, S.-H., Lee, S. Y., Yang, S.-M., & Yi, G.-R. (2011). Self-assembled colloidal structures for photonics. *NPG Asia Materials, 3*(1), 25-33. doi:10.1038/asiamat.2010.192

Kinney, M. A., Hookway, T. A., Wang, Y., & McDevitt, T. C. (2014). Engineering three-dimensional stem cell morphogenesis for the development of tissue models and scalable regenerative therapeutics. *Ann Biomed Eng, 42*(2), 352-367. doi:10.1007/s10439-013-0953-9

Koh, L.-D., Cheng, Y., Teng, C.-P., Khin, Y.-W., Loh, X.-J., Tee, S.-Y., . . . Han, M.-Y. (2015). Structures, mechanical properties and applications of silk fibroin materials. *Progress in Polymer Science, 46*, 86-110. doi:10.1016/j.progpolymsci.2015.02.001

Kola, I. (2008). The state of innovation in drug development. *Clin Pharmacol Ther, 83*(2), 227-230. doi:10.1038/sj.clpt.6100479

Kontturi, E., & Vuorinen, T. (2008). Indirect evidence of supramolecular changes within cellulose microfibrils of chemical pulp fibers upon drying. *Cellulose, 16*(1), 65-74. doi:10.1007/s10570-008-9235-3

Kopanska, K. S., Alcheikh, Y., Staneva, R., Vignjevic, D., & Betz, T. (2016). Tensile Forces Originating from Cancer Spheroids Facilitate Tumor Invasion. *PLOS ONE, 11*(6), e0156442. doi:10.1371/journal.pone.0156442

Kopecek, J. (2009). Hydrogels from Soft Contact Lenses and Implants to Self-Assembled Nanomaterials. *J Polym Sci A Polym Chem, 47*(22), 5929-5946. doi:10.1002/pola.23607

Krens, S. G., & Heisenberg, C.-P. (2011). Cell sorting in development. In *Current topics in developmental biology* (Vol. 95, pp. 189-213): Elsevier.

Kundu, J., Chung, Y. I., Kim, Y. H., Tae, G., & Kundu, S. C. (2010). Silk fibroin nanoparticles for cellular uptake and control release. *Int J Pharm, 388*(1-2), 242-250. doi:10.1016/j.ijpharm.2009.12.052

Kuo, C. J., & Curtis, C. (2018). Organoids reveal cancer dynamics. *Nature, 556*(7702), 441-442. doi:10.1038/d41586-018-03841-x

Kuznetsova, T. G., Starodubtseva, M. N., Yegorenkov, N. I., Chizhik, S. A., & Zhdanov, R. I. (2007). Atomic force microscopy probing of cell elasticity. *Micron, 38*(8), 824-833. doi:10.1016/j.micron.2007.06.011

Laaksonen, P., Walther, A., Malho, J. M., Kainlauri, M., Ikkala, O., & Linder, M. B. (2011). Genetic engineering of biomimetic nanocomposites: diblock proteins, graphene, and nanofibrillated cellulose. *Angew Chem Int Ed Engl, 50*(37), 8688-8691. doi:10.1002/anie.201102973

Lagerwall, J. P. F., Schütz, C., Salajkova, M., Noh, J., Hyun Park, J., Scalia, G., & Bergström, L. (2014). Cellulose nanocrystal-based materials: from liquid crystal self-assembly and glass formation to multifunctional thin films. *NPG Asia Materials, 6*(1), e80-e80. doi:10.1038/am.2013.69

Lahiji, R., Reifenberger, R., Raman, A., Rudie, A. W., & Moon, R. J. (2008). *Characterization of cellulose nanocrystal surfaces by SPM.* Paper presented at the NSTI Nanotechnology Conference and Trade Show, Nanotechnology 2008. Vol. 1-3 CDROM: 2008 June 1-5, Boston, Massachusetts. Boca Raton, FL: CRC Press, 2008: ISBN: 9781420085112 (CD-ROM): 1420085115 (CD-ROM): pages 704-707.

Lakes, R. (1993). Materials with structural hierarchy. *Nature, 361*(6412), 511-515. doi:10.1038/361511a0

Lancaster, M. A., Renner, M., Martin, C. A., Wenzel, D., Bicknell, L. S., Hurles, M. E., . . . Knoblich, J. A. (2013). Cerebral organoids model human brain development and microcephaly. *Nature, 501*(7467), 373-379. doi:10.1038/nature12517

Landry, J., Bernier, D., Ouellet, C., Goyette, R., & Marceau, N. (1985). Spheroidal aggregate culture of rat liver cells: histotypic reorganization, biomatrix deposition, and maintenance of functional activities. *J Cell Biol, 101*(3), 914-923. doi:10.1083/jcb.101.3.914

Laschke, M. W., & Menger, M. D. (2017). Life is 3D: Boosting Spheroid Function for Tissue Engineering. *Trends Biotechnol, 35*(2), 133-144. doi:10.1016/j.tibtech.2016.08.004

Leask, A., & Abraham, D. J. (2004). TGF-beta signaling and the fibrotic response. *FASEB J, 18*(7), 816-827. doi:10.1096/fj.03-1273rev

Lebedeva, M. A., Palmieri, E., Kukura, P., & Fletcher, S. P. (2020). Emergence and Rearrangement of Dynamic Supramolecular Aggregates Visualized by Interferometric Scattering Microscopy. *ACS Nano, 14*(9), 11160-11168. doi:10.1021/acsnano.0c02414

Lee, H.-C., Lee, T.-W., Kim, T.-H., & Park, O. O. (2004). Fabrication and characterization of polymer/nanoclay hybrid ultrathin multilayer film by spin self-assembly method. *Thin Solid Films, 458*(1-2), 9-14. doi:10.1016/j.tsf.2003.11.117

Lehn, J.-M. (1988). Supramolecular Chemistry—Scope and Perspectives Molecules, Supermolecules, and Molecular Devices(Nobel Lecture). *Angewandte Chemie International Edition in English, 27*(1), 89-112. doi:10.1002/anie.198800891

Lepeltier, E., Bourgaux, C., & Couvreur, P. (2014). Nanoprecipitation and the "Ouzo effect": Application to drug delivery devices. *Adv Drug Deliv Rev, 71*, 86-97. doi:10.1016/j.addr.2013.12.009

Lessel, M., Bäumchen, O., Klos, M., Hähl, H., Fetzer, R., Paulus, M., . . . Jacobs, K. (2015). Self-assembled silane monolayers: an efficient step-by-step recipe for high-quality, low energy surfaces. *Surface and Interface Analysis, 47*(5), 557-564. doi:10.1002/sia.5729

Li, F., Josephson, D. P., & Stein, A. (2011). Colloidal assembly: the road from particles to colloidal molecules and crystals. *Angew Chem Int Ed Engl, 50*(2), 360-388. doi:10.1002/anie.201001451

Li, J.-L., & Liu, X.-Y. (2010). Architecture of Supramolecular Soft Functional Materials: From Understanding to Micro-/Nanoscale Engineering. *Advanced Functional Materials, 20*(19), 3196-3216. doi:10.1002/adfm.201000744

Li, M., & Stewart, A. G. (2021). Translational Pharmacology and Clinical Trials. In *Reference Module in Biomedical Sciences*: Elsevier.

Li, M., Wang, L. J., Li, D., Cheng, Y. L., & Adhikari, B. (2014). Preparation and characterization of cellulose nanofibers from de-pectinated sugar beet pulp. *Carbohydr Polym, 102*, 136-143. doi:10.1016/j.carbpol.2013.11.021

Lim, J., Yeap, S. P., Che, H. X., & Low, S. C. (2013). Characterization of magnetic nanoparticle by dynamic light scattering. *Nanoscale Res Lett, 8*(1), 381. doi:10.1186/1556-276X-8-381

Lin, N., & Liu, X. (2015). Correlation between hierarchical structure of crystal networks and macroscopic performance of mesoscopic soft materials and engineering principles. *Chemical Society Reviews, 44*(21), 7881-7915.

Lin, R. Z., & Chang, H. Y. (2008). Recent advances in three-dimensional multicellular spheroid culture for biomedical research. *Biotechnol J, 3*(9-10), 1172-1184. doi:10.1002/biot.200700228

Lin, Z. (2013). *Evaporative self-assembly of ordered complex structures*: World Scientific.

Livolant, F., & Leforestier, A. (1996). Condensed phases of DNA: Structures and phase transitions. *Progress in Polymer Science, 21*(6), 1115-1164. doi:10.1016/s0079-6700(96)00016-0

Lopa, S., Piraino, F., Kemp, R. J., Di Caro, C., Lovati, A. B., Di Giancamillo, A., . . . Moretti, M. (2015). Fabrication of multi-well chips for spheroid cultures and implantable constructs through rapid prototyping techniques. *Biotechnol Bioeng, 112*(7), 1457-1471. doi:10.1002/bit.25557

Lozano-Perez, A. A., Rivero, H. C., Perez Hernandez, M. D. C., Pagan, A., Montalban, M. G., Villora, G., & Cenis, J. L. (2017). Silk fibroin nanoparticles: Efficient vehicles for the natural antioxidant quercetin. *Int J Pharm, 518*(1-2), 11-19. doi:10.1016/j.ijpharm.2016.12.046

Lu, Q., Zhang, X., Hu, X., & Kaplan, D. L. (2010). Green process to prepare silk fibroin/gelatin biomaterial scaffolds. *Macromol Biosci, 10*(3), 289-298. doi:10.1002/mabi.200900258

Lu, Q., Zhu, H., Zhang, C., Zhang, F., Zhang, B., & Kaplan, D. L. (2012). Silk self-assembly mechanisms and control from thermodynamics to kinetics. *Biomacromolecules, 13*(3), 826-832. doi:10.1021/bm201731e

Lu, S., Wang, X., Lu, Q., Zhang, X., Kluge, J. A., Uppal, N., . . . Kaplan, D. L. (2010). Insoluble and flexible silk films containing glycerol. *Biomacromolecules, 11*(1), 143-150. doi:10.1021/bm900993n

Lu, Z., Rezk, A., Jativa, F., Yeo, L., & Zhang, X. (2017). Dissolution dynamics of a suspension droplet in a binary solution for controlled nanoparticle assembly. *Nanoscale, 9*(36), 13441-13448. doi:10.1039/C7NR02704D

Luu, O., David, R., Ninomiya, H., & Winklbauer, R. (2011). Large-scale mechanical properties of Xenopus embryonic epithelium. *Proc Natl Acad Sci U S A, 108*(10), 4000-4005. doi:10.1073/pnas.1010331108

Lv, Q., Cao, C., Zhang, Y., Ma, X., & Zhu, H. (2005). Preparation of insoluble fibroin films without methanol treatment. *Journal of Applied Polymer Science, 96*(6), 2168-2173. doi:10.1002/app.21682

Ma, H.-l., Jiang, Q., Han, S., Wu, Y., Tomshine, J. C., Wang, D., . . . Liang, X.-J. (2012). Multicellular tumor spheroids as an in vivo–like tumor model for three-dimensional imaging of chemotherapeutic and nano material cellular penetration. *Molecular imaging, 11*(6), 7290.2012. 00012.

Ma, P. X. (2004). Scaffolds for tissue fabrication. *Materials Today, 7*(5), 30-40. doi:10.1016/s1369-7021(04)00233-0

Macchiarini, P., Jungebluth, P., Go, T., Asnaghi, M. A., Rees, L. E., Cogan, T. A., . . . Birchall, M. A. (2008). Clinical transplantation of a tissue-engineered airway. *Lancet, 372*(9655), 2023-2030. doi:10.1016/S0140-6736(08)61598-6

Mackay, R. A. (2003). Applications of self-assembly to chemical biological defense. In B. Robinson (Ed.), *Self-assembly* (pp. 17-24).

Manning, M. L., Foty, R. A., Steinberg, M. S., & Schoetz, E. M. (2010). Coaction of intercellular adhesion and cortical tension specifies tissue surface tension. *Proc Natl Acad Sci U S A, 107*(28), 12517-12522. doi:10.1073/pnas.1003743107

Marchessault, R. H., Morehead, F. F., & Walter, N. M. (1959). Liquid Crystal Systems from Fibrillar Polysaccharides. *Nature, 184*(4686), 632-633. doi:10.1038/184632a0

Mariani, J., Coppola, G., Zhang, P., Abyzov, A., Provini, L., Tomasini, L., . . . Vaccarino, F. M. (2015). FOXG1-Dependent Dysregulation of GABA/Glutamate Neuron Differentiation in Autism Spectrum Disorders. *Cell, 162*(2), 375-390. doi:10.1016/j.cell.2015.06.034

Marin, A. G., Gelderblom, H., Susarrey-Arce, A., van Houselt, A., Lefferts, L., Gardeniers, J. G., . . . Snoeijer, J. H. (2012). Building microscopic soccer balls with evaporating colloidal fakir drops. *Proc Natl Acad Sci U S A, 109*(41), 16455-16458. doi:10.1073/pnas.1209553109

Marinkovic, A., Liu, F., & Tschumperlin, D. J. (2013). Matrices of physiologic stiffness potently inactivate idiopathic pulmonary fibrosis fibroblasts. *American journal of respiratory cell and molecular biology, 48*(4), 422-430. doi:10.1165/rcmb.2012-0335OC

Markx, G. H., & Buckle, A.-M. (2008). Tissue engineering: AC electrokinetics. In *Encyclopedia of biomaterials and biomedical engineering* (pp. 2628-2635): CRC Press.

Mathur, A. B., & Gupta, V. (2010). Silk fibroin-derived nanoparticles for biomedical applications. *Nanomedicine (Lond), 5*(5), 807-820. doi:10.2217/nnm.10.51

McCulley, D., Wienhold, M., & Sun, X. (2015). The pulmonary mesenchyme directs lung development. *Current opinion in genetics & development, 32*, 98-105. doi:10.1016/j.gde.2015.01.011

McKeen, L. W. (2013). Plastic Films in Food Packaging : Materials, Technology and Applications. In S. Ebnesajjad (Ed.). Norwich, UNITED STATES: Elsevier Science & Technology Books.

Metzger, W., Sossong, D., Bächle, A., Pütz, N., Wennemuth, G., Pohlemann, T., & Oberringer, M. (2011). The liquid overlay technique is the key to formation of co-culture spheroids consisting of primary osteoblasts, fibroblasts and endothelial cells. *Cytotherapy, 13*(8), 1000-1012.

Mgharbel, A., Delanoe-Ayari, H., & Rieu, J. P. (2009). Measuring accurately liquid and tissue surface tension with a compression plate tensiometer. *HFSP J, 3*(3), 213-221. doi:10.2976/1.3116822

Mileni, M. P. (2003). Nanocrystals: Size and Shape Control. In B. H. Robinson (Ed.), *Self-assembly*: IOSS Press.

Mitke, A., Schuliga, M., Harris, T., Jativa, F. J., Lee, P., Jaffar, J., . . . Stewart, A. G. (2017). Soft Microenvironments Effectively Suppress Fibrogenesis Pathways in Control but Not in Idiopathic Pulmonary Fibrosis (IPF)-Derived Fibroblasts. In *D29. UNRAVELING THE EXTRACELLULAR MATRIX* (pp. A7249-A7249): American Thoracic Society.

Mitke, A. B., Harris, T., Langenbach, S., Schuliga, M., Jativa, F., Lee, P., . . . Stewart, A. (2018). Softening Cellular Microenvironments Augments Glucocorticoid Actions. In

B29. LUNG ECM ENVIRONMENT: NOVEL FINDINGS AND MODELS IN FIBROSIS (pp. A2931-A2931): American Thoracic Society.

Mitke, A. B., Harris, T., Schuliga, M., Jativa, F. G., Lee, P., Jaffar, J., . . . Stewart, A. (2018). Synergism Between Glucocorticoids and Prostaglandin E₂ Modulate Fibrogenesis Pathways. In *A73. DIFFUSE PARENCHYMAL LUNG DISEASE: NOVEL MECHANISMS, BIOMARKERS, AND THERAPEUTICS* (pp. A2350-A2350): American Thoracic Society.

Moradian-Oldak, J., Leung, W., & Fincham, A. G. (1998). Temperature and pH-dependent supramolecular self-assembly of amelogenin molecules: a dynamic light-scattering analysis. *J Struct Biol, 122*(3), 320-327. doi:10.1006/jsbi.1998.4008

Morimoto, M., Liu, Z., Cheng, H. T., Winters, N., Bader, D., & Kopan, R. (2010). Canonical Notch signaling in the developing lung is required for determination of arterial smooth muscle cells and selection of Clara versus ciliated cell fate. *J Cell Sci, 123*(Pt 2), 213-224. doi:10.1242/jcs.058669

Moscona, A. (1952). Cell suspensions from organ rudiments of chick embryos. *Experimental Cell Research, 3*(3), 535-539. doi:10.1016/0014-4827(52)90077-3

Moscona, A. (1957). The Development in Vitro of Chimeric Aggregates of Dissociated Embryonic Chick and Mouse Cells. *Proc Natl Acad Sci U S A, 43*(1), 184-194. doi:10.1073/pnas.43.1.184

Moshksayan, K., Kashaninejad, N., Ebrahimi Warkiani, M., Lock, J., Moghadas, H., Firoozabadi, B., . . . Nguyen, N.-T. (2018). Spheroids-on-a-chip: Recent advances and design considerations in microfluidic platforms for spheroid formation and culture. *Sensors and Actuators B Chemical, 263*. doi:10.1016/j.snb.2018.01.223

Mottaghitalab, F., Farokhi, M., Shokrgozar, M. A., Atyabi, F., & Hosseinkhani, H. (2015). Silk fibroin nanoparticle as a novel drug delivery system. *J Control Release, 206*(206), 161-176. doi:10.1016/j.jconrel.2015.03.020

Moulton, B., & Zaworotko, M. J. (2001). From molecules to crystal engineering: supramolecular isomerism and polymorphism in network solids. *Chem Rev, 101*(6), 1629-1658. doi:10.1021/cr9900432

Mozafari, M. R., Reed, C. J., Rostron, C., & Hasirci, V. (2005). A review of scanning probe microscopy investigations of liposome-DNA complexes. *J Liposome Res, 15*(1-2), 93-107. doi:10.1081/lpr-64965

Mu, X., & Gray, D. G. (2014). Formation of Chiral Nematic Films from Cellulose Nanocrystal Suspensions Is a Two-Stage Process*(31)*, 9256.

Mueller-Klieser, W. (1987). Multicellular spheroids. A review on cellular aggregates in cancer research. *J Cancer Res Clin Oncol, 113*(2), 101-122. doi:10.1007/BF00391431

Murray, M. M., & Spector, M. (1999). Fibroblast distribution in the anteromedial bundle of the human anterior cruciate ligament: the presence of alpha-smooth muscle actin-positive cells. *J Orthop Res, 17*(1), 18-27. doi:10.1002/jor.1100170105

Murrow, L. M., Weber, R. J., & Gartner, Z. J. (2017). Dissecting the stem cell niche with organoid models: an engineering-based approach. *Development, 144*(6), 998-1007. doi:10.1242/dev.140905

Mwangi, T. K., Bowles, R. D., Tainter, D. M., Bell, R. D., Kaplan, D. L., & Setton, L. A. (2015). Synthesis and characterization of silk fibroin microparticles for intra-articular drug delivery. *International Journal of Pharmaceutics*(1-2), 7. doi:10.1016/j.ijpharm.2015.02.059

Nair, S. S., Zhu, J. Y., Deng, Y., & Ragauskas, A. J. (2014). Characterization of cellulose nanofibrillation by micro grinding. *Journal of Nanoparticle Research, 16*(4), 1-10. doi:10.1007/s11051-014-2349-7

Nakamura, T., & Sato, T. (2018). Advancing Intestinal Organoid Technology Toward Regenerative Medicine. *Cell Mol Gastroenterol Hepatol, 5*(1), 51-60. doi:10.1016/j.jcmgh.2017.10.006

Nam, K. H., Smith, A. S., Lone, S., Kwon, S., & Kim, D. H. (2015). Biomimetic 3D Tissue Models for Advanced High-Throughput Drug Screening. *J Lab Autom, 20*(3), 201-215. doi:10.1177/2211068214557813

Napolitano, A. P., Chai, P., Dean, D. M., & Morgan, J. R. (2007). Dynamics of the self-assembly of complex cellular aggregates on micromolded nonadhesive hydrogels. *Tissue Eng, 13*(8), 2087-2094. doi:10.1089/ten.2006.0190

Nematollahi, Z., Tafazzoli-Shadpour, M., Zamanian, A., Seyedsalehi, A., Mohammad-Behgam, S., Ghorbani, F., & Mirahmadi, F. (2017). Fabrication of Chitosan Silk-based Tracheal Scaffold Using Freeze-Casting Method. *Iranian biomedical journal, 21*(4), 228-239. doi:10.18869/acadpub.ibj.21.4.228

Neto, A. I., Correia, C. R., Oliveira, M. B., Rial-Hermida, M. I., Alvarez-Lorenzo, C., Reis, R. L., & Mano, J. F. (2015). A novel hanging spherical drop system for the generation of cellular spheroids and high throughput combinatorial drug screening. *Biomater Sci, 3*(4), 581-585. doi:10.1039/c4bm00411f

Nguyen, A. T., Huang, Q. L., Yang, Z., Lin, N., Xu, G., & Liu, X. Y. (2015). Crystal Networks in Silk Fibrous Materials: From Hierarchical Structure to Ultra Performance*(9-10)*, 1039.

Ninomiya, H., & Winklbauer, R. (2008). Epithelial coating controls mesenchymal shape change through tissue-positioning effects and reduction of surface-minimizing tension. *Nat Cell Biol, 10*(1), 61-69. doi:10.1038/ncb1669

Noble, P. W., Albera, C., Bradford, W. Z., Costabel, U., Glassberg, M. K., Kardatzke, D., . . . Group, C. S. (2011). Pirfenidone in patients with idiopathic pulmonary fibrosis (CAPACITY): two randomised trials. *Lancet, 377*(9779), 1760-1769. doi:10.1016/S0140-6736(11)60405-4

Numata, K., & Kaplan, D. L. (2010). Silk-based delivery systems of bioactive molecules. *Adv Drug Deliv Rev, 62*(15), 1497-1508. doi:10.1016/j.addr.2010.03.009

Nypelo, T., Rodriguez-Abreu, C., Kolen'ko, Y. V., Rivas, J., & Rojas, O. J. (2014). Microbeads and hollow microcapsules obtained by self-assembly of pickering magneto-responsive cellulose nanocrystals. *ACS Appl Mater Interfaces, 6*(19), 16851-16858. doi:10.1021/am504260u

O'Connor, M. K., & Hruska, C. B. (2005). Effect of tomographic orbit and type of rotation on apparent myocardial activity. *Nucl Med Commun, 26*(1), 25-30. doi:10.1097/00006231-200501000-00005

Ochbaum, G., & Bitton, R. (2018). Using small-angle X-ray scattering (SAXS) to study the structure of self-assembling biomaterials. In H. S. Azevedo & R. M. P. da Silva (Eds.), *Self-assembling Biomaterials* (pp. 291-304): Woodhead Publishing.

Ogawa, M., Miyata, T., Nakajimat, K., Yagyu, K., Seike, M., Ikenaka, K., . . . Mikoshibat, K. (1995). The reeler gene-associated antigen on Cajal-Retzius neurons is a crucial molecule for laminar organization of cortical neurons. *Neuron, 14*(5), 899-912.

Okabayashi, H.-F., Ishida, M., & O'Connor, C. J. (2003). The Self-Assembly of Oligopeptides. In B. H. Robinson (Ed.), *Self-Assembly*: IOSS Press.

Oksman, K., Mathew, A. P., Bondeson, D., & Kvien, I. (2006). Manufacturing process of cellulose whiskers/polylactic acid nanocomposites. *Composites Science and Technology, 66*(15), 2776-2784. doi:10.1016/j.compscitech.2006.03.002

Ortega-Arroyo, J., & Kukura, P. (2012). Interferometric scattering microscopy (iSCAT): new frontiers in ultrafast and ultrasensitive optical microscopy. *Phys Chem Chem Phys, 14*(45), 15625-15636. doi:10.1039/c2cp41013c

Ozkan, M., Pisanic, T., Scheel, J., Barlow, C., Esener, S., & Bhatia, S. N. (2003). Electro-optical platform for the manipulation of live cells. *Langmuir, 19*(5), 1532-1538.

Paik, T., Ko, D. K., Gordon, T. R., Doan-Nguyen, V., & Murray, C. B. (2011). Studies of liquid crystalline self-assembly of GdF(3) nanoplates by in-plane, out-of-plane SAXS. *ACS Nano, 5*(10), 8322-8330. doi:10.1021/nn203049t

Panalytical, M. (2021). Grazing incidence small-angle X-ray scattering (GISAXS). Retrieved from https://www.malvernpanalytical.com/en/products/technology/xray-analysis/xray-scattering/grazing-incidence-small-angle-x-ray-scattering

Pandey, J. K., Reddy, K. R., Mohanty, A. K., & Misra, M. (2014). *Handbook of polymernanocomposites. processing, performance and application*: Springer.

Pang, B., Jiang, G., Zhou, J., Zhu, Y., Cheng, W., Zhao, D., . . . Yu, H. (2020). Molecular-Scale Design of Cellulose-Based Functional Materials for Flexible Electronic Devices. *Advanced Electronic Materials, 7*(2), 2000944. doi:10.1002/aelm.202000944

Paquet-Mercier, F., Lefèvre, T., Auger, M., & Pézolet, M. (2013). Evidence by infrared spectroscopy of the presence of two types of β-sheets in major ampullate spider silk and silkworm silk. *Soft Matter, 9*(1), 208-215. doi:10.1039/c2sm26657a

Parfitt, D. A., Lane, A., Ramsden, C. M., Carr, A. F., Munro, P. M., Jovanovic, K., . . . Cheetham, M. E. (2016). Identification and Correction of Mechanisms Underlying Inherited Blindness in Human iPSC-Derived Optic Cups. *Cell Stem Cell, 18*(6), 769-781. doi:10.1016/j.stem.2016.03.021

Park, J. H., Noh, J., Schutz, C., Salazar-Alvarez, G., Scalia, G., Bergstrom, L., & Lagerwall, J. P. (2014). Macroscopic control of helix orientation in films dried from cholesteric liquid-crystalline cellulose nanocrystal suspensions. *Chemphyschem, 15*(7), 1477-1484. doi:10.1002/cphc.201400062

Patch, K., & Smalley, E. (2003). *Self-assembly: the natural way to make things* (K. Patch & E. Smalley Eds.): Technology Research News.

Pauchard, L., & Allain, C. (2003). Mechanical instability induced by complex liquid desiccation. *Comptes Rendus Physique, 4*(2), 231-239. doi:10.1016/s1631-0705(03)00027-6

Pauli, C., Hopkins, B. D., Prandi, D., Shaw, R., Fedrizzi, T., Sboner, A., . . . Rubin, M. A. (2017). Personalized In Vitro and In Vivo Cancer Models to Guide Precision Medicine. *Cancer discovery, 7*(5), 462-477. doi:10.1158/2159-8290.CD-16-1154

Pecora, R. (2000). Dynamic Light Scattering Measurement of Nanometer Particles in Liquids. *Journal of Nanoparticle Research, 2*(2), 123-131. doi:10.1023/a:1010067107182

Peng, W., Unutmaz, D., & Ozbolat, I. T. (2016). Bioprinting towards Physiologically Relevant Tissue Models for Pharmaceutics. *Trends Biotechnol, 34*(9), 722-732. doi:10.1016/j.tibtech.2016.05.013

Pereira, R. F. P., Silva, M. M., & de Zea Bermudez, V. (2015). Bombyx moriSilk Fibers: An Outstanding Family of Materials. *Macromolecular Materials and Engineering, 300*(12), 1171-1198. doi:10.1002/mame.201400276

Perez, S., & Samain, D. (2010). Structure and engineering of celluloses. *Adv Carbohydr Chem Biochem, 64*(64), 25-116. doi:10.1016/S0065-2318(10)64003-6

Petersen, T. H., Calle, E. A., Zhao, L., Lee, E. J., Gui, L., Raredon, M. B., . . . Niklason, L. E. (2010). Tissue-engineered lungs for in vivo implantation. *Science, 329*(5991), 538-541. doi:10.1126/science.1189345

Phillips, H., & Steinberg, M. (1978). Embryonic tissues as elasticoviscous liquids. I. Rapid and slow shape changes in centrifuged cell aggregates. *Journal of cell science, 30*(1), 1-20.

Phillips, H. M., & Steinberg, M. S. (1969). Equilibrium measurements of embryonic chick cell adhesiveness. I. Shape equilibrium in centrifugal fields. *Proc Natl Acad Sci U S A, 64*(1), 121-127. doi:10.1073/pnas.64.1.121

Philp, D., & Stoddart, J. F. (1996). Self-Assembly in Natural and Unnatural Systems. *Angewandte Chemie International Edition, 35*(11), 1154.

Pietra, F., Rabouw, F. T., Evers, W. H., Byelov, D. V., Petukhov, A. V., de Mello Donega, C., & Vanmaekelbergh, D. (2012). Semiconductor nanorod self-assembly at the liquid/air interface studied by in situ GISAXS and ex situ TEM. *Nano Lett, 12*(11), 5515-5523. doi:10.1021/nl302360u

Pinheiro, A. V., Han, D., Shih, W. M., & Yan, H. (2011). Challenges and opportunities for structural DNA nanotechnology. *Nat Nanotechnol, 6*(12), 763-772. doi:10.1038/nnano.2011.187

Pizzey, C. L., Pomerantz, W. C., Sung, B. J., Yuwono, V. M., Gellman, S. H., Hartgerink, J. D., . . . Abbott, N. L. (2008). Characterization of nanofibers formed by self-assembly of beta-peptide oligomers using small angle x-ray scattering. *J Chem Phys, 129*(9), 095103. doi:10.1063/1.2955745

Poesio, P., Beretta, G. P., & Thorsen, T. (2009). Dissolution of a liquid microdroplet in a nonideal liquid-liquid mixture far from thermodynamic equilibrium. *Phys Rev Lett, 103*(6), 064501. doi:10.1103/PhysRevLett.103.064501

Pohl, H. A. (1972). Electrical forming of masses of living cells. *Journal of Colloid and Interface Science, 39*(2), 437-438. doi:10.1016/0021-9797(72)90045-8

Qi, Y., Wang, H., Wei, K., Yang, Y., Zheng, R. Y., Kim, I. S., & Zhang, K. Q. (2017). A Review of Structure Construction of Silk Fibroin Biomaterials from Single Structures to Multi-Level Structures. *Int J Mol Sci, 18*(3), 237. doi:10.3390/ijms18030237

Qian, J., Li, X., Lunn, D. J., Gwyther, J., Hudson, Z. M., Kynaston, E., . . . Manners, I. (2014). Uniform, high aspect ratio fiber-like micelles and block co-micelles with a crystalline pi-conjugated polythiophene core by self-seeding. *J Am Chem Soc, 136*(11), 4121-4124. doi:10.1021/ja500661k

Qin, S., Hu, Y., Tian, X., Tian, Y., Liu, W., & Zhao, L. (2020). Modification of cellulose nanocrystals by self-assembly nucleation agents to improve poly(L-lactide) nanocomposite' properties. *Cellulose, 27*(8), 4337-4353. doi:10.1007/s10570-020-03069-x

Qin, Z.-Y., Tong, G., Chin, Y. C. F., & Zhou, J.-C. (2011). Preparation of ultrasonic-assisted high carboxylate content cellulose nanocrystals by tempo oxidation. *BioResources, 6*(2).

Radmacher, M., Tillamnn, R. W., Fritz, M., & Gaub, H. E. (1992). From molecules to cells: imaging soft samples with the atomic force microscope. *Science, 257*(5078), 1900-1905. doi:10.1126/science.1411505

Raghu, G., Collard, H. R., Egan, J. J., Martinez, F. J., Behr, J., Brown, K. K., . . . Fibrosis, A. E. J. A. C. o. I. P. (2011). An official ATS/ERS/JRS/ALAT statement: idiopathic pulmonary fibrosis: evidence-based guidelines for diagnosis and management. *Am J Respir Crit Care Med, 183*(6), 788-824. doi:10.1164/rccm.2009-040GL

Raghu, G., & Selman, M. (2015). *Nintedanib and pirfenidone. New antifibrotic treatments indicated for idiopathic pulmonary fibrosis offer hopes and raises questions*: American Thoracic Society.

Raghuwanshi, V. S., Ochmann, M., Hoell, A., Polzer, F., & Rademann, K. (2014). Deep eutectic solvents for the self-assembly of gold nanoparticles: a SAXS, UV-Vis, and TEM investigation. *Langmuir, 30*(21), 6038-6046. doi:10.1021/la500979p

Rao, X., Huang, X., Zhou, Z., & Lin, X. (2013). An improvement of the 2^(-delta delta CT) method for quantitative real-time polymerase chain reaction data analysis. *Biostatistics, bioinformatics and biomathematics, 3*(3), 71-85.

Ravi, S., & Chaikof, E. L. (2010). Biomaterials for vascular tissue engineering. *Regen Med, 5*(1), 107-120. doi:10.2217/rme.09.77

Reis, C. P., Neufeld, R. J., Ribeiro, A. J., & Veiga, F. (2006). Nanoencapsulation I. Methods for preparation of drug-loaded polymeric nanoparticles. *Nanomedicine, 2*(1), 8-21. doi:10.1016/j.nano.2005.12.003

Revol, J. F. (1982). On the cross-sectional shape of cellulose crystallites in Valonia ventricosa. *Carbohydrate Polymers, 2*(2), 123-134. doi:10.1016/0144-8617(82)90058-3

Revol, J. F., Bradford, H., Giasson, J., Marchessault, R. H., & Gray, D. G. (1992). Helicoidal self-ordering of cellulose microfibrils in aqueous suspension. *Int J Biol Macromol, 14*(3), 170-172. doi:10.1016/s0141-8130(05)80008-x

Revol, J. F., Godbout, J. D. L., & Gray, D. G. (1995). I. P. WO.

Revol, J. F., Godbout, L., Dong, X. M., & Gray, D. G. (1994, 1994). *Chiral nematic suspensions of cellulose crystallites; phase separation and magnetic field orientation*, Great Britain.

Revol, J. F., & Marchessault, R. H. (1993). In vitro chiral nematic ordering of chitin crystallites. *Int J Biol Macromol, 15*(6), 329-335. doi:10.1016/0141-8130(93)90049-r

Richeldi, L., Costabel, U., Selman, M., Kim, D. S., Hansell, D. M., Nicholson, A. G., . . . du Bois, R. M. (2011). Efficacy of a tyrosine kinase inhibitor in idiopathic pulmonary fibrosis. *N Engl J Med, 365*(12), 1079-1087. doi:10.1056/NEJMoa1103690

Richeldi, L., du Bois, R. M., Raghu, G., Azuma, A., Brown, K. K., Costabel, U., . . . Investigators, I. T. (2014). Efficacy and safety of nintedanib in idiopathic pulmonary fibrosis. *N Engl J Med, 370*(22), 2071-2082. doi:10.1056/NEJMoa1402584

Rimann, M., & Graf-Hausner, U. (2012). Synthetic 3D multicellular systems for drug development. *Curr Opin Biotechnol, 23*(5), 803-809. doi:10.1016/j.copbio.2012.01.011

Rockwood, D. N., Preda, R. C., Yucel, T., Wang, X., Lovett, M. L., & Kaplan, D. L. (2011). Materials fabrication from Bombyx mori silk fibroin. *Nat Protoc, 6*(10), 1612-1631. doi:10.1038/nprot.2011.379

Rossi, G., Manfrin, A., & Lutolf, M. P. (2018). Progress and potential in organoid research. *Nat Rev Genet, 19*(11), 671-687. doi:10.1038/s41576-018-0051-9

Sabari, J., Lax, D., Connors, D., Brotman, I., Mindrebo, E., Butler, C., . . . Foty, R. A. (2011). Fibronectin matrix assembly suppresses dispersal of glioblastoma cells. *PLOS ONE, 6*(9), e24810. doi:10.1371/journal.pone.0024810

Sacanna, S., Irvine, W. T., Chaikin, P. M., & Pine, D. J. (2010). Lock and key colloids. *Nature, 464*(7288), 575-578. doi:10.1038/nature08906

Saelee, K., Yingkamhaeng, N., Nimchua, T., & Sukyai, P. (2016). An environmentally friendly xylanase-assisted pretreatment for cellulose nanofibrils isolation from sugarcane bagasse by high-pressure homogenization. *Industrial Crops and Products, 82*, 149-160. doi:10.1016/j.indcrop.2015.11.064

Salmenpera, P., Kankuri, E., Bizik, J., Siren, V., Virtanen, I., Takahashi, S., . . . Vaheri, A. (2008). Formation and activation of fibroblast spheroids depend on fibronectin-integrin interaction. *Exp Cell Res, 314*(19), 3444-3452. doi:10.1016/j.yexcr.2008.09.004

Salmenpera, P., Karhemo, P. R., Rasanen, K., Laakkonen, P., & Vaheri, A. (2016). Fibroblast spheroids as a model to study sustained fibroblast quiescence and their crosstalk with tumor cells. *Exp Cell Res, 345*(1), 17-24. doi:10.1016/j.yexcr.2016.05.005

Salthe, S. N. (2012). Hierarchical Structures. *Axiomathes, 22*(3), 355-383. doi:10.1007/s10516-012-9185-0

Sato, M., Theret, D. P., Wheeler, L. T., Ohshima, N., & Nerem, R. M. (1990). Application of the micropipette technique to the measurement of cultured porcine aortic endothelial cell viscoelastic properties. *J Biomech Eng, 112*(3), 263-268. doi:10.1115/1.2891183

Sato, T., Vries, R. G., Snippert, H. J., van de Wetering, M., Barker, N., Stange, D. E., . . . Clevers, H. (2009). Single Lgr5 stem cells build crypt-villus structures in vitro without a mesenchymal niche. *Nature, 459*(7244), 262-265. doi:10.1038/nature07935

Schiele, N. R., von Flotow, F., Tochka, Z. L., Hockaday, L. A., Marturano, J. E., Thibodeau, J. J., & Kuo, C. K. (2015). Actin cytoskeleton contributes to the elastic modulus of embryonic tendon during early development. *J Orthop Res, 33*(6), 874-881. doi:10.1002/jor.22880

Schleich, A. (1967). Studies on aggregation of human ascites tumor cells. *Eur J Cancer, 3*(4), 243-246. doi:10.1016/0014-2964(67)90003-5

Schubert, S., Delaney, J. J. T., & Schubert, U. S. (2011). Nanoprecipitation and nanoformulation of polymers: from history to powerful possibilities beyond poly(lactic acid). *Soft Matter, 7*(5), 1581-1588. doi:10.1039/c0sm00862a

Schuliga, M., Jaffar, J., Berhan, A., Langenbach, S., Harris, T., Waters, D., . . . Stewart, A. G. (2017). Annexin A2 contributes to lung injury and fibrosis by augmenting factor Xa fibrogenic activity. *Am J Physiol Lung Cell Mol Physiol, 312*(5), L772-L782. doi:10.1152/ajplung.00553.2016

Schuliga, M., Javeed, A., Harris, T., Xia, Y., Qin, C., Wang, Z., . . . Stewart, A. G. (2013). Transforming growth factor-beta-induced differentiation of airway smooth muscle cells is inhibited by fibroblast growth factor-2. *American journal of respiratory cell and molecular biology, 48*(3), 346-353. doi:10.1165/rcmb.2012-0151OC

Schuliga, M., Javeed, A., Harris, T., Xia, Y., Qin, C., Wang, Z., . . . Stewart, A. G. (2013). Transforming growth factor–β–induced differentiation of airway smooth muscle cells Is inhibited by fibroblast growth Factor–2. *American journal of respiratory cell and molecular biology, 48*(3), 346-353.

Schuliga, M. J., See, I., Ong, S. C., Soon, L., Camoretti-Mercado, B., Harris, T., & Stewart, A. G. (2009). Fibrillar collagen clamps lung mesenchymal cells in a nonproliferative and noncontractile phenotype. *American journal of respiratory cell and molecular biology, 41*(6), 731-741. doi:10.1165/rcmb.2008-0361OC

Schutz, C., Agthe, M., Fall, A. B., Gordeyeva, K., Guccini, V., Salajkova, M., . . . Bergstrom, L. (2015). Rod Packing in Chiral Nematic Cellulose Nanocrystal Dispersions Studied by Small-Angle X-ray Scattering and Laser Diffraction. *Langmuir, 31*(23), 6507-6513. doi:10.1021/acs.langmuir.5b00924

Sebastian, A., Buckle, A. M., & Markx, G. H. (2006). Formation of multilayer aggregates of mammalian cells by dielectrophoresis. *Journal of Micromechanics and Microengineering, 16*(9), 1769. doi:10.1088/0960-1317/16/9/003/meta

Shamir, E. R., & Ewald, A. J. (2014). Three-dimensional organotypic culture: experimental models of mammalian biology and disease. *Nat Rev Mol Cell Biol, 15*(10), 647-664. doi:10.1038/nrm3873

Shi, P., & Goh, J. C. H. (2012). Self-assembled silk fibroin particles: Tunable size and appearance. *Powder Technology, 215-216*, 85-90. doi:10.1016/j.powtec.2011.09.012

Shopsowitz, K. E., Qi, H., Hamad, W. Y., & Maclachlan, M. J. (2010). Free-standing mesoporous silica films with tunable chiral nematic structures. *Nature, 468*(7322), 422-425. doi:10.1038/nature09540

Silva, T. C. F., Habibi, Y., Colodette, J. L., Elder, T., & Lucia, L. A. (2012). A fundamental investigation of the microarchitecture and mechanical properties of tempo-oxidized

nanofibrillated cellulose (NFC)-based aerogels. *Cellulose, 19*(6), 1945-1956. doi:10.1007/s10570-012-9761-x

Sim, J. H., Dong, S., Roemhild, K., Kaya, A., Sohn, D., Tanaka, K., . . . Esker, A. R. (2015). 2-Hydroxypropyltrimethylammonium xylan adsorption onto rod-like cellulose nanocrystal. *J Colloid Interface Sci, 440*, 119-125. doi:10.1016/j.jcis.2014.10.071

Sims, R. E., Mabee, W., Saddler, J. N., & Taylor, M. (2010). An overview of second generation biofuel technologies. *Bioresour Technol, 101*(6), 1570-1580. doi:10.1016/j.biortech.2009.11.046

Siró, I., & Plackett, D. (2010). Microfibrillated cellulose and new nanocomposite materials: a review. *Cellulose, 17*(3), 459-494. doi:10.1007/s10570-010-9405-y

Skalli, O., Ropraz, P., Trzeciak, A., Benzonana, G., Gillessen, D., & Gabbiani, G. (1986). A monoclonal antibody against alpha-smooth muscle actin: a new probe for smooth muscle differentiation. *J Cell Biol, 103*(6 Pt 2), 2787-2796. doi:10.1083/jcb.103.6.2787

Skardal, A., Shupe, T., & Atala, A. (2016). Organoid-on-a-chip and body-on-a-chip systems for drug screening and disease modeling. *Drug Discov Today, 21*(9), 1399-1411. doi:10.1016/j.drudis.2016.07.003

Song, Y., Lu, Z., Yang, H., Zhang, S., & Zhang, X. (2016). Dissolution of Sessile Microdroplets of Electrolyte and Graphene Oxide Solutions in an Ouzo System. *Langmuir, 32*(40), 10296-10304. doi:10.1021/acs.langmuir.6b02837

Song, Y., Yang, H., Wang, Y., Chen, S., Li, D., Zhang, S., & Zhang, X. (2013). Controlling the assembly of graphene oxide by an electrolyte-assisted approach. *Nanoscale, 5*(14), 6458-6463. doi:10.1039/c3nr01188g

Sontheimer-Phelps, A., Hassell, B. A., & Ingber, D. E. (2019). Modelling cancer in microfluidic human organs-on-chips. *Nat Rev Cancer, 19*(2), 65-81. doi:10.1038/s41568-018-0104-6

Sporty, J. L., Horalkova, L., & Ehrhardt, C. (2008). In vitro cell culture models for the assessment of pulmonary drug disposition. *Expert Opin Drug Metab Toxicol, 4*(4), 333-345. doi:10.1517/17425255.4.4.333

Steinberg, M. S. (1963). Reconstruction of tissues by dissociated cells. Some morphogenetic tissue movements and the sorting out of embryonic cells may have a common explanation. *Science, 141*(3579), 401-408. doi:10.1126/science.141.3579.401

Stepanek, M., Kosovan, P., Prochazka, K., Janata, M., Netopilik, M., Plestil, J., & Slouf, M. (2010). Self-assembly of poly(4-methylstyrene)-g-poly(methacrylic acid) graft copolymer in selective solvents for grafts: scattering and molecular dynamics simulation study. *Langmuir, 26*(12), 9289-9296. doi:10.1021/la1001682

Stetefeld, J., McKenna, S. A., & Patel, T. R. (2016). Dynamic light scattering: a practical guide and applications in biomedical sciences. *Biophysical reviews, 8*(4), 409-427. doi:10.1007/s12551-016-0218-6

Stewart, A., Harris, T., Jativa, F., Jaffar, J., Lee, P. V. S., Westall, G., . . . Berhan, A. (2019). Stiffness: A 'Master Regulator' of Human Lung Fibroblast Phenotypic Plasticity? In *A19. LESS IDIOPATHIC: STRUCTURAL AND FUNCTIONAL ABNORMALITIES IN IPF* (pp. A1043-A1043): American Thoracic Society.

Stewart, A. G., Harris, T., Wong, A., Jativa, F., Chen, W., & Lee, P. (2015). Airway Smooth Muscle Spheroids: Stiffness and Glucocorticoid Responsiveness. In *B17. ASTHMA-PHENOTYPE NICHE VIEWED THROUGH THE LENS OF PHYSICS: FOCUSED ON AIRWAY SMOOTH MUSCLE* (pp. A2470-A2470): American Thoracic Society.

Stewart, A. G., Jativa, F. R., Schuliga, M., Wang, Z., Harris, T., Jaffar, J., . . . Lee, P. V. (2016). Increased Stiffness and Changes in TGFbeta-Induced Gene Expression in

Lung Fibroblast Spheroids from IPF Fibroblasts. In *A109. REMODELING AND THE MATRIX* (pp. A7804-A7804): American Thoracic Society.

Stewart, A. G., Li, M., Langenbach, S., Harris, T., Keenan, C., Jativa, F. J., . . . Westall, G. (2017). Steroid-Enhancing Casein Kinase Inhibitors Have Anti-Fibrotic Efficacy. In *D29. UNRAVELING THE EXTRACELLULAR MATRIX* (pp. A7247-A7247): American Thoracic Society.

Stewart, A. G., Xia, Y. C., Harris, T., Royce, S., Hamilton, J. A., & Schuliga, M. (2013). Plasminogen-stimulated airway smooth muscle cell proliferation is mediated by urokinase and annexin A2, involving plasmin-activated cell signalling. *British journal of pharmacology, 170*(7), 1421-1435. doi:10.1111/bph.12422

Sutherland, R. M. (1988). Cell and environment interactions in tumor microregions: the multicell spheroid model. *Science, 240*(4849), 177-184. doi:10.1126/science.2451290

Sutherland, R. M., Inch, W. R., McCredie, J. A., & Kruuv, J. (1970). A multi-component radiation survival curve using an in vitro tumour model. *Int J Radiat Biol Relat Stud Phys Chem Med, 18*(5), 491-495. doi:10.1080/09553007014551401

Sutherland, R. M., McCredie, J. A., & Inch, W. R. (1971). Growth of multicell spheroids in tissue culture as a model of nodular carcinomas. *J Natl Cancer Inst, 46*(1), 113-120.

Swatloski, R. P., Spear, S. K., Holbrey, J. D., & Rogers, R. D. (2002). Dissolution of cellulose [correction of cellose] with ionic liquids. *J Am Chem Soc, 124*(18), 4974-4975. doi:10.1021/ja025790m

Tahiri, C., & Vignon, M. R. (2000). TEMPO-oxidation of cellulose: Synthesis and characterisation of polyglucuronans. *Cellulose, 7*(2), 177-188.

Takebe, T., & Wells, J. M. (2019). Organoids by design. *Science, 364*(6444), 956-959. doi:10.1126/science.aaw7567

Tan, H., Diddens, C., Lv, P., Kuerten, J. G., Zhang, X., & Lohse, D. (2016). Evaporation-triggered microdroplet nucleation and the four life phases of an evaporating Ouzo drop. *Proc Natl Acad Sci U S A, 113*(31), 8642-8647. doi:10.1073/pnas.1602260113

Tandon, S., Kandasubramanian, B., & Ibrahim, S. M. (2020). Silk-Based Composite Scaffolds for Tissue Engineering Applications. *Industrial & Engineering Chemistry Research, 59*(40), 17593-17611. doi:10.1021/acs.iecr.0c02195

Taniguchi, H., Ebina, M., Kondoh, Y., Ogura, T., Azuma, A., Suga, M., . . . Pirfenidone Clinical Study Group in, J. (2010). Pirfenidone in idiopathic pulmonary fibrosis. *Eur Respir J, 35*(4), 821-829. doi:10.1183/09031936.00005209

Tansil, N. C., Li, Y., Koh, L. D., Peng, T. C., Win, K. Y., Liu, X. Y., & Han, M. Y. (2011). The use of molecular fluorescent markers to monitor absorption and distribution of xenobiotics in a silkworm model. *Biomaterials, 32*(36), 9576-9583. doi:10.1016/j.biomaterials.2011.08.081

Taylor, R. W., & Sandoghdar, V. (2019). Interferometric Scattering Microscopy: Seeing Single Nanoparticles and Molecules via Rayleigh Scattering. *Nano Lett, 19*(8), 4827-4835. doi:10.1021/acs.nanolett.9b01822

Thakur, V. K., & Thakur, M. K. (2015). *Eco-friendly polymer nanocomposites : chemistry and applications*: Springer.

Theret, D. P., Levesque, M. J., Sato, M., Nerem, R. M., & Wheeler, L. T. (1988). The application of a homogeneous half-space model in the analysis of endothelial cell micropipette measurements. *J Biomech Eng, 110*(3), 190-199. doi:10.1115/1.3108430

Tronin, A., Lvov, Y., & Nicolini, C. (1994). Ellipsometry and x-ray reflectometry characterization of self-assembly process of polystyrenesulfonate and polyallylamine. *Colloid & Polymer Science, 272*(10), 1317-1321. doi:10.1007/bf00657788

Tuinier, R. (2016). A Simple Free Energy for the Isotropic-Nematic Phase Transition of Rods. *Advances in Condensed Matter Physics, 2016*, 1-6. doi:10.1155/2016/5871826

Tung, Y. C., Hsiao, A. Y., Allen, S. G., Torisawa, Y. S., Ho, M., & Takayama, S. (2011). High-throughput 3D spheroid culture and drug testing using a 384 hanging drop array. *Analyst, 136*(3), 473-478. doi:10.1039/c0an00609b

Turksen, K. (2018). *Cell biology and translational medicine*: Springer Nature.

Uetani, K., & Yano, H. (2013). Self-organizing capacity of nanocelluloses via droplet evaporation. *Soft Matter, 9*(12), 3396-3401. doi:10.1039/c3sm27822k

Vaheri, A., Enzerink, A., Rasanen, K., & Salmenpera, P. (2009). Nemosis, a novel way of fibroblast activation, in inflammation and cancer. *Exp Cell Res, 315*(10), 1633-1638. doi:10.1016/j.yexcr.2009.03.005

Vitale, S. A., & Katz, J. L. (2003). Liquid Droplet Dispersions Formed by Homogeneous Liquid−Liquid Nucleation: "The Ouzo Effect". *Langmuir, 19*(10), 4105-4110. doi:10.1021/la026842o

Vogel, N., Retsch, M., Fustin, C. A., Del Campo, A., & Jonas, U. (2015). Advances in colloidal assembly: the design of structure and hierarchy in two and three dimensions. *Chem Rev, 115*(13), 6265-6311. doi:10.1021/cr400081d

Volkov, V., Ferreira, A. V., & Cavaco-Paulo, A. (2015). On the Routines of Wild-Type Silk Fibroin Processing Toward Silk-Inspired Materials: A Review. *Macromolecular Materials and Engineering, 300*(12), 1199-1216. doi:10.1002/mame.201500179

Vollrath, F., Porter, D., & Holland, C. (2013). The science of silks. *MRS bulletin, 38*(1), 73-80.

Walker, A. A., Holland, C., & Sutherland, T. D. (2015). More than one way to spin a crystallite: multiple trajectories through liquid crystallinity to solid silk. *Proceedings: Biological Sciences, 282*(1809), 1.

Wang, A., Huang, J., & Yan, Y. (2014). Hierarchical molecular self-assemblies: construction and advantages. *Soft Matter, 10*(19), 3362-3373. doi:10.1039/c3sm53214c

Wang, H., Gurau, G., & Rogers, R. D. (2012). Ionic liquid processing of cellulose. *Chem Soc Rev, 41*(4), 1519-1537. doi:10.1039/c2cs15311d

Wang, M., Liechti, K. M., Wang, Q., & White, J. M. (2005). Self-assembled silane monolayers: fabrication with nanoscale uniformity. *Langmuir, 21*(5), 1848-1857. doi:10.1021/la048483y

Wang, P. X., & MacLachlan, M. J. (2018). Liquid crystalline tactoids: ordered structure, defective coalescence and evolution in confined geometries. *Philos Trans A Math Phys Eng Sci, 376*(2112). doi:10.1098/rsta.2017.0042

Wang, X., Yucel, T., Lu, Q., Hu, X., & Kaplan, D. L. (2010). Silk nanospheres and microspheres from silk/pva blend films for drug delivery. *Biomaterials, 31*(6), 1025-1035. doi:10.1016/j.biomaterials.2009.11.002

Wang, Y., Kim, B. J., Peng, B., Li, W., Wang, Y., Li, M., & Omenetto, F. G. (2019). Controlling silk fibroin conformation for dynamic, responsive, multifunctional, micropatterned surfaces. *Proc Natl Acad Sci U S A, 116*(43), 21361-21368. doi:10.1073/pnas.1911563116

Wenk, E., Merkle, H. P., & Meinel, L. (2011). Silk fibroin as a vehicle for drug delivery applications. *J Control Release, 150*(2), 128-141. doi:10.1016/j.jconrel.2010.11.007

Whitesides, G. M., & Boncheva, M. (2002). Beyond molecules: self-assembly of mesoscopic and macroscopic components. *Proc Natl Acad Sci U S A, 99*(8), 4769-4774. doi:10.1073/pnas.082065899

Whitesides, G. M., & Grzybowski, B. (2002). Self-Assembly at All Scales. *Science, 295*(5564), 2418.

Wicklein, B., & Salazar-Alvarez, G. (2013). Functional hybrids based on biogenic nanofibrils and inorganic nanomaterials*(18),* 5469. Retrieved from

https://search.ebscohost.com/login.aspx?direct=true&AuthType=sso&db=edsbl&AN=RN330793672&site=eds-live&scope=site&custid=s2775460

Winters, B. S., Shepard, S. R., & Foty, R. A. (2005). Biophysical measurement of brain tumor cohesion. *Int J Cancer, 114*(3), 371-379. doi:10.1002/ijc.20722

Wirz, W., Antoine, M., Tag, C. G., Gressner, A. M., Korff, T., Hellerbrand, C., & Kiefer, P. (2008). Hepatic stellate cells display a functional vascular smooth muscle cell phenotype in a three-dimensional co-culture model with endothelial cells. *Differentiation, 76*(7), 784-794. doi:10.1111/j.1432-0436.2007.00260.x

Wongpinyochit, T., Johnston, B. F., & Seib, F. P. (2016). Manufacture and Drug Delivery Applications of Silk Nanoparticles. *J Vis Exp*(116). doi:10.3791/54669

Xiao, L., Lu, G., Lu, Q., & Kaplan, D. L. (2016). Direct Formation of Silk Nanoparticles for Drug Delivery. In (Vol. 2, pp. 2050-2057).

Xu, G., Gong, L., Yang, Z., & Liu, X. Y. (2014). What makes spider silk fibers so strong? From molecular-crystallite network to hierarchical network structures. *Soft Matter, 10*(13), 2116-2123. doi:10.1039/c3sm52845f

Yan, X., Delgado, M., Fu, A., Alcouffe, P., Gouin, S. G., Fleury, E., . . . Bernard, J. (2014). Simple but Precise Engineering of Functional Nanocapsules through Nanoprecipitation*(27)*, 7030.

Yang, H., Song, Y., Downton, M. T., Wang, S., Xu, J., Hou, Z., & Zhang, X. (2015). Tailoring graphene oxide assemblies by pinning on the contact line of a dissolving microdroplet. *Soft Matter, 11*(43), 8479-8483. doi:10.1039/c5sm01731a

Yang, H., Wang, Y., Song, Y., Qiu, L., Zhang, S., Li, D., & Zhang, X. (2012). Assembling of graphene oxide in an isolated dissolving droplet. *Soft Matter, 8*(44), 11249-11254. doi:10.1039/c2sm26794b

Yang, J., Wu, K., Konak, C., & Kopecek, J. (2008). Dynamic light scattering study of self-assembly of HPMA hybrid graft copolymers. *Biomacromolecules, 9*(2), 510-517. doi:10.1021/bm701001f

Yang, Y., Dicko, C., Bain, C., Gong, Z., Jacobs, R. J., Shao, Z., . . . Vollrath, F. (2012). Behavior of silk protein at the air-water interface. *Soft Matter, 8*(37), 9705-9712.

Yeh, H.-J., & Smith, J. S. (1994). Fluidic self-assembly of microstructures and its application to the integration of GaAs on Si. *Proceedings IEEE Micro Electro Mechanical Systems An Investigation of Micro Structures, Sensors, Actuators, Machines and Robotic Systems*, 279-284. doi:10.1109/MEMSYS.1994.555822

Yong, J., Chen, F., Yang, Q., Du, G., Shan, C., Bian, H., . . . Hou, X. (2015). Bioinspired transparent underwater superoleophobic and anti-oil surfaces. *Journal of Materials Chemistry A, 3*(18), 9379-9384.

Yoon, H. H., Bhang, S. H., Shin, J. Y., Shin, J., & Kim, B. S. (2012). Enhanced cartilage formation via three-dimensional cell engineering of human adipose-derived stem cells. *Tissue Eng Part A, 18*(19-20), 1949-1956. doi:10.1089/ten.TEA.2011.0647

Zarrintaj, P., Manouchehri, S., Ahmadi, Z., Saeb, M. R., Urbanska, A. M., Kaplan, D. L., & Mozafari, M. (2018). Agarose-based biomaterials for tissue engineering. *Carbohydr Polym, 187*, 66-84. doi:10.1016/j.carbpol.2018.01.060

Zhang, D., Jian, J., Xie, Y., Gao, S., Ling, Z., Lai, C., . . . Dumont, M.-J. (2022). Mimicking skin cellulose hydrogels for sensor applications. *Chemical Engineering Journal, 427*, 130921. doi:10.1016/j.cej.2021.130921

Zhang, H., Nayak, S., Wang, W., Mallapragada, S., & Vaknin, D. (2017). Interfacial Self-Assembly of Polyelectrolyte-Capped Gold Nanoparticles. *Langmuir, 33*(43), 12227-12234. doi:10.1021/acs.langmuir.7b02359

Zhang, R., Yang, J., Chu, T. W., Hartley, J. M., & Kopecek, J. (2015). Multimodality imaging of coiled-coil mediated self-assembly in a "drug-free" therapeutic system. *Adv Healthc Mater, 4*(7), 1054-1065. doi:10.1002/adhm.201400679

Zhang, S. Y., Regulacio, M. D., & Han, M. Y. (2014). Self-assembly of colloidal one-dimensional nanocrystals. *Chem Soc Rev, 43*(7), 2301-2323. doi:10.1039/c3cs60397k

Zhang, X., Lu, Z., Tan, H., Bao, L., He, Y., Sun, C., & Lohse, D. (2015). Formation of surface nanodroplets under controlled flow conditions. *Proc Natl Acad Sci U S A, 112*(30), 9253-9257. doi:10.1073/pnas.1506071112

Zhang, X., Wang, Y., Watanabe, S., Uddin, M., & Li, D. (2011). Evaporation-induced flattening and self-assembly of chemically converted graphene on a solid surface. *Soft Matter, 7*(19), 8745-8748.

Zhang, X. H., Maeda, N., & Craig, V. S. (2006). Physical properties of nanobubbles on hydrophobic surfaces in water and aqueous solutions. *Langmuir, 22*(11), 5025-5035. doi:10.1021/la0601814

Zhang, Y. H., & Lynd, L. R. (2004). Toward an aggregated understanding of enzymatic hydrolysis of cellulose: noncomplexed cellulase systems. *Biotechnol Bioeng, 88*(7), 797-824. doi:10.1002/bit.20282

Zhao, H.-P., Feng, X.-Q., & Gao, H. (2007). Ultrasonic technique for extracting nanofibers from nature materials. *Applied Physics Letters, 90*(7), 073112. doi:10.1063/1.2450666

Zhao, Z., Gu, J., Zhao, Y., Guan, Y., Zhu, X. X., & Zhang, Y. (2014). Hydrogel thin film with swelling-induced wrinkling patterns for high-throughput generation of multicellular spheroids. *Biomacromolecules, 15*(9), 3306-3312. doi:10.1021/bm500722g

Zhao, Z., Li, Y., & Xie, M. B. (2015). Silk fibroin-based nanoparticles for drug delivery. *Int J Mol Sci, 16*(3), 4880-4903. doi:10.3390/ijms16034880

Zheng, Y., Bai, H., Huang, Z., Tian, X., Nie, F. Q., Zhao, Y., . . . Jiang, L. (2010). Directional water collection on wetted spider silk. *Nature, 463*(7281), 640-643. doi:10.1038/nature08729

Zhou, C. Z., Confalonieri, F., Jacquet, M., Perasso, R., Li, Z. G., & Janin, J. (2001). Silk fibroin: structural implications of a remarkable amino acid sequence. *Proteins, 44*(2), 119-122. doi:10.1002/prot.1078

Zhou, J., Zhang, B., Shi, L., Zhong, J., Zhu, J., Yan, J., . . . He, D. (2014). Regenerated silk fibroin films with controllable nanostructure size and secondary structure for drug delivery. *ACS Appl Mater Interfaces, 6*(24), 21813-21821. doi:10.1021/am502278b

Zhu, P., Harris, T. V., Driver, M. S., Campbell, C. B., Pratt, L. R., & Papadopoulos, K. D. (2009). Dissolution Kinetics of [Hmim][BF4] Ionic Liquid Droplets in 1-Pentanol. *The Journal of Physical Chemistry C, 113*(37), 16458-16463. doi:10.1021/jp9052693

Zupkauskas, M. (2019). *Colloidal self-assembly: particle synthesis, functionalisation and applications.* (Doctoral Dissertation). University of Cambridge, Retrieved from https://search.ebscohost.com/login.aspx?direct=true&AuthType=sso&db=edsble&AN=edsble.774694&site=eds-live&scope=site&custid=s2775460 Available from EBSCOhost edsble database.

Chapter 10: Annex

This chapter includes a detailed account of thesis contributions and the published versions of Chapter 4 and Chapter 5.

10.1 Thesis contributions

10.1.1 Chapter 4

For the development of the research presented in this chapter, I initially performed a thorough evaluation of the literature related to silk self-assembling, part of which has been included in the literature review chapter. I designed the experimental set-up, performed the dissolution experiments, characterized samples and analyzed all the data. Finally, I drafted the manuscript and prepared all the images and figures.

More specifically:

- I designed, built, and optimized the droplet dissolution experimental set-up. This includes vials acquisition and modifications, optimization of the contact angle equipment (OCA20), trial of different droplet volumes and solutions, and post-sample drying and processing (3.2).
- I prepared the (OTS)-coated silicon hydrophobic substrates (3.1.1). I ordered silk fibroin from Advanced Biomatrix (3.3.1), reagents and materials were provided by the research laboratory (3.1.4).
- I performed the droplet dissolution experiments including: samples and materials preparation, equipment set-up, image acquisitions and post processing of silk spheres (3.3.2).
- I took all the optical images of the silk spheres including the transparency images with a dotted pattern. I also measured the transmittance with a microspectrophotometer as shown in Figures 4.1, 4.2, and 4.3 (3.3.2, 3.3.3).
- I prepared all silk spheres for SEM including mounting and gold coating. I also imaged the spheres microstructure, processed the images for publication and calculated the porosity as shown in Figures 4.4, 4.5, 4.6 and 4.7 (3.3.3).

- I analyzed all the droplet dissolution data and prepared plots and figures as shown in Figures 4.8 and 4.9 (3.3.2).
- I also prepared the visual abstract shown in Figure 4.1 and all the droplet dissolution videos which are included in the supporting information of the online version of the published manuscript.

Prof. X. Zhang provided research guidance and editorial feedback throughout the research process and therefore is the only co-author of the manuscript.

10.1.2 Chapter 5

The study of cellulose self-assembly was carried out under the supervision of Prof. X. Zhang and with the collaboration of a Swedish team comprised by Dr. B. Wicklein, Dr. C. Schütz and Prof. L. Bergström, all of which are co-authors in the published version of this chapter.

As in the previous chapter, I designed and built the set-up for the dissolution experiments and performed the characterization of the cellulose spheres microstructures. I provided photos and detailed description of the set-up to the Swedish collaborators, who in turn performed Polarized Optical Microscopy (POM) to observe the birefringence domains.

More specifically:

- Cellulose nanocrystals were provided to the Melbourne and Swedish teams by Dr. M. Salajkova (3.4.1).
- I prepared a literature review on CNC self-assembling which was later expanded and included in Chapter 2 of the thesis.
- I designed, built, and optimized the CNC droplet dissolution set-up by evaluating different droplet volumes and ethanol concentrations and designed schematics as shown in Fig 5.1a. I shared a report with the literature review as well as detailed descriptions of the set-up with the collaborators (3.2.2).

- I prepared the OTS hydrophobic substrate for the dissolution experiments. I sent additional substrates to the Swedish collaborators so they can replicate the experiments (3.1.1).
- I performed the droplet dissolution dynamics experiments for different ethanol concentrations, collected all the data and dried the cellulose spheres samples (3.4.2).
- I analyzed the droplet dissolution data, prepared the plots, and calculated the dissolution rates as shown in Figure 5.2 and Table 5.1 (3.4.2).
- Dr. B. Wicklein and Dr. C. Schütz replicated the experiments and performed Polarized Optical Microscopy (POM) to observe birefringent domains and tactoids as shown in Fig 5.3 and 5.4. Dr. M. Agthe designed the cell shown in Fig 1.b (3.4.3).
- I collected and edited optical images of droplet dissolution and cellulose self-assembly as shown in Figure 5.2 and 5.5 (3.4.2).
- I dried and prepared the cellulose spheres for SEM including gold coating for each ethanol concentration. Dr. C. Schütz also performed SEM imaging of cellulose spheres. These images can be found in Fig 5.6 and 5.7 (3.4.4).
- For Transmission Electron Microscopy (TEM), I embedded the cellulose spheres in LR white resin and incubated them. Dr. S. Crawford assisted in the sectioning of cellulose spheres and we jointly conducted the staining of the ultra-thin sections. I did the TEM imaging of the cellulose sections and prepared the images for publication as shown in Fig 5.8 (3.4.4).
- I jointly designed the schematic of the CNC assembly process shown in Fig 5.9 with Dr. Wicklein and Dr. C. Schütz. I prepared the first schematics and Dr. W. the final version.
- Prof. X. Zhang and Prof. L. Bergström contributed with experimental guidance and editorial feedback.

I prepared the first manuscript draft using the literature review on CNC self-assembling, analysis of the droplet dissolution experiments and the SEM/TEM microstructure characterization. Dr. B. Wicklein reorganized the manuscript and expanded the content by including the results of the polarized light microscopy and the relevance of the observed birefringent domains in the CNC self-assembling process. As such I was assigned the first authorship while Dr B. Wicklein was qualified as communicating and last author.

10.1.3 Chapter 6

In this study, I cultured the 3D mesenchymal spheroids and built a medium-throughput method to determine their mechanical properties. For the development of this project I was trained in wet lab techniques including human cell culturing methods (monolayer and 3D), living cell imaging and cell and tissue processing for histological examination (fixing ,embedding, sectioning) and immunohistochemistry staining. I have also enhanced my SEM and TEM skills by learning the processing methods for living cells (fixation, embedding, critical point drying and staining).

More specifically:

- Ms. T. Harris prepared the cell lines from donors' lungs and we jointly passaged the cell lines. We also jointly prepared the Dulbercco's Modified Eagle's Media (DMEM) and serum-free DMEM (3.5.1, 3.5.4).
- I prepared the low adherence 96 well round plates with Poly-HEMA to be used for the culture of 3D spheroids jointly with Dr. A. Berham (3.5.5).
- I cultured the 3D spheroids by displacing cells in a flask with trypsin and re-suspending in the low-adhesion plates (3.5.1).
- I took the images of the spheroids self-assembling process at different time points. I also analyzed the self-assembling data and created plots as shown in Fig 6.2 (3.5.9).

- I fixed the spheroids with osmium tetraoxide for SEM and TEM characterization (3.5.8). I rinsed the spheroids and performed serial dilution from 0% to 100% ethanol concentration vials in 20% increments.
- I followed the critical point drying method to prepare spheroids samples for SEM. I mounted spheroids in carbon strips and gold coated them. For TEM, I embedded the spheroids in LR-white resin. Dr S. Crawford performed the sectioning, and we jointly performed the staining of the grids (3.5.8).
- I did the SEM and TEM imaging of all the samples using the electron microscope. I processed the images and prepared them for the thesis as shown in Fig. 6.3 (3.5.8).
- I processed the spheroids for IHC staining. I fixed the spheroids with NBF, washed and embedded them in agarose. Samples were processed overnight into paraffin by the Biomedical Sciences Histology Facility (3.5.6).
- I used the microtome to cut the paraffin blocks into 3 μm sections and added them to slides. I stained the samples with Mayer's Haematoxylin and Eosin. I imaged the samples as shown in Fig. 6.3c (3.5.6).
- I built, designed, and optimized the spheroids micropipette aspirations set-up. I also crafted the micropipettes used for aspiration (3.5.10).
- I cultured the spheroids, measured the mechanical properties, and collected aspiration images. I also prepared schematics of the process as shown in Fig. 6.4 (3.6).
- The image analysis software was jointly developed with Mr. Yanqi Wu (3.6). For each set of experiments, I optimized the image detection of aspiration images (3.6.1), determined aspiration length (3.6.2) and validated the aspiration results (3.6.3).
- I analyzed the aspiration data and did the statistical analyses. I created the plots shown in Fig 6.4 and Fig 6.5 and summarized the data shown in Table 6.1 (3.7).

- Finally, I also made the schematics of spheroids cross-section shown in Fig. 6.6. This project was carried under the supervision of Prof P. V. Lee and Prof. A. Stewart.

The study in which this chapter is based will be submitted for publication as myself the first author.

10.1.4 Chapter 7

For the continuation of the study of single parenchymal fibroblast cells and spheroids, I was trained in additional wet-lab techniques including cell proliferation, viability assays, drug treatment, and RT-qPCR. I also learned the techniques for immunofluorescence staining of spheroids and monocultures.

More specifically:

- As in the previous chapter, Ms. T. Harris prepared the cell lines from donors' lungs, we jointly passaged the lines (3.5.1, 3.5.3) and prepared DMEM and serum-free DMEM. I prepared the Poly-HEMA coated plates jointly with Dr. A. Berham (3.5.5).
- I cultured 3D spheroids in low adhesion plates and cultured the fibroblasts in 2D-flat bottom 96-well plates (3.5.1).
- I imaged the self-assembling process of IPF and non-IPF fibroblast spheroids jointly with Ms. T. Harris (3.5.9). I analyzed the images and created the plots shown in Fig 7.1.
- I determined the mechanical properties of IPF and non-IPF spheroids using the same micropipette aspiration set-up I designed and built from the previous chapter. Dr. Zhexing Wang and I also adapted this micropipette aspiration set-up to perform single cell aspiration and determine their mechanical properties (3.5.10).
- As previously, I for each set of micropipette aspiration experiments, I optimized the image detection of aspiration images (3.6.1), determined aspiration length (3.6.2) and

validated the aspiration results (3.6.3). I also prepared plots and schematics as shown in Fig 7.2.

- Gene expression was performed jointly with Dr A. Berhan and Ms. T. Harris (3.5.3).
- I fixed the spheroids with NBF and embedded them in agarose. Samples were processed overnight into paraffin by the Biomedical Sciences Histology Facility. I used the microtome to cut the paraffin blocks into serial sections and added them to slides (3.5.6).
- Paraffin-embedded IPF and non-IPF lung tissue was obtained from the Alfred Tissue Biobank for Interstitial Lung Disease and serial sections were cut by Ms S. Langenbach (3.5.6).
- For IHC staining of lung tissue and spheroid sections, I prepared the reagents and solutions and did Haematoxylin and Eosin (HE) and Masson's Trichrome staining jointly with Ms S. Langenbach as shown in Fig. 7.3 (3.5.6).
- The IF staining of spheroids and flat bottom plates as well as imaging was jointly performed with Ms T Harris. I processed the images for the thesis as shown in Fig 7.4 (3.5.7).

This project was carried out under the supervision of Prof P. V. Lee and Prof. A. Stewart. Part of the results on this chapter have already been published where I have been included as a co-author.

10.2 Publications

1. Reprinted under Creative Commons license (CC BY-NC 3.0). Open Access publication: Confined self-assembly of cellulose nanocrystals in a shrinking droplet, F. Jativa, C. Schütz, L. Bergström, X. Zhang and B. Wicklein, Soft Matter, 2015, 11, 5374 DOI:10.1039/C5SM00886G

2. Reprinted with permission from Transparent Silk Fibroin Microspheres from Controlled Droplet Dissolution in a Binary Solution, Fernando Jativa and Xuehua Zhang, Langmuir, 2017, 33 (31), 7780-7787, DOI: 10.1021/acs.langmuir.7b01579. Copyright 2017 American Chemical Society.

Soft Matter

PAPER

View Article Online
View Journal | View Issue

Cite this: *Soft Matter*, 2015, **11**, 5374

Confined self-assembly of cellulose nanocrystals in a shrinking droplet†

Fernando Jativa,[ab] Christina Schütz,[cd] Lennart Bergström,[c] Xuehua Zhang[b] and Bernd Wicklein‡*[d]

Received 15th April 2015,
Accepted 4th June 2015

DOI: 10.1039/c5sm00886g

www.rsc.org/softmatter

We have studied how cellulose nanocrystals (CNC) self-assemble into liquid crystalline phases in shrinking, isolated droplets. By adjusting the water dissolution rate of an aqueous CNC droplet immersed in a binary toluene–ethanol mixture we can control the final morphology of the consolidated microbead. At low ethanol concentration in the surrounding fluid dense microbeads of spherical morphology are produced while collapsed core–shell particles are obtained at high ethanol concentration. Polarized light microscopy was used to follow the spatial evolution and coalescence of birefringent spheroids during droplet shrinkage. Electron microscopy reveals the resultant nematic microstructure. This method of confined CNC assembly provides thus the possibility to prepare ordered microbeads, which can be useful as templates or for their optical properties.

Introduction

Disintegration of plant fibres by *e.g.* acid hydrolysis liberates nanocellulose in different forms.[1] The outstanding mechanical properties and good chemical durability of this biodegradable biopolymer[2] makes it an important component in the fabrication of devices and new materials for various technical and biomedical applications.[3,4] Gray and coworkers showed that the rod-like cellulose nanocrystals (CNC) can form liquid crystalline phases[5–7] and recent work has illustrated how environmentally benign high-performance materials can be designed by biomimetic self-assembly routes.[3,8] In this way, chiral nematic films can be prepared that display optical properties such as iridescence or birefringence.[9,10]

Previous work has shown that the formation of the chiral nematic phase primarily depends on the aspect ratio, the CNC concentration and on particle interactions.[5,11] Liquid crystal self-assembly competes with gelation and/or glass formation at high CNC concentrations where the mobility of the CNC rods becomes restricted locking the system into an arrested or "frozen" state.[11] While the (equilibrium) phase behavior of CNC at low and moderate concentrations (up to 1–7 vol%) is relatively well understood,[11] the assembly at higher concentrations and under confined conditions has only been sparsely investigated. Recent work by Mu and Gray[12] suggests that modifying the onset of gelling by *e.g.* the addition of glucose, can control the helicoidal arrangement of CNC rods in dried films.

While evaporation of water from a dilute dispersion of CNC that is spread onto a substrate can produce films with chiral nematic structures, studies on how to produce CNC materials with a chiral nematic structure in other shapes, *e.g.* as microspheres, are sparse. Structured nanocellulose microspheres are of interest for controlled delivery of *e.g.* drugs and fragrances.[13] Assemblies of optically active colloidal particles can also be used to produce discrete colloidal crystals with photonic properties or serve as templates for synthesis of inverted opals.[14,15] Using shape anisotropic colloids such as the rod-shaped cellulose nanocrystals opens up possibilities for producing microspheres with diverse microstructures (ordered or amorphous) and different textures (nematic, smectic, or cholesteric).[16,17]

The most common method to form spherical colloidal arrays is based on evaporation induced self-assembly of drops of colloidal dispersions.[16,18–20] However, the control over the drying rate is not always easy and may thus compromise the quality of the assembled structure.[19] Zhang and coworkers[21,22] have recently shown how two dimensional nanosheets can assemble into microspheres by dissolution of an isolated droplet dispersion that is immersed in a binary liquid phase. This method allows the dissolution rate to be controlled by the composition of the surrounding binary liquid phase and also yield assemblies in the form of microbeads.

[a] *Department of Mechanical Engineering, University of Melbourne, Parkville, VIC 3010, Australia*
[b] *Department of Civil, Environmental & Chemical Engineering, RMIT University, Melbourne, VIC 3001, Australia*
[c] *Department of Materials and Environmental Chemistry, Stockholm University, 106 91 Stockholm, Sweden*
[d] *Wallenberg Wood Science Center, KTH, Teknikringen 56, 100 44 Stockholm, Sweden. E-mail: bernd@icmm.csic.es*

† Electronic supplementary information (ESI) available. See DOI: 10.1039/c5sm00886g

‡ Present address: Materials Science Institute of Madrid-CSIC, Spain.

Here, we study shrinking droplets of aqueous cellulose nanocrystal dispersions by a combination of real-time polarized microscopy of the emerging liquid crystalline phase with electron microscopy of the surface and fractured spheres. We show that liquid crystalline tactoids that form at low shrinkage rates first occur close to the surface of the droplet and then eventually fuse together and form large ordered domains as the CNC concentration increases. The CNC assembly is arrested at high shrinkage rates and results in the formation of a rigid shell at the droplet surface that eventually results in collapsed dry spheres with a hollow interior.

Experimental section

1. Materials and chemicals

Cellulose nanocrystals (CNC) were prepared by hydrochloric acid hydrolysis of Tempo (2,2,6,6-tetramethylpiperidine-1-oxyl)-mediated oxidized cellulose nanofibres (CNF) displaying surface –COOH groups.[23] In brief, hydrochloric acid was added to 1 g of CNF to reach a final concentration of 2.5 M and the mixture was heated to 130 °C for 6 h. The reaction was quenched by dilution with deionized water. The resulting suspension was washed and the precipitant was collected and dialyzed against de-ionized water. After dialysis the suspension was sonicated for 10 min (Sonics Vibracell, USA) and centrifuged to obtain isolated nanocrystals. The concentration of the final CNC dispersion was 0.75 vol% and polyelectrolyte titration revealed a surface charge of 0.31 mmol g^{-1}. The crystals have a length distribution of 264 ± 118 nm and a thickness distribution of 2.9 ± 1.3 nm as determined by analysis of AFM images (Fig. S1, ESI†). The crystals consist of tightly packed β(1–4) linked D-glucose chains held together by extensive hydrogen bonding and van der Waals forces,[2] which effectively impede water penetration and subsequent swelling.[24]

2. Droplet dissolution rate

Dissolution of aqueous droplets containing 0.3 or 0.75 vol% CNC was carried out in 20 ml of different binary toluene–ethanol solutions containing 0.5, 1, 5, 10, and 15 vol% of ethanol, respectively. Toluene (≥99.9 vol%) and ethanol (98 vol%) were purchased from Sigma-Aldrich. Droplets of 1–10 μl were placed on hydrophobic octadecyltrichlorosilane (OTS) coated silicon substrates,[25] which were immersed in the binary solution. The experiment was performed in a glass vial that was cleaned with a sodium hydroxide solution (10 g ml^{-1}) for 30 min, rinsed with Milli-Q® water and ethanol and finally oven dried at 60 °C before usage. The dissolution dynamics were assessed by monitoring the droplet size over time. A contact angle measurement system (OCA20, Dataphysics Instruments GmbH, Germany) recorded side-view images of the shrinking droplet in a sealed glass container at different times (Fig. S2, ESI†). Each image was analyzed using automated shape recognition software (SCA202, DataPhysics Instruments), which evaluated the shape of the droplet and calculated its volume and the equivalent radius of a sphere, respectively.

3. Droplet imaging

Real-time polarized video microscopy of the liquid crystal formation in the shrinking droplets was performed using a Nikon Eclipse FN1 light microscope (Japan). The aqueous CNC-containing droplet was placed in a custom-made, aluminium container with a cover plate that has a glass window to allow for reflection polarized microscopy imaging. The container was placed between cross-polarizers and the videos were recorded using an inline camera with 2 megapixel CCD sensor (Kappa Zelos-02150C GV, Kappa Optronics GmbH, Germany). The frame rate was adjusted according to the shrinkage rate of the droplets.

4. Microstructural characterization

The surface of air-dried CNC microspheres was imaged by scanning electron microscopy (SEM). The microspheres were deposited on double-sided carbon tape and coated with either gold or carbon nanoparticles. The SEM images were acquired using a Philips XL30 field-emission (FE)-SEM and a JEOL JSM-7401F FE microscope for high-resolution SEM images. The internal structure of dried CNC spheres was characterized by transmission electron microscopy (TEM) of ultramicrotome-sectioned samples. CNC spheres were incubated twice in 100% LR-white resin and subsequently embedded in capped gelatin capsules. After a polymerization step at 60 °C for 24 h the embedded spheres were sectioned with a diamond knife on a Leica Ultracut S microtome and ultra-thin sections (90 nm) were collected onto formvar-coated TEM grids. The sections were sequentially stained with saturated uranyl acetate for 10 min and triple lead stain for 5 min[26] and viewed in an FEI Tecnai Spirit transmission electron microscope at 120 kV. Images were captured with a Gatan Eagle digital camera at a resolution of 2k × 2k pixels.

Results and discussion

Liquid crystalline phase formation in a shrinking droplet

We have followed the evolution of a liquid crystalline phase in the confined space of an isolated, shrinking CNC-containing droplet immersed in a binary toluene–ethanol mixture (Fig. 1). The contact angle of the shrinking droplet residing on the hydrophobized substrate is so high (~155°) that the spherical shape of the droplet is maintained throughout the drying process (see Fig. S3, ESI†).

Fig. 2a demonstrates that the droplet shrinkage rate greatly increases with the ethanol concentration in the surrounding toluene solution. The shrinkage curves show that the droplets initially expand (Fig. 2b), which can be related to an uptake of ethanol into the aqueous CNC dispersion. After the initial expansion, the size of the droplet decreases steadily until the shrinkage is hindered by the assembled CNC rods. The shrinkage of the droplets can be described by a linear decrease of the droplet radius, R, as a function of time (see Fig. 2). Such a shrinkage rate dependency has been observed previously and related with non-ideal mixing of multi-component droplets in partially immiscible liquids.[21,27] Additionally, convective effects can be expected from the observed droplet vibration during

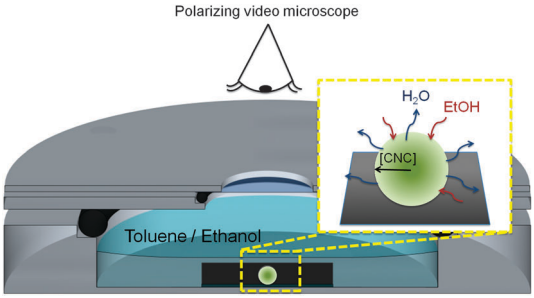

Fig. 1 Schematic of the cell used for polarized video microscopy imaging of the shrinking droplets. The CNC droplet (light green) is placed on a hydrophobic OTS-silicon substrate (black) and recorded in reflection mode. The diffusion of water and ethanol as well as the resultant radial CNC concentration gradient are illustrated.

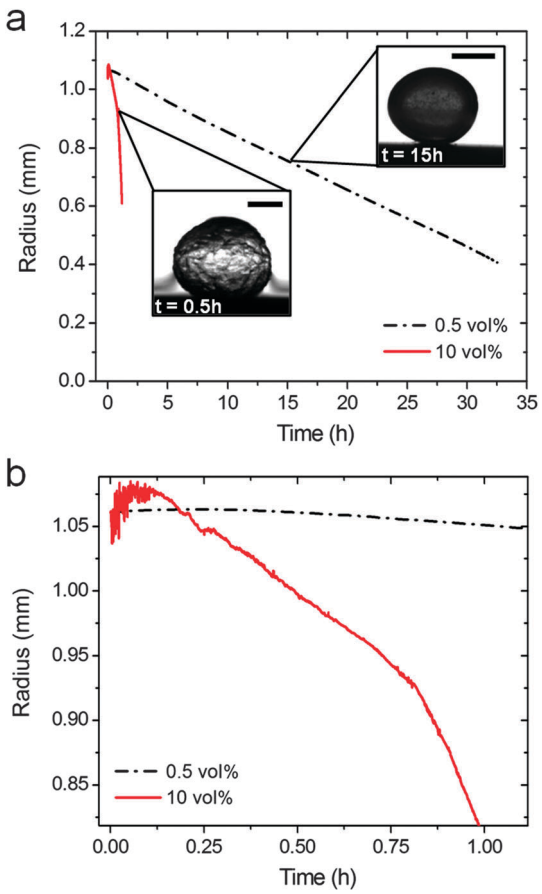

Fig. 2 Shrinkage curves of CNC-containing droplets in EtOH–toluene solutions containing 0.5 vol% EtOH (dashed line) and 10 vol% EtOH (solid line) (a). The inset photographs show side views of the shrinking droplets in the respective solutions (scale bars are 600 μm). The initial droplet volume was 5 μl and the initial CNC concentration was 0.75 vol%. The curves show the entire shrinkage process until the droplet is solidified. (b) Magnification of the shrinkage curves at the initial stage, showing the droplet expansion in 10 vol% EtOH due to the intake of the liquid from the surrounding phase and a change of slope at 0.8 h.

dissolution. Such motions can effectively disturb the boundary layer around the droplet and as a consequence significantly enhance water diffusion into the surrounding phase.[28,29] At high ethanol concentration (10 vol%) a change in the curvature of the shrinkage curve is observed (Fig. 2b). This may be related with self-propelled droplet movement on the hydrophobic substrate[28,30] during the first stage of the shrinkage process.

Table 1 tabulates the shrinkage rates for the region where the shrinking droplet radius is between 40 and 80% of the initial radius, corresponding to CNC concentrations between 1 and 13 vol%. The shrinkage rates differ by more than one order of magnitude, which provides the possibility to control the assembly dynamics and consequently the particle packing as will be discussed below.

We have followed the formation and evolution of birefringent ordered domains within the shrinking CNC dispersion droplets by polarized video microscopy, illustrated in Fig. 1. It is well established that colloidally stable CNC dispersions undergo an isotropic-to-nematic phase transformation as the CNC concentration increases and birefringent, liquid crystalline domains emerge under cross-polarized light.[6,10] The carboxylated CNC system shows a biphasic region from an onset concentration of 0.4 vol% CNC until 0.75 vol% for the fully developed liquid crystalline phase (Fig. S4, ESI†). Fig. 3 shows that as the CNC dispersion droplets shrink and the CNC concentration within the droplet increases, highly mobile spherical liquid crystalline domains, *i.e.* tactoids[6,31] are formed. The absence of black extinction lines in the polarized images of the tactoids suggests that the carboxylated cellulose nanocrystals used in this work do not develop a helical arrangement under the dynamic conditions

Table 1 Shrinkage rates for CNC droplets in different toluene–ethanol solutions

Ethanol [%]	Droplet shrinkage rate[a] [10^{-3} μm s^{-1}]	Standard deviation
0.5	5.6	0.9
1	8.3	1.3
5	33	9
10	58–230	—

[a] The shrinkage rate was calculated from the time dependent decrease of the droplet radius. The shrinkage rate was averaged by a minimum of 3 experiments for each ethanol concentration.

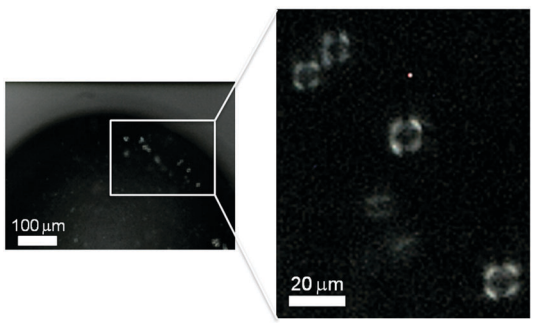

Fig. 3 Birefringent domains in the interphase region of a shrinking CNC dispersion droplet observed under polarized light. The droplet contained 0.3 vol% CNC and was immersed in a toluene/5 vol% ethanol solution. The image was taken 1.4 h after immersion. The tactoids display a Maltese cross indicating the orientation of the crossed polarisers.

of this study. In fact, the phase separation and formation of the helical pitch in dispersions of these nanocrystals is time dependent[32] and was observed only after several months of equilibrium (Fig. S5, ESI†).

The tactoids first appear close to the interface with the surrounding toluene/ethanol solvent. This observation indicates a radial CNC concentration gradient within the shrinking droplet. Previous work on self-assembling nanoparticles during evaporation-induced assembly has shown that the competition between the diffusion rate and the droplet shrinkage rate can result in significant concentration gradients close to the interface.[33] We have estimated the diffusion constant for freely rotating CNC rods and infinite dilution based on the Stoke–Einstein relation to $D = 8.1 \times 10^{-13}$ m^2 s^{-1}, which is comparable to values for CNC previously reported in literature.[34] Comparison of diffusion distances estimated from $(2Dt)^{1/2}$[33] with the droplet shrinkage rate suggests that diffusion is not able to keep up with the shrinking liquid–liquid interface when the ethanol concentration in the surrounding fluid is 5% or above. These estimates thus corroborate the observations of tactoid formation close to the liquid–liquid interface in Fig. 3. Similar solute concentration gradients were also observed in evaporating colloidal droplets leading in some cases to the so-called skin effect.[20,35]

There is a significant difference in the time-dependent evolution of the liquid crystalline phase during droplet shrinkage at 5 and 15% EtOH in the surrounding fluid. Fig. 4a shows that discrete tactoids in CNC dispersion droplets immersed in solutions containing 5% EtOH emerge about 1–2 h after immersion. The tactoids gradually grow in number and then coalesce to finally form an entirely birefringent microbead. In contrast, fast droplet shrinkage at 15% EtOH in the surrounding solution leads to a different consolidation path where large birefringent, halo-like regions instantly emerge at the interface of the droplet (Fig. 4b, 0.2 h). These metastable birefringent regions only exist for a relatively short period of time until they are replaced by large tactoids (Fig. 4b, 0.75 h) that with time merge to form a stable, birefringent shell.

The very high droplet shrinkage rate associated with this high ethanol concentration appears to result in a rapid increase of the CNC concentration at the interface, which induced the formation of a thin liquid crystalline "skin" at the droplet surface. However, the subsequent dissolution of this skin suggests that the convection inside the rapidly shrinking and erratically moving droplet may reduce the local CNC concentration below the phase boundary. After this initial stage the droplet stopped moving about and it appears that the fast droplet shrinkage produces a stable supersaturation of CNC at the interface leading to large tactoids. These highly concentrated CNC clusters can form a rigid shell-like structure, which may resist further droplet shrinkage (Fig. 5). The buckling of the shell may be due to the mechanical instability in response to the shrinkage of the droplet, similar to the buckling of the emulsion droplet shells caused by the rapid droplet contraction.[36] It should be noted that the entire droplet shrinkage process is finished after less than 2 h at 15% EtOH while the consolidation process can take as long as 37 h at 0.5% EtOH.

Microstructure of CNC microspheres

We find that the CNC assemblies formed in <5 vol% ethanol have an oblate, ellipsoid-like shape (Fig. 6a) while the assemblies formed at higher ethanol concentrations (>10 vol%) adopt a collapsed, discoidal shape (Fig. 6b). The average diameter of the dry, oblate microbeads is $\sim$300–800 μm, which corresponds to a final volume about 1–10% of the initial droplet volume. The final microbead size depends on the initially dispensed droplet volume and on the ethanol concentration, generally resulting in smaller microbeads at low shrinkage rates (*i.e.* low vol% EtOH).

The SEM image in Fig. 7a shows that the surface of the CNC microbeads displays an open, crumpled structure with multiple sheets folded one over another. In fact, the CNC rods appear to be oriented within these sheets adopting an overall nematic order with local helicoidal nanocrystal arrangement (inset Fig. 7b). The nematic texture is observed independently of the droplet shrinkage rate, reflecting thus the tactoid formation during the dissolution process.

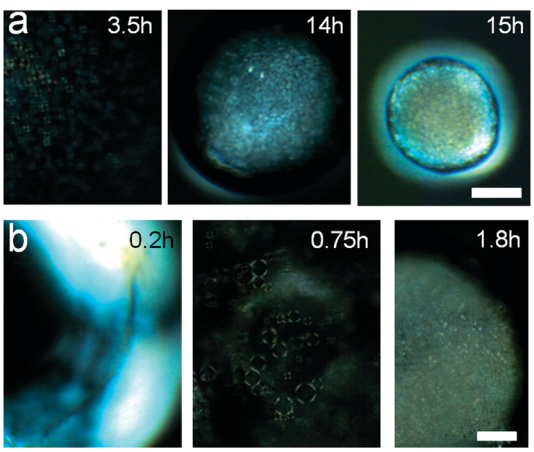

Fig. 4 The time evolution of liquid crystalline phase in shrinking CNC droplets. Reflection polarized microscopy images of a droplet in: (a) toluene/5 vol% ethanol (a) and (b) toluene/15 vol% ethanol, taken at different times during the shrinking process. The initial CNC concentration of the droplets was 0.3 vol%. Birefringent domains appear bright under cross polarized light. The scale bar is 100 μm.

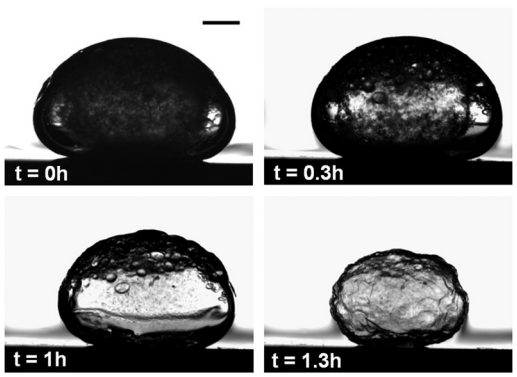

Fig. 5 Side view images of a shrinking CNC droplet with an initial volume of 10 μl in a toluene/10 vol% ethanol solution. The images show the formation of a shell-like structure during rapid droplet shrinkage. The scale bar is 600 μm.

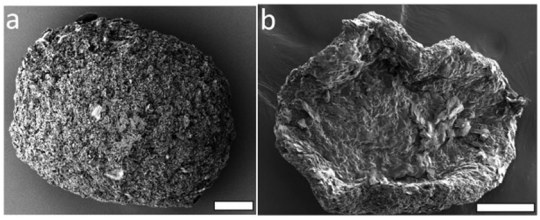

Fig. 6 SEM images of dried CNC microbeads formed in toluene solutions containing (a) 0.5 vol% and (b) 10 vol% ethanol. The scale bars are 100 μm.

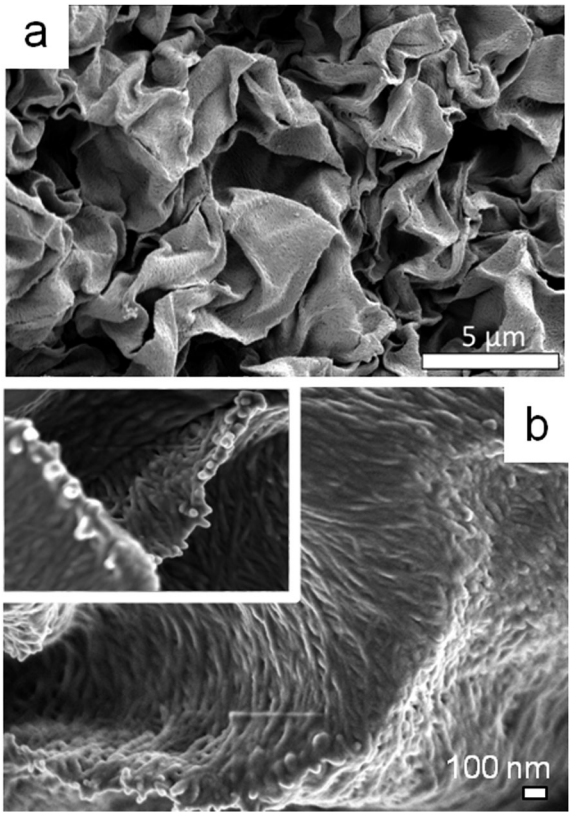

Fig. 7 SEM image of the surface of a CNC microbead formed in toluene/0.5 vol% EtOH (a). A high resolution (HR)-SEM micrograph of the surface of a microbead formed in toluene/5 vol% EtOH (b). The inset shows a magnified view on twisted CNC rods. The scale bar is for both images the same.

The TEM images of ultramicrotome-sectioned solid spheres show a textured interior with densely packed and aligned CNC rods with intercrystal distances of less than 5 nm (Fig. 8). The CNC rods display nematic ordering within discrete domains of different predominant orientations that hints to a local helical order (Fig. 8b and c). Conversely, we did not observe any pitch lines or reflection colours in the assembled spheres, which is a difference compared to thin CNC films commonly produced from slow evaporation of CNC suspensions.[8,10,12] Such films often show iridescent colours originating from the helicoidal arrangement of the nanocrystals and pitch lines during solvent evaporation. A principal reason for this difference may be related with the fast, non-equilibrium assembly of the nanocrystals

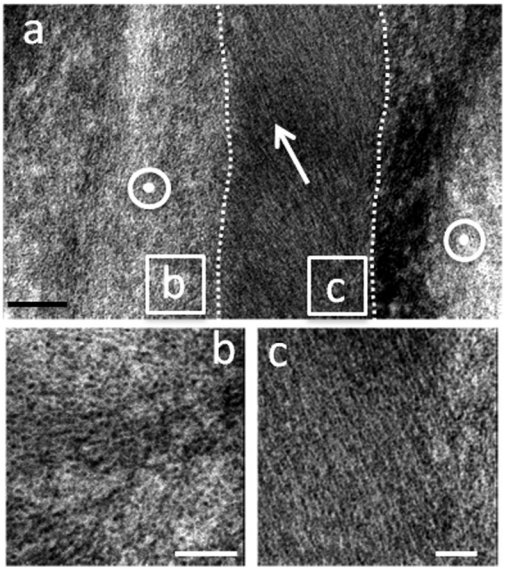

Fig. 8 The internal microstructure of a dried CNC microbead formed in toluene/1 vol% ethanol. The bead was ultramicrotome-sectioned through the centre of the particle and transmission electron microscopy reveals zones of different CNC rod orientation (separated by dotted lines) (a). The rods are aligned normal to the plane of the section (b) or in the plane (c). The circles in (a) indicate the normal orientation and the arrow the in-plane orientation. Scale bares are 100 nm (a) and 50 nm (b, c).

inside the shrinking droplets. In fact, this CNC dispersion requires several months of equilibrium before a chiral nematic phase separation occurs (Fig. S5, ESI†). This finding underpins the importance of the kinetics on cellulose nanocrystal self-assembly.[37]

Model for dissolution-driven CNC self-assembly

A schematic description summarizing the evolution of the microstructures obtained at low and at high ethanol concentration in the surrounding solvent phase is presented (Fig. 9). At ethanol concentrations below 5 vol%, the droplet shrinkage rate is sufficiently small to ensure a gradual and radial increase of the CNC concentration. This process results in the formation of liquid crystalline tactoids in the interphase region, which subsequently merge together and form an ordered, nematic phase in the entire volume of the droplet (Fig. 9a) In contrast, at high droplet shrinkage rates (Fig. 9b) the droplet immediately forms a thin and flexible birefringent "skin" at the interface (see Fig. 4b, panel 0.2 h) since the droplet dissolves very fast and the CNC concentration close to the surface rapidly jumps above the critical concentration for the isotropic-to-nematic transformation. However, this birefringent surface layer is readily disturbed or even dissolved, as evidenced by the disappearance of the bright zones (see Fig. 4b, panel 0.75 h.) as the droplet continues to shrink. Eventually, a shell surrounding a depleted, empty sphere is produced, which buckles and collapses upon drying. Such mechanical instabilities have previously been attributed to the formation of permeable rigid "skins" during the drying of colloidal sessile droplets,[20] or the dissolving of microdroplets of nanosheet suspensions.[22]

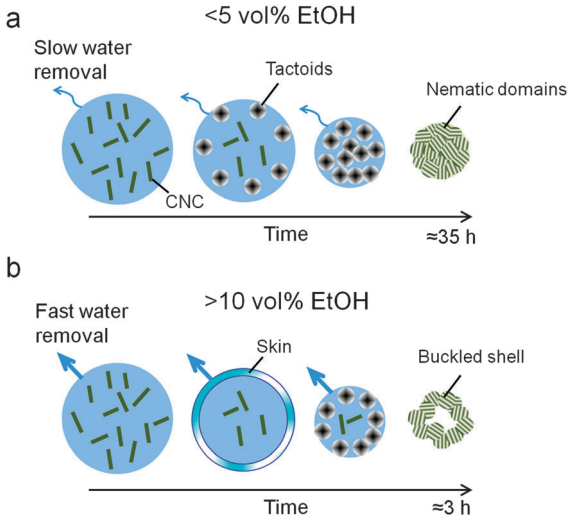

Fig. 9 Schematic description of the CNC assembly process as function of the ethanol concentration. (a) Slow water dissolution rates at <5 vol% ethanol lead to a gradual CNC concentration increase until an anisotropic CNC phase (tactoids) is formed. Over time, these tactoids merge to a solid spheroid. (b) High water dissolution rates at >10 vol% ethanol causes a rapid increase of the CNC concentration and a birefringent "skin" is formed at the interface. This layer undergoes tactoid transformation and subsequent formation of a shell covering a depleted and hollow droplet.

Conclusions

We studied the relationship of CNC self-assembly in shrinking droplets with the water dissolution rate of the droplet immersed in a binary toluene–ethanol mixture. The dissolution rate of the CNC droplet strongly depends on the composition of the bulk liquid. Dense spheroid beads were produced at low dissolution rate or collapsed discoidal particles at high water removal rates. This allows for the effective control of the morphology of the resultant colloidal assemblies by adjusting the ratio of the two liquids in the bulk phase. Remarkably, however, is that the nematic microstructure of the assemblies appears to be independent of the dissolution rate, presumably as result of the tactoid formation at early stages of the dissolution process. Self-assembling of CNCs in the confined space of isolated droplets not only provides fundamental insights in the structural evolution of liquid crystalline CNC phases but also offers precise nanostructures that can be advantageous for photonic or nanotechnological applications.

Acknowledgements

LB, BW and CS acknowledge the Wallenberg Wood Science Center and the Swedish foundation for strategic research for financial support. XHZ acknowledges the support from the Australian Research Council (FT120100473, DP140100805) and FJ thanks the Ecuadorian Government for a SENESCYT scholarship and the University of Melbourne for the "Summer research experience" program. The authors thank Michael Agthe for the design of the cell used in polarized microscopy imaging. Dr Salajkova is thanked for providing the cellulose and Cris Luengo for the MatLab script used to determine the CNC width distribution. Simon Crawford is acknowledged for his assistance with microtome sectioning and electron microscopy imaging, respectively.

References

1 I. Siró and D. Plackett, *Cellulose*, 2010, **17**, 459–494.
2 R. J. Moon, A. Martini, J. Nairn, J. Simonsen and J. Youngblood, *Chem. Soc. Rev.*, 2011, **40**, 3941–3994.
3 B. Wicklein and G. Salazar-Alvarez, *J. Mater. Chem. A*, 2013, **1**, 5469–5478.
4 A. Dufresne, *Nanocellulose: From Nature to High Performance Tailored Materials*, Walter de Gruyter, 2012.
5 J. F. Revol, L. Godbout, X. M. Dong and D. G. Gray, *Liq. Cryst.*, 1994, **16**, 127–134.
6 J. F. Revol, H. Bradford, J. Giasson, R. H. Marchessault and D. G. Gray, *Int. J. Biol. Macromol.*, 1992, **14**, 170–172.
7 Y. Habibi, L.A. Lucia and O. J. Rojas, *Chem. Rev.*, 2010, **110**, 3479–3500.
8 A. G. Dumanli, G. Kamita, J. Landman, H. van der Kooij, B. J. Glover, J. J. Baumberg, U. Steiner and S. Vignolini, *Adv. Opt. Mater.*, 2014, **2**, 646–650.
9 J. Kelly, M. Giese, K. E. Shopsowitz, W. Y. Hamad and M. J. MacLachlan, *Acc. Chem. Res.*, 2014, **47**, 1088–1096.
10 J. H. Park, J. Noh, C. Schütz, G. Salazar-Alvarez, G. Scalia, L. Bergström and J. P. F. Lagerwall, *ChemPhysChem*, 2014, **15**, 1477–1484.
11 J. P. F. Lagerwall, C. Schütz, M. Salajkova, J. Noh, J. Hyun Park, G. Scalia and L. Bergström, *NPG Asia Mater.*, 2014, **6**, e80.
12 X. Mu and D. G. Gray, *Langmuir*, 2014, **30**, 9256–9260.
13 T. Nypelö, C. Rodriguez-Abreu, Y. V Kolen'ko, J. Rivas and O. J. Rojas, *ACS Appl. Mater. Interfaces*, 2014, **6**, 16851–16858.
14 F. Li, D. P. Josephson and A. Stein, *Angew. Chem., Int. Ed.*, 2011, **50**, 360–388.
15 K. E. Shopsowitz, H. Qi, W. Y. Hamad and M. J. MacLachlan, *Nature*, 2010, **468**, 422–425.
16 S.-Y. Zhang, M. D. Regulacio and M.-Y. Han, *Chem. Soc. Rev.*, 2014, **43**, 2301–2323.
17 V. R. Dugyala, S. V. Daware and M. G. Basavaraj, *Soft Matter*, 2013, **9**, 6711–6725.
18 A. G. Marín, H. Gelderblom, A. Susarrey-Arce, A. van Houselt, L. Lefferts, J. G. E. Gardeniers, D. Lohse and J. H. Snoeijer, *Proc. Natl. Acad. Sci. U. S. A.*, 2012, **109**, 16455–16458.
19 K. Uetani and H. Yano, *Soft Matter*, 2013, **9**, 3396.
20 L. Pauchard and C. Allain, *C. R. Phys.*, 2003, **4**, 231–239.
21 H. Yang, Y. Wang, Y. Song, L. Qiu, S. Zhang, D. Li and X. Zhang, *Soft Matter*, 2012, **8**, 11249–11254.
22 Y. Song, H. Yang, Y. Wang, S. Chen, D. Li, S. Zhang and X. Zhang, *Nanoscale*, 2013, **5**, 6458–6463.
23 M. Salajková, L. A. Berglund and Q. Zhou, *J. Mater. Chem.*, 2012, **22**, 19798–19805.
24 M. Müller, C. Czihak, H. Schober, Y. Nishiyama and G. Vogl, *Macromolecules*, 2000, **33**, 1834–1840.

25 X. Zhang, N. Maeda and V. Craig, *Langmuir*, 2006, **22**, 5025–5035.
26 T. Sato, *J. Electron Microsc.*, 1968, **17**, 158–159.
27 T. Ban, T. Yamada, A. Aoyama, Y. Takagi and Y. Okano, *Soft Matter*, 2012, **8**, 3908–3916.
28 P. Poesio, G. Beretta and T. Thorsen, *Phys. Rev. Lett.*, 2009, **103**, 064501.
29 P. Zhu, T. Harris and M. Driver, *J. Phys. Chem. C*, 2009, **113**, 16458–16463.
30 T. Ban, A. Aoyama and T. Matsumoto, *Chem. Lett.*, 2010, **39**, 1294–1296.
31 Y. Bouligand, F. Livolant, F. L. The and J. De Physique, *J. Phys.*, 1984, **45**, 1899–1923.
32 C. F. Castro-Guerrero and D. G. Gray, *Cellulose*, 2014, **21**, 2567–2577.
33 T. P. Bigioni, X.-M. Lin, T. T. Nguyen, E. I. Corwin, T. A. Witten and H. M. Jaeger, *Nat. Mater.*, 2006, **5**, 265–270.
34 J. H. Sim, S. Dong, K. Röemhild, A. Kaya, D. Sohn, K. Tanaka, M. Roman, T. Heinze and A. R. Esker, *J. Colloid Interface Sci.*, 2015, **440**, 119–125.
35 R. Duggal, F. Hussain and M. Pasquali, *Adv. Mater.*, 2006, **18**, 29–34.
36 S. Sacanna, W. T. M. Irvine, P. M. Chaikin and D. J. Pine, *Nature*, 2010, **464**, 575–578.
37 C. Schütz, M. Agthe, A. B. Fall, K. Gordeyeva, V. Guccini, M. Salajkova, T. S. Plivelic, J. P. F. Lagerwall, G. Salazar-Alvarez and L. Bergström, *Langmuir*, 2015, DOI: 10.1021/acs.langmuir.5b00924.

LANGMUIR

Article

pubs.acs.org/Langmuir

Transparent Silk Fibroin Microspheres from Controlled Droplet Dissolution in a Binary Solution

Fernando Jativa[†,‡] and Xuehua Zhang*[,‡,§]

[†]Department of Biomedical Engineering, University of Melbourne, Parkville, Victoria 3010, Australia

[‡]Soft Matter & Interfaces Group, School of Engineering, RMIT University, Melbourne, Victoria 3001, Australia

[§]Physics of Fluids Group, Department of Science and Engineering, Mesa+ Institute and J. M. Burgers Centre for Fluid Dynamics, University of Twente, P.O. Box 217, 7500 AE Enschede, The Netherlands

Supporting Information

ABSTRACT: Silk is a natural polymer with a broad range of potential applications in textiles, advanced materials, biomedical devices, and drug delivery. The ability to control the morphology and assembly of silk fibroin is essential for the fabrication of silk-based structured materials. Here, we report an effective and simple approach based on droplet dissolution for weaving silk fibroin into spheres of several hundred micrometers in diameter. The spheres possess regular wrinkled microstructures on the surface and switchable transparency for visible light. To produce these silk spheres, we immersed a sessile microdrop of the silk fibroin aqueous solution in a surrounding phase of ethanol in toluene at low concentration (<10%). The droplet experienced a two-phase process: the first phase of volume expansion due to the intake of organic solvents from the surrounding phase and the second phase of droplet dissolution. The dissolution rate is closely related to the dynamics of the droplet, while the resulting microstructure of the silk microsphere is simply adjusted by the composition of the surrounding solution. At high concentrations of ethanol, silk fibroin formed a thin shell around the droplet during the initial expansion of the droplet in volume. As the droplet shrank at a later stage, the shell around the droplet wrinkled and crumpled, leading to regular ridges and crevices on the microsphere surface. This work demonstrates that controlled droplet dissolution may be explored as a novel and effective way to tailor microstructures of silk assemblies. The as-prepared silk microspheres may be potentially used as optical units or microcarriers.

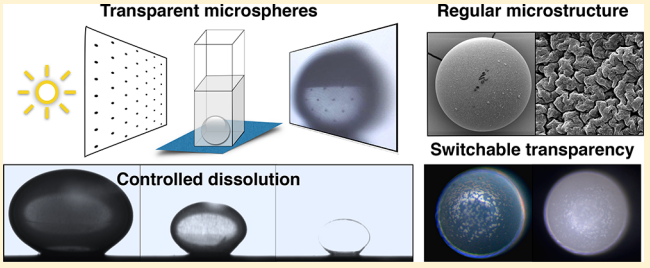

1. INTRODUCTION

As a unique natural polymer, silk possesses biocompatibility and excellent mechanical and wetting properties, promising important applications in advanced materials, biomedical devices, and drug delivery.[1−4] The ability to control the morphology and assembly of the silk fibroin is essential for the structure and functionality of silk-based materials. Several studies have evaluated the effectiveness of silk as a tool for drug delivery using self-assembled particles,[5−12] while others have focused on the development of effective protocols for the formation of the silk spheres.[13,14] Because it became possible to suspend regenerated silk fibroin in water with different concentrations, flexible solution-based methods have been developed to process silk. A recent review has summarized more than ten different methods for particle formation, including desolvation/coacervation, salting out from water, supercritical fluid technologies, electrospraying, microemulsion, and polymer blend.[9]

As an important step in many methods, an organic solvent, such as acetone or ethanol, is often used as an antisolvent, added directly into a bulk suspension of silk fibroin to induce the formation of nanoparticles. This process of dissolvation consists of reducing the solubility of the protein leading to phase separation. For instance, silk fibroin nanoparticles have been prepared by using dimethyl sulfoxide,[6] ethanol,[15] and polyvinyl alcohol.[16] In a different configuration, the dissolution of a sessile droplet of a colloidal suspension may be potentially utilized to assemble the colloids into regular assemblies with desirable microstructures. This process based on droplet dissolution is particularly flexible when the surrounding phase consists of a cosolvent and an antisolvent of the droplet liquid. It is possible to achieve a vast range of shrinkage rate by simply varying the combination and ratio of the two solvents in the surrounding phase, highly complementary to droplet evaporation-driven self-assembly and pattern formation.[17−24] The solubility of the solvents is analogical to a ternary mixture in the phenomenon named Ouzo effect,[25−27] solvent shifting, or nanoprecipitation.[28−30] Our recent work has demonstrated the possibility of droplet dissolution for assembling graphene oxide (GO) snowballs and nanocellulose microspheres.[31−33]

It is known that a pure liquid droplet on a substrate may dissolve rapidly, shrink at different rates, or even self-propel or

Received: May 11, 2017
Revised: July 9, 2017
Published: July 11, 2017

DOI: 10.1021/acs.langmuir.7b01579
Langmuir 2017, 33, 7780−7787

split in the binary solution with different ratios of the cosolvent and the antisolvent.[34−36] For a droplet comprising colloidal particle suspension, the droplet behaviors are expected to be also influenced by the properties and interactions of the colloids dispersed within the droplet. In a similar process of solubility reduction, it has been observed that silica nanoparticles in the suspension could form a thin layer upon contact with an immiscible solvent.[37,38] Considering the large size and slow diffusion of silk fibroin, we also expect that interfacial enrichment of the silk fibroin may have a significant implication for the solvent transport across the droplet and the formation of the microstructure on the superficial layer of the assembled silk.

In this work, we investigate the behaviors of a silk solution droplet on a substrate immersed in a binary solution and explore the possibility of controlling the morphology and assembly of silk proteins by the controlled droplet dissolution. The binary liquid phase consists of ethanol as the cosolvent and toluene as the antisolvent. The in situ images revealed interfacial enrichment of silk fibroins and initial volume expansion of the droplet from the intake of the surrounding phase. By the end of droplet dissolution, we obtained silk microspheres that possess regular microstructures controllable by the ratio of solvents in the surrounding phase. Interestingly, the transparency of the silk spheres to visible light is switchable by hydration and dehydration processes. We will first present the final microstructures of the silk microspheres and then the two-phase behaviors of the droplet immersed in the binary solution that led to the formation of these silk spheres. The main factor for varying the sphere morphology will be the ratio of the cosolvent and antisolvent in the surrounding phase, while other conditions (i.e., temperature, liquid volume, and initial droplet size) are constant in all experiments. We will also briefly show the effect of other antisolvents on the interfacial precipitation of silk. This work clearly demonstrates that the droplet dissolution process provides new opportunities for making silk spheres with regular and tunable surface microstructures and desirable optical properties.

2. RESULTS

2.1. Switchable Transparency of Silk Protein Microspheres. We examined the transparency of silk spheres obtained by varying the concentration of ethanol in the binary solution. Representative optical images in Figure 1 show the top view of two silk protein spheres obtained in 1 and 5% ethanol solutions. The former is transparent with some small white patches on the surface, whereas the latter is entirely white. The microspectrophotometry measurements of the as-prepared spheres show that the transmittance increases in the visible spectrum between 400 and 700 nm for both spheres. For the sphere prepared in 1% ethanol, the transmittance is above 75% at a wavelength longer than 500 nm, whereas the white sphere from 5% ethanol solution remains below 20% transmittance within the visible spectrum.

The sphere was stable and remained transparent for an extended period under ambient condition and became opaque only after drying for several days in air. The loss of transparency was possibly attributed to removal of the moisture from the sphere surface with time. When exposed to water, however, the sphere became transparent again in less than 1 min.

To reveal the recovered transparency of the sphere in water, we tried to see through the sphere immersed in water and were able to obtain a clear image of a pattern of regular dots printed on a piece of white paper. The dot pattern in Figure 2A was placed in front of the sphere that was submerged in water in Figure 2B. Light was illuminated first through the white paper with the pattern, then through the sphere, and finally reached the camera. The image recorded by the camera (Figure 2C) shows the dot pattern with the alignment matching the one printed on the paper, exactly similar to an image obtained through a transparent glass marble. This test confirmed the underwater transparency of the assembled silk sphere. When the hydrated sphere was taken out from water, it remained transparent, and once dried after a long period, it turned into white color again. This process of hydration and dehydration could be repeated to make the sphere transparent and opaque correspondingly. For comparison, the spheres prepared in 0.5% ethanol solution showed similar optical properties. However, the dry sphere prepared in 5% ethanol solution was opaque all of the time both in air and in water.

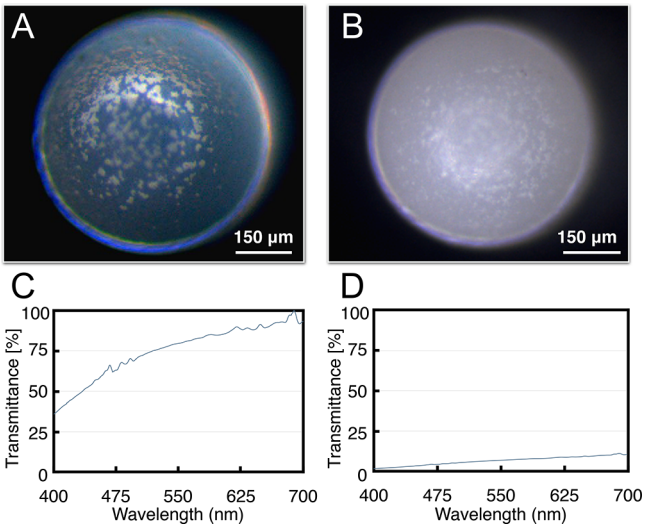

Figure 1. Optical images of two silk microspheres in air. (A) Transparent silk protein sphere prepared in 1% ethanol solution. (B) Opaque silk protein sphere prepared in 5% ethanol solution. Transmittance spectrum for the spheres obtained in 1% (C) and 5% (D) ethanol solution.

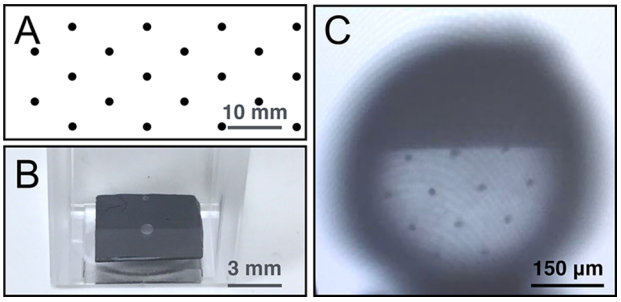

Figure 2. Transparency of the hydrated sphere. (A) Dotted pattern printed on a piece of paper that was placed behind the silk sphere. (B) Transparent silk sphere immersed in water. Before immersion in water, the sphere was obtained from droplet dissolution in 1% ethanol solution and then dried in air for several days. (C) Optical image of the dotted pattern observed through the sphere.

2.2. Surface Microstructures of Transparent and Opaque Silk Spheres. The detailed morphology of the prepared silk spheres was characterized by a scanning electronic

DOI: 10.1021/acs.langmuir.7b01579
Langmuir 2017, 33, 7780−7787

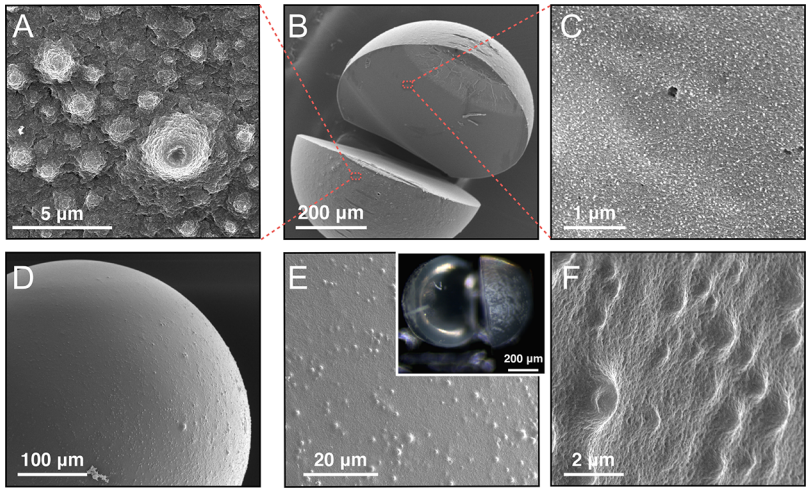

Figure 3. SEM images of two transparent silk spheres formed in (A−C) 1% ethanol solution and (D−F) 0.5% ethanol solution. (A) Outer surface of 1% ethanol spheres presents small truncated cones. (B,C) Inside of the spheres is highly regular with only slight imperfections. (D−F) Sphere obtained by 0.5% ethanol solution shows similar truncated microcones on the surface but with lower numbers and a smoother surrounding area. The inset in (E) shows the optical image of the transparent sphere that is cut in half.

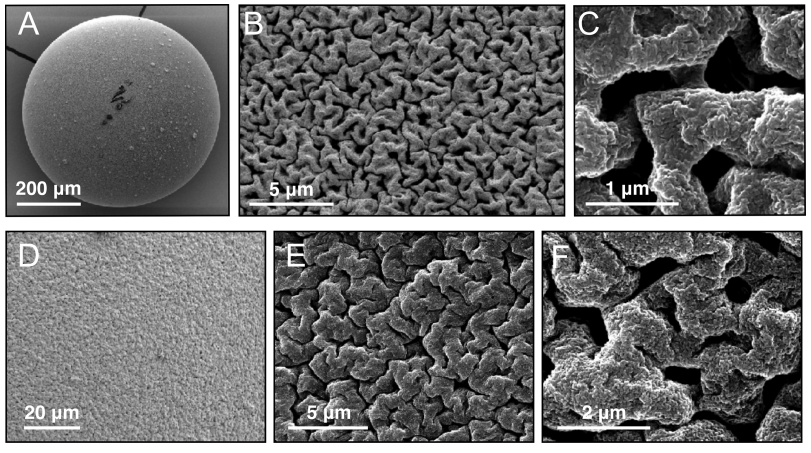

Figure 4. SEM images of white silk spheres. SEM image of the sphere formed in toluene solutions containing 5 vol % (A−C) and 7% (D−F) ethanol solution.

microscope (SEM) as shown in Figures 3 and 4. We observed submicron bumps over the surface of the sphere obtained from the droplet dissolution in 1% ethanol solution. Similar morphological structures were also observed for spheres prepared from a lower ethanol concentration. Figure 3 shows a smoother surface covered with submicrometer bumps when 0.5% ethanol solution was used as the surrounding phase. Careful examination of the inner structure by cutting through the sphere shows that the inside is solid and uniform.

The images in Figures 4 and 5 show the sectional and superficial surface microstructures of the spheres obtained in 5 and 7% ethanol solutions. These spheres are nontransparent with morphological structures that are significantly different from transparent silk spheres prepared from the solution with low concentration of ethanol. There are ridges and crevices on the sphere surface, like the morphology of a walnut. The image analysis reveals that the ridges are ∼500 nm on average in width. They are uniform and are present over the entire sphere surface. The ridges are more densely packed on the sphere obtained in 7% ethanol solution. There are some clear imperfections, and nonuniform layers cross the sectional surfaces. From the solution with the concentration of ethanol

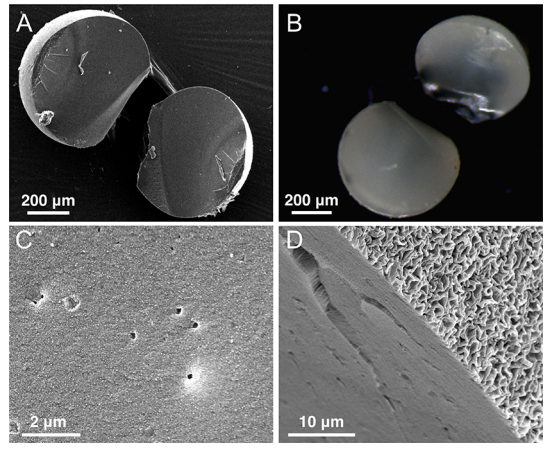

Figure 5. Inner structures of nontransparent silk spheres prepared in 5% ethanol solution. (A) SEM and (B) optical images of nontransparent sphere after being cut through. (C,D) Image of the sectional surface of the cut sphere. There are some imperfections and several nonuniform layers cross the surface.

DOI: 10.1021/acs.langmuir.7b01579
Langmuir 2017, 33, 7780−7787

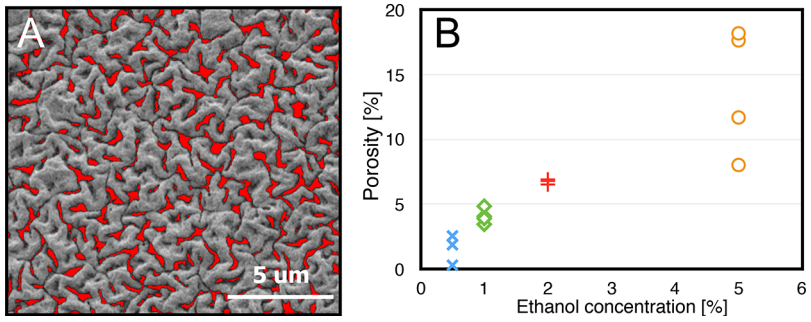

Figure 6. Surface porosity calculation. (A) Example of a threshold for a given surface image. (B) Surface porosity of the silk microspheres as a function of ethanol concentration in the surrounding phase. As the ethanol concentration is lower, the spheres are more smooth.

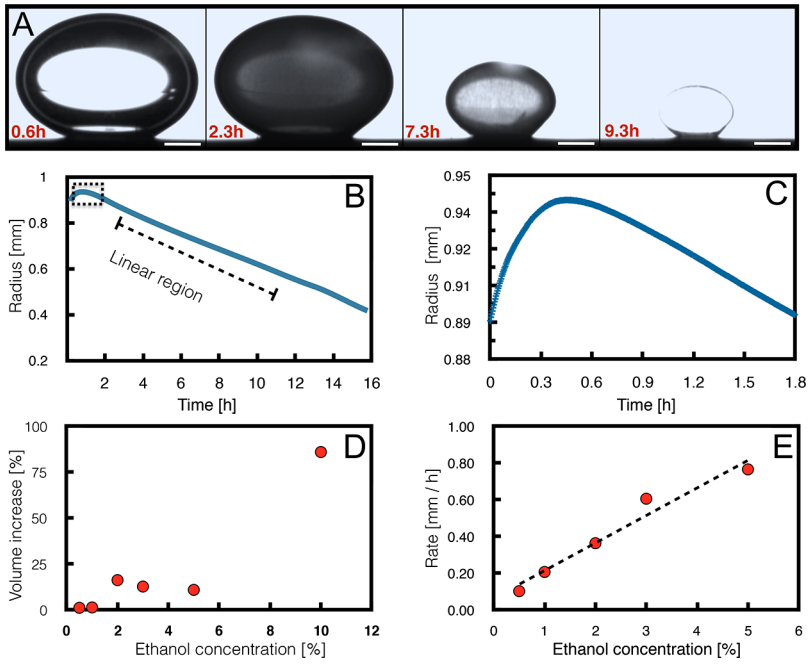

Figure 7. Silk fibroin 3 μL droplet in 2% ethanol solution. (A) Time-course snapshots of the droplet. Initially precipitation of fibroin proteins makes the droplet opaque. As the droplet shrank, it became transparent again, resulting in a transparent 3D silk sphere by the end. The length of scale bars in the images is 400 μm. (B) Plot of the radius of silk fibroin droplet as a function of time. Here, the radius is equivalent to a half of the maximal lateral extension of the droplet. (C) At the beginning, there is an increase in the drop volume as organic solvents diffuse in the droplet to achieve equilibrium. (D) Volume increase from the first phase of the droplet immersed in the solution of different ethanol concentrations. (E) Plot of silk dissolution rates as a function of the ethanol concentration.

above 10%, we could not obtain spherical silk structures anymore because the droplet dissolved rapidly upon contact with the surrounding phase.

We took several SEM images of the surface of each sphere and analyzed the surface porosity of the spheres. The plot in Figure 6 shows that the surface porosity of the silk surface increases with the increase in the ethanol concentration in the solution up to 5%.

2.3. Dynamical Behaviors of the Silk Solution Droplet in the Binary Solution. To understand the dependence of the morphological features of the silk spheres on the composition of the binary solution, we followed the evolution of a silk droplet upon immersion into the surrounding phase with different concentrations of ethanol. The initial concentration of ethanol in the solution was set from 0.5 to 10%. The drop shrinkage was recorded for the entire duration of the dissolution. The representative time course snapshots of the droplet in 2% ethanol solution at different dissolution times are shown in Figure 7A. The videos are provided in the Supporting Information.

The plots of the droplet radius as a function of time in Figure 7B,C show typical two-phase dynamics. The initial phase is marked by an increase in the droplet size. Compared with the initial droplet volume, a substantial increase in the droplet volume by 16% was observed for the first half an hour after immersion of the droplet in the binary solution at 2% ethanol concentration. The most significant droplet expansion was observed in 10% ethanol solution, reaching ~80% volume increase. By contrast, negligible volume expansion was observed at the concentration of ethanol below 1%. The results suggest that the volume expansion is influenced by the concentration of ethanol in the surrounding phase. After a peak in the volume, the droplet gradually transited to dissolution, and the second phase commenced. The most important feature in the second phase is the approximate linear relationship between the droplet radius and dissolution time as shown in Figure 7C.

DOI: 10.1021/acs.langmuir.7b01579
Langmuir 2017, 33, 7780−7787

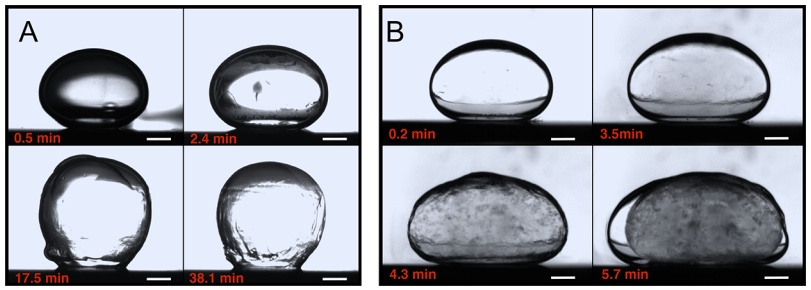

Figure 8. Snapshots of silk solution droplet in (A) 10% ethanol in toluene and (B) decane solutions. At the beginning, there is an increase in the drop volume as the ethanol diffuse in the droplet. Initial precipitation of fibroin proteins makes the droplet opaque. The fibroin forms a skin around the droplet. Length of the scale bar: 400 μm.

To quantify the dissolution rate of the silk droplet in the second phase, we fit the linear region in the plot of droplet radius versus time with a line as shown in Figure 7B. The shrinkage rate of the droplet radius at the second phase is represented by the slope of the linear fitting in the second phase. The plot of the dissolution rate as a function of the ethanol concentration in Figure 7E shows that the dissolution rate is faster with increase in the concentration of ethanol in the solution. The dissolution rate increased by ~8 times as the concentration of ethanol in the surrounding phase increased from 0.5 to 5%, suggesting that the dissolution rate of the droplet is finely tunable by the concentration of ethanol in the bulk phase.

We also noticed that a thin layer gradually spread from the bottom of the droplet, and then, the entire droplet becomes black in the video. Interestingly, near the end of the shrinkage, the droplet slowly became transparent again as shown in Figure 7A. The initial volume expansion and the shell formation are particularly pronounced in the solution with a high concentration of ethanol. Figure 8 shows some representative snapshots of droplets in 10% ethanol solutions. The droplet volume increased rapidly and reached 1.7 times the initial volume in the first half an hour. Such rapid expansion in the droplet volume clearly suggests quick intake of a large volume of liquid from the surrounding phase. It is evident that a thin shell of the protein formed at the droplet surface and wrinkled as the droplet volume reduced. Such initial volume expansion and shell formation were also observed for the binary solution of ethanol and decane, where all of the silk precipitated very quickly, and the aqueous droplet even moved away from the empty silk shell in Figure 8B.

Once the dissolution process was complete, all bulk liquids were carefully removed from the system and the spheres were left in air to dry naturally. Depending on the binary solution which the droplet was immersed in, the spheres shrank to a different extent from drying. Following a solution of 2% ethanol, no sphere compression was observed. However, after the solution of 10% ethanol, the sphere size decreased by 40% after drying. The extent of the sphere shrinkage lay in between for intermediate ethanol concentrations. This compression may further alter the microstructures of the spheres and hence their optical properties. Consequently, the spheres prepared in 5% ethanol solution were not transparent in air, although they were by the end of the droplet dissolution.

3. DISCUSSION

The above two-phase behavior of a silk droplet in the binary solution is similar to that reported for a droplet consisting of other nanocolloids, such as GO or nanocellulose,[31,33,39] which also exhibited an initial growth phase and then a dissolution phase upon immersion in a binary solution. The dissolution rate in the second phase generally increased with the concentration of the cosolvent in the surrounding phase. However, compared with these colloidal suspensions, the duration of the initial expansion phase is approximately 10 times longer for a silk droplet. On the other hand, a droplet of pure water or electrolyte solutions in the binary solution did not experience the first phase of expansion; instead, it dissolved much faster in the first phase than in the second phase.[39] The substantial intake of organic solvents from the binary solution may be due to gel-like structures of silk fibroin at the interface,[40] which delays the establishment of an interfacial zone around the droplet and the transition to the dissolution phase. In our view, the duration of the initial expansion is influenced most significantly by the concentration of the cosolvent in the surrounding phase and the interfacial behaviors of the dispersed colloids in the droplet. Compared with the interfacial properties of the dispersed colloids or molecules, how strong they bind water molecules in the bulk may be less important, given that their initial concentration is so low in the droplet. Therefore, we did not observe an initial expansion for an electrolyte solution droplet. The expansion of GO suspension droplet was not as significant as silk, although GO was also well-dispersed in water.

The intake of organic solvents from the surrounding phase may have significant implications on the stability and behaviors of the protein in the droplet. It is expected that mixing the organic solvents in the droplet may lead to changes in protein spatial structures and formation of the aggregates. In several relevant systems, Chen et al. have extensively studied silk protein stability when ethanol is added to a silk 2D film or aqueous solution.[41,42] They showed that adding ethanol to a silk solution created a phase in which β-sheets formed. The rate of β-sheet nucleation was proportional to the ethanol concentration in the solution. Furthermore, they also showed that β-sheet formation follows three steps: slow β-sheet nucleation, fast aggregation, and finally slow perfection.[41] The presence of β-sheet in assembled structures may contribute to the transparency of the spheres prepared under the conditions with low ethanol concentration.

When a droplet is in contact with the solution at high concentration of ethanol (i.e., 10% in toluene or in decane), the rapid intake of organic solvents and the mixing between water and organic solvent in the interfacial zone of the droplet contribute to interfacial precipitation of proteins and the formation of a shell around the droplet. Later on, this shell became crumpled and wrinkled from compression owing to

DOI: 10.1021/acs.langmuir.7b01579
Langmuir 2017, 33, 7780−7787

droplet dissolution, and therefore, the as-prepared silk spheres acquired such a distinct surface morphology full of crevices and ridges. When the concentration of ethanol is reduced to 2% or even less, the slow intake of organic solvents into the droplet may not induce a large amount of aggregation at an initial stage, which explains the initial transparency of the droplet. However, as the droplet dissolved with time, more aggregates formed, and consequently, the droplet became opaque. The transparency acquired by the droplet at the late stage may be attributed to the rearrangement of the silk with droplet dissolution. The slow dissolution rate at low concentration of ethanol may also explain the absence of strong shell formation and less rough surface of the final silk sphere.

The transparency of the silk spheres could be preserved for a few days in air, suggesting its prolonged stability. The moisture on the sphere surface layer appears to be important for the high transparency. As the sphere becomes completely dehydrated in air, it becomes opaque. The dehydrated microspheres are rehydrated in short time upon immersion in water, suggesting possibly that the hydration of only the interfacial layer is essential. The mechanism for this switchable transparency of the silk microsphere may be different from the well-known optical properties of Japanese skeleton flowers.[43] The color of this white flower originates from the reflection of light from the structures of the dry petals. The wet petals become transparent when it rains because of the refractive index matching between water trapped in the petals and the cellular interface.[43] Although water is essential for the transparency of both the flower and the silk sphere, the former turns white as soon as the surrounding medium changes to air. However, the silk spheres are transparent under water and remain so even after being taken out into air, as long as the top layer remains moisturized. Furthermore, the silk spheres can remain transparent after being cut into half (see the images in Supporting Information).

Intake of organic solvents may also lead to the oversaturation of toluene and the nucleation of toluene nanodroplets in the interfacial zone of the droplet. This phenomenon of the spontaneous formation of nanodroplets is analogous to Ouzo effect,[25−27] solvent shifting, or nanoprecipitation in a bulk ternary mixture;[28−30] surface nanodroplets by solvent exchange;[44] or the formation of nanodroplets in an Ouzo droplet owing to preferential evaporation of the cosolvent.[45] These toluene microdroplets may be coated and stabilized by the fibroin as the droplet shrank at the second phase, leading to the submicrometer bumps on the silk spheres. Elimination of these microbumps in future work may be a way to further improve the transparency of the silk spheres.

4. CONCLUSIONS

In summary, we demonstrate that controlled droplet dissolution in a binary surrounding phase may be an effective approach to obtain silk spheres with tunable surface microstructures. The ratio of the cosolvent and the antisolvent in the surrounding phase is essential for adjusting the surface morphology and transparency of the assembled silk spheres. Upon immersion in the solution, the droplet intakes the organic phase, which showed significant influence on the stability and arrangement of the silk in the later phase of the droplet dissolution. At low concentrations of the cosolvent, the initial volume expansion from solvent intake is less and the subsequent dissolution rate is also slower. The as-prepared sphere acquired less rough surface and exhibited switchable transparency. At high concentrations of the cosolvent and fast expansion−dissolution rates, a thin shell of the precipitated protein formed, wrapping around the droplet. Wrinkling and crumpling of the shell with droplet dissolution gave rise to the ridges and crevices on the surface of the assembled silk spheres. The process based on the droplet dissolution is simple, versatile, and effective in tuning the detailed surface microstructures of a silk sphere. The transparent spheres may be used as an optical element under water. Although not transparent, the silk spheres with a rough surface may be potentially used as microcarriers owing to their tunable porosity.

5. EXPERIMENTAL SECTION

5.1. Materials and Chemicals. The silk from the supplier (Advanced BioMatrix, San Francisco USA) was a partially hydrolyzed silk fibroin II solution at the concentration of 5% (w/v). Toluene (99.9 vol %, Sigma-Aldrich) and ethanol (98 vol %, Sigma-Aldrich) were used as received. Water was prepared from a Milli-Q unit (18.2 MΩ·cm, Millipore, Merck Australia). A glass vial was used as the container for the droplet dissolution. The vial was cleaned with a sodium hydroxide solution, rinsed with water and ethanol, and dried in an oven at 60 °C before use. The hydrophobic substrates were octadecyltrichlorosilane (OTS)-coated silicon substrates, which were prepared by following the protocols in literature.[46−48]

The silk from the supplier (Advanced BioMatrix, San Francisco USA) was a partially hydrolyzed silk fibroin II at the concentration of 5% (w/v) in an aqueous solution. To prepare the solution, whole cocoons, harvested from domesticated *Bombyx mori* in China, were degummed and processed into a liquid protein solution using heavy inorganic salts. The solution was then desalted, tested, and packaged. One of the key features of the silk fibroin solution is the preservation of the fibroin light chain at around 25 kDa.

5.2. Setup for the Droplet Dissolution. The binary solution of ethanol and toluene of different concentrations was put inside of the glass vial. The substrate of OTS−Si was placed at the bottom of the vial. A droplet of 3 μL of silk solution was placed above the substrate, and then, the top of the vial was sealed by a film to avoid solvent evaporation. A contact angle measurement system (OCA20, DataPhysics Instruments GmbH, Germany) was used to monitor and record the droplet with time. The side-view video of the droplet was analyzed using shape recognition software (SCA202, DataPhysics Instruments) to obtain droplet height, volume, and contact angle. At the end of the droplet dissolution, the solution was removed carefully and the silk spheres were taken out for characterization. For comparison, we tested the process of drying a drop of silk fibroin solution on the same substrate in air. In this way, we did not obtain a silk sphere, but a spherical cap due to the smaller contact angle of the drop in air and the pinned boundary of the evaporating drop.

5.3. Characterization of the Microstructure of Silk Microspheres. The microstructure of the silk spheres was examined using a field-emission scanning electron microscope (FESEM). Dry silk sphere samples were mounted onto 12 mm aluminum stubs with double-sided carbon tabs. The samples were then coated with gold using a Xenosput sputter coater (Dynavac, Wantirna South, Australia) and imaged with a Philips XL30 field-emission scanning electron microscope (Philips, Eindhoven, Netherlands) at a voltage of 2.0−15 kV.

To cut a sphere, we first placed it in the SEM stub adhesive surface and proceeded to cut it by pressing against a blade. To examine whether the cutting process might influence the morphology of the sectional surface, we cut several spheres and found that sectioned spheres exhibit similar features in their internal structure, suggesting the nanostructures in the inner area of the sphere were not affected. We also observed some fractures and cracks on the sphere caused by cutting, for example, as shown in the top panels of Figure 3.

The silk absorbance and transmittance spectra were obtained using a microspectrophotometer (CRAIC Technologies, USA) equipped with a 15× objective and a xenon lamp. The spectra were recorded in the visible range of 400 and 700 nm, at 50 scans per measurement.

DOI: 10.1021/acs.langmuir.7b01579
Langmuir 2017, 33, 7780−7787

The data were analyzed with proprietary spectral software. The surface pore (porosity) area fraction was determined from SEM images by using image analysis software (ImageJ). Images from different areas of the sphere were analyzed to determine the averaged surface porosity area fraction on the silk sphere.

■ ASSOCIATED CONTENT

Supporting Information

The Supporting Information is available free of charge on the ACS Publications website at DOI: 10.1021/acs.langmuir.7b01579.

Dissolving droplets in the surrounding phase of 1, 2, 5 and 10% ethanol in toluene, and of 10% ethanol in decane (AVI)

Blackening of the entire droplet (AVI)

Initial volume expansion and shell formation (AVI)

Wrinkling and crumpling of the shell with droplet dissolution (AVI)

■ AUTHOR INFORMATION

Corresponding Author

*E-mail: xuehua.zhang@rmit.edu.au.

ORCID

Xuehua Zhang: 0000-0001-6093-5324

Notes

The authors declare no competing financial interest.

■ ACKNOWLEDGMENTS

X.Z. acknowledges the support from the Australian Research Council (FT120100473, DP140100805). We also acknowledge technical support from the RMIT Micro-Nano Research Facility and discussions with Helmuth Moehwald on quantification of the porosity. F.J. acknowledges the support from the Ecuadorian Government for a SENESCYT scholarship.

■ REFERENCES

(1) Zheng, Y.; Bai, H.; Huang, Z.; Tian, X.; Nie, F.-Q.; Zhao, Y.; Zhai, J.; Jiang, L. Directional Water Collection on Wetted Spider Silk. *Nature* **2010**, *463*, 640−643.

(2) Volkov, V.; Ferreira, A. V.; Cavaco-Paulo, A. On the Routines of Wild-Type Silk Fibroin Processing Toward Silk-Inspired Materials: A Review. *Macromol. Mater. Eng.* **2015**, *300*, 1199−1216.

(3) Koh, L.-D.; Cheng, Y.; Teng, C.-P.; Khin, Y.-W.; Loh, X.-J.; Tee, S.-Y.; Low, M.; Ye, E.; Yu, H.-D.; Zhang, Y.-W.; Han, M.-Y. Structures, Mechanical Properties and Applications of Silk Fibroin Materials. *Prog. Polym. Sci.* **2015**, *46*, 86−110.

(4) Qi, Y.; Wang, H.; Wei, K.; Yang, Y.; Zheng, R.-Y.; Kim, I.; Zhang, K.-Q. A Review of Structure Construction of Silk Fibroin Biomaterials from Single Structures to Multi-Level Structures. *Int. J. Mol. Sci.* **2017**, *18*, 237.

(5) Wang, X.; Yucel, T.; Lu, Q.; Hu, X.; Kaplan, D. L. Silk Nanospheres and Microspheres from Silk/PVA Blend Films for Drug Delivery. *Biomaterials* **2010**, *31*, 1025−1035.

(6) Kundu, J.; Chung, Y.-I.; Kim, Y. H.; Tae, G.; Kundu, S. C. Pharmaceutical Nanotechnology: Silk Fibroin Nanoparticles for Cellular Uptake and Control Release. *Int. J. Pharm.* **2010**, *388*, 242−250.

(7) Numata, K.; Kaplan, D. L. Silk-Based Delivery Systems of Bioactive Molecules. *Adv. Drug Delivery Rev.* **2010**, *62*, 1497−1508.

(8) Wenk, E.; Merkle, H. P.; Meinel, L. Review: Silk Fibroin As a Vehicle for Drug Delivery Applications. *J. Controlled Release* **2011**, *150*, 128−141.

(9) Zhao, Z.; Li, Y.; Xie, M.-B. Silk Fibroin-Based Nanoparticles for Drug Delivery. *Int. J. Mol. Sci.* **2015**, *16*, 4880−4903.

(10) Mwangi, T. K.; Bowles, R. D.; Tainter, D. M.; Bell, R. D.; Kaplan, D. L.; Setton, L. A. Pharmaceutical Nanotechnology: Synthesis and Characterization of Silk Fibroin Microparticles for Intra-Articular Drug Delivery. *Int. J. Pharm.* **2015**, *485*, 7−14.

(11) Mottaghitalab, F.; Farokhi, M.; Shokrgozar, M. A.; Atyabi, F.; Hosseinkhani, H. Review: Silk Fibroin Nanoparticle As a Novel Drug Delivery System. *J. Controlled Release* **2015**, *206*, 161−176.

(12) Lozano-Pérez, A. A.; Rivero, H. C.; Hernández, M. d. C. P.; Pagán, A.; Montalbán, M. G.; Víllora, G.; Cénis, J. L. Silk Fibroin Nanoparticles: Efficient Vehicles for the Natural Antioxidant Quercetin. *Int. J. Pharm.* **2017**, *518*, 11−19.

(13) Xiao, L.; Lu, G.; Lu, Q.; Kaplan, D. L. Direct Formation of Silk Nanoparticles for Drug Delivery. *ACS Biomater. Sci. Eng.* **2016**, *2*, 2050−2057.

(14) Wongpinyochit, T.; Johnston, B. F.; Seib, F. P. Manufacture and Drug Delivery Applications of Silk Nanoparticles. *J. Visualized Exp.* **2016**, *116*, No. e54669.

(15) Reis, C. P.; Neufeld, R. J.; Ribeiro, A. J.; Veiga, F. Nanoencapsulation I. Methods for Preparation of Drug-Loaded Polymeric Nanoparticles. *Nanomedicine* **2006**, *2*, 8−21.

(16) Shi, P.; Goh, J. C. H. Self-Assembled Silk Fibroin Particles: Tunable Size and Appearance. *Powder Technol.* **2012**, *215*−*216*, 85−90.

(17) Deegan, R. D.; Bakajin, O.; Dupont, T. F.; Huber, G.; Nagel, S. R.; Witten, T. A. Capillary Flow As the Cause of Ring Stains From Dried Liquid Drops. *Nature* **1997**, *389*, 827−829.

(18) Hu, H.; Larson, R. G. Evaporation of a Sessile Droplet on a Substrate. *J. Phys. Chem. B* **2002**, *106*, 1334−1344.

(19) Cazabat, A.-M.; Guéna, G. Evaporation of Macroscopic Sessile Droplets. *Soft Matter* **2010**, *6*, 2591−2612.

(20) Marin, A. G.; Gelderblom, H.; Susarrey-Arce, A.; van Houselt, A.; Lefferts, L.; Gardeniers, J. G. E.; Lohse, D.; Snoeijer, J. H. Building Microscopic Soccer Balls with Evaporating Colloidal Fakir Drops. *Proc. Natl. Acad. Sci. U.S.A.* **2012**, *109*, 16455−16458.

(21) Zhang, X.; Wang, Y.; Watanabe, S.; Uddin, M. H.; Li, D. Evaporation-Induced Flattening and Self-assembly of Chemically Converted Graphene on a Solid Surface. *Soft Matter* **2011**, *7*, 8745−8748.

(22) Erbil, H. Y. Evaporation of Pure Liquid Sessile and Spherical Suspended Drops: A Review. *Adv. Colloid Interface Sci.* **2012**, *170*, 67−86.

(23) Lin, Z. *Evaporative Self-Assembly of Ordered Complex Structures*; World Scientific, 2012.

(24) *Droplet Wetting and Evaporation: From Pure to Complex Fluids*; Brutin, D., Ed.; Elsevier, 2015.

(25) Vitale, S. A.; Katz, J. L. Liquid Droplet Dispersions Formed by Homogeneous Liquid−Liquid Nucleation: "The Ouzo Effect". *Langmuir* **2003**, *19*, 4105−4110.

(26) Aschenbrenner, E.; Bley, K.; Koynov, K.; Makowski, M.; Kappl, M.; Landfester, K.; Weiss, C. K. Using the Polymeric Ouzo Effect for the Preparation of Polysaccharide-Based Nanoparticles. *Langmuir* **2013**, *29*, 8845−8855.

(27) Lepeltier, E.; Bourgaux, C.; Couvreur, P. Nanoprecipitation and the "Ouzo effect": Application to Drug Delivery Devices. *Adv. Drug Delivery Rev.* **2014**, *71*, 86−97.

(28) Aubry, J.; Ganachaud, F.; Addad, J.-P. C.; Cabane, B. Nanoprecipitation of Polymethylmethacrylate by Solvent Shifting: 1. Boundaries. *Langmuir* **2009**, *25*, 1970−1979.

(29) Schubert, S.; Delaney, J. T., Jr.; Schubert, U. S. Nanoprecipitation and Nanoformulation of Polymers: From History to Powerful Possibilities Beyond Poly(Lactic Acid). *Soft Matter* **2011**, *7*, 1581−1588.

(30) Yan, X.; Delgado, M.; Fu, A.; Alcouffe, P.; Gouin, S. G.; Fleury, E.; Katz, J. L.; Ganachaud, F.; Bernard, J. Simple but Precise Engineering of Functional Nanocapsules through Nanoprecipitation. *Angew. Chem., Int. Ed.* **2014**, *53*, 6910−6913.

DOI: 10.1021/acs.langmuir.7b01579
Langmuir 2017, 33, 7780−7787

(31) Yang, H.; Wang, Y.; Song, Y.; Qiu, L.; Zhang, S.; Li, D.; Zhang, X. Assembling of Graphene Oxide in an Isolated Dissolving Droplet. *Soft Matter* **2012**, *8*, 11249−11254.
(32) Yang, H.; Song, Y.; Downton, M. T.; Wang, S.; Xu, J.; Hou, Z.; Zhang, X. Tailoring Graphene Oxide Assemblies by Pinning on the Contact Line of a Dissolving Microdroplet. *Soft Matter* **2015**, *11*, 8479−8483.
(33) Jativa, F.; Schütz, C.; Bergström, L.; Zhang, X.; Wicklein, B. Confined Self-Assembly of Cellulose Nanocrystals in a Shrinking Droplet. *Soft Matter* **2015**, *11*, 5374−5380.
(34) Poesio, P.; Beretta, G. P.; Thorsen, T. Dissolution of a Liquid Microdroplet in a Nonideal Liquid-Liquid Mixture Far from Thermodynamic Equilibrium. *Phys. Rev. Lett.* **2009**, *103*, 064501.
(35) Ban, T.; Aoyama, A.; Matsumoto, T. Self-Generated Motion of Droplets Induced by Korteweg Force. *Chem. Lett.* **2010**, *39*, 1294−1296.
(36) Dietrich, E.; Wildeman, S.; Visser, C. W.; Hofhuis, K.; Kooij, E. S.; Zandvliet, H. J. W.; Lohse, D. Role of Natural Convection in the Dissolution of Sessile Droplets. *J. Fluid Mech.* **2016**, *794*, 45−67.
(37) Graužinytė, M.; Forth, J.; Rumble, K. A.; Clegg, P. S. Particle-Stabilized Water Droplets that Sprout Millimeter-Scale Tubes. *Angew. Chem., Int. Ed.* **2015**, *54*, 1456−1460.
(38) Haase, M. F.; Stebe, K. J.; Lee, D. Continuous Fabrication of Hierarchical and Asymmetric Bijel Microparticles, Fibers, and Membranes by Solvent Transfer-Induced Phase Separation (STRIPS). *Adv. Mater.* **2015**, *27*, 7065−7071.
(39) Song, Y.; Lu, Z.; Yang, H.; Zhang, S.; Zhang, X. Dissolution of Sessile Microdroplets of Electrolyte and Graphene Oxide Solutions in an Ouzo System. *Langmuir* **2016**, *32*, 10296−10304.
(40) Yang, Y.; Dicko, C.; Bain, C. D.; Gong, Z.; Jacobs, R. M. J.; Shao, Z.; Terry, A. E.; Vollrath, F. Behavior of Silk Protein at the Air−Water Interface. *Soft Matter* **2012**, *8*, 9705−9712.
(41) Chen, X.; Shao, Z.; Knight, D. P.; Vollrath, F. Conformation Transition Kinetics of Bombyx Mori Silk Protein. *Proteins* **2007**, *68*, 223−231.
(42) Chen, X.; Knight, D. P.; Shao, Z.; Vollrath, F. Conformation Transition in Silk Protein Films Monitored by Time-Resolved Fourier Transform Infrared Spectroscopy: Effect of Potassium Ions on Nephila Spidroin Films. *Biochemistry* **2002**, *41*, 14944.
(43) Yong, J.; Chen, F.; Yang, Q.; Du, G.; Shan, C.; Bian, H.; Farooq, U.; Hou, X. Bioinspired Transparent Underwater Superoleophobic and Anti-Oil Surfaces. *J. Mater. Chem. A* **2015**, *3*, 9379.
(44) Zhang, X.; Lu, Z.; Tan, H.; Bao, L.; He, Y.; Sun, C.; Lohse, D. Formation of Surface Nanodroplets under Controlled Flow Conditions. *Proc. Natl. Acad. Sci. U.S.A.* **2015**, *112*, 9253−9257.
(45) Tan, H.; Diddens, C.; Lv, P.; Kuerten, J. G. M.; Zhang, X.; Lohse, D. Evaporation-Triggered Microdroplet Nucleation and the Four Life Phases of an Evaporating Ouzo Drop. *Proc. Natl. Acad. Sci. U.S.A.* **2016**, *113*, 8642−8647.
(46) Wang, M.; Liechti, K. M.; Wang, Q.; White, J. M. Self-Assembled Silane Monolayers: Fabrication With Nanoscale Uniformity. *Langmuir* **2005**, *21*, 1848−1857.
(47) Zhang, X. H.; Maeda, N.; Craig, V. S. J. Physical Properties of Nanobubbles on Hydrophobic Surfaces in Water and Aqueous Solutions. *Langmuir* **2006**, *22*, 5025−5035.
(48) Lessel, M.; Bäumchen, O.; Klos, M.; Hähl, H.; Fetzer, R.; Paulus, M.; Seemann, R.; Jacobs, K. Self-Assembled Silane Monolayers: An Efficient Step-by-Step Recipe for High-Quality, Low Energy Surfaces. *Surf. Interface Anal.* **2015**, *47*, 557−564.

DOI: 10.1021/acs.langmuir.7b01579
Langmuir 2017, 33, 7780−7787